Imperial College London

Polyurethane Corrugated Composites for Morphing Wing Applications

by

Kitchanon Ruangjirakit

Department of Aeronautics
Imperial College London
London SW7 2AZ

A thesis submitted to Imperial College London for the degree of
Doctor of Philosophy

October 2013

Abstract

The morphing wing can be considered as a wing with seamless control surfaces and high-lift devices, which is capable of changing its shape during flight. As a result, an aircraft with the morphing wing can fly multi-mission tasks effectively and efficiently. The morphing wing should be stiff in spanwise direction to withstand aerodynamic and actuation loads while, in chordwise direction, the wing should be compliant in order to allow shape change. In this thesis, corrugated carbon fibre reinforced polyurethane composite is introduced as a candidate for the skin of morphing wing applications as the corrugated composite is considered highly anisotropic.

A parametric study of three corrugated profiles (sinusoidal, trapezoidal and U-shape) with different amplitudes and unit cell lengths was performed numerically using finite element analysis and compared with analytical model in order to investigate the effects of the corrugation geometry on the mechanical response under tensile load. The results indicate that the trapezoidal profile offers the lowest extensional stiffness followed by U-shape and sinusoidal, respectively. In terms of corrugation geometry, the extensional stiffness of the corrugation is inversely proportional to both unit cell length and amplitude.

An aerodynamic analysis of an aerofoil with corrugated lower skin was performed experimentally at four different Reynolds numbers and compared with an aerofoil with smooth skin. The conclusion drawn from the wind tunnel testing is that the aerofoil with corrugated skin on the pressure side is feasible to be used for a morphing wing of a small unmanned aerial vehicle (UAV) that operates at Reynolds number of approximately 10^5.

A bench-top demonstrator was constructed as a proof of concept and experimentally tested for repeatability and structural integrity. Moreover, the mechanical advantage was evaluated through a simple experiment.

Declaration of Originality

I hereby confirm that the work presented in this thesis is the personal work of the author and that the work of others is appropriately referenced.

Kitchanon Ruangjirakit

Acknowledgements

With the deepest gratitude, I would like to thank my supervisor, Professor Lorenzo Iannucci, for his magnificent support and inspirational advice. His guidance and encouragement contributed decisively to improve my academic maturity.

I would like to also thank Mr.Senior and Mr.Cole from the Composites Laboratory, Mr.James and Mr.Hutchins from Aeronautics workshop, and Mr. Meggyesi for great advice and helpful assistance. I would like to acknowledge Dr.Ankersen for his useful suggestions on finite element analysis.

Special thanks to all my colleagues who share the same office with me and also those who are next door. Without you, my life at college would not be fulfilled.

This research would not be possible without the support from the Royal Thai Government, who funded my studies in the UK from A-level to PhD. Their initiative of investing in degrees abroad to improve an academic personnel in Thailand is truly admirable.

I would like to wholeheartedly thank my friends and flatmates: Apinya, Aukkarapoan, Arpamas, Ploy, Benjapon, Pheeraphat, Naporn and Tuckie, for keeping me entertained and motivated and for their supportive encouragement.

Last but not least, I am deeply indebted to my parents, my brother and my beloved girlfriend for their attentive and caring support and for their warm embrace throughout my time pursuing this PhD.

K. Ruangjirakit
London, October 2013

Contents

Abstract **1**

Declaration of Originality **2**

Acknowledgements **3**

Contents **7**

List of Figures **13**

List of Tables **15**

Nomenclature **21**

1 Introduction **22**

1.1 Overview and Motivation 22

1.2 Research Objectives 27

1.3 Statement of Originality 28

1.4 Outline of the Thesis 29

2 Literature Review **30**

2.1 Benefits and Limitations of a Morphing Aircraft 30

2.2 Overview of Morphing Wing Concepts 35

2.3 Introduction to Smart Materials, Actuators and Structures . . . 45

2.3.1 Piezoelectric materials 46

2.3.2 Shape Memory Alloys (SMAs) and Shape Memory Polymers (SMPs) 47

2.3.3 Electroactive polymers (EAPs) 49

2.3.4 Multi-stable structures 50

2.4 Overview of Corrugated Composite Skin Concept 51

2.5 Flexible Composite Skin for Morphing Wing 56

2.5.1 Introduction to polyurethanes . . . 56
2.5.2 Carbon fibre reinforced polyurethane composites and its applications . . . 58
2.6 Chapter Summary . . . 61

3 Carbon Fibre Reinforced Polyurethane Composite: Fabrication and Characterisation 63
3.1 Fabrication of Carbon Fibre Reinforced Polyurethane Composite 64
3.1.1 Manufacturing technique . . . 64
3.1.2 Material selection process . . . 68
3.1.3 Manufacturing process of test specimens . . . 72
3.2 Characterisation of Carbon Fibre Reinforced Polyurethane Composite . . . 78
3.2.1 Tensile test . . . 78
3.2.2 Compression test . . . 80
3.2.3 In-plane shear test . . . 81
3.2.4 Flexural test . . . 84
3.2.5 Comments on the test results . . . 87
3.2.6 Neat resin tensile test . . . 88
3.3 Chapter Summary . . . 94

4 Carbon Fibre Reinforced Polyurethane Corrugated Composite 96
4.1 Tensile Test of Corrugated Composite . . . 97
4.1.1 Infusion of corrugated composite panel . . . 97
4.1.2 Specimen preparation . . . 106
4.1.3 Tensile test of corrugated specimens . . . 108
4.2 Finite Element Model of Corrugated Composite . . . 112
4.2.1 Generation of finite element model of carbon fibre reinforced polyurethane corrugated composite . . . 113
4.2.2 Validation of the finite element corrugated model . . . 121
4.3 Parametric Study of Corrugated Composite Structure . . . 125
4.3.1 Analytical models of corrugated composites . . . 125
4.3.2 Effects of cross-sectional profiles on corrugated structural response under tensile load . . . 131
4.3.3 Effects of dimensions of corrugation on corrugated structural response under tensile load . . . 137
4.4 Chapter Summary . . . 139

5 Aerodynamic Analysis of a Morphing Wing With Corrugated Skin 142
5.1 Previous Studies on Aerodynamic of Corrugated Wing 142
5.2 Wind Tunnel Test 143
5.2.1 Design of wind tunnel models 143
5.2.2 Testing procedure 146
5.3 Results and Discussion 151
5.3.1 Possible sources of error 152
5.3.2 Comparison between smooth conventional aerofoil and analytical results 153
5.3.3 Comparison between smooth conventional and corrugated aerofoils 156
5.3.4 Further recommendations 159
5.4 Chapter Summary 161

6 Conceptual Design of a Corrugated Composite Aerofoil Bench-top Model 163
6.1 Design and Analysis of the Bench-top Model 163
6.1.1 Finite element analysis of the bench-top model 168
6.2 Manufacturing 172
6.3 Experimental Testing 174
6.3.1 Results and discussion 175
6.3.2 Material problems observed during the experimental testing 179
6.4 Chapter Summary 180

7 Concluding Remarks 181
7.1 Conclusions 181
7.2 Recommendations for Future Research 184

References 185

A Experimental Test Results of Flat Specimens 201
A.1 Tensile Test 201
A.2 Compression Test 206
A.3 In-plane Shear Test 211
A.4 Flexural test 213
A.5 Evaluation of machine compliance 214
A.6 Neat Resin Tensile Test 217

B Wind Tunnel Test Results **219**

B.1 Aerodynamic Characteristics of Conventional Wing (NACA 4412) 219

B.2 Comparison Between Conventional and Corrugated Wings . . . 222

List of Figures

1.1 Key areas in morphing wing design 23
1.2 Drawing of a dragonfly forewing. 24
1.3 Different wing geometries of a hawk from low speed flight (left) to high speed flight (right). 24

2.1 Graphical representation showing morphing benefit in terms of penalty factor against fuel consumption. 33
2.2 "Radar" or "Spider" plot. 34
2.3 Overview of the content in NASA's Morphing Project. 36
2.4 An artist's rendering of NASA's morphing aircraft. 37
2.5 Phase 2 wind tunnel model of DARPA Smart Wing programme. 39
2.6 ETDM concept. 39
2.7 NextGen Batwing concept. 40
2.8 The articulated cells concept. 41
2.9 Illustration of compliant adaptive trailing edge. 42
2.10 Belt-rib concept. 42
2.11 DLR finger concept. 43
2.12 Illustration of (a) planform view and (b) span view of HECS wing. 44
2.13 Possible fuel bladder configurations. 44
2.14 Chiral core aerofoil. 45
2.15 Maximum stroke versus blocked force for piezoelectric actuators. 47
2.16 Stiffness variation with temperature of SMPs. 48
2.17 Stack sequence of a multi-stable panel. 50
2.18 Stable configurations of a multi-stable panel. 50
2.19 Corrugated composites concept. 53
2.20 Typical dragonfly wing profiles at different locations along spanwise direction. 54
2.21 Corrugated sandwich structure of MSP. 55
2.22 Durometer scales. 57

2.23 Flexible Matrix Composite (FMC) and PAM X-Frame actuator. 60
2.24 Morphing wing with carbon fibre reinforced polyurethane composite skin actuated by a RMA. 61

3.1 Schematic of vacuum-bagged mandrel assembly. 65
3.2 (a) In-plane flow and (b) Through-plane flow. 67
3.3 Pressure gradient during infusion. 68
3.4 Different weave styles: plain (left), twill (middle) and satin (right). 71
3.5 Lay-up sequence of the RIFT method. 73
3.6 Instruments set-up prior to infusion. 74
3.7 Ultrasonic C-Scan images of two panels (6 plies) manufactured from different runs. 76
3.8 Ultrasonic C-Scan images of two panels (6 plies) manufactured side-by-side. 76
3.9 Schematic drawings of compressive, tensile and shear specimens showing different end-tab configurations. 77
3.10 Stress-strain curves of tensile specimens in warp direction. . . . 79
3.11 Stress-strain curves of tensile specimens in weft direction. 80
3.12 Optical micrographs of tensile specimen in (a) warp and (b) weft directions. 80
3.13 Example of stress-strain curve of compressive test in warp direction. 82
3.14 Example of stress-strain curve of compressive test in weft direction. 83
3.15 Optical micrograph of compressive specimen. 83
3.16 In-plane shear stress-strain relationship of carbon/PU laminates. 84
3.17 Schematic drawing of the flexural specimens. 85
3.18 Flexural stress-strain relationships of specimens in warp direction. 86
3.19 Flexural stress-strain relationships of specimens in weft direction. 87
3.20 Woven carbon fibre fabric (a) warp dominate surface and (b) weft dominate surface. 87
3.21 Ultrasonic C-scan images from different infusions. 89
3.22 Dog-bone specimen. 90
3.23 An example of load-displacement plot used to calculate the machine compliance. 92
3.24 Example of stress-strain curve of tensile test of Biresin® G27 LR. 93
3.25 Images of failed specimens and fracture surface 94

4.1 Different cross-sectional profiles of the corrugation. 97
4.2 Schematic drawing of the corrugated mould. 98
4.3 Photo of the aluminium corrugated mould. 98
4.4 Lay-up sequence for RIFT of corrugated panels. 98
4.5 Infusion process of a preliminary run. 101
4.6 Top and bottom surfaces of a panel from a preliminary run. . . 101
4.7 Inserts used to pre-form carbon fabric. 103
4.8 Pre-form fabric and peel ply on mould. 104
4.9 Photo of 'pleats' used in later infusions. 105
4.10 Surface finish of a corrugated composite panel from a later run. 106
4.11 Panel placed on the mould before vacuum curing process of epoxy adhesive. 107
4.12 Tensile load-displacement relationship of corrugated carbon/PU laminates. 109
4.13 A corrugated composite specimen during tensile test. 110
4.14 Tensile load-displacement relationship of corrugated composite specimens. 111
4.15 Optical micrograph of a corrugated tensile specimen showing delamination at the curved region. 112
4.16 Optical micrograph of a corrugated tensile specimen showing microbuckling region on the compression face. 113
4.17 Schematic drawing of the FE corrugated model with constraints (a quarter of a repeated cell). 114
4.18 Continuum element. 116
4.19 Typical traction-separation response. 118
4.20 Load-displacement curves of different values of t_n^0 as compared to experimental results. 122
4.21 Load-displacement curves of different values of $G_{n,c}$ as compared to experimental results. 123
4.22 Load-displacement curves of different mesh sizes with experimental results. 125
4.23 Finite element model showing delamination initiated from curved regions. 126
4.24 Load-displacement curves of analytical model, finite element model and experiment. 127

4.25 Comparison of initial stiffness (initial slope of load-displacement curve) of sinusoidal corrugated profile (A = 7.5 mm and λ = 15 mm) obtained from each approach. 134
4.26 Comparison of initial stiffness (initial slope of load-displacement curve) of each corrugation profile. 136
4.27 Finite element model of sinusoidal profile showing delamination. 137
4.28 Finite element model of trapezoidal profile showing delamination. 138
4.29 Finite element model of U-shape profile showing delamination. . 139
4.30 Results from parametric study of sinusoidal corrugation. 140
4.31 Results from parametric study of trapezoidal corrugation. 141
4.32 Results from parametric study of U-shape corrugation. 141

5.1 NACA 4412 aerofoil. 144
5.2 Schematic drawings of smooth conventional aerofoil and corrugated skin aerofoil 145
5.3 Wing setup in the wind tunnel. 146
5.4 Variable of drag coefficient with Reynolds number of a cylinder. 147
5.5 Plot of Λ against t/c. 151
5.6 Lift coefficient of conventional wing at different angles of attack (Re = 280,000). 154
5.7 Drag coefficient of conventional wing at different angles of attack (Re = 280,000). 155
5.8 Analytical and experimental lift curves of conventional and corrugated aerofoils (Re = 280,000). 156
5.9 Lift coefficient of corrugated wing at different angles of attack (Re = 280,000). 157
5.10 Drag coefficient of corrugated wing at different angles of attack (Re = 280,000). 158
5.11 Drag polar of corrugated wing at different angles of attack (Re = 280,000). 158

6.1 NACA 0014 aerofoil. 164
6.2 N-216 NEXLINE from Physik Instrumente. 166
6.3 Firgelli linear actuator with controller LAC, potentiometer and batteries. 167
6.4 Schematic drawing of the aerofoil section with corrugated lower skin. 168

6.5 Finite element model of the bench-top demonstrator with boundary conditions. . . . 169
6.6 Finite element model of the bench-top demonstrator with mesh. 171
6.7 Trailing edge downwards deflection. . . . 171
6.8 Trailing edge upwards deflection. . . . 172
6.9 Finite element model with curved structures added to the top skin. . . . 172
6.10 Finite element model with trapezoidal structures added to the top skin. . . . 172
6.11 Mould used for the corrugated composite lower skin. . . . 173
6.12 Assembly of the bench-top demonstrator. . . . 174
6.13 Complete setup of experimental testing of corrugated aerofoil. . 174
6.14 Tralling edge deflection (downward) of actual model and FE model. . . . 175
6.15 Tralling edge deflection (upward) of actual model and FE model. 176
6.16 Plot of required actuation force against actuation arm movement. 177
6.17 Aerofoil model with the weight attached to the trailing edge. . . 178

A.1 Stress-strain curves of tensile test in warp direction (longitudinal). 202
A.2 Stress-strain curves of tensile test in warp direction (transverse). 203
A.3 Stress-strain curves of tensile test in weft direction (longitudinal). 203
A.4 Stress-strain curves of tensile test in weft direction (transverse). 204
A.5 Stress-strain curves of compressive specimens in warp direction. 207
A.6 Stress-strain curves of compressive specimens in warp direction (continued). . . . 208
A.7 Stress-strain curves of compressive specimens in weft direction. . 209
A.8 Stress-strain curves of in-plane shear test. . . . 211
A.9 Load-displacement curves measured from machine cross-head and strain gauge used to calculate the machine compliance. . . . 215
A.10 Load-displacement curves measured from machine cross-head and strain gauge used to calculate the machine compliance (continued). . . . 216
A.11 Stress-strain curves of neat resin tensile test. . . . 217

B.1 Lift and drag curves of conventional wing at different Reynolds numbers. . . . 220
B.2 Lift and drag curves of conventional wing at different Reynolds numbers (continued). . . . 221

B.3 Comparison of aerodynamic properties at Re = 280,000. 222
B.4 Comparison of aerodynamic properties at Re = 397,000. 223
B.5 Comparison of aerodynamic properties at Re = 497,000. 224
B.6 Comparison of aerodynamic properties at Re = 596,000. 225

List of Tables

2.1 Effects of geometrical parameters of the wing on aircraft performance. 32
2.2 Summary of smart materials and actuators. 52
2.3 Advantages of Polyurethanes over Conventional Rubbers. 57

3.1 Advantages against disadvantages of RIFT. 69
3.2 Properties of mixed polyurethane resin compared with Hexflow® RTM6 and Adiprene® K TE92. 70
3.3 Comparison of properties between each weave style. 71
3.4 Properties of the woven carbon fibre tape from Eurocarbon. . . 72
3.5 Dimensions of flat test specimens 77
3.6 Mechanical properties obtained from tensile test of flat carbon/PU specimens. 79
3.7 Young's moduli and ultimate compressive strengths obtained from compression test of flat carbon/PU specimens. 81
3.8 In-plane shear modulus and strength obtained from in-plane shear test of flat carbon/PU specimens. 82
3.9 Dimensions of flexural test specimens [1]. 84
3.10 Summary of flexural moduli and strengths in warp and weft directions. 87
3.11 Dimensions of dog-bone specimen. 90
3.12 Comparison of mechanical properties obtained from experiment and technical data sheet. 93

4.1 Dimensions of the corrugated mould. 99
4.2 Dimensions of the corrugated composite tensile specimen. 107
4.3 Dimensions of the finite element corrugated composite model. . 114
4.4 Mechanical properties of the lamina. 115
4.5 Surface-based cohesive behaviour parameters for carbon/epoxy composite. 121

4.6 Surface-based cohesive behaviour parameters for carbon/polyurethane composite. 124
4.7 Analytical expressions for sinusoidal corrugations. 128
4.8 Analytical expressions for trapezoidal corrugations. 129
4.9 Analytical expressions for U-shape corrugations. 130
4.10 Dimensions of each corrugation profile used in finite element and analytical models. 131
4.11 Dimensions of FE flexural models. 133
4.12 Mechanical properties of each sub-layer. 133
4.13 Summary of advantages and limitations of each approach. . . . 135

6.1 Properties of VeroBlack FullCure 870. 165
6.2 Dimensions of the corrugated lower skin of the bench-top model. 168
6.3 A summary of the mesh of each instance of the FE aerofoil model. 170
6.4 Mechanical efficiency evaluation of the bench-top demonstrator. 179

A.1 Dimensions of flat tensile specimens 202
A.2 Raw data from tensile test. 205
A.3 Dimensions of flat compressive specimens 206
A.4 Raw data from compression test. 210
A.5 Raw data from in-plane shear test. 212
A.6 Raw data from flexural test in warp direction. 213
A.7 Raw data from flexural test in weft direction. 213
A.8 Data used to calculate machine compliance. 216
A.9 Raw data from neat resin tensile test. 218

Nomenclature

Abbreviations

AAF	Air-to-Air Fighter
AAW	Active Aeroelastic Wing
AFRL	Air Force Research Laboratory (US)
CFD	Computational Fluid Dynamics
CFRP	Carbon Fibre Reinforced Plastic
CO_2	Carbon Dioxide
CO	Carbon Monoxide
CRG	Cornerstone Research Group (US)
DARPA	Defense Advanced Research Projects Agency (US)
DCB	Double Cantilever Beam
DLR	Deutsches Zentrum für Luft- und Raumfahrt (Germany)
DSLR	Digital Single Lens Reflex
EAP	Electroactive Polymer
ETDM	Eccentric Torque-tube Disk Mechanism
FE	Finite Element
FMC	Flexible Matrix Composite
GFRP	Glass Fibre Reinforced Plastic
HECS	Hyper-Elliptic Cambered Span concept

ICI	Imperial Chemical Industries (UK)
ICSTM	Imperial College of Science, Technology and Medicine (UK)
ISO	International Organization for Standadization
MACW	Mission Adaptive Compliant Wing
MAV	Micro Air Vehicle
MAW	Mission Adaptive Wing
MFC	Macro-Fibre Composite
MIT	Massachusetts Institute of Technology (US)
MSP	Morphing Skin Panel
NASA	National Aeronautics and Space Agency (US)
NGC	Northrop Grumman Corporation (US)
NO_x	Nitrogen Oxides
PAM	Pneumatic Artificial Muscle
PIV	Particle Image Velocimetry
PMMA	Poly(methyl methacrylate)
PTFE	Polytetrafluoroethylene
PTMG	Polytetramethylene Glycol
PU	Polyurethane
RIFT	Resin Infusion under Flexible Tooling
RMA	Rubber Muscle Actuator
RTM	Resin Transfer Moulding
SMA	Shape Memory Alloy
SMP	Shape Memory Polymer
TE	Trailing Edge

TML	Tokyo Sokki Kenkyojo Co., Ltd. (Japan)
UAV	Unmanned Aerial Vehicle
VARTM	Vacuum-Assisted Resin Transfer Moulding

Greek Letters

α	Angle of attack [degrees]
δ_n, δ_s, δ_t	Traction separations for surface-based cohesive behaviour [mm]
δ_n^0, δ_s^0, δ_t^0	Peak values of contact separation when the separation is purely along the contact normal or purely in the first or the second shear direction, respectively [mm]
ϵ_{11}	Strain in global x-direction
ϵ_{22}	Strain in global y-direction
ϵ_f	Flexural strain
λ	Wavelength of the corrugation [mm]
μ	Air dynamic viscosity [kg/(m·s)]
ν_{12}	Poisson's ratio in x-y plane
ω	Angular velocity [rad/s]
ρ_∞	Density of air [kg/m^3]
ρ_c	Density of carbon fibre reinforced polyurethane [kg/m^3]
σ_f	Flexural stress [Pa]
σ	Tensile stress [Pa]
$\tau_{12,u}$	In-plane shear strength in x-y plane [Pa]
θ_x, θ_y, θ_z	Rotation about x, y or z axis [degree or radian]

Variables

A_0	Initial cross-sectional area of the laminates [m^2]
A	Amplitude of the corrugation [mm]

AR	Aspect ratio of a wing
A_{xx}	Equivalent extensional rigidity/stiffness [N/m]
b	Wing span [m]
C_D	Drag coefficient
C_{d0}	Zero-lift drag coefficient of an aerofoil
c	Chord of the aerofoil [m]
C_l	Lift coefficient of an aerofoil
C_{Lmax}	Maximum wing lift coefficient
$C_{m,25\%c}$	Pitching moment coefficient about a quarter chord point of an aerofoil
CTE	Coefficient of Thermal Expansion [1/°C]
D	Drag [N]
d	Drag force per unit span[N/m]
D_{coh}	Scalar damage variable of cohesive surface
E_{11}	Young's modulus in global x-direction [Pa]
E_{22}	Young's modulus in global y-direction [Pa]
E_f	Flexural modulus [Pa]
E_{xx}	Equivalent tensile elastic modulus [Pa]
G_{12}	In-plane shear modulus in x-y plane [Pa]
G_{13}	In-plane shear modulus in x-z plane [Pa]
G_{23}	In-plane shear modulus in y-z plane [Pa]
G_c	Critical energy release rate [N/m]
$G_{n,c}, G_{s,c}, G_{t,c}$	Critical fracture energies required to cause failure in the normal and two shear directions, respectively [N/m]
G_n, G_s, G_t	Work done by traction in the normal and two shear directions, respectively [N/m]

$\mathbf{K}$	Elastic constitutive matrix for surface-based cohesive behaviour
L	Lift [N]
l	Lift force per unit span [N/m]
$m_{25\%c}$	Pitching moment per unit span about a quarter chord point [N·m]
P	Applied load [N]
r	Radius of the U-shape corrugation [m]
Re	Reynolds number
$\bar{t}_n, \bar{t}_s, \bar{t}_t$	Contact stress components predicted by the elastic traction-separation behaviour for the current separation without damage [N/mm^2]
T_g	Glass transition temperature [°C]
t	Thickness of the corrugated panel [m]
t_n, t_s, t_t	Traction stresses for surface-based cohesive behaviour [N/mm^2]
t_n^0, t_s^0, t_t^0	Peak values of the contact stress when the separation is either purely normal to the interface or purely in the first or the second shear direction, respectively [N/mm^2]
U_∞	Free stream velocity [m/s]
UCS_{11}	Ultimate Compressive Strength in global x-direction [Pa]
UCS_{22}	Ultimate Compressive Strength in global y-direction [Pa]
UTS_{11}	Ultimate Tensile Strength in global x-direction [Pa]
UTS_{22}	Ultimate Tensile Strength in global y-direction [Pa]
u_{xx}	Elongation of a corrugation unit cell [m]
u_x, u_y, u_z	Translation in x, y or z direction [mm]
w	Width of the corrugated panel [m]
$(-)_{sine}$	Relating to sinusoidal corrugations

$(-)_{trap}$	Relating to trapezoidal corrugations
$(-)_{Ushape}$	Relating to U-shape corrugations

Chapter 1

Introduction

1.1 Overview and Motivation

In the aerospace industry, one of the ultimate goals that aircraft designers have been pursuing is to improve the performance of an aircraft in order to fly a range of flight conditions efficiently. The deployment of conventional flaps or slats in current commercial aircrafts allows the aircraft to fly in various flight conditions, but the performance at each condition is not optimised. One potential solution to overcome this problem is through continuous shape change of the wing during flight. In fact, this concept of having a wing which is able to radically change its shape during flight can be defined as a *'morphing wing'*. This is not a new idea. It was first implemented in their successful controlled and powered flight by The Wright Brothers dated back to December 1903. The Wright Flyer, the first heavier-than-air vehicle, was controlled using a set of pulleys and cables to twist the wingtips in order to generate control forces. This approach was termed as wing warping at that time [2]. Since then, as the speed and payloads of the aircraft increase, discrete control surfaces in the form of elevators and ailerons have been used extensively to provide control and stability [3]. The morphing wing concept introduces many complicated problems for engineers to solve. These complications include a requirement for a more efficient actuation system, an optimised distribution of sensors, and a flexible skin [4]. This has led to a great number of extensive research studies throughout the world to reduce the limitations of implementing the morphing wing concept to an aircraft.

The design of a morphing wing requires an integration of four key areas as shown in figure 1.1 [5]. The flight performance depends on flow characteristics

around the wing, therefore, an aerodynamic analysis must be performed to evaluate the best morphing strategy. Structural elasticity is the property that provides shape change and, simultaneously, carries internal and external loads such that the required aerodynamic shape is maintained throughout the morphing process. Actuators and sensors are used to drive actuation mechanism in order to change the shape of the wing and to monitor the current flight condition state. Lastly, control systems provide the correct amount of shape change according to the flight conditions and adjust the amount of power required to drive the actuator.

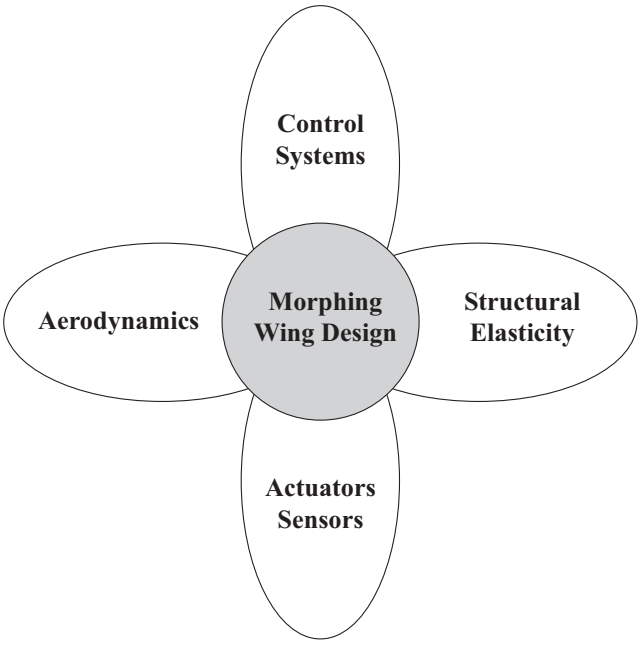


Figure 1.1: Key areas in morphing wing design, adapted from [5].

The inspiration of the morphing wing concept comes mainly from the flight of birds and insects. The configuration of the bird's wing and tail can be constantly changed in flight to maximise flying performance subject to different flight conditions (see figure 1.3). For example, a hawk is able to spread its wing to increase the aspect ratio and loiter in a low speed/high endurance flight using air currents and thermals at high altitude. Immediately after detecting a prey, the wing is furled to high speed/high manoeuvrability configuration in order to dash down at high speed to catch the pray [6]. Not only the wings of various birds are thoroughly studied, a number of insect wings are also of great interest, particularly the wings of the dragonfly. The wing sections of the dragonfly are non-smooth (as shown in figure 1.2) and, therefore, have adverse effects on aerodynamic performance. However, recent studies [7, 8] suggested

that at low Reynolds number (Re<70,000), non-smooth wing profile, similar to dragonfly's wing, generates higher lift to drag ratio. This is due to unsteady vortex structures generated in the valley sections of the wing that energise the flow such that the flow separation is suppressed [9, 10]. Moreover, Kim *et al.* [11] suggested that an increase in lift of the corrugated aerofoil occurs as a result of the corrugations on the pressure side, while the corrugations on the suction side do not contribute to the lift production. This low Reynolds number wing section is useful and suitable for low speed air vehicle such as Micro Air Vehicles (MAVs) .

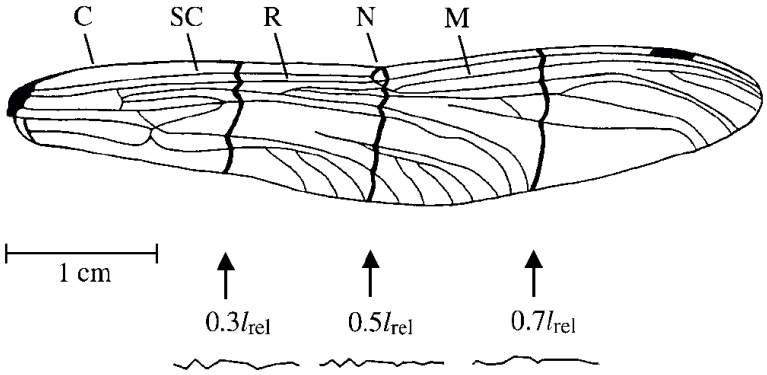


Figure 1.2: Drawing of a dragonfly forewing [10].

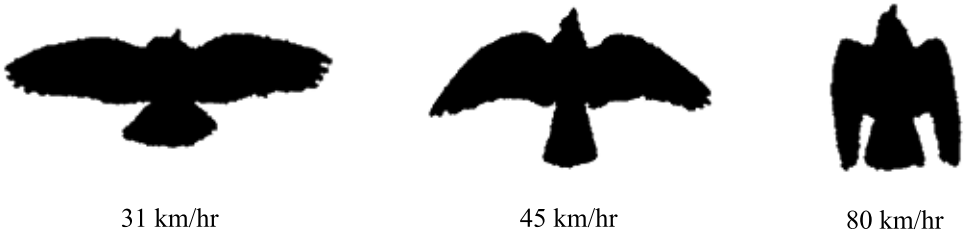


Figure 1.3: Different wing geometries of a hawk from low speed flight (left) to high speed flight (right), adapted from [6].

Morphing technology is not only restricted to applications related to wings, but can also be broadly applied to a variety of parts of an aircraft. Jha and Kudva [4] showed a change in positions of Concorde's nose and visor as an example of fuselage morphing and thrust vectoring in V22 Osprey as an example of engine morphing. Although fuselage and engine morphing is possible, wing is considered to be the most influential part of the aircraft as the flight characteristics and aircraft stability are determined by the air flow around the wing.

Therefore, most of research studies in morphing technology for aeronautical applications focus on wing morphing.

The morphing wing technology not only attracts aircraft manufacturers, but has also been developed for military applications, such as, Unmanned Aerial Vehicle (UAV) . Lower aerodynamic load on UAVs increases the possibility of morphing wing technology to be deployed efficiently [12]. UAVs which need initial high speed flight, loiter at low speed for a certain amount of time before returning to its base, can benefit from morphing wing concept. Extending the wing provides an increase in aspect ratio that is superior in low speed loitering whereas, sweptback wing performs better when fast turn and dash are required. As a result, the flight envelope of a UAV with morphing capability could be expanded [13]. Moreover, the drag can also be decreased and the fuel consumption is minimised so that the UAV can fly a multi-mission task more efficiently. Minimum fuel consumption not only means that the UAV can be operated at a lower cost, but also implies that CO, CO_2 and NO_x emissions are less which make a morphing UAV an environmentally friendly air vehicle [14]. In addition to cost savings and *'greener'* UAVs, morphing technology also provides stealth capability to UAVs as the sharp edges of discrete parts are eliminated [6, 12].

Although many morphing concepts have been proposed over the years, a great deal of attention is paid to the design of internal structures while the importance of a compliant skin remains lacking until recently. This is due to the fact that the skin requires a compromise between compliance and stiffness which introduces complications during design process. The skin must be compliant in order to allow shape change, yet stiff enough to withstand aerodynamic and actuation loads, and to maintain required wing profile [15]. The conflicting requirements of the skin lead to development of various concepts. One concept that has received a considerable amount of attention and becomes the main focus of this research is the corrugated composite skin concept. This concept was first proposed by Yokozeki *et al.* [16] as the corrugated structure offers stiffness in the direction parallel to the corrugations and flexibility in the direction transverse to the corrugations. Later researchers from the University of Bristol adopted the corrugated composites idea from Yokozeki *et al.* [16] but using trapezoidal profile. Moreover, three types of fibres which are carbon, glass, and aramid, were investigated and compared with each other [17, 18].

Thill *et al.* [7, 19] also performed a parametric study of corrugated composites of different corrugation profiles, and aerodynamic analysis of a morphing wing with sinusoidal corrugated skin. Finally, Thill *et al.* [20] manufactured a wing demonstrator and tested the corrugated sandwich skin concept in the wind tunnel.

Although Thill and his team from the University of Bristol could introduce corrugated composite skin in a working morphing wing, there were limitations associated with the manufacturing process and current resin system. Thill *et al.* [17] stated that the quality of the corrugated laminates could be improved if the resin transfer moulding (RTM) process was used. Also, epoxy resin is known for brittleness with the ultimate tensile strain of approximately 3-4%. Therefore, in this research study, Resin Infusion under Flexible Tooling (RIFT), which is a variant of the vacuum-assisted RTM process, was introduced and developed to manufacture flat and corrugated composite laminates. Moreover, a more compliant polyurethane (PU) resin system was also introduced. The PU system not only offers higher maximum strain but also cost effective as it can be fully cured without the need for an autoclave. Therefore, low-cost morphing wing applications can be mass produced efficiently. Full detail of the research by Yokozeki *et al.* [16], Thill *et al.* [20] and other researchers working on corrugated composite concept will be further reviewed and discussed in chapter 2.

Another important feature of the morphing wing to be considered is the actuation mechanism. According to Iannucci and Fontanazza [21], the actuation structure for morphing wing should exhibit the following properties:

- Relatively fast dynamics
- Capability to operate over a wide range of flight conditions
- Capability of high recoverable strains
- Capability to combine sensors and actuators
- Low power consumption
- High reliability

Over the past decades, smart materials such as shape memory alloys (SMAs), shape memory polymers (SMPs), auxetic material and piezoelectric material, to name but a few, have become one of the most widely used materials in aerospace field [15]. These smart materials make the morphing wing with seamless control surfaces and high lift devices possible by utilising them as

components of actuation mechanism since they respond effectively to thermal, electrical and magnetic fields [13]. The main advantage of using smart materials in morphing wing is that the weight of the wing can be greatly reduced when a conventional hydraulic actuator is replaced by a smart actuator [22]. However, there are some limitations of using smart actuators. In the case of SMAs, the response time is not fast enough to be used as an actuator for control surfaces since the time required to deflect a control surface is of order of milliseconds, while the response time of the SMAs is normally of order of seconds. Another limitation of some smart materials, for example elctroactive polymers (EAPs), is that large strain can be achieved while only small amount of force is generated whereas a good actuator should be able to produce high actuation force and be able to achieve high strain. Therefore, a suitable smart actuator for morphing wing application should be carefully selected in order to increase the overall performance of the aircraft [23, 24].

1.2 Research Objectives

The main research aim is to develop a corrugated composite concept to be used as a skin of a morphing wing as well as introducing a new resin system (polyurethane) to replace a conventional brittle epoxy system. This unconventional resin system gives more flexibility than epoxy resin, however, it is not widely used, especially in aerospace field, as a matrix for composite laminates. Therefore, a thorough study of carbon fibre reinforced polyurethane resin needs to be conducted in order to understand the characteristics of such a material.

Carbon/polyurethane composite laminates are used to fabricate a corrugated skin for a morphing wing. In order to design a suitable corrugated structure, an understanding of the mechanical properties of carbon/polyurethane corrugated composite needs to be determined. In this research, experimental studies were performed jointly with numerical analysis to allow a detailed understanding of the skin. Another aspect which is also a focus of this research is the aerodynamic performance of the morphing wing with corrugated skin. Wind tunnel tests together with numerical analysis were performed to investigate the overall performance of the wing if enhanced with a corrugated skin. In the last stage of this study, a prototype of the wing section was manufac-

tured to demonstrate that carbon/polyurethane corrugated skin is a potential solution for morphing wing application.

To summarise, the main objectives of this research are outlined as follows:

1. To develop a manufacturing technique to fabricate flat and corrugated carbon/polyurethane composite panels.
2. To evaluate mechanical properties of carbon fibre reinforced polyurethane laminates.
3. To evaluate structural behaviours of carbon/polyurethane corrugated composite.
4. To investigate aerodynamic performance of the wing with corrugated skin and compared with a conventional smooth wing.
5. To manufacture a prototype of the morphing wing to prove the corrugated composite skin concept.

1.3 Statement of Originality

This research programme mainly focuses on the design of an adaptive wing with composite corrugated skin. Although the corrugated skin concept has previously been investigated by a number of researchers, there is no study which combines polyurethane resin with carbon fibre and use RIFT to manufacture corrugated composite. Moreover, a surface-based cohesive behaviour integrated within ABAQUS (version 6.10) was used to numerically investigate the delamination of different carbon/polyurethane corrugated profiles. It should be noted that the delamination analysis of a corrugated structure using the surface-based cohesive behaviour has never been performed before. Finally, a bench-top demonstrator of an aerofoil with lower corrugated skin is proposed. The difference between the bench-top model proposed in this research programme and the models proposed elsewhere is that the corrugation's geometry (amplitude and unit cell length) varies from behind the spar towards the trailing edge, while the corrugation's geometry in other research studies remains unchanged from the spar to the trailing edge. To the author's knowledge, the tailored-corrugated skin has never been published in any literature.

1.4 Outline of the Thesis

This thesis consists of seven chapters and is structured as follows:

Chapter 1 is an introductory chapter where an overview as well as objectives of the research are outlined.

Chapter 2 presents a literature survey of benefits and limitations of morphing wing technology, previous studies on various morphing wing concepts with particular attention to corrugated composite skin, and an overview of potential smart materials and actuators suitable for morphing wing application.

Chapter 3 discusses material selection and manufacturing process of flat and corrugated test specimens. In addition, tensile, compressive and in-plane shear test results of flat specimens are presented and discussed.

Chapter 4 discusses the manufacturing process and structural behaviour under tensile load of corrugated specimens. This chapter also discusses the results from a parametric study of different corrugated profiles and geometries using a commercial finite element software, ABAQUS version 6.10.

Chapter 5 explores the aerodynamic performance of the wing with corrugated skin compared with a conventional smooth wing by means of wind tunnel test and numerical evaluation.

Chapter 6 presents the design of a morphing wing prototype with carbon/polyurethane corrugated composite skin. Also, the design of actuation mechanism and manufacturing process of the bench-top wing demonstrator will be discussed in detail.

Chapter 7 concludes all the findings from this research and provides potential further work.

Chapter 2

Literature Review

In order to obtain a complete picture of morphing wing technologies, a literature survey of previous research was undertaken focusing on five main aspects:

(i) Benefits and limitations of a morphing aircraft
(ii) Various morphing wing concepts
(iii) Smart materials, actuators and structures
(iv) Carbon fibre reinforced polyurethane laminates
(v) Corrugated composite skin concept

2.1 Benefits and Limitations of a Morphing Aircraft

Many research programmes have been conducted to study aerodynamic advantages and structural complexity of a morphing wing using different approaches. The ultimate goal is to design the best generic morphing wing that can be installed on any aircraft. However, there is no single conclusion to which approach is the best since the design process of a morphing aircraft depends heavily upon mission requirements. One design can be regarded as the best design for one aircraft but can be considered as unsuitable for another air vehicle. It is difficult to quantitatively compare benefits and penalties among various morphing concepts as each design is dominated by mission requirements. In some cases, a morphing structure may have adverse effects over conventional structure in terms of complexity and weight. However, the overall performance of the morphing aircraft may outperform the effects of the additional mass. Therefore, in order to quantify benefits or penalties of

a specific morphing concept, a careful and technology-specific study must be performed for a particular concept and cannot be used to study trade-offs of other concepts [25, 26].

Wickenheiser and Garcia [27] studied the aerodynamic benefits of a morphing wing using an extension of Weissinger's method based on classical Prandtl's lifting-line theory. This method can be utilised as a tool for preliminary design of a morphing wing. The lifting-line theory was chosen over computational fluid dynamics (CFD) approach due to its simplicity. Moreover, remeshing was not required when the configuration of the wing changes. Gull wings were used as an example to demonstrate the accuracy of the numerical method. The results showed that when the wing's curvature was increased, lift and lift-to-drag efficiency were decreased. This confirmed morphing usefulness in loiter to high-speed flight reconfiguration. The only limitation of this method arose when viscous effects dominate, this method must be used with caution since the results became more inaccurate. In comparison to CFD analysis, the Weissinger's method is valid for preliminary design where the viscous effects are minimal. This research study only focused on aerodynamic analysis of a morphing wing, while the structural design was not discussed.

Jha and Kudva [4] summarised the effects of aircraft performance when each geometrical parameter of the wing such as wing plan area, wing sweep, aspect ratio, etc., is changed while other parameters remain unchanged (table 2.1). This particular research also reviewed early morphing aircrafts including Burnelli GX-3, Republic XF-91, Messerschmitt P-1101, etc., as well as fuselage and engine morphing applications. Jha and Kudva [4] also addressed some technical challenges encountered in the design process including the need for suitable skin and actuator.

A question of whether improved aerodynamic benefits provided by a morphing wing offset the penalties associated with additional weight and energy consumption was addressed by Moorhouse [28]. The detailed mission for a national supersonic air-to-air fighter (AAF) aircraft was used because each segment of the mission requires significant compromise for configurations with fixed geometry. Wing geometrical parameters such as wing sweep, span, camber, etc., were allowed to change simultaneously for each mission segment but within set constraints. There were two types of penalties considered herein

Table 2.1: Effects of geometrical parameters of the wing on aircraft performance, adapted from [4].

Parameter		**Effects of Variablility** - all other parameters unchanged
Wing Plan Area	$\Uparrow$	**Increased** lift, load factor capability.
	$\Downarrow$	**Decreased** parasitic drag.
Wing Aspect Ratio	$\Uparrow$	**Increased** L/D, loiter time, cruise distance, turn rates. **Decreased** engine requirements.
	$\Downarrow$	**Increased** maximum speed. **Decreased** parasitic drag.
Wing Dihedral	$\Uparrow$	**Increased** rolling moment capability, lateral stability.
	$\Downarrow$	**Increased** maximum speed.
Wing Sweep	$\Uparrow$	**Increased** critical Mach number, dihedral effect. **Decreased** high-speed drag.
	$\Downarrow$	**Increased** C_{Lmax}.
Wing Taper Ratio		Wing efficiency (spanwise lift distribution). Induced drag.
Wing Twist Distribution		Prevents tip stall behaviour. Spanwise lift distribution.
Aerofoil Camber		Zero-lift angle of attack, aerofoil efficiency, separation behaviour.
Aerofoil Thickness/Chord Ratio	$\Uparrow$	**Improved** low-speed aerofoil performance.
	$\Downarrow$	**Improved** high-speed aerofoil performance.
Leading Edge Radius	$\Uparrow$	**Improved** low-speed aerofoil performance.
	$\Downarrow$	**Improved** high-speed aerofoil performance.
Aerofoil Thickness Distribution		Aerofoil characteristics, laminar/turbulent transition.

which were weight and fuel penalties. The weight penalty arises from an assumption that a morphing wing is heavier than a conventional fixed wing due to heavier actuation mechanism while the fuel penalty is taken from the power increase to actuate the morphing wing. The results are shown graphically in figure 2.1 as a plot of wing weight penalty factor against fuel consumed in pound-mass (lbm). The shaded region in the plot represents the fuel saving region. Outside this region, either or both fuel and weight penalties outweigh the aerodynamic advantage of the morphing wing. For example, if the structural weight of the morphing wing is six times heavier than a conventional fixed wing and the power required to drive the actuation mechanism is 75% higher than the fixed wing; the performance point on the plot lies outside the fuel saving region and, therefore, yields no benefit. Although this research pro-

vided a methodology to quantify the penalties of adopting morphing concept, it was limited to only one particular mission.

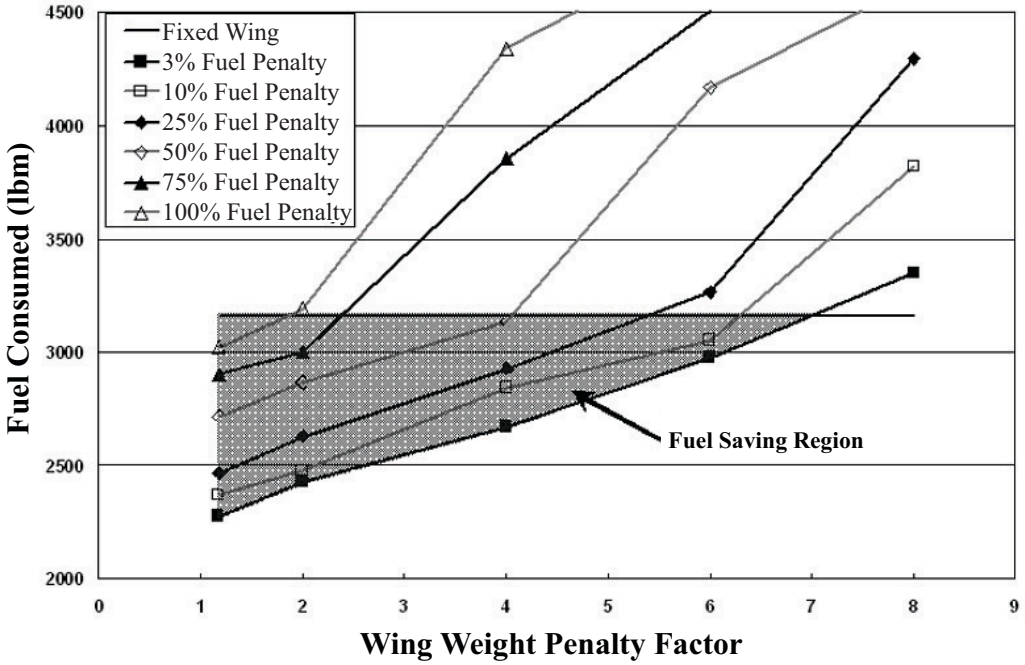


Figure 2.1: Graphical representation showing morphing benefit in terms of penalty factor against fuel consumption, adapted from [28].

Smith *et al.* [29] also studied benefits of morphing wing on air-to-air fighter capable of changing wing sweep, wing span, root chord length and tip chord length. The results of this study showed that the benefits gained from morphing wing in terms of aerodynamic performance offset penalties arising from fuel consumption and weight of actuator.

A research study [30] suggested that if current high-lift devices are replaced by morphing systems, mass and costs of the aircraft could be drastically reduced as the complexity of high-lift systems is decreased. Moreover, take-off gross weight and engine thrust requirements could also be reduced [31, 32]. Spillman [33] stated that if variable gapless wing camber is introduced, reductions in drag, mass and operating costs can be realised.

Joshi *et al.* [34] investigated the impact of a morphing wing on aircraft performance and provided a method to compare various morphing strategies. The baseline aircraft used in this study was the BQM-34 Firebee unmanned target drone aircraft. Eleven flight conditions representing various aircraft mission

segments were used. Aspect ratio, root, tip and mean aerodynamic chords and the leading edge sweep were computed using four parameters: wing area, wingspan, taper ratio and quarter-chord sweep. Then these four geometric parameters were varied to evaluate maximum and minimum performance metric for each mission segment. The results of the investigation were presented graphically using a "radar plot" or a "spider plot" (figure 2.2) which provides a way to examine the impact of a morphing wing on aircraft's performance for each of 11 flight segments. The outer radius of the spider plot indicates the best possible performance for corresponding segment. An additional trade study was performed to determine the benefit of a morphing aerofoil with a fixed wing planform. The result of the spider plot suggested that the aircraft with a wing capable of telescoping, chord extension and variable sweep performs better than aerofoil morphing and fixed wing, respectively.

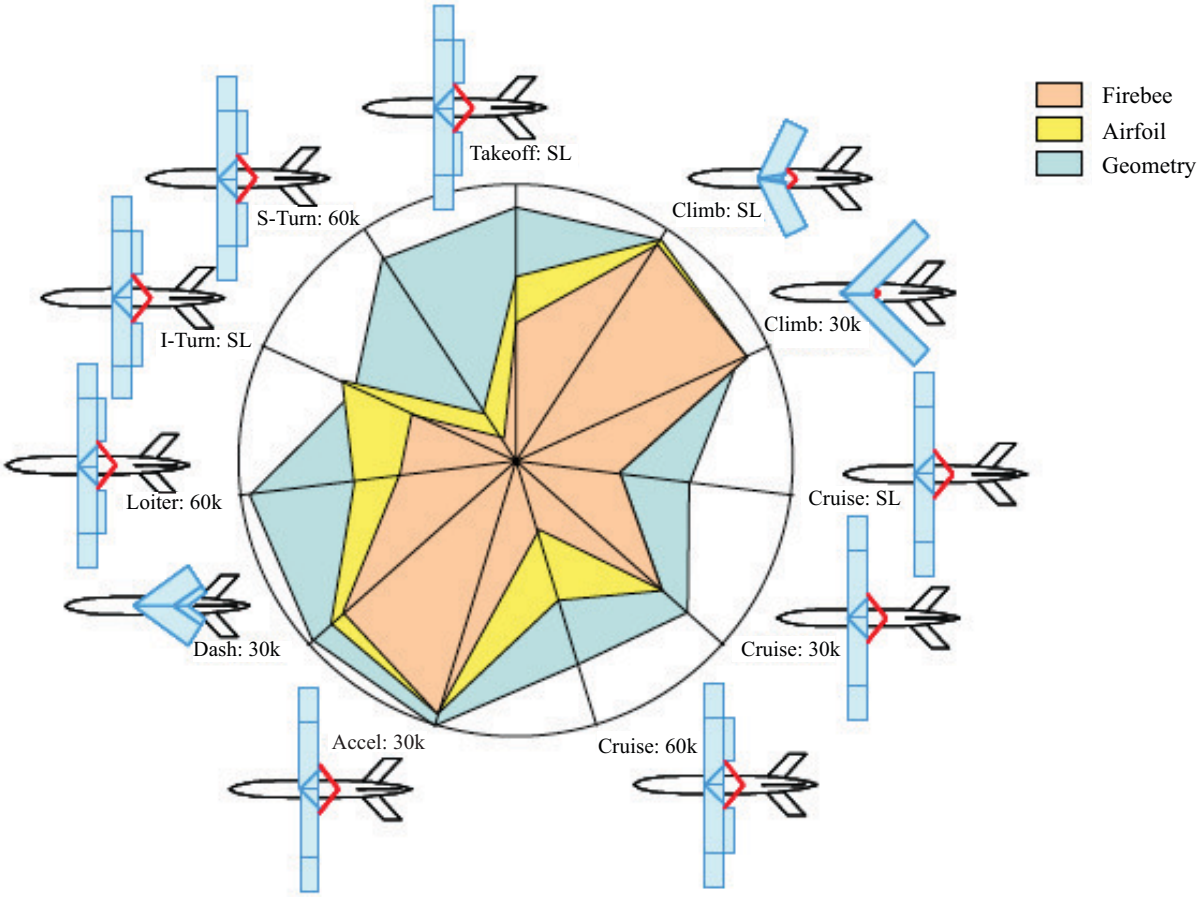


Figure 2.2: "Radar" or "Spider" plot, adapted from [34].

Rodriguez [35] suggested that a fleet of morphing aircrafts, each can oper-

ate over a wide range of mission objectives, is more beneficial than a fleet of different types of aircraft, each is optimised for one particular mission. Both fleets are able to accomplish mission objectives, however, lower maintenance and support requirements together with operational flexibility lead to lower costs in the case of morphing aircrafts.

Apart from benefits of morphing wing concept, some technical challenges were also identified. The first practical limitation of implementing morphing idea to current aircrafts is structural flexibility and integrity [36]. The skin of the wing should be flexible to be morphed, however, its stiffness has to be high enough to withstand aerodynamic pressure and internal load induced by actuation mechanism. The second obstruction is the design and selection of appropriate actuation system. A lightweight, small and efficient actuation system is desirable, and currently under extensive research [4]. It is yet to be fabricated, however. The last practical issue is how to optimise the distribution of sensors and actuators [28].

Benefits and limitations of morphing aircraft have been addressed in this section. It should be highlighted that trade-off study between morphing concepts is highly dependent on mission requirements. The factors that limit the morphing capability of the wing are associated with actuation mechanism, appropriate skin and distribution of sensors and actuators.

2.2 Overview of Morphing Wing Concepts

As briefly mentioned in chapter 1 that the morphing wing concept was first implemented by the Wright brothers in their flying machine. The Wright brothers realised that control and stability are of paramount importance for a successful flight. At that time no ailerons and flaps were invented, therefore, control of the flying machine was executed using flexibility of the wing through pulleys and cables [37]. After the successful first flight of the Wright brothers, several wing warping concepts were proposed. The first US patent for variable camber wing was filed in 1916 [38]. In 1920, Parker [39] proposed a variable camber wing the shape of which could be changed passively under aerodynamic load. An increase in speed and payload navigated the development in morphing wing to a new direction. The flexible wing fabricated from fabric was

replaced by stiff metallic structure in order to withstand higher aerodynamic and actuation loads as well as to suppress aeroelastic phenomena. Discrete control surfaces and high-lift systems have been employing as a means for shape change. These systems are not very efficient for every flight segment, therefore, many morphing research programmes have been established to investigate the feasibility to replace discrete components with a seamless morphing wing.

The National Aeronautics and Space Agency (NASA) was one of the first pioneers to develop morphing technology. It established a morphing project to conduct research on advanced technologies and integrated component concepts to improve efficiency and make multi-point adaptability in air and space vehicles possible [40]. The definition of the word *morphing* in the context of NASA's research was defined as "...efficient, multi-point adaptability and it includes macro, micro, structural and/or fluidic approaches..." [41]. From this definition, three main research areas which are adaptive structural morphing, micro-aero adaptive control, and biologically-inspired flight systems, could be derived and is depicted in figure 2.3.

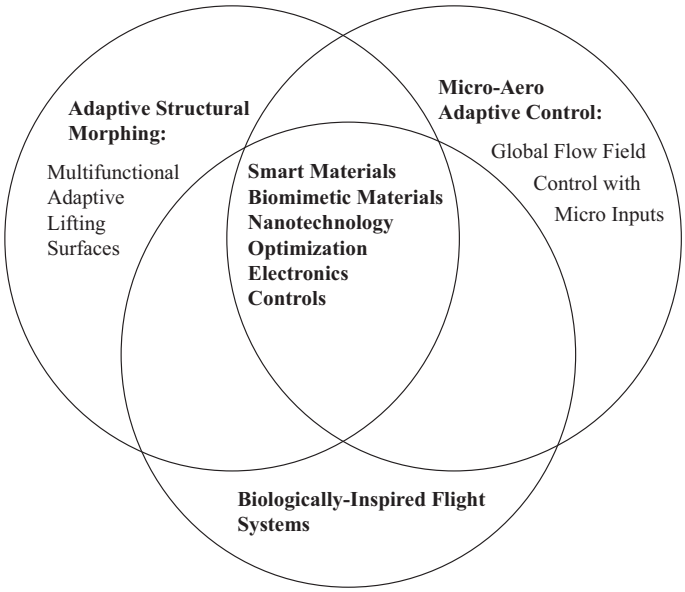


Figure 2.3: Overview of the content in NASA's Morphing Project [41].

Figure 2.4 shows an artist's impression of NASA's advanced morphing aircraft. The wings as well as engine inlets and nozzles can undergo shape change. At high speed, the wing is able to sweep back in order to reduce drag induced by a shock wave. NASA predicts that this type of morphing aircraft will fly by 2030 [42, 43].

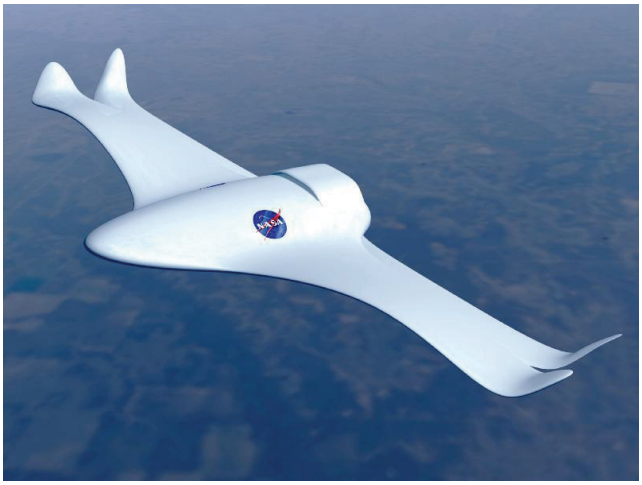


Figure 2.4: An artist's rendering of NASA's morphing aircraft [42].

One of the first morphing research programmes in the 1970s was the Mission Adaptive Wing (MAW) . This programme aimed to develop a wing which is capable of changing its cross-sectional shape in flight by using internal hydraulic-actuated mechanisms [44]. The US Air Force Research Laboratory (AFRL) at Wright-Patterson was in charge of managing the programme while the flight tests were conducted by NASA Dryden Flight Research Center. The wings of F-111 were modified such that on each side of the wing there are one trailing edge and three leading edge flexible segments made of flexible fibre-glass and actuated by hydraulic servos in order to vary the wing camber [45, 46]. Fifty-nine flight tests were performed and the results were satisfactory. An improvement in L/D characteristics could be observed at Mach number of 0.8 and altitude of 44,000 ft [47]. Moreover, the bending moment at wing root as well as structural loads could be reduced for the same load factor [48]. However, the programme was finally abandoned mainly because increases in weight, complexity, volume and mechanical performance significantly offset the aerodynamic benefits.

In mid-1990s, AFRL Wright-Patterson Air Force Base, NASA Dryden Flight Research Center and Boeing Phantom Works initiated Active Aeroelastic Wing (AAW) research programme, which used modified F/A-18 (later designated as X-53) as a test aircraft [49]. The main objectives of this programme were to increase control power, to reduce drag, manoeuvre loads and mass, and to enlarge flight envelope by twisting the wing[50, 51]. The twist in the wing was caused by leading edge flaps and trailing edge control surfaces.

As a result, roll authority at high speed could be made possible without causing an increase in wing stiffness and weight [52].

The US Defense Advanced Research Projects Agency (DARPA) together with AFRL and NASA initiated a smart wing programme. The aim of this programme was to develop control surfaces manufactured from smart materials [53]. The novel smart material-based control surfaces were used to provide improved aerodynamic and aeroelasticity. In the first phase of the programme (January 1995 to February 1999), the team led by Northrop Grumman Corporation (NGC) developed and investigated SMA-based hingeless, smoothly contoured trailing edge control surfaces and actively variable wing twist using SMA torque tubes [54]. In May 1996 and June 1998, two wind tunnel tests were conducted using two 16% scaled models, one conventional and the other incorporating the features stated above, to evaluate the concepts and quantify performance improvement. The results of these tests indicated an improvement in lift and rolling moment achieved by using hingeless, smoothly contoured control surfaces. However, an important limitation brought forward to phase 2 was the low bandwidth achievable from SMA-based actuator [55]. In phase 2, new types of conceptual design of actively cooled SMA-, electroactive polymer-, piezo-hydraulic pump-, and piezo-motor-based actuators were investigated. The selection made was based on trade studies of many factors such as availability, efficiency, ease and cost of manufacturing, and risk. The final selection was the state-of-the-art ultrasonic piezo-electric motor [56]. The torque generated by the piezo-electric motor was then transmitted to deflect the trailing edge control surface using an eccentuator, a bent beam which converts rotary motion at one end to vertical force at the other. Wind tunnel tests were conducted using 30% scaled model (figure 2.5) at Mach number ranging from 0.3 to 0.8 and the dynamic pressure of up to 300 pounds per square foot (psf). The results showed a deflection rate of over 80°/sec and maximum deflections of over 20° [57]. Also, an improvement of approximately 17% in rolling moment coefficient and pitching moment coefficient at 15° of control surface deflection were achieved [58].

The initial design of the eccentuator from DARPA/AFRL/NASA smart wing programme was modified and utilised in a novel actuation system, an eccentric torque-tube disk mechanism (ETDM) [59, 60] . This mechanism was proposed to be mounted at the trailing edge (TE) as shown in figure 2.6. An-

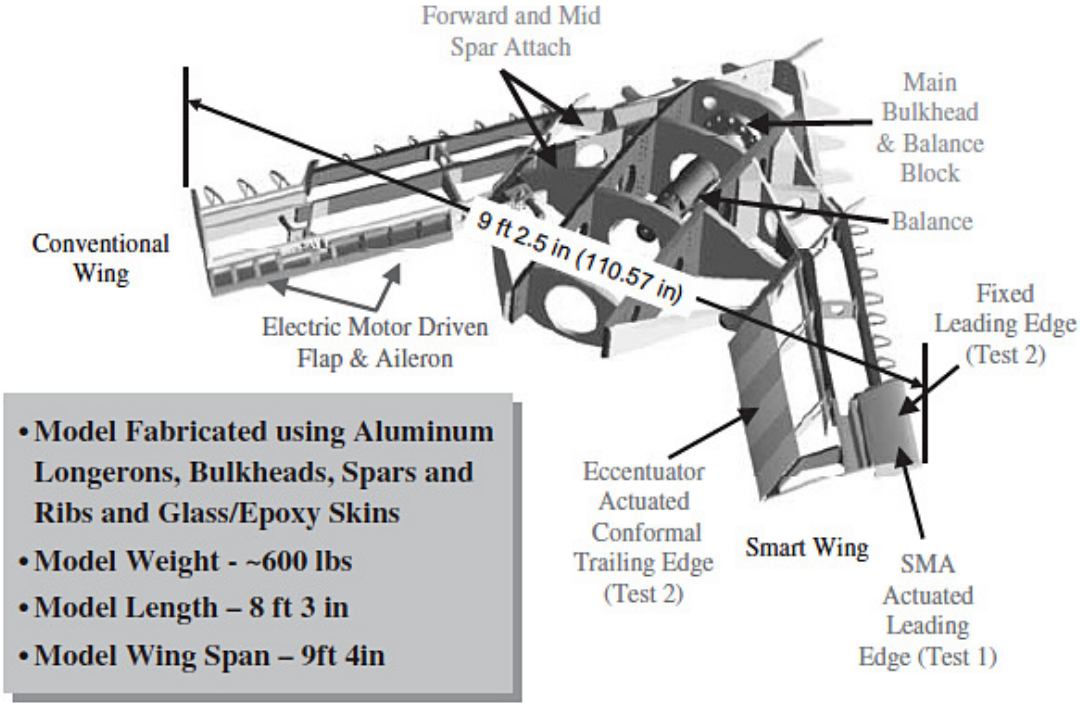


Figure 2.5: Phase 2 wind tunnel model of DARPA Smart Wing programme [53].

other feature of this design was the open sliding trailing edge, which allows maximum trailing edge deflection with minimum power required [5, 59, 60].

Lockheed Martin proposed a morphing concept in which the wing can be folded out of plane. This concept was intended to apply to a small UAV and believed to increase wing surface area by as much as 2.8 times when the wing is unfolded. This configuration is favourable when loitering. This morphing idea was known under the name of Z-wing morphing project. In the folding region, the skin was seamless and fabricated initially from shape memory polymers developed by Cornerstone Research Group (CRG). However, fabric reinforced

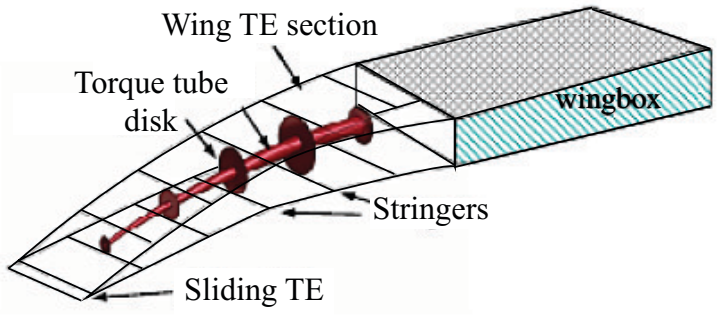


Figure 2.6: ETDM concept, adapted from [5].

silicone based material was chosen for the wind tunnel model. This was due to an issue with electrical resistive heating system [61]. Another issue with the skin was the non-linear behaviour due to creep when actuated. In order to prevent the skin from flapping during the folding operation, a vacuum pump was used to draw the skin into a cavity [62]. Initially, the actuation system was to be based on linear thermopolymer actuators. However, later during wind tunnel testing, electrical rotary motors were used to increase reliability and reduce weight, complexity and operating time [63].

NextGen Aeronautics, with support from Boeing Phantom Works advanced research and development organisation, developed a sliding wing concept that can undergo sweep changes from 15° to 35°, area change of 40%, and span change of 30% during flight at flight speed of approximately 50 m/s. The wing consists of silicone elastomeric skin which could be stretched up to 100% and lightweight moving ribbon substructure actuated with single electro-mechanical actuation system. The endoskeleton wingbox structure is attached to the fuselage at 4 attachment points. The wing could withstand the aerodynamic load of 19,150 Pa [64]. Anderson, Cowan and Piatak [65] addressed a few structural issues related to the design of revolute joints, which may arise during morphing process and suggested that new analytical and testing approaches are required. According to NextGen Aeronautics [66], the aircrafts were known as MFX-1 and MFX-2 corresponding to two successful flight tests, however, it was known generally as the Batwing concept (figure 2.7).

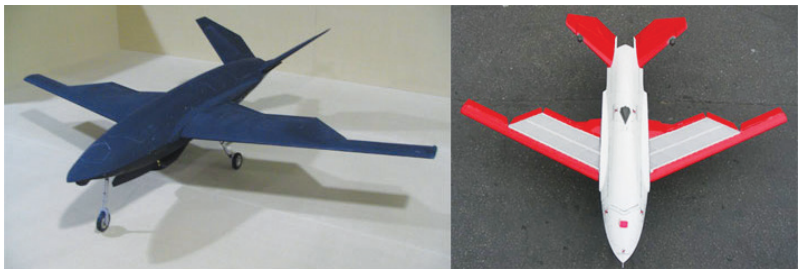


Figure 2.7: NextGen Batwing concept [66].

In 2006, FlexSys Inc. [67] developed an adaptive wing concept with seamless control surfaces and high lift devices which could be morphed on demand. This concept was known as the Mission Adaptive Compliant Wing (MACW). In this design, the flap could be deflected up to ±10° at the speed up to 20°/sec using a conventional electro-mechanical actuator. Moreover, the flap could be

twisted differentially up to 1°/foot along the span [68]. The test results suggested that the range of the aircraft could be extended by 15% or more by optimising L/D throughout the mission. Also, fuel and weight savings, and higher control authority could be realised [69]

Articulated cells concept (figure 2.8) was another camber change concept that was developed based on a strategy to map the mean camber profile onto the maximum and minimum camber profiles in the simplest possible way requiring minimum actuation power. The latest design consisted of four rigid boxes connected together by hinges making it possible to perform roll control with a higher bandwidth requirement. The main advantages of this concept were accurate and repeatable shape change, low activation energy and reliable actuation system. However, the main drawback was the requirement for a smooth skin [5].

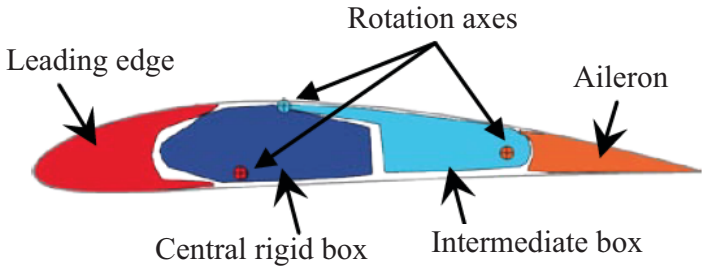


Figure 2.8: The articulated cells concept [5].

Many research studies were conducted to develop compliant mechanisms for adaptive structures. Compliant mechanism can be defined as a hingeless mechanism which uses elastic properties of its constituent elements to transmit motion and/or force [68]. The main purpose to develop the compliant mechanism was to eliminate backlash, wear, weight and maintenance problems [70]. The optimisation process for compliant mechanism used one of two approaches: load-path approach and continuous density-based approach [71]. Shili, Wenjie and Shujun [72] presented a systematic approach using MATLAB and ANSYS to design a compliant structure for adaptive trailing edge. The genetic algorithm (GA), which is an optimisation method that simulates the heuristic selection rule in nature, was implemented in MATLAB. Then the ANSYS was used to perform finite element analysis taking into account geometric nonlinearities. The results of this study showed that the trailing edge section could be deflected from 0° to 9.3° and it was also confirmed with experimen-

tal tests. Santer and Pellegrino [73] proposed a design of adaptive compliant leading edge using modified technique based on a load-path approach. In the load-path approach, an initial structural network can be specified at the beginning of the design process and the optimal structure is sought after required constraints and target goal are specified. This modified technique was verified by the movement of leading edge demonstrator after displacement actuation of 4.8 cm was applied (figure 2.9).

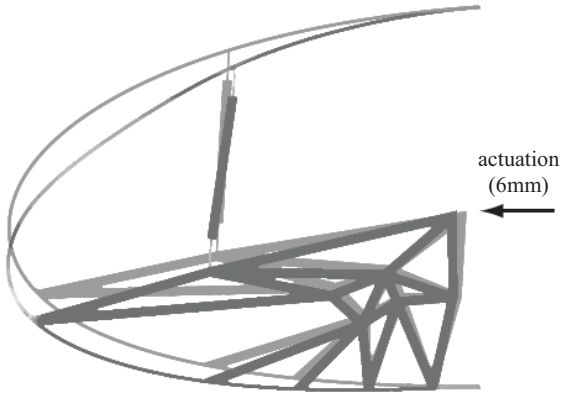


Figure 2.9: Illustration of compliant adaptive trailing edge [73].

A morphing concept developed at Deutsches Zentrum für Luft- und Raumfahrt (DLR), Germany, using compliant mechanism approach was the belt-rib concept (figure 2.10). The ribs of the wing were removed while a number of spars was increased. In addition, the spars were placed at different angle along the trailing edge and connected to the skin using compliant hinges such that the camber of the wing could be changed [74, 75]. The deflection of 5° and maximum strain of 0.099% were observed during the experiments [76]. However, no information regarding actuation loads or long term performance were discussed.

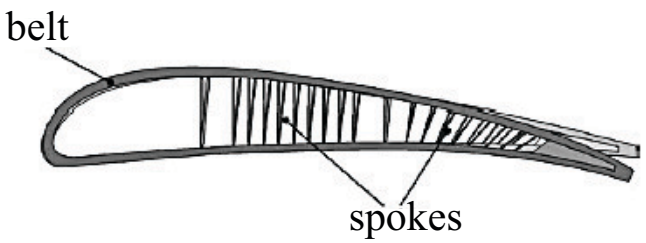


Figure 2.10: Belt-rib concept [76].

Another biological-inspired concept developed by DLR was the "finger concept" (figure 2.11). In this concept, the ribs at the trailing edge were replaced by a few plate like elements linked together. These elements could be rotated relative to each other similar to the way human fingers move as the name of the concept suggests. The plate elements were manufactured from metal and carbon fibre reinforced plastic (CFRP) and the wing was actuated by electrical motors [77, 78].

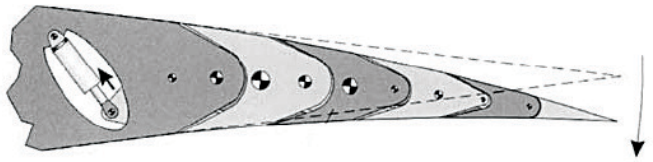
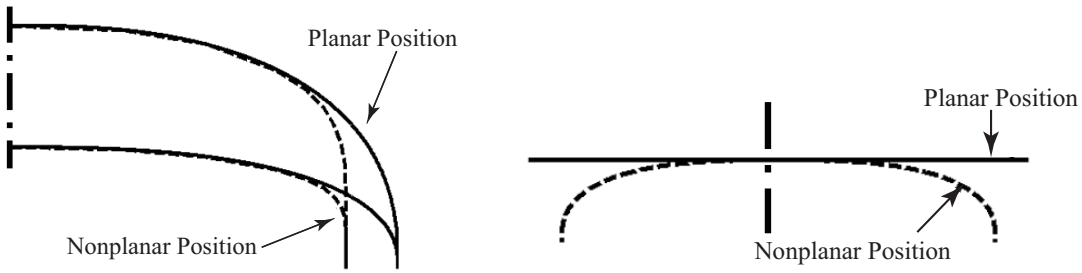


Figure 2.11: DLR finger concept [78].

Another morphing wing concept developed by NASA Langley Research Center was the Hyper-Elliptic Cambered Span (HECS) wing. Wiggins *et al.* [79] and Stubbs [80] presented a single-degree-of-freedom mechanism using a scissor-like linkage to translate the motion of one end to other sections along the span of the HECS wing to transform the wing from a planar to a non-planar configuration (figure 2.12). In addition, an issue of selecting an appropriate material for skin was also addressed. A smooth compliant skin was required to gain maximum aerodynamic benefits. Lazos and Visser [81] performed aerodynamic comparison between various HECS wing models and baseline elliptic planform. The results showed that better lift-to-drag ratio could be attained from the HECS wings. Ramrakhyani *et al.* [82] presented an alternative design of the HECS wing for a UAV weighing 3000 pounds (lbs) using a tendon-actuated compliant cellular truss. The results suggested that the weight of the HECS wing was comparable to conventional wing except that the in-plane and out-of-plane deflections were larger.

Gano and Renaud [83] presented an alternative concept for morphing technology called "variform wing concept". In this concept, the fuel is stored in the balloon-like bladders inside the wing structure that can shrink as the fuel level decreases (figure 2.13). This shrinkage slowly changes the shape of the aerofoil and, consequently, results in an increase in L/D ratio. Maximising this ratio allows the aircraft to fly further on the same amount or less fuel. This research only studied the feasibility of adopting this concept to improve



(a) Planform view **(b)** Span view

Figure 2.12: Illustration of (a) planform view and (b) span view of HECS wing [79]

the performance of the aircraft but no information on materials and structural design was provided.

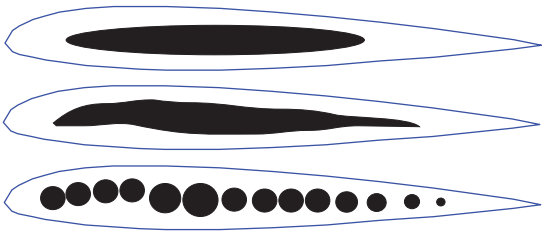


Figure 2.13: Possible fuel bladder configurations [83].

A hexagonal chiral structure, introduced by Lakes [84] and extensively studied by Prall and Lakes [85], is a cellular network that exhibits negative in-plane Poisson's ratio that leads to a high shear modulus. Moreover, some degree of in-plane bending is realised. A component with chiral honeycomb structure may be able to attain higher torsional and shear loads compared to the same component made from solid materials [86]. The unique characteristics of chiral structure are attractive so that an aerofoil with chiral honeycomb core was proposed [87]. The compliant characteristics of chiral honeycomb can be used to achieve chordwise bending. In addition, the deformation mechanisms of the chiral structure allow continuous deformations of the aerofoil [88]. The chiral structure can undergo large deformation while the strains in each member are within the elastic range of the material. This property is of importance to achieve repeatablity [89, 90]. Bettini *et al.* [91] addressed that the isotropic material used in previous studies was not expected to provide optimal performance. Therefore, Bettini *et al.* [91] proposed an aerofoil with chiral honeycomb structure made from composite materials (figure 2.14). The experimental results suggested that the morphing performance could be

improved. In addition, cohesive elements were used in numerical analysis to simulate the failure of the adhesive film. The numerical approach was also used to identify failure strength of the composite chiral structure of different geometric characteristics and lay-up sequence of the unit cells.

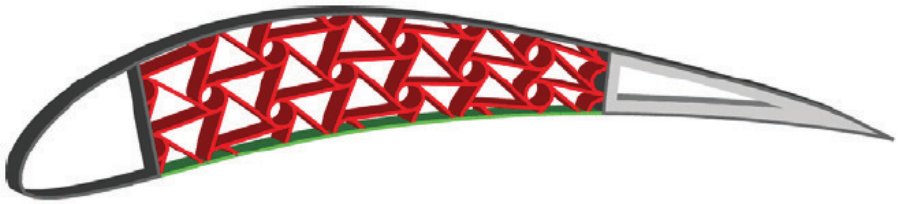


Figure 2.14: Chiral core aerofoil [91].

This section presents various morphing wing research programmes. Some of the programmes were abandoned at the end, as the trade-off study showed that an increase in structural weight and complexity of actuation mechanism outweighs aerodynamic benefits. Many concepts focused on designing of an internal structure while only a few addressed a requirement for appropriate flexible skin. In the next section, smart materials and actuators will be reviewed in order to investigate the most suitable actuator for this research.

2.3 Introduction to Smart Materials, Actuators and Structures

Smart actuators, as defined by Pons [24], are devices that "able to autonomously optimise their operating point in response to external or internal disturbances". The invention and development of smart materials and actuators leads to the breakthrough of morphing or adaptive technologies. Smart materials have received a great attention from aeronautical and aerospace engineers and scientists. Smart actuators can be utilised in a new innovative stability control system in order to improve the performance of an aircraft. Yousefi-Koma and Zimcik [22] addressed several limitations of conventional automatic control systems with servo-valve/hydraulic actuators as follows:

- Multiple energy conversions (mechanical, hydraulic, electrical).
- Large number of parts which leads to potential failure sites and large weight penalty.

- High vulnerability of the hydraulic network.
- Frequency bandwidth limitation.

Moreover, Yousefi-Koma and Zimcik [22] also proposed some advantages of smart actuators as listed below:

- Electrical energy is converted directly to high-freqeuncy linear motion.
- Electrical energy is easier to transmit throughout the aircraft.
- Implementation of smart-materials induced-strain actuation eliminates the need for bulky hydraulic power systems and relies on electrical-to-mechanical conversion.

In this section, piezoelectric, shape memory alloys and polymers, and electroactive polymers as well as multi-stable structures will be reviewed. These materials have received a great amount of attention in aeronautical research studies in recent years, in particular, in the morphing wing research.

2.3.1 Piezoelectric materials

Piezoelectric materials are the materials that exhibit electro-mechanical coupling known as piezoelectric effect. This effect can be demonstrated by placing electrodes on the material. When a piece of piezoelectric material undergoes mechanical deformation, electrical currents are induced across the electrodes. The piezoelectric effect is a reversible effect, which means that the mechanical response can be induced upon application of electrical signal. This reciprocal property of piezoelectric material is known as converse piezoelectric effect [23, 24].

The static performance of the piezoelectric actuator highly depends upon the geometrical configurations. Stack piezoelectric actuators provide high force in the range of 10^2 to 10^5 N while the stroke is very low of the order of a few micrometres to a few millimetres. Piezoelectric benders, also known as "multimorph" [24], can produce a medium stroke up to 10 mm. However, the force is limited to the range between 10^{-2} and 10^2 N. Inchworm actuators [24], which are actuators that utilise piezoelectric actuators to drive a shaft, can generate a force in the similar range as benders, while the stroke remains very high and can be unlimited in some configurations. Figure 2.15 shows the force against

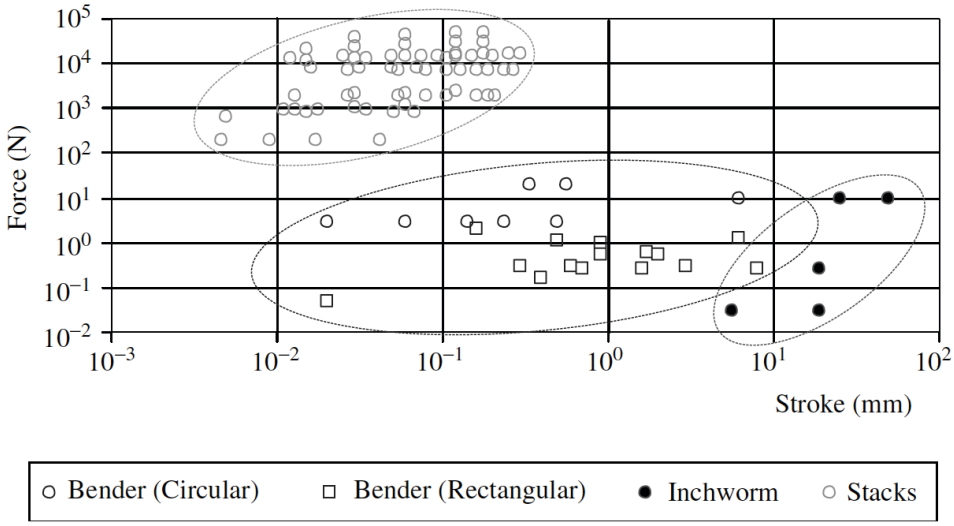


Figure 2.15: Maximum stroke versus blocked force for piezoelectric actuators [24].

the stroke of each type of piezoelectric actuators.

Due to high mechanical stiffness, low mass, and fast sensing response, piezoelectric actuators have been selected for many applications to control noise and vibration. Many applications in aerospace [22, 92], including flow control and adaptive wing applications, are presented and discussed. Moreover, a number of finite element (FE) techniques have been developed to analyse structures containing piezoelectric fibre-reinforced composite actuator [93] and to investigate non-linear response of active laminated piezoelectric plates using the non-linear laminate theory, a non-linear finite element methodology and an incremental-iterative solutions [94].

2.3.2 Shape Memory Alloys (SMAs) and Shape Memory Polymers (SMPs)

Shape Memory Alloys and Shape Memory Polymers both work on the same principle of converting thermal input into mechanical response. The SMAs and SMPs exhibit shape memory effect upon heating and cooling. This effect is a property which very large strains can be recovered upon application of heat above a critical temperature as a result of phase transformation. For SMA such as nickel-titanium-based SMA, it remains in austenitic phase at high temperature and, when the temperature is reduced, the material phase transforms into martensite. This phase transformation induces large mechanical strains.

Another property of SMAs is the 'pseudoelasticity', also known as 'superelasticity', which can be defined as the capability of SMAs to undergo large deformations (up to 10% to 15% strain) when a load is applied and be able to fully recover when unloading [23]. In SMP, however, the shape memory effect is controlled by chemical and physical cross-links, which influences the glass transition temperature, T_g [95]. Above this transition temperature, the elastic modulus of the material decreases so that it can be easily deformed. The deformed shape remains throughout the cooling process. The material will exhibit the memory effect or return to its undeformed shape when it is heated above T_g again [96].

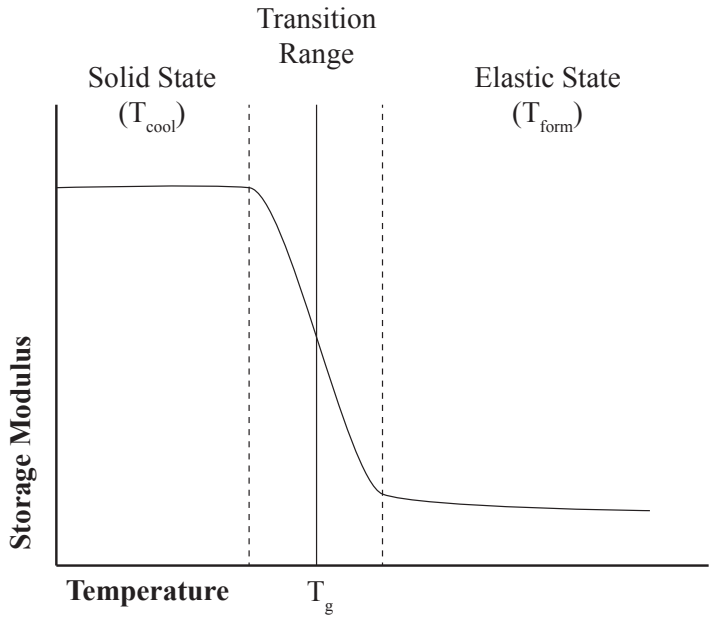


Figure 2.16: Stiffness variation with temperature of SMPs, adapted from [96].

The advantage of SMAs and SMPs over piezoelectric actuators is that they can generate much larger strains. However, the time response is slow compared to conventional actuators. Loewy [92] also addressed another issue when using the SMAs. In order to hold actuated deflections, heat losses must be replaced to sustain the actuating temperature. The pseudoelastic effect enables SMAs to be used in vibration suppression and position control devices, especially in robotic applications as presented by Loh, Yokoi and Arai [97] and Mavroidis [98]. The use of carbon fibre reinforced SMP matrix as a trailing edge skin of a morphing wing was presented by James *et al.* [99]. When the temperature is increased, the stiffness of SMP matrix reduces dramatically, therefore, the

trailing edge can be deflected. As the temperature decreases, the SMP material regains its integrity and, hence, the deflected trailing edge remains in its stable configuration. The main problems with this concept, however, were slow response and heat loss during actuation process [5]. The SMAs and SMPs can also be used in many aerospace applications as an actuator as proposed by Kang *et al.* [100] and Song and Ma [101].

2.3.3 Electroactive polymers (EAPs)

Electroactive polymer (EAP), also referred to as "artificial muscles", is an emerging class of materials which exhibits electro-mechanical coupling. EAPs are soft materials that, upon application of electric current, can undergo a large deformation. The EAPs can be divided into two major groups depending on activation mechanisms: Electronic EAP and Ionic EAP [102]. The electronic EAPs generally require high voltages (>150V/μm). However, they exhibits high mechanical energy density as well as rapid response time in the range of milliseconds. In addition, the property to hold induced strains under application of DC voltage makes it attractive to robotic applications [103]. The ionic EAPs, on the other hand, are driven by diffusion of ions and require lower driving voltages in the range of 1-5 V. However, they have to be operated in wet state or in solid electrolytes. Bending actuation is produced which leads to lower actuation forces. Moreover, the response time is slower than the electronic EAPs [104].

The EAPs are superior to piezoelectric, SMP and SMA actuators in terms of higher stroke. For dielectric elastomer actuators, the relative stroke can be as large as 300–400% and it can be as low as approximately 5% in the case of conducting polymer actuator. In contrast to the relative stroke, the stress attainable by EAP actuators is relatively low. The stress generated by the dielectric elastomer actuators is of order of 50 MPa while the conducting polymer actuator can produce the stress of 1 MPa. Some of the EAP applications are related to bioengineering field, such as conducting polymer actuators as blood vessel connectors. Other EAP devices are designed for robotic applications where large range of motion but low force is required. There are some studies on using EAP actuators as sensors, such as the use of ionomeric sensor as a shear sensor for underwater applications [23, 24].

2.3.4 Multi-stable structures

Multi-stable structures can be defined as the structures which are able to exhibit many distinct structurally-stable deformation states. This is caused by residual stress fields induced during cool down process in unsymmetric laminates. The themal stresses are generated by the mismatch coefficients of thermal expansion of each layer. Bending and twisting moments are also generated within laminate due to unsymmetric stack sequence. The advantage of using multi-stable structures is that an actuator is only used to activate snap-through from one stable configuration to another. Therefore, the actuator is not required to maintain the shape of stable state. This makes multi-stable structure an energy efficient smart structure [105, 106].

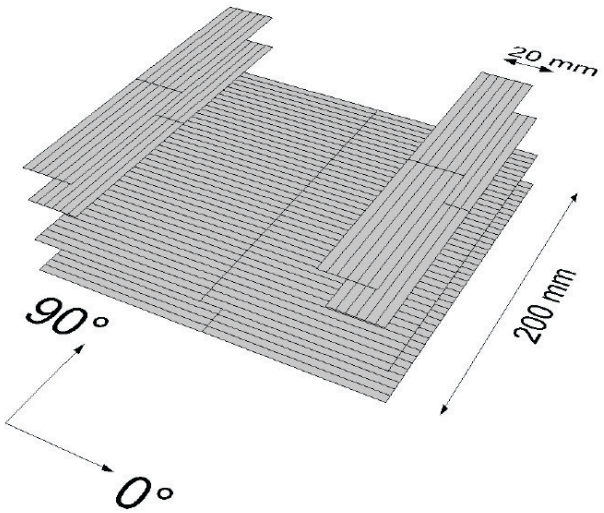
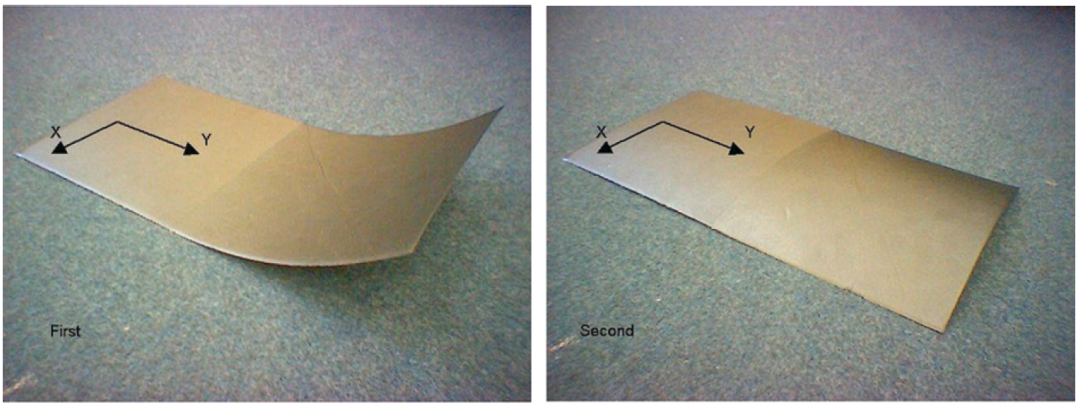


Figure 2.17: Stack sequence of a multi-stable panel [105].



(a) First stable stage **(b)** Second stable stage

Figure 2.18: Stable configurations of a multi-stable panel [106].

The influence of the thermal load on the bi-stable composite laminates was experimentally and numerically investigated by Giddings *et al.* [107]. It was found that the maximum deflection of the bi-stable composite laminates decreases as the temperature increases. This was because the epoxy system (M21 in this case) is softened in the temperature range of 50 – 120 °C. In other words, the coefficient of thermal expansion (CTE), elastic and shear moduli are reduced in this temperature range. Therefore, one problem of the bi-stable composite laminates are that they are temperature depended.

Giddings *et al.* [108] investigated the characteristics of bi-stable composites actuated using a macro fibre piezoelectric actuator. The results showed linear relationships between blocking force and free displacement with applied voltage. Bowen *et al.* [109] confirmed that large changes in shape and deflections could be achieved using piezoelectric patches. However, variability in the shape and deflections can be observed due to hysteretic nature of the actuator. Portela *et al.* [110] used Macro-Fibre Composite (MFC) actuator to activate snap-through process and performed finite element analysis to predict two stable geometries. This research team also studied buckling mechanism as well as evaluated feasibility of using the MFC actuator. Mattioni *et al.* [111] presented a design of a variable sweep wing which consists of two spars with an interconnected truss-rib structure. The spar-web was considered to be made of multi-stable structure in order to increase the moment of inertia to withstand bending stresses and to behave like an elastic hinge in order to change the sweep angle. However, a selection of promising choice of skin was not presented.

A summary of advantages and disadvantages of each type of smart material and actuator is presented in table 2.2.

2.4 Overview of Corrugated Composite Skin Concept

Corrugated structures are often used as a core of a sandwich structure as they offer extreme anisotropic mechanical properties. The corrugated structures are stiff in longitudinal direction (direction parallel to the corrugations) and flexible in transverse direction (direction perpendicular to the corrugations). Yokozeki *et al.* [16] realised the anisotropic properties of corrugated

Table 2.2: Summary of smart materials and actuators.

Types of smart actuator	Advantages	Disadvantages
Piezoelectric actuator	• Fast response • High force	• Low stroke
SMAs and SMPs	• Large strain	• Slow response
Electroactive polymers (EAPs)	• High stroke	• Low force generated
Multi-stable structures	• Actuator is required to only activate snap-through • Large deformation	• Non-smooth variation between each configuration • Temperature depended

structures and proposed U-shape corrugated composites as a candidate for morphing wing's skin (figure 2.19). In their study, corrugated composite panels were manufactured from carbon fibre plain woven fabrics prepreg system. Tensile and bending tests were also performed in both in-plane parallel and transverse to corrugation directions in order to evaluate stiffnesses and strengths of the corrugated composites. Yokozeki *et al.* [16] also proposed a few ideas to improve aerodynamic performance of the corrugated skin by filling the valley sections with flexible rubber. However, it is suggested that a flexible thin film could be used instead of the flexible rubber for better performance. In order to increase the stiffness in longitudinal direction, CFRP rods were installed along the corrugations. This method is proven to be a promising method to strengthen the corrugated skin in longitudinal direction without a loss of flexibility in the transverse direction [15].

Several research studies on dragonfly wings have provided useful information on the aerodynamic performance of a wing with a non-smooth profile. Typical dragonfly wing profiles are shown in figure 2.20. It can be clearly observed that the dragonfly wing profiles consist of well-defined corrugated configurations and the corrugation varies along the spanwise direction. The non-smooth wing profile is regarded as aerodynamic inefficient design and

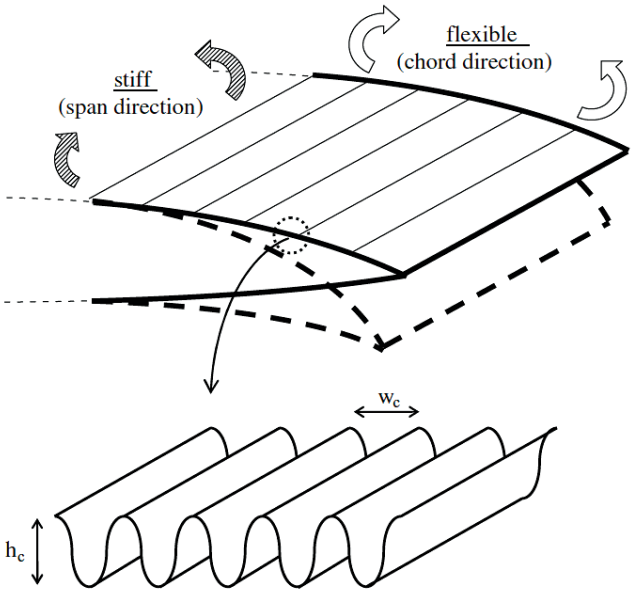


Figure 2.19: Corrugated composites concept [16].

has never been used for conventional aircraft wings. However, research in biomimetic field showed that the corrugated profiles of dragonfly wings perform better than a smooth profile at low Reynolds number. Tamai *et al.* [9] investigated the flow field around three aerofoils: corrugated, smooth and flat plate. Particle Image Velocimetry (PIV) technique was used to capture flow field around the aerofoils. It was found that at low Reynolds number (Re = 34,000), corrugated profile is able to suppress flow separation to a higher angle of attack. This is attributed to vortices induced in the valley sections that help energise the flow outside the vortices to overcome adverse pressure gradient. Kesel [10] performed a comparative study of a flat plate, curved plate, a narrow asymmetric profile and various profiles from dragonfly forewing with some of them having valley sections filled. Two Reynolds number below critical Reynolds number (7,880 and 10,000) were considered to ensure laminar boundary layer. At Reynolds number of 10,000, the lift produced from the corrugated profile is very similar to that of curved and flat plates while the drag characteristics are similar to the flat plate. Kim *et al.* [11] performed numerical investigation on aerodynamic performance of dragonfly aerofoil at three different Reynolds numbers: 150, 1,400 and 10,000. The results suggested that an increase in lift is a result of having corrugations on the pressure side (lower surface) only. Also, corrugations near the leading edge help reduce the drag.

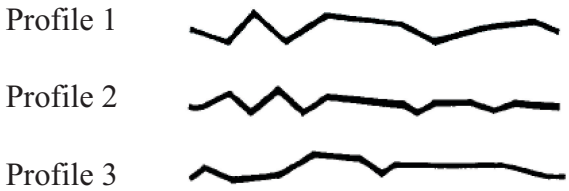


Figure 2.20: Typical dragonfly wing profiles at different locations along spanwise direction, adapted from [10].

Kobayashi *et al.* [112] performed a wind tunnel test of a seamless variable camber aerofoil consisting of corrugated composite underlying structure at the aft section. Two types of parameters, which are steady lift coefficient and unsteady lift coefficient, were investigated in this study. The morphing aerofoil was placed in a uniform flow of 15 m/s and the Reynolds number (Re) was 2.0×10^5. The trailing edge of the aerofoil could be deflected down to a maximum of 30 degrees at an angular velocity (ω) of 0.98 and 3.93 radians per second. The results from the wind tunnel tests showed that the maximum value of steady lift coefficient is comparable to ordinary plain flaps. Unsteady tests showed that at angle of attack (α) less than static stall angle of cambered wing, the unsteady lift coefficient increases as the deflection angle and angle of attack increase. At angle of attack greater than stall angle of cambered wing, the maximum unsteady lift coefficient changes with the angular velocity.

Thill *et al.* [17] also adopted the corrugated composite concept and used a variety of woven fibre/epoxy prepregs, such as, aramid, glass and carbon to manufacture trapezoidal corrugated laminates. The corrugated specimens of different thickness, corrugation pitch and fibre type were then tested under tensile and flexural loadings to study the effects of constituent materials and geometries of corrugation on overall structural behaviours. The results from this study suggested that the use of preimpregnated tape lay-up is unsuitable for manufacturing good-quality corrugated composite panels. Thill *et al.* [19] also performed an investigation on different corrugation profiles and conducted a parametric study on geometry of corrugated composite structures. The results from this study suggested that the corrugation profile that provides the highest strain was the re-entrant corrugations while the highest modulus could be achieved from triangular corrugations. Another investigation of trapezoidal corrugated aramid/epoxy laminates under large tensile displacements transverse to the corrugation direction was done by Thill *et al.* [18]. A three-stage

behaviour, which were initial elastic stage, large deformations occurring at corner region stage, and material stiffness dominant stage, of the structure stress against global strain response was identified. Aerodynamic analysis of corrugated aerofoils was also performed by Thill *et al.* [7]. Aerofoils with corrugated skin of different profiles and geometry in the aft ⅓ of the chordwise section were studied experimentally and numerically. The results showed that corrugated skin has adverse effects on aerodynamic performance. However, the detrimental effects can be minimised by carefully selecting corrugation profiles and geometry and the speed in which the aircraft operates. It was also found that low amplitude and low wavelength corrugation gives the best aerodynamic performance while the shape of the profiles has only minor effects. Moreover, the aerodynamic performance can be enhanced by recessing the corrugations within the aerofoil as the lift curve slope $\left(\frac{dC_l}{d\alpha}\right)$ can be restored to the same value as in the case of smooth aerofoil while the zero-lift drag coefficient ($C_{d,0}$) remains unchanged. In addition to experimental and analytical investigations of corrugated composites, Thill *et al.* [20] also successfully implemented morphing skin panels (MSPs) in the trailing edge region of the wing. The MSPs were manufactured from corrugated sandwich structures and actuated with an internal actuation mechanism consisting of two cross-bar elements connected to a lead screw. The wind tunnel test results of the wing with MSP showed an increase in chord length of up to 4% while the deflection of control surface of up to 12° could be achieved.

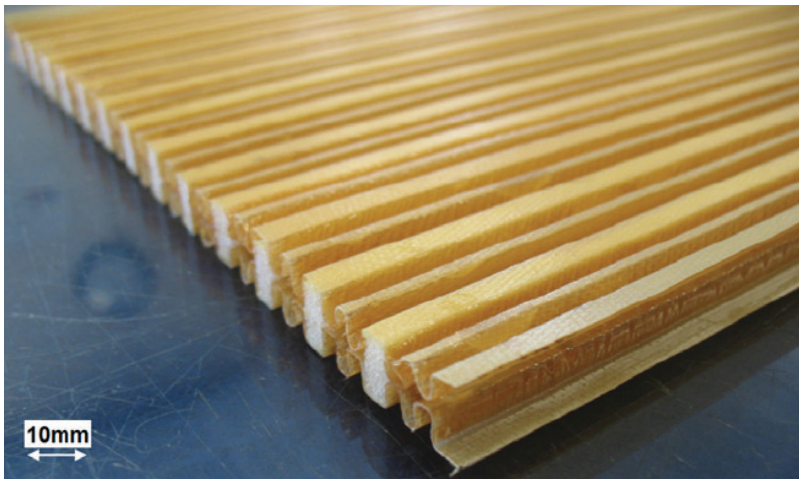


Figure 2.21: Corrugated sandwich structure of MSP [20].

2.5 Flexible Composite Skin for Morphing Wing

This section is important for the development of suitable skin for a morphing wing. As discussed earlier in this chapter, various concepts have focused on the design of substructures and actuation mechanisms. A few concepts identified the importance of flexible skin. One interesting concept was to use the corrugated composite as a skin of a morphing wing. However, the materials used in previous research studies were carbon, glass or kevlar prepregs in which the epoxy resin system generally exhibits low maximum strain (approximately 2-3%). If the epoxy system was replaced by a more flexible resin system (maximum strain of more than 15%), the structural performance of the corrugated composite skin would be improved. One resin system that was suggested by Kikuta [113] as a promising candidate for skin of the morphing wing is polyurethane. Therefore, the polyurethane resin system was selected in this research programme.

2.5.1 Introduction to polyurethanes

Historical overview

Polyurethanes were first discovered by Otto Bayer and his coworkers at I.G. Farbenindustrie in Germany (now becomes Bayer A.G.). Initially, the development of polyurethanes was to duplicate the synthetic process of polyamide fibres [114]. Later in 1937, the first patent was filed by this research group [115]. Subsequent patents were also issued to DuPont [116] and Imperial Chemical Industires (ICI) [117] to cover elastomeric properties of polyurethanes.

Chemistry

Polyurethanes are organic polymers which contain the urethane group in the structure. Typically, a urethane linkage is synthesised by reacting an isocyanate group with a hydroxyl (alcohol) group [118]:

$$\underset{\text{Isocyanate}}{\mathrm{R{-}N{=}C{=}O}} \; + \; \underset{\text{Alcohol}}{\mathrm{R'{-}OH}} \; \rightleftharpoons \; \underset{\text{Ester of a carbamic acid}}{\mathrm{R{-}NH{-}CO{-}OR'}}$$

Then, polyurethanes can be produced by adding polyisocyanates and polyalcohol (polyol) with a catalyst and other additives. Depending on different poly-

isocyanates or polyol constituents, polyurethanes can be made in the form of liquid, foam or solid [119]. Polyurethanes are normally categorised to be in the same group as rubbers and can be used in high-performance applications across various fields. Typical applications of polyurethanes include medical implants, electrical encapsulation, engineering components, etc. Table 2.3 summarises advantages of polyurethanes over conventional rubbers.

Table 2.3: Advantages of Polyurethanes over Conventional Rubbers [120].

	Polyurethanes	**Conventional Elastomers**
Processing	Low-to-medium capital costs	High capital costs
Mixing	Bucket and stirrer	Open mill
	Machine optional	Intensive Mixing; for example, Banbury
Moulds	Lightweight	Heavy duty
	Made from a simple model	
Finishing	Repairs simple	Repairs complex

Basic properties

The polyurethanes are used widely in engineering applications because they exhibit elasticity characteristics of rubber while possessing high resistance to tear propagation and abrasion. The hardness of polyurethanes varies between Shore A 30-100 and Shore D 20-75. The variation in the hardness of polyurethanes is attributed to different chemical structures [113]. The A and D Durometer scales are shown in figure 2.22.

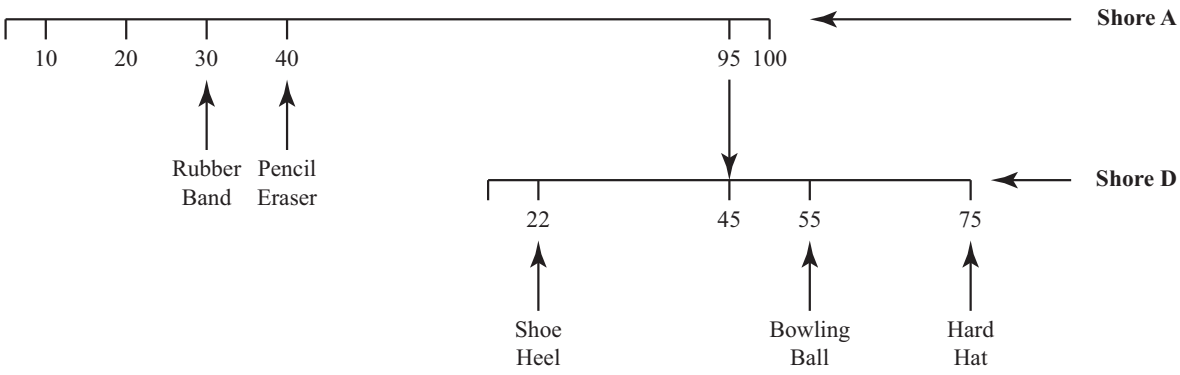


Figure 2.22: Durometer scales, adapted from [113].

Not only is hardness of the polyurethanes affected by chemical structures, but Young's modulus and tensile strength also vary greatly. Typical values of

Young's modulus range from 5 to 2,000 MPa, while the tensile strength varies between 25 to 75 MPa [118]. The stress-strain relationship of polyurethanes is affected by strain rate and temperature. It was found that as the temperature increases, the moduli at fixed strain decrease [121]. The operating temperature of polyurethanes was shown to be between -40°C and 80°C for long-term use. However, for short-term use, the upper bound temperature can be raised to 120°C [114]. According to Oertel [119], the harder the polyurethane product (more isocyanate and chain extender), the higher the service temperature.

2.5.2 Carbon fibre reinforced polyurethane composites and its applications

Kikuta [113] investigated characteristics of various materials to be used as a skin of a morphing wing. Although none of the materials considered in this study meets all the requirements for morphing wing skin, two materials that seemed to work best are shape memory polymer and polyurethane, were highlighted. As indicated by Kikuta [113], SMPs meet the fundamental requirements for a morphing wing skin. If these types of materials are engineered to be easier to handle, they could be the potential materials for a future morphing wing skin. The only disadvantage of SMPs is the need for a heat source to activate shape changing process. Another material that performed the best among other materials investigated by Kikuta [113] is polyurethane (Tecoflex® 80A). The disadvantage of this class of material is its ability to withstand high aerodynamic pressure load. If the polyurethane could be modified to withstand high pressure load while retaining its strain characteristics, it could be used efficiently as a morphing wing skin.

In order to improve inter-laminar shear strength and impact resistance of the composite materials, Haggis *et al.* [122] proposed polyurethane resin reinforced with carbonised fibres in which the polyurethane resin has a heat distortion temperature of 50°C. The composition of polyurethane resin, which has a quick-curing property, was proposed by Fukami and Kataoka [123]. The polyurethane resin can be cured in 1 to 3 minutes at a temperature range between 40°C and 60°C. Fukami and Kataoka [123] also proposed to reinforce the quick-curing polyurethane resin with long-fibre mat. The long-fibre mat includes carbon, glass, aramid fibres, etc., in the form of a chopped strand mat, a continuous strand mat, a surfacing mat, cloth, roving cloth, or the like. The hybrid of two or more fibres can also be used.

Borda *et al.* [124] studied characteristics of polyurethane elastomer reinforced with unidirectional continuous carbon fibres with different coatings (uncoated, coated with epoxy and coated with polyester). The experimental results showed that maximum stress and Young's modulus of carbon/PU composite were 3-5 and 4-10 times higher than raw polyurethane resin, respectively. In addition, it was found that the relationships of Young's modulus and maximum stress against carbon fibre content were linear. In other words, the Young's modulus and maximum stress of carbon/PU composite linearly increases as the carbon fibre content increases.

Effects of fabrication conditions and mechanical properties of glass fibre reinforced thermoplastic elastomer composite were investigated by Shonaike and Matsuo [125]. The resin used in this study was polybuthylene-polyester elastomer (trade name Pelprene). The results from tensile tests showed that tensile strengths in 0° direction increases with increasing impregnation time because the void content reduces as impregnation time increases, while in 45° and 90°, the tensile strengths are independent of impregnation time. Another conclusion obtained by Shonaike and Matsuo [125] was that the Double Cantilever Beam (DCB) method for mode I fracture toughness evaluation is not suitable for this thermoplastic elastomer composite. This is attributed to flexible nature of the elastomer.

Peel [126] and Peel and Jensen [127] highlighted the importance of flexible and compliant structures and emphasised that fibre-reinforced elastomeric composites are well suited for such structures. Four types of fibre-reinforced elastomer composites, namely, cotton fibre reinforced urethane rubber, cotton fibre reinforced silicone rubber, glass fibre reinforced urethane rubber, and glass fibre reinforced silicone rubber, were fabricated. The ply-angle of the laminates was varied between 0° and 90° at the increment of 15°. The aforementioned composites were tested experimentally in tension. The results indicated that the extensional axial stiffness of fibres was improved when impregnated in elastomers. In addition to experimental tests, a nonlinear model was also developed to accurately predict the response of fibre reinforced elastomer composites.

Applications of flexible composite skin

Bubert *et al.* [128] proposed a conceptual design of a morphing skin and substructure of a wing capable of changing its span as shown in figure 2.23. The substructure of the wing was zero Poisson's ratio honeycomb structure while the skin was made of a soft and thin elastomeric sheet with orthotropic carbon fibre reinforcement called a flexible matrix composite (FMC) . This combination of substructure and skin would be able to provide strength in out-of-plane direction without greatly inducing in-plane stiffness, hence, a substantial reduction in actuation force can be achieved. Since this concept focused on providing changes in wingspan, a special type of actuation mechanism using pneumatic artificial muscle (PAM), called PAM X-Frame, was designed. This morphing skin concept was proven to be feasible via various types of tests, namely, tensile, bending, and lap shear tests. Finally, a complete aerofoil section with proposed substructure was presented.

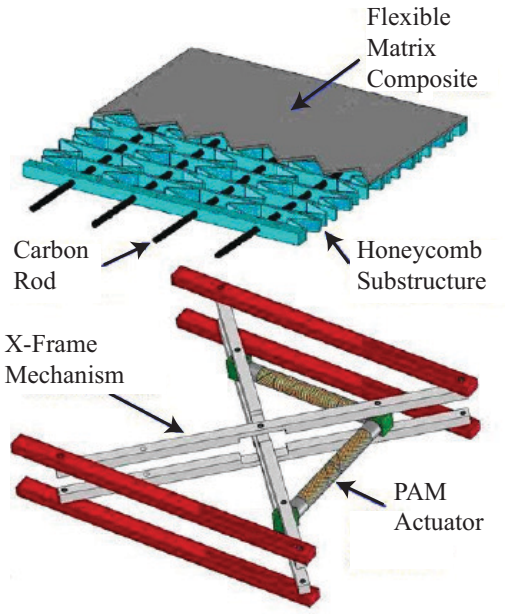


Figure 2.23: Flexible Matrix Composite (FMC) and PAM X-Frame actuator [128].

An alternative concept, which adopted the auxetic skin idea and used PAM actuator, as shown in figure 2.24 was presented by Peel *et al.* [129]. The skin of the wing was made of carbon fibre reinforced polyurethane composite and the wing was actuated by a rubber muscle actuator (RMA) . In order to avoid buckling in the lower skin, the joints between rigid wing box and lower trailing edge skin and between lower and upper trailing edge skins were designed to

slide over each other for simplicity.

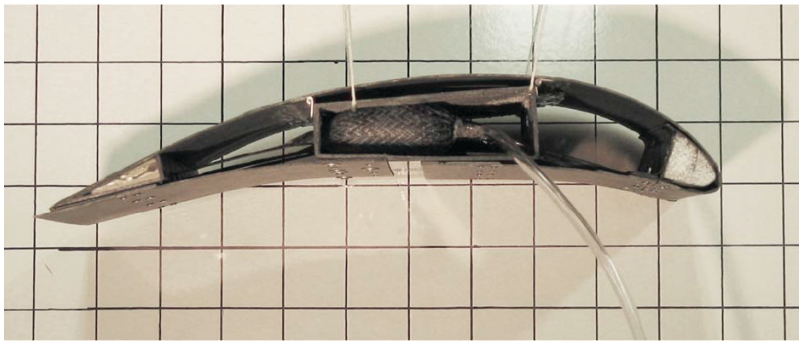


Figure 2.24: Morphing wing with carbon fibre reinforced polyurethane composite skin actuated by a RMA [129].

2.6 Chapter Summary

To summarise, chapter 2 presented a comprehensive literature survey in the field of morphing wing. The chapter was divided into five main sections. The first section discussed the benefits and limitations of developing and implementing morphing technology in a real aircraft. The second section was devoted to numerous morphing aircraft research programmes and concepts. Some of the research programmes were abandoned at the end mainly because the weight penalty and structural complexity of the actuation mechanism outweighed the benefits obtained from implementing the technology. The third section discussed various smart materials and actuators and their advantages and disadvantages if utilised as an actuator in a morphing wing. The fourth section introduced an overview of the corrugated composite skin concept. The corrugated structure is recognised for its extreme anisotropy and became the main focus of this research. The last section highlighted the importance of flexible composite skin for a morphing wing. The epoxy resin system used in conventional composites was replaced by the polyurethane resin system. Therefore, a background knowledge of polyurethanes was reviewed. A number of studies on fibre-reinforced elastomer composites were discussed and a few examples of morphing wing applications were presented.

As highlighted in chapter 1 and in this chapter that the main focus of this research involves the design of a morphing wing with corrugated carbon/PU composite skin concept. Therefore, basic mechanical properties of carbon/PU

composite will be evaluated. Moreover, an analysis of carbon/PU corrugated composite will be performed and discussed in subsequent chapters.

Chapter 3

Carbon Fibre Reinforced Polyurethane Composite: Fabrication and Characterisation

In chapter 2, previous studies on carbon fibre reinforced polyurethane composite were discussed. However, basic mechanical properties of such a composite were not reported. Therefore, this chapter will present methods to evaluate basic mechanical properties of carbon/PU composite. Mechanical testings were performed to measure moduli and strengths of the carbon/PU composite in various loading conditions.

This chapter is divided into two main sections: fabrication and characterisation of carbon/PU composite. In the fabrication section, a manufacturing technique used to fabricate carbon/PU composite is introduced and discussed. Then, material selection process is presented and followed by manufacturing process of the test specimens. The characterisation section presents experimental test methods in accordance with international standards to evaluate mechanical properties of the carbon/PU composite. In addition, failure mechanisms associated with each loading condition are discussed with photos taken from an optical microscope.

3.1 Fabrication of Carbon Fibre Reinforced Polyurethane Composite

3.1.1 Manufacturing technique

Previous manufacturing techniques

The corrugated laminates used in the research by Yokozeki *et al.* [16] and Thill *et al.* [17] were manufactured from woven pre-impregnated fabrics. The manufacturing methods in the previous investigations [16, 17] were very similar, in that they involved hand lay-up of preparegs onto a mould. A heat source was used to 'soften' up the prepregs to ease the formation of the prepregs into the mould, especially at the peaks and troughs of corrugations. The entire tools were then vacuum bagged in order to provide necessary clamping force. After vacuum bagging, the prepregs were cured in an autoclave following curing cycle specified by prepreg's manufacturer.

The prepregs of different fibre types were used in previous studies because the manufacturing process for such prepregs is well established. In the fabrication of corrugated composites, Thill *et al.* [17] stated that the quality of finished products could be improved if resin transfer moulding technique could be used. Three types of inconsistencies in the finished corrugated composites were noticed by Thill *et al.* [17] and are listed below:

1. Misalignment of fibre with corrugation direction.
2. Fibre and laminate do not follow corrugation contour.
3. Non-uniform fibre volume fraction and thickness throughout the specimens.

Non-uniform fibre orientation was clearly observed at the curved regions of the corrugated profile. In addition, the horizontal sections of the trapezoidal corrugation seem to be resin rich, while the slanted sections are drier.

Another disadvantage of using pre-impregnated fabrics is the need for curing at elevated temperature and pressure in an autoclave. This is an expensive process as large amount of energy is required for heat generation. As a consequence, the manufacturing cost is high.

Peel [126] has developed a technique for fabricating flat fibre reinforced elastomer laminates. This involved pre-impregnation of cotton and glass fibres in elastomeric resin. The prepregs were prepared by filament winding process in which the resin coated fibre was wound on to a rectangular mandrel as shown in figure 3.1. Five layers of fibre were wound on the mandrel for each run. The fibre had to be coated with resin manually as the resin was too viscous to be used in a regular filament winding bath. To prevent bonding between each layer, a sheet of teflon-coated pourous peel-ply was wrapped around the mandrel. After the winding process, the whole mandrel was vacuum bagged and cured in the autoclave. Once the prepregs were cured, they were removed from the mandrel and can be used in traditional lamination process. It was also highlighted that processing parameters and a good knowledge of elastomer are very important in producing high quality prepregs.

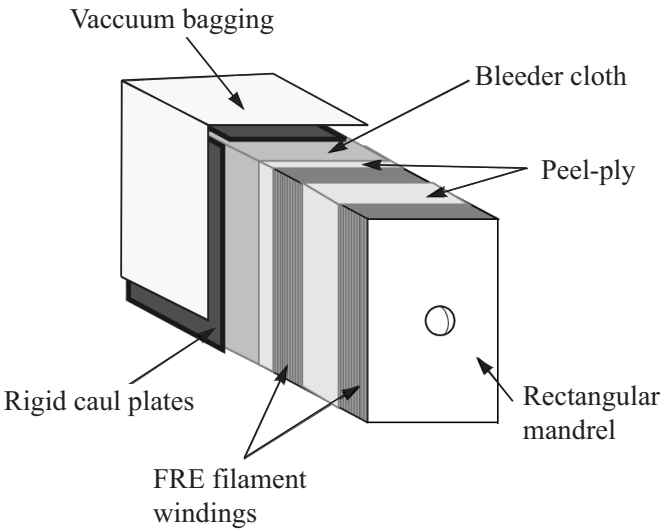


Figure 3.1: Schematic of vacuum-bagged mandrel assembly, adapted from[129].

Resin Infusion under Flexible Tooling (RIFT)

Thill *et al.* [17] suggested RTM as an alternative process to produce better quality and reproducible composite laminates. However, they did not take the idea further. Peel [129], on the other hand, investigated the feasibility of using Vacuum-Assisted Resin Transfer Moulding (VARTM) process. A three-part mould was used to manufacture test specimens. It was suggested that this process has a potential to produce very high quality and reproducible specimens. Nonetheless, it was set aside and filament winding was chosen for

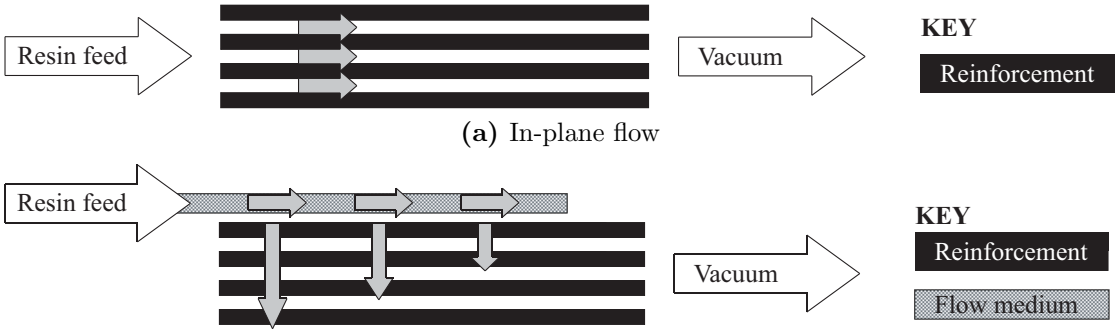
the fabrication route as there were many problems with the VARTM process. The complications were due to high viscosity of the elastomeric resin. It was mentioned that flowing resin caused dry fabric to move and bunch up against resin outlet. In order to prevent the movement, a greater compaction force was applied but this led to another issue in which the fabric was compressed and became denser which restricted resin flow. Due to high viscosity, it is also difficult to remove air bubbles trapped in the resin. In the study conducted by Peel [129], the viscosity of the resin used in the study was not stated.

In the RTM process, resin flow distance is relatively large compared to other processes. Therefore, the most significant property of the resin is viscosity. Low viscosity is preferred, otherwise the resin cannot be drawn from the reservoir. Summerscales and Searle [130] suggested that the maximum limit of resin viscosity for RTM is 800 mPa·s, while Williams *et al.* [131] recommended that viscosity of the RTM process should be approximately 200-300 mPa·s.

The RTM is widely used as an alternative manufacturing method to the traditional prepregs layup and autoclave. Many aerospace components such as radomes, bullet fairings and propeller blades, have been produced using this method [132]. The main advantages of the RTM are lower labour cost, shorter process time and better quality products. It is a flexible process and many variants of the RTM have been developed, one of which is Resin Infusion under Flexible Tooling (RIFT).

The RIFT method is one variant of the RTM process. However, only a single side tool face is required for the process instead of multiple-part mould. The other side is replaced by a vacuum bag. It is an economical way of manufacturing composites since the labour, tooling and running costs can be greatly reduced as the autoclave is not required. In the RTM for high performance components, tooling costs are normally very high, especially with large structures. This is because the tools must be able to withstand the moulding pressure. However, in the RIFT method, which only single mould face is used, it is suitable for manufacturing components with moderate stiffness [131]. Fibre volume fractions of the laminates produced by RIFT are generally higher than RTM. In the RTM, fibre density is defined by tool cavity. But in RIFT, a further compaction is possible once the fibre is wetted out as it becomes lubricated [133].

There are two main variations of RIFT that use liquid resin and dry fabric systems: in-plane flow and through-plane flow as shown in figure 3.2 [130]. The main difference between the two is that, in the through-plane flow a layer of distribution medium is placed on top of dry fabrics. In the in-plane flow infusion, resin is only infused along fibre direction from the inlet tube to the vacuum port. The movement of the resin is caused by pressure gradient. The distribution medium is an open weave fabric that has high permeability. Hence, in the infusion process, the resin will travel through the distribution layer. It then soaks one side of the surface and is impregnated through fabric thickness. The two processes occur simultaneously. The use of distribution medium also improves surface finish on the flexible tool side.



(a) In-plane flow

(b) Through-plane flow

Figure 3.2: (a) In-plane flow and (b) Through-plane flow, adapted from [130].

In the normal RTM process, the product's dimensions are constrained by rigid moulding structure. However, for RIFT, one tool face is flexible. Unlike the RTM, the dimensions of the laminates, especially thickness, can vary along the infusing direction. This is undesirable as it means that fibre volume fraction, and the mechanical properties are inconsistent within the part. Tackitt and Walsh [133] identified two mechanisms that stimulate changes in laminate thickness: lubrication-compaction and pressure gradient. Just after the infusion front, the fabric is further compact as it becomes lubricated by the resin. However, beyond the front there is a transition which causes an increase in thickness. The pressure gradient (figure 3.3) between the inlet and vacuum port leads to a gradient in thickness. Tackitt and Walsh [133] also discovered that a thickness gradient generated from a point source was lower than a line source. This was explained by lower infusion velocity in the point source case, which also implies lower pressure gradient. Thus, in an application where the

dimensions of a component are critical, a slower infusion is essential. There is a suggestion that after the infusion process, the vacuum bag can be sealed off to allow pressure inside the bag to equilibrate, and uniform thickness may be achieved.

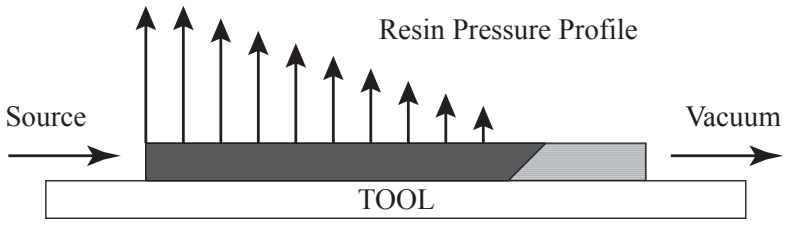


Figure 3.3: Pressure gradient during infusion, adapted from [130].

Table 3.1 shows advantages and disadvantages of RIFT process summarised by Summerscales [130].

3.1.2 Material selection process

Composite materials normally consist of two distinct constituents: 1. fibre, which is the main load bearing structure, and 2. matrix, which is a supporting material that transmits load to the fibre. The net properties of the composites depend heavily upon the choice of matrix and reinforcement. Therefore, selection of appropriate fibres and matrix for a particular application is of paramount important. In aerospace field, carbon fibre reinforced plastic (CFRP) is a type of composites used extensively in many parts of an aircraft. The simplest way to manufacture a CFRP structure is to lay plies of carbon prepreg at different angles corresponding to the load paths of the application. The main resin system used in aerospace industry is epoxy as it offers high stiffness and low density. However, it is not well suited for adaptive structures due to low maximum elongation at break (normally 2-3%). Hence, a new type of resin system, which is more flexible than epoxy, is required. Elastomeric resin, especially polyurethane, has been used recently in aeronautical field in the form of a foam core in a sandwich structure due to its low density. In addition, polyurethane can be fabricated in a liquid form and, when mixed with a hardener, a solid block of polyurethane can be cast with different mechanical properties depending on chemical substances and added fillers. As a result, polyurethane resin system was considered to be an appropriate choice

Table 3.1: Advantages against disadvantages of RIFT [130].

Advantages	Disadvantages
• It can be used for most resin systems.	• The process is relatively complex and requires different skills to hand lamination.
• It can be used with most conventional fabrics.	• Greater emphasis is placed on pre-moulding preparation than on the actual moulding process.
• Large structural components can be fabricated.	• The process is sensitive to leaks in mould tool and bag.
• Material costs are lower than prepregs and vacuum bagging.	• Unlike prepregs, the quality control of resin mixing is in-house.
• It is more consistent than wet-laid components with minimal modification of tooling.	• The requirement for very low resin viscosity may compromise thermal and mechanical properties.
• Higher volume fraction leads to improved mechanical properties.	• Uneven flow may result in unimpregnated areas.
• Microstructure is uniform and void content is minimal relative to hand lamination.	• It cannot easily be implemented for honeycomb core laminate.
• Cored structure can be produced in a single flow process.	

for the type of resin used in this research.

Initially at the beginning of this research, a sample of commercially available polyurethane elastomer was provided from Chemtura. This product is known under the trade name "Adiprene® K TE92" and it is a single-component PTMG-based liquid urethane. The main advantages associated to single-component form of this resin is that it is less toxic and easier to process than the two-part counterpart. However, as the RIFT process was considered to be the main manufacturing method, Adiprene® K TE92 was too viscous and not suitable for such process.

As the viscosity of the resin is the key for RIFT technique, Hexflow® RTM6 from Hexcel, which is a common epoxy resin system used in RTM pro-

cess of aerospace applications, was used as a reference for comparing different polyurethane resins commercially available in the market. The viscosity of the Hexflow® RTM6 resin is 33 mPa·s at 80°C (infusion temperature). From initial market research, it was found that the typical viscosity of elastomeric polyurethanes is still high for RIFT. The elastomeric polyurethane that has the lowest viscosity was Biresin® 407 from Sika® with the viscosity of 600 mPa·s. Therefore, castable polyurethanes were considered instead of the elastomeric polyurethanes. However, the main drawback of castable polyurethanes is that the viscosity is directly proportional to the maximum strain. Moreover, as the viscosity decreases, the pot life (the time period in which the mixed resin is useable) also decreases. This introduces a difficulty to find a suitable polyurethane resin for RIFT that has satisfactory processing properties. Among various castable polyurethanes considered herein, a resin system from Sika® was selected due to its low viscosity and moderate maximum strain at break. The selected polyurethane resin was Biresin® G27 LR. This resin can be used with 2 hardeners: Biresin® G27 and Biresin® G27 weiß. In this research, the Biresin® G27 LR resin was mixed with Biresin® G27 hardener as the maximum strain is higher while the mixed viscosity is within the limit for the RIFT method. The properties of the mixed polyurethane resin are shown and compared with Hexflow® RTM6 and Adiprene® K TE92 in table 3.2.

Table 3.2: Properties of mixed polyurethane resin compared with Hexflow® RTM6 and Adiprene® K TE92.

	Hexflow® RTM6 [134]	**Adiprene® K TE92 [135]**	**Biresin® G27 LR [136]**
Viscosity [mPa·s]	33	3320	approx.120
Shore hardness	N/A	A92	D70
E-modulus [MPa]	2,890	7.9	730
Tensile strength [MPa]	75	35.8	25
Elongation at break [%]	3.4	480	30
Compressive strength [MPa]	N/A	N/A	35

Although the mixed viscosity of Biresin® G27 LR is approximately 4 times higher than the Hexflow® RTM6, it is well within the recommended limit to be used in the RIFT. In addition, the elongation at break is approximately 10 times higher which is beneficial for adaptive structures.

Another constituent that needs to be considered is the fibre. In this research, carbon fibre was initially selected due to its high strength to weight ratio and thermal stability. There are many types of carbon dry fabric available in the market such as unidirectional (UD), woven and braided, etc. Final selection was made towards woven dry fabric as it offers better dimensional stability and drape ability than the conventional UD fabric. Within the woven fabric class, there are also many types of weave style (figure 3.4), each with different properties as shown in table 3.3.

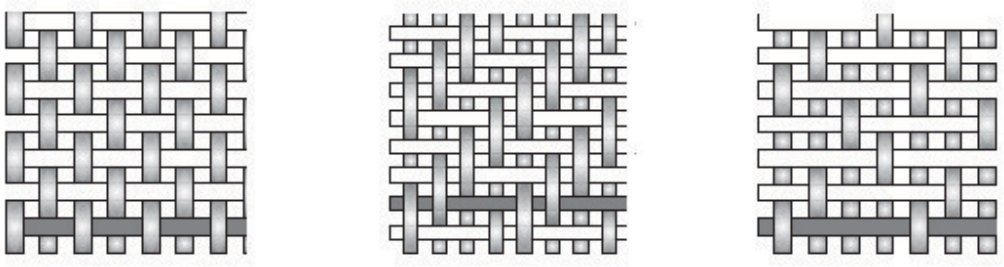


Figure 3.4: Different weave styles: plain (left), twill (middle) and satin (right), adapted from[137].

Table 3.3: Comparison of properties between each weave style, adapted from [137]

Property	Plain	Twill	Satin	Basket	Leno	Mock leno
Good stability	****	***	**	**	*****	***
Good drape	**	****	*****	***	*	**
Low porosity	***	****	*****	**	*	***
Smoothness	**	***	*****	**	*	***
Balance	****	****	**	****	**	****
Symmetrical	*****	***	*	***	*	****
Low crimp	**	***	*****	**	**/*****	**

Key: *****=Excellent, ****=Good, ***=Acceptable, **=Poor, *=Very poor

Considering the complex structure of corrugated composite skin of the morphing wing in which the unit cell length and the amplitude of a corrugation are small, the drapability of the fibre is important. According to table 3.3, a decision for the most suitable weave pattern for corrugated composites based on drapability and overall performance was made towards satin style. The dry carbon woven fabric tape was purchased from Eurocarbon and the specifications of the product are provided in table 3.4.

Table 3.4: Properties of the woven carbon fibre tape from Eurocarbon [138]

Property	Value
Weave pattern	5-harness satin
Length [m]	100
Width [m]	0.1
Weight [g/m^2]	±320
Reinforcement yarn	
- Warp	3K T300 50A
- Weft	3K T300 50A
Setting	
-Warp	8 threads/cm
-Weft	4 threads (×2)/cm

3.1.3 Manufacturing process of test specimens

Resin Infusion under Flexible Tooling (RIFT)

As discussed earlier that the main manufacturing route for carbon/PU composite is the RIFT. Therefore, only the bottom part of the mould is required while the top part is replaced by a flexible vacuum bag. Prior to resin infusion, the carbon fabric tape was cut to a length of 30 cm. Due to the slippery nature of carbon, as soon as the carbon tape was cut, the yarn at the ends of the fabric became lose and the weave pattern became distorted. Therefore, the ends of the fabric were taped as soon as the fabric was cut. Taping the ends of the fabric should not have any effect on the specimens because the ends of the finished panel would be cut and discarded. The infusion process was performed on a flat aluminium plate. In order to prevent the excess resin sticking to the plate, the bottom mould was wrapped with a releasing film. It was discovered during the preliminary runs that the surface finish could be improved by placing a layer of distribution medium on both top and bottom surfaces. In the very first run, the distribution medium was only placed on the top surface. This resulted in some dry spots on the bottom surface. The distribution layer provides some space and helps resin to flow between the fibre and the vacuum bag. Moreover, the distribution medium allows air bubbles to move easily to the outlet tube. The distribution medium should cover the entire carbon fibre surface and extended to contact the inlet and outlet tubes. It is essential to make sure that the peel plies cover all of the fabric area in order to ensure that the panel would be easily demoulded after cured. To speed up the process, as well as to reduce the amount of consumable materials

used, two flat panels were manufactured in each infusion process. This was done by placing two sets of fabrics side-by-side with no gap between them. From preliminary runs, it was found that leaving a gap between the two sets, the resin preferred to flow in the gap rather than infusing through fabric. As a result, the fabrics were not wetted evenly.

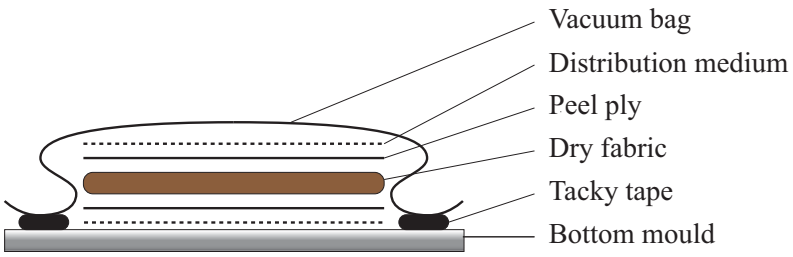


Figure 3.5: Lay-up sequence of the RIFT method.

The inlet and outlet tubes were placed at each end of the fabrics and were secured in place by a strip of tacky tape. Then, the breather cloth was folded and placed next the to the outlet tube. The breather cloth was found to help absorb the excess resin before it enters the outlet tube, which is connected to the vacuum pump. If the resin flows into the outlet tube, it will be cured and completely block the tube. Therefore, the infusion process must be stopped once the resin front reaches the breather cloth at the outlet. When the setup was completed, tacky tape was laid around the fabrics. Then, the vacuum bag was placed on top of the carbon fabrics and seal on the tacky tape. A great care must be taken at this step not to shift the lay-up as the fabrics slide easily. A minor degree of fibre misalignment may lead to significant reduction in stiffness and strength. Once the vacuum bag was securely placed on the tacky tape and checked for air tightness, the air was pumped out using a vacuum pump until the pressure reached 28 inHg. Then, the vacuum pump was turned off and the pressure was checked again. The pressure should remain unchanged if the vacuum bag is properly sealed. However, if the pressure drops, the tacky tape should be re-checked, especially around the inlet and outlet tubes.

To prepare the resin for infusion process, the resin and hardener were degassed in the vacuum oven to remove any air bubbles trapped as suggested in the technical data sheet supplied by Sika®. This process helps reduce void content in the finished product. The resin and hardener were mixed in the ratio of 1 to 1. The mixture must be stirred for 15 seconds to ensure that both parts are well mixed. For conventional epoxy system, the resin and the hard-

ener are normally mixed thoroughly and then degassed in a vacuum chamber. However, this could not be done for the polyurethane system as the pot life was very short. Therefore, the polyurethane system and hardener were degassed before mixing.

The infusion process began by switching on the vacuum pump with the inlet tube held closed with a G-clamp. Then the end of the inlet tube was immersed into the resin reservoir. The G-clamp was then slowly released manually to let the resin flow into the dry fabrics. The infusion rate is very critical in this type of setup. Fast infusion resulted in high void content as the air bubbles could not travel to the resin/air front and were trapped within the resin. As mentioned earlier that if the resin front reaches the outlet tube, the infusion process must be ceased to prevent tube clogging. Moreover, the pot life of the resin is very short (4-5 minutes), therefore, the infusion process must be complete within this timeframe. In this study, the mixed resin was infused into dry fabric at the rate of approximately 250 ml/min. It should also be noted that the panel size shown in figure 3.6 is 300 mm by 200 mm.

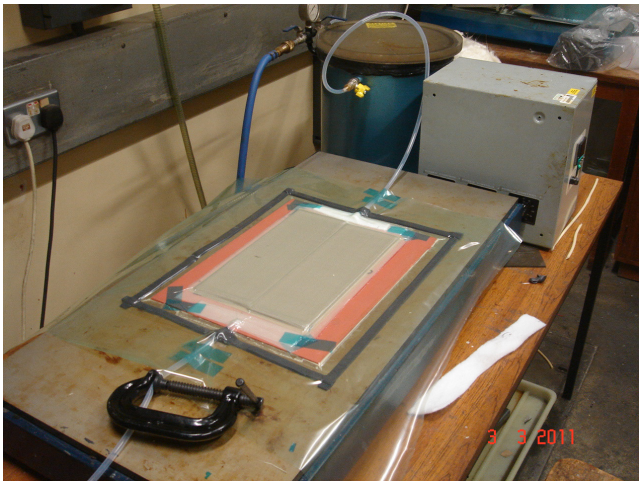


Figure 3.6: Instruments set-up prior to infusion.

As soon as the resin reached the end of the dry fabrics, the inlet was clamped and no more resin could enter the infusion area. However, the outlet tube was kept open and connected to the vacuum pump. This was to allow as much air bubbles to be removed as possible. The composite panel was left to cure in the mould for 90 minutes. This is within the recommended demoulding time by Sika®. The panels were removed from the mould and left to post-cure for three more days at room temperature before machining to the required

dimensions.

Ultrasonic C-scan

Prior to machining the specimens to recommended geometry, the ultrasonic C-scan was used to check the quality of each composite panel. This method provides a quick and non-destructive measure of air bubbles trapped inside the laminates. Furthermore, the results from the ultrasonic C-scan can be displayed graphically on screen, therefore, it is easy to visualise and identify usable portion of the panel.

The attenuation of the returned signal was measured. Full attenuation indicates that there are defects, such as voids and cracks, present in the composites. Low and uniform attenuation indicates that the composite panel under inspection contains low void content and the resin is distributed uniformly over the panel. Figure 3.7a shows a C-scan image of the panel from a preliminary run. The red and white patches represent high void content area in the panel. The problem with this particular run was that the resin infusion rate was not controlled and, therefore, the infusion rate was high. As a result, the amount of air bubbles trapped in the panel was also high. This problem was prevented in later runs by clamping the inlet hose so that resin flow rate could be controlled. Moreover, in this run there was an air leak and loss of pressure that eventually led to more void formation in the panel.

Figure 3.7b shows a C-scan image of a 12-ply panel. Dry portions towards the outlet end (left hand side) as well as around the edges of the laminate can be clearly observed. This suggested that the resin flows much faster around the edges than in the middle section. It should also be noted that the infusion time of a thick laminate was much slower than a thinner one.

Figures 3.8a and 3.8b are images from the ultrasonic C-scans of two panels manufactured side-by-side in a later run. It can be seen that the void contents are much lower, represented by blue and purple patches, in comparison to the C-scan images of the preliminary run. The only areas where high void contents are presented are around the edges which could be trimmed off later. The images also show that the quality of the two panels were almost identical. This confirms that there were no problems with infusing two panels side-by-side,

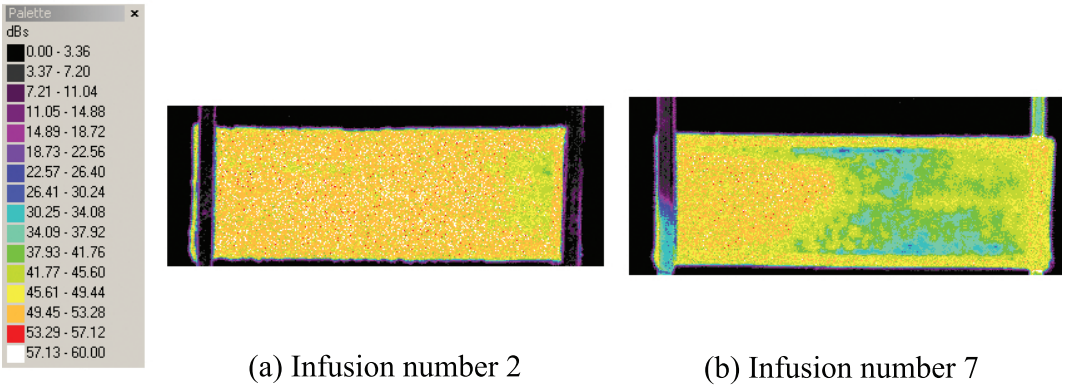


Figure 3.7: Ultrasonic C-Scan images of two panels (6 plies) manufactured from different runs.

and the quality of the laminate could be controlled by reducing infusion rate.

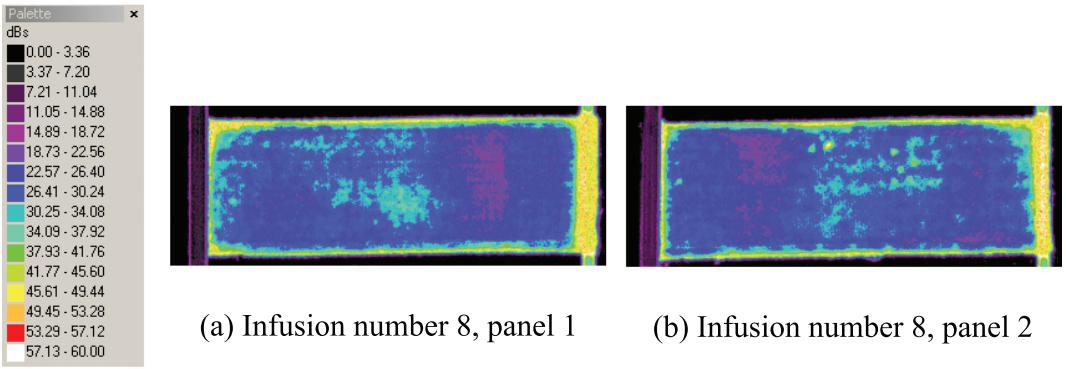


Figure 3.8: Ultrasonic C-Scan images of two panels (6 plies) manufactured side-by-side.

Specimen preparation

Once the results from the ultrasonic C-scan were satisfactory, the composite panels were trimmed from the composite laminates to remove unusable portions using a diamond tipped saw. The surfaces of the area that will be bonded with the end-tabs were grit blasted in order to ensure a good grip between the end-tabs and the laminates. The end-tabs were cut from a GFRP sheet to the required size using a wet diamond tipped saw. After the end-tabs were cut, one side of the surface was grit blasted in the same way as the composite panels. The bonding surfaces of the composite panels and the end-tabs were cleaned with solvents to remove dust and contaminants. A two-part Araldite 2011 epoxy adhesive was applied to both bonding surfaces. The

bonded panels were placed on a vacuum table for curing over night. The vacuum table was used to ensure even clamping force on the bonding area. The end-tabbed panels were then cut to size as specified in the ISO standards for each test as shown in table 3.5 with an exception to tensile and compressive specimens in weft direction and shear specimens due to limited width of the carbon fibre tape. In order to ensure flat and parallel edges and correct width and length, the edges around the specimens were carefully ground and cleaned.

For compressive specimens, two PTFE (polytetrafluoroethylene) strips were used to create 45° resin fillets. One end of the end-tabs near the test section must be chamfered at 45° while the end-tabs of the tensile and shear specimens do not have to be chamfered as shown in figure 3.9.

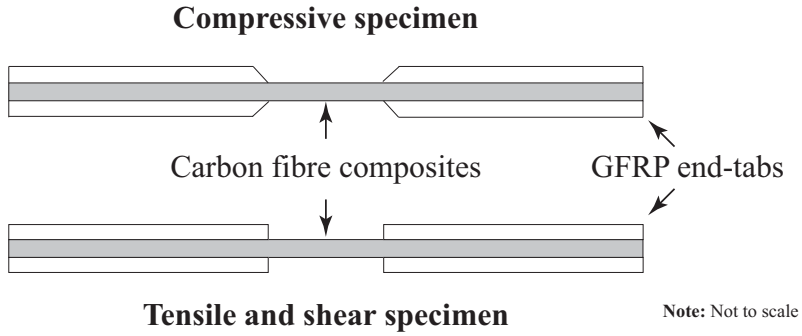


Figure 3.9: Schematic drawings of compressive, tensile and shear specimens showing different end-tab configurations.

Table 3.5: Dimensions of flat test specimens

Type of test	**Tensile**		**Compression**		**In-plane shear**
Standards/Method	**ISO 527 [139, 140]**		**ICSTM**		**±45 tension** [a]
Direction	**Warp**	**Weft** [a]	**Warp**	**Weft** [a]	**ISO 14129 [141]**
Length (mm)	250	90	100	85	100
Width (mm)	25	25	9.90	9.90	25
Thickness (mm)	2	2	4	4	2
Gauge length (mm)	150	30	10	10	40

[a] Dimensions are different from those specified in the standards/test method due to limited width of the carbon fibre tape.

After all specimens were machined to required size, a biaxial strain gauge of type YEFCA-5 (TML) was mounted to tensile and shear specimens while

two uniaxial gauges of type BFLA-2-3 (TML) were attached to the top and bottom surfaces of the compressive specimens in order to check whether column bending had occured.

3.2 Characterisation of Carbon Fibre Reinforced Polyurethane Composite

3.2.1 Tensile test

The tensile specimens were tested using a 10-tonne universal testing machine (Instron) at a loading rate of 2 mm·min^{-1}. The data acquisition system recorded four outputs: load, displacement and strains from biaxial strain gauges. Tensile stresses in warp and weft directions were calculated from applied load divided by laminate's initial cross-sectional area as shown in equation 3.1.

$$\sigma = \frac{P}{A_0}. \tag{3.1}$$

Figures 3.10 and 3.11 show typical stress-strain curves of tensile test in warp and weft directions, respectively. In the warp direction, the initial part of the curve was linear up to approximately 0.1% strain when the stiffness of some specimens started to change. The changes in stiffness were caused by the straightening out of the undulated longitudinal fibres and matrix crack initiation in the transverse direction. After this point, the load was mainly carried by the carbon fibre until ultimate failure. In the weft direction, the changes in stiffness could also be observed at around 0.1% strain but to a lesser extent.

The tensile Young's modulus in the warp (E_{11}) and weft (E_{22}) direction was calculated from the tangent of the slope of stress-strain curves above the nonlinear regime (approximately between 0.35 - 0.45% strain). The tensile test results are summarised in table 3.6.

The in-plane Poisson's ratio (ν_{12}) was calculated from the longitudinal (ϵ_{11}) and transverse (ϵ_{22}) strains above the nonlinear regime in the warp direction using equation 3.2:

$$\nu_{12} = -\frac{\epsilon_{22}}{\epsilon_{11}}. \tag{3.2}$$

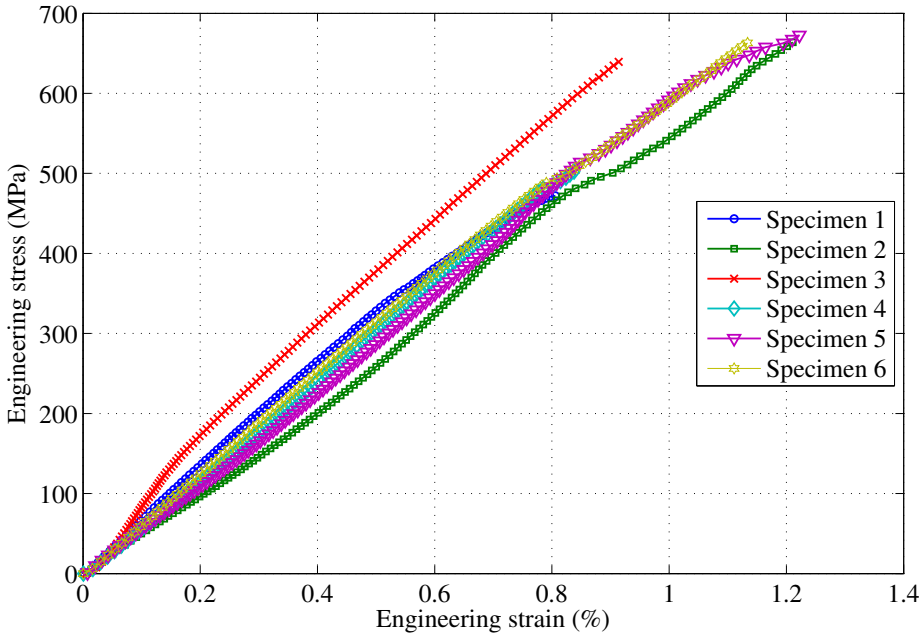


Figure 3.10: Stress-strain curves of tensile specimens in warp direction.

Table 3.6: Mechanical properties obtained from tensile test of flat carbon/PU specimens.

E_{11} **(GPa)**	E_{22} **(GPa)**	ν_{12}	UTS_{11}[a] **(MPa)**	UTS_{22}[a] **(MPa)**
62.47 (3.94)[b]	63.10 (4.31)[b]	0.06 (0.022)[b]	602.97 (83.15)[b]	552.10 (18.03)[b]

[a] UTS denotes ultimate tensile strength.
[b] Value in parentheses indicates standard deviation.

It can be noticed that the values of E_{11} and E_{22} were slightly different by 1%. Also the UTS_{11} and UTS_{22} differed by 8.44%. This is attributed to different architecture of the fibres in warp and weft directions as shown in table 3.4, although the total number of fibres in the two directions is similar (8 threads/cm) and the specimens were fabricated in such a way that the lay-up was balanced by flipping the plies above the mid-plane upside down. Another factor that could affect the results is manufacturing variability as the resin flow rate was controlled manually. Further detail on manufacturing variability will be discussed later in this chapter.

Optical micrographs taken from failed specimens (figures 3.12a and 3.12b) revealed matrix cracks in the transverse direction in both warp and weft specimens. This was believed to occur first and resulted in changes of tensile

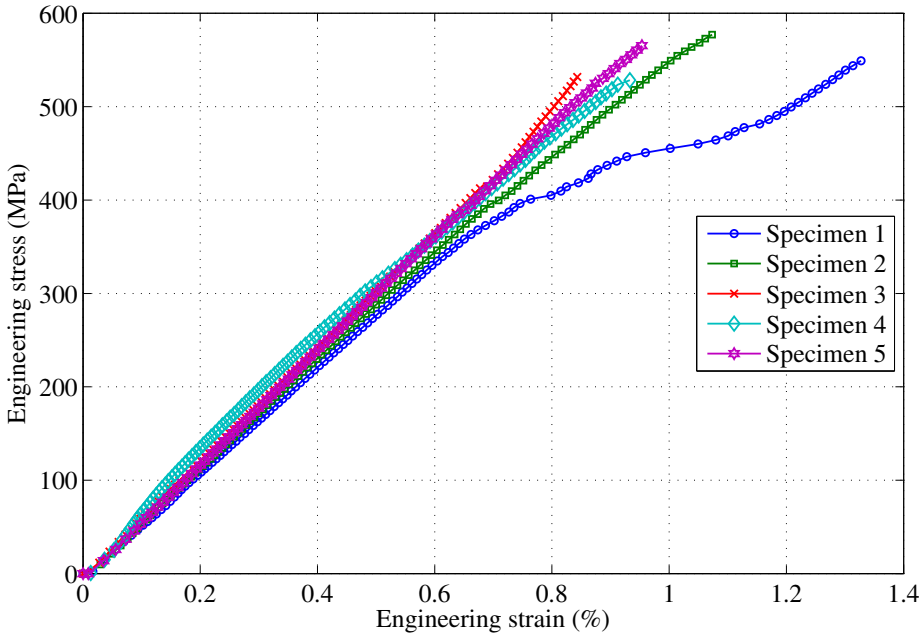
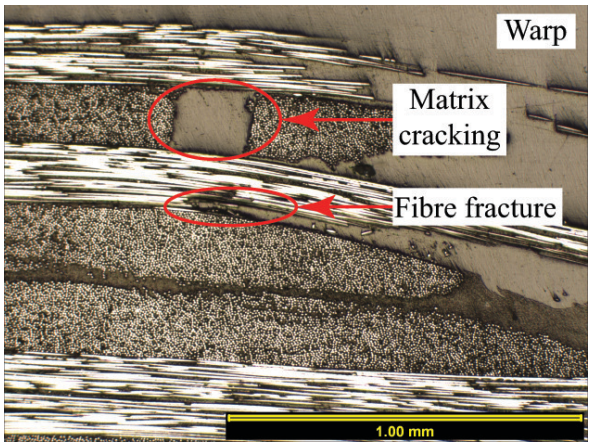
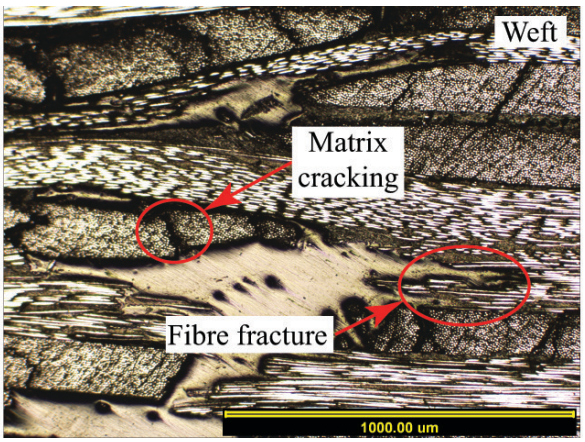


Figure 3.11: Stress-strain curves of tensile specimens in weft direction.

Young's modulus. The load was then carried mainly by carbon fibres in longitudinal direction until fibre fracture occurred which caused catastrophic failure of the specimen.



(a) Warp direction



(b) Weft direction

Figure 3.12: Optical micrographs of tensile specimen in (a) warp and (b) weft directions.

3.2.2 Compression test

The purpose of the compression tests was to measure compressive moduli and strengths in warp and weft directions. The tests were performed on a

Zwick universal testing machine at a loading rate of 2 mm·min^{-1}. The ICSTM method developed at Imperial College London was chosen as it consistently gives higher compressive strength than other methods with low scatter [142]. Typical compressive stress-strain curves in both directions are shown in figures 3.13 and 3.14. The compressive moduli ($E_{c,11}$ and $E_{c,22}$) and strengths in warp (UCS_{11}) and weft (UCS_{22}) directions are shown in table 3.7 with the number in parentheses indicating standard deviation. Similar to tensile test, the values of $E_{c,11}$ and $E_{c,22}$, and UCS_{11} and UCS_{22} were slightly different due to different fibre architecture in warp and weft directions and manufacturing variability.

Table 3.7: Young's moduli and ultimate compressive strengths obtained from compression test of flat carbon/PU specimens.

Direction	Value
Warp ($E_{c,11}$)	57.75 (2.98)[b] GPa
Warp (UCS_{11})[a]	299.95 (20.69)[b] MPa
Weft ($E_{c,22}$)	58.61 (13.31)[b] GPa
Weft (UCS_{22})[a]	262.40 (11.80)[b] MPa

[a] UCS denotes ultimate compressive strength.
[b] Value in parentheses indicates standard deviation.

Microscopic examination of compressive specimens (figure 3.15) showed kink band formation at undulated region of the fibres in longitudinal direction. In this region, local shear stresses between reinforcement and matrix were higher than in the flat region. This caused an instability that led to fibre microbuckling. The fibre tows in the transverse direction also failed in transverse compression indicated by 45° angled fracture.

3.2.3 In-plane shear test

The in-plane shear test was performed using a uniaxial tensile test method on ±45° specimens. This test method was selected due to simplicity and low cost. The test was carried out on the Instron testing machine at a loading rate of 2 mm·min^{-1}. Stress-strain relationships of all specimens are shown in figure 3.16. The in-plane shear stress (τ_{12}) and the corresponding in-plane shear strain (γ_{12}) of the ±45° specimen were derived from measured stress (σ_{11}) and strains in longitudinal (ϵ_{11}) and transverse (ϵ_{22}) directions as expressed in equations 3.3 and 3.4.

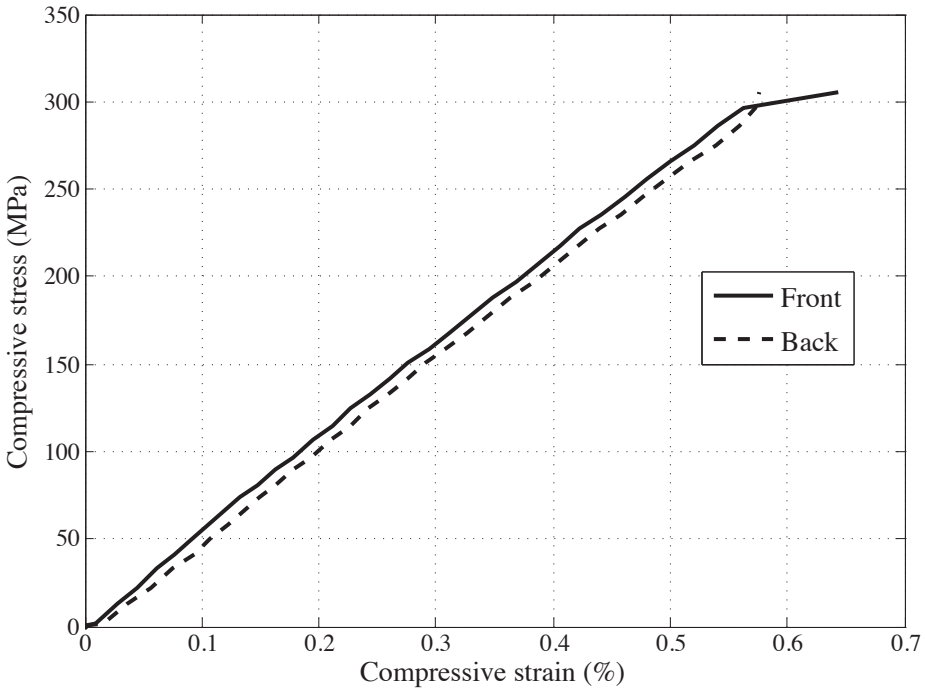


Figure 3.13: Example of stress-strain curve of compressive test in warp direction.

$$\tau_{12} = \frac{\sigma_{11}}{2}, \tag{3.3}$$

$$\gamma_{12} = \epsilon_{11} - \epsilon_{22}. \tag{3.4}$$

The in-plane shear modulus (G_{12}) was computed from the tangent of the stress-strain curve between 0.1% and 0.5% shear strain. The values of in-plane shear modulus and in-plane shear strength are shown in table 3.8. Again, the values in parentheses identify the standard deviation.

Table 3.8: In-plane shear modulus and strength obtained from in-plane shear test of flat carbon/PU specimens.

Property	**Value**
In-plane shear modulus (G_{12})	2.04 (0.17)[a] GPa
In-plane shear strength ($\tau_{12,u}$)	38.10 (1.43)[a] MPa

[a] Value in parentheses indicates standard deviation.

The in-plane shear strength and maximum shear strain cannot be shown graphically in figure 3.16 because the biaxial strain gauge failed before the

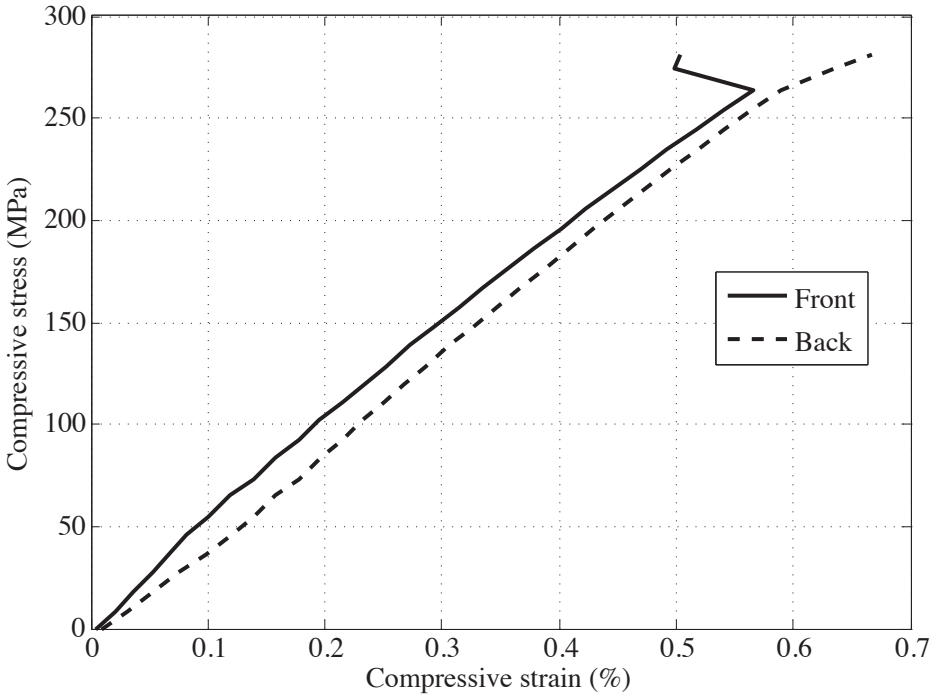


Figure 3.14: Example of stress-strain curve of compressive test in weft direction.

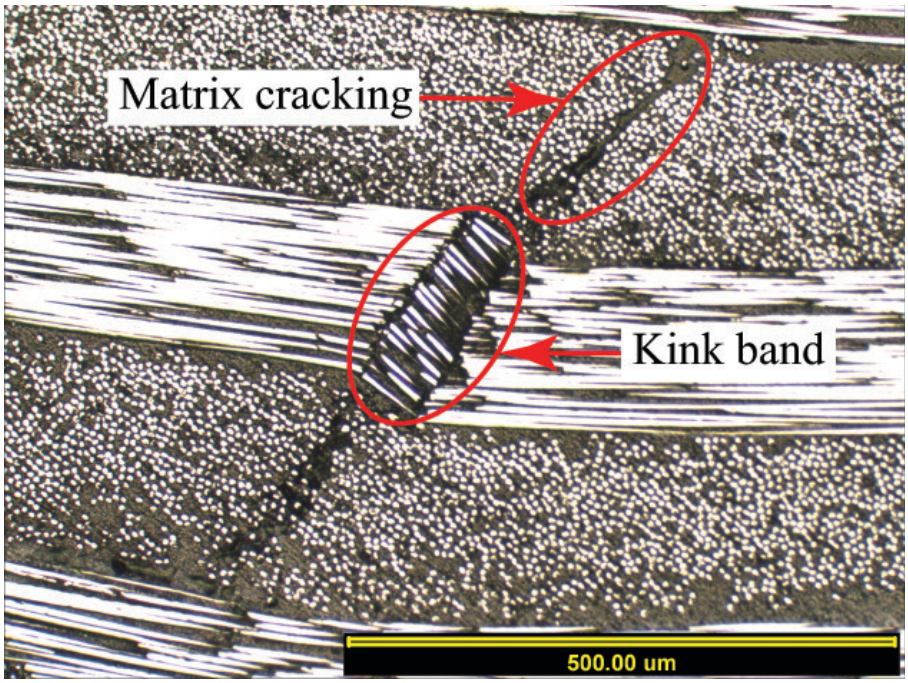


Figure 3.15: Optical micrograph of compressive specimen.

maximum strength and strain were reached. However, the maximum in-plane shear strength could be calculated from the applied load obtained from the testing machine.

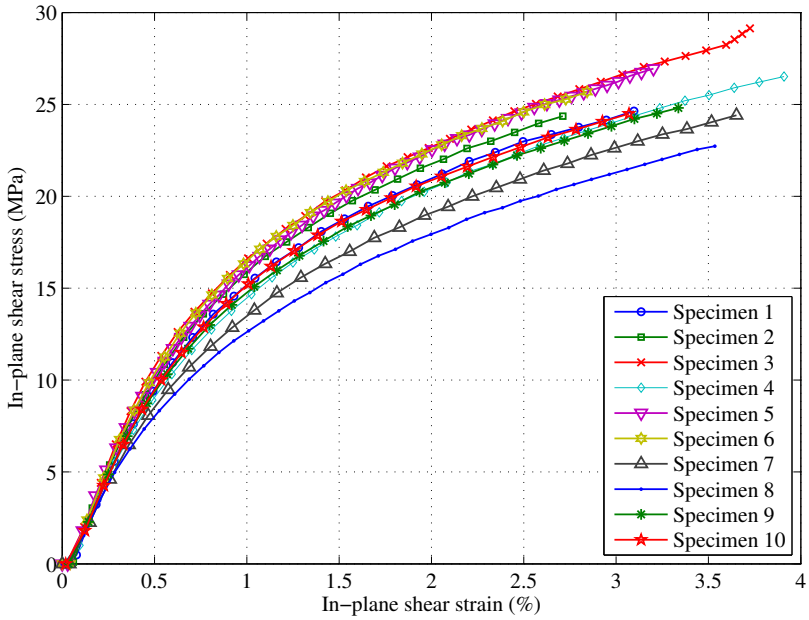


Figure 3.16: In-plane shear stress-strain relationship of carbon/PU laminates.

The nonlinear stress-strain relationships as observed in figure 3.16 were attributed to matrix yielding and delamination. This was caused by straightening out of the undulated fibres and internal friction due to fibre sliding after debonding from the matrix. Also, the variation of the curves are attributed to the manufacturing variability.

3.2.4 Flexural test

The flexural test was performed to measure flexural moduli and strengths in warp and weft directions. The specimens were tested on the Instron testing machine using three-point bending method (ISO 14125 [1] standard). The dimensions of the specimen are presented in table 3.9. Each specimen was tested with a midpoint deflection rate of 1mm/min until complete failure.

Table 3.9: Dimensions of flexural test specimens [1].

Dimension	Warp	Weft
Span, L (mm)	80	80
Width, b (mm)	15	15
Thickness, h (mm)	2	2

The specimens in warp and weft directions were manufactured from the same specimen but cut in different directions. Figure 3.17 shows a schematic drawing of warp and weft specimens that have the same number of piles (6 plies) but the orientation of each ply is different.

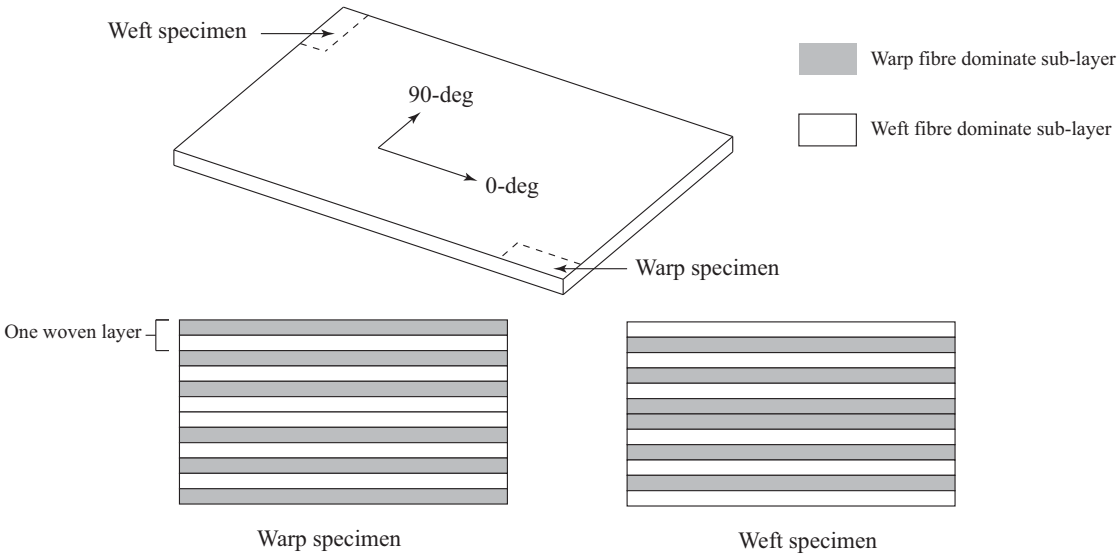


Figure 3.17: Schematic drawing of the flexural specimens.

The flexural stress (σ_f), flexural strain (ϵ_f) and flexural modulus (E_f) could be calculated using equations 3.5, 3.6 and 3.7, respectively.

$$\sigma_f = \frac{3FL}{2bh^2} \tag{3.5}$$

where F is the applied load (N),

$$\epsilon_f = \frac{6sh}{L^2} \tag{3.6}$$

where s is the mid-point deflection (mm),

$$E_f = 500(\sigma_f'' - \sigma_f') \tag{3.7}$$

where σ_f'' and σ_f' are flexural stresses measured at $\epsilon_f = 0.0005$ and 0.0025, respectively.

The flexural stress-strain relationships of the specimens in both warp and

weft directions are shown in figures 3.18 and 3.19. It can be seen from the flexural stress-strain curves that the flexural stress varies linearly until the specimen reaches its elastic limit. Beyond the elastic limit, the flexural stress dramatically drops and 'snap' sound could be heard. However, no damage were visible on the surfaces of the specimen. The results also imply that there were no delamination up to failure. As the test continued, the flexural stresses reduced further and the cracks could be seen through specimen's thickness. A summary of the flexural moduli and strengths are shown in table 3.10. There are 2 factors influencing the difference in the flexural properties in warp and weft directions. The first factor is the stacking sequence of the specimens in warp and weft directions as shown in figure 3.17. Another factor is the amount of fibres in warp and weft directions, which will be discussed later.

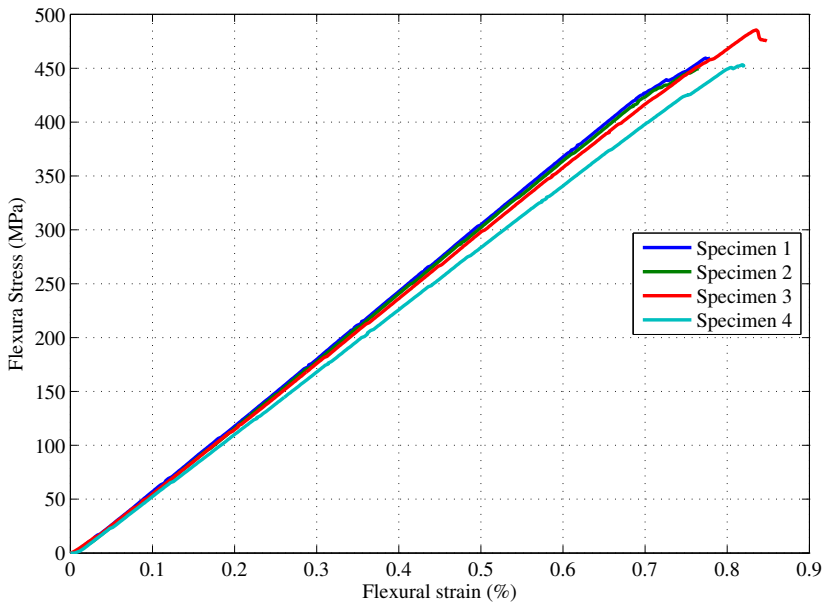


Figure 3.18: Flexural stress-strain relationships of specimens in warp direction.

The difference in mechanical properties between warp and weft directions indicates that the amount of material in the two directions is different. A closer investigation of the woven carbon fabric as shown in figure 3.20 illustrates that the weft direction has more fibres than the warp direction. This seems to confirm the tensile and compression test results which higher Young's modulus in the weft direction was observed.

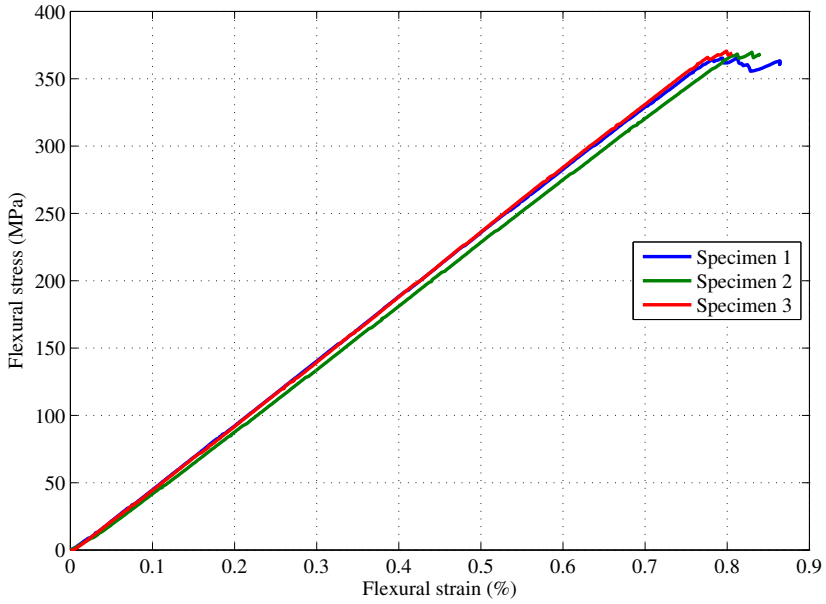


Figure 3.19: Flexural stress-strain relationships of specimens in weft direction.

Table 3.10: Summary of flexural moduli and strengths in warp and weft directions.

Property	Value	Unit
E_f (warp)	60.08 (1.77)[a]	GPa
E_f (weft)	46.80 (0.81)[a]	GPa
Flexural strength (warp)	459.10 (11.58)[a]	MPa
Flexural strength (weft)	365.82 (4.54)[a]	MPa

[a] Value in parentheses indicates standard deviation.

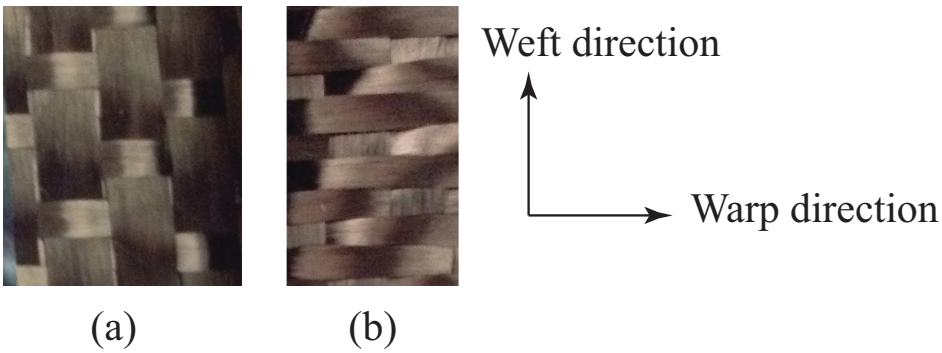


Figure 3.20: Woven carbon fibre fabric (a) warp dominate surface and (b) weft dominate surface.

3.2.5 Comments on the test results

High values of standard deviation

It can be noticed from the experimental results of flat specimens that the values of standard deviation of moduli and strengths were high. This was

due to slight inconsistency of resin flow rate during manufacturing. During the infusion process, the inlet tube was clamped by a G-clamp and manually released to start resin infusion procedure. The manually-controlled resin infusion caused the variation in the quality of the final product. Figure 3.21 shows the ultrasonic C-scan images of different composite laminates from different infusions under the same condition. All laminates shown in figure 3.21 were used to fabricate test specimens. It can be clearly seen from the images that the quality of the laminates from each run varied slightly from each other. In order to rectify the problem, it is recommended that a disposable valve is connected at the inlet tube to regulate the resin flow rate.

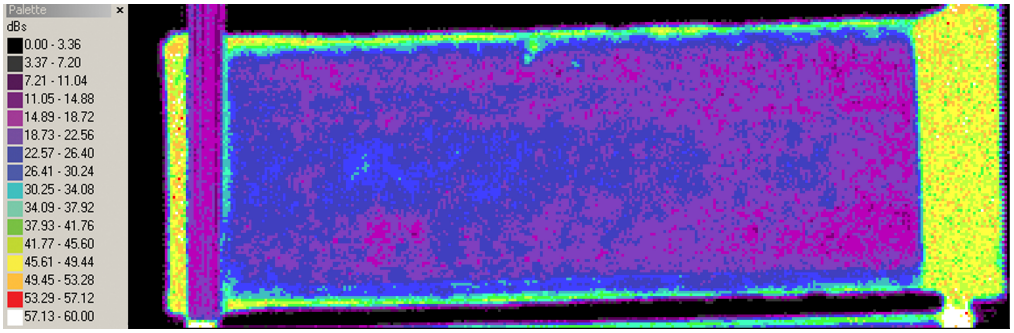
Low ultimate tensile strain

From the tensile stress-strain relationships in both warp and weft directions (figures 3.10 and 3.11), it can be noted that the maximum strain is less than 1% which is at the same order of the ultimate tensile strain of carbon/epoxy composites. This was expected to be higher as the elongation at break of the mixed Biresin® G27 LR is 30%, compared to 3.4% of the Hexflow® RTM6 (table 3.2). Low value of ultimate tensile strain was thought to be arisen from mechanical properties of the neat resin. Therefore, a simple tensile test of the neat resin was performed to compare the value of elongation at break with the technical data sheet. The discussion of the results is reported in the following section.

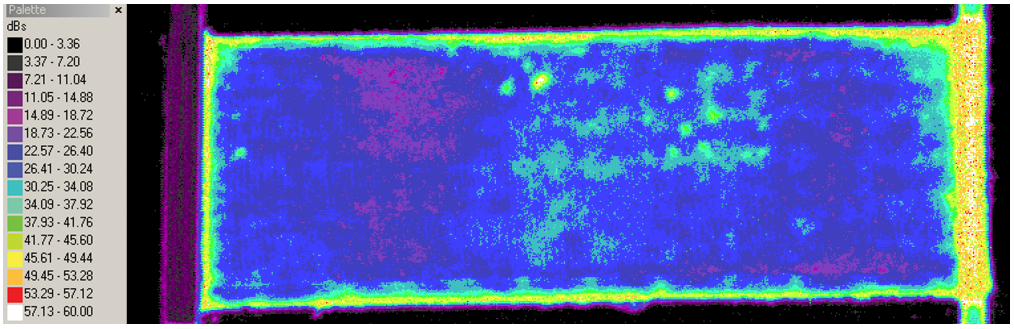
3.2.6 Neat resin tensile test

The tensile test of the neat resin was performed to verify that the ultimate tensile strain is similar to the value specified in the technical data sheet of Biresin® G27 LR [136]. The neat resin tensile test was conducted following the procedures specified in the ISO 527-2 [143].

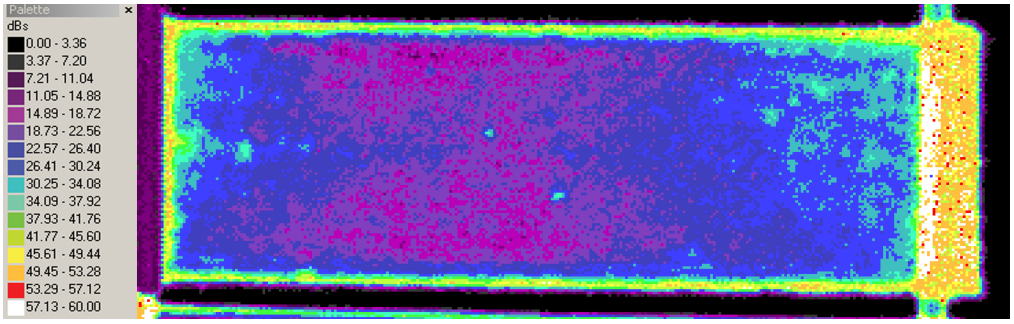
To prepare test specimens, the resin and hardener were measured and then degassed in a vacuum chamber. Then the resin and hardener were mixed thoroughly and poured onto a preheated rectangular mould (70°C) as specified in the guidance from the manufacturer. After 90 minutes, the resin was demoulded and post-cured at room temperature for 3 days in order to obtain maximum performance. The edges of the bulk resin were trimmed using a



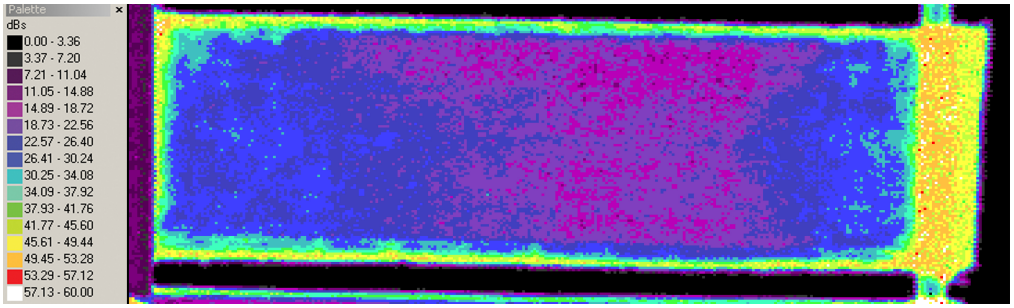
(a) Run number 4



(b) Run number 8.2



(c) Run number 9.1



(d) Run number 9.2

Figure 3.21: Ultrasonic C-scan images from different infusions.

diamond tipped saw before machining each specimen into a dog-bone shape. The last step in preparing the test specimens involved grinding the dog-bone coupons to the required size as specified in figure 3.22 and table 3.11.

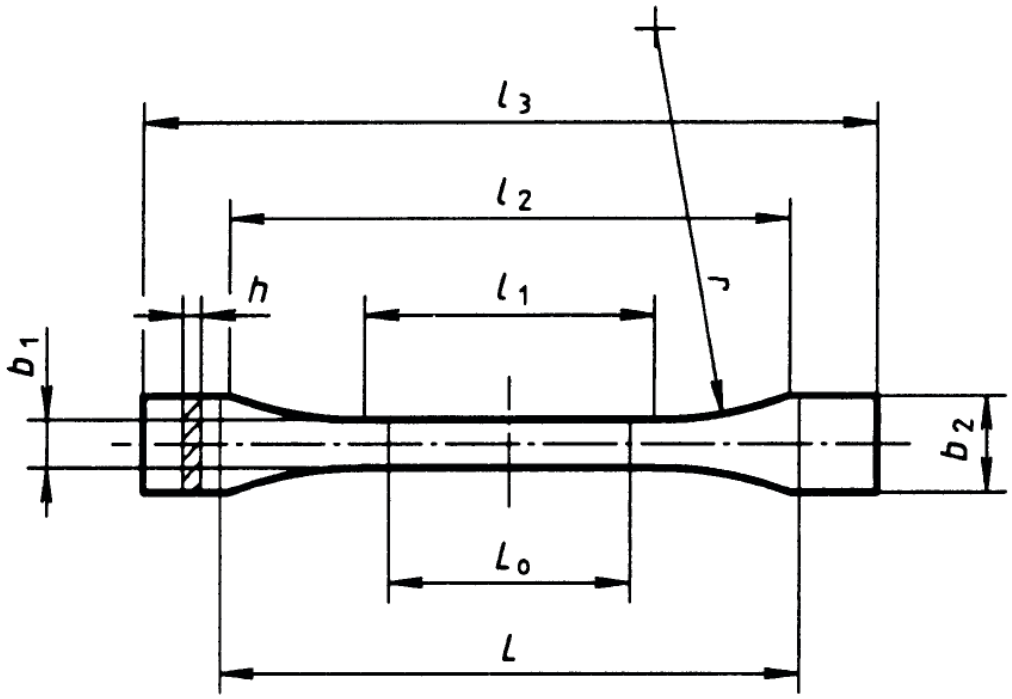


Figure 3.22: Dog-bone specimen [143].

Table 3.11: Dimensions of dog-bone specimen [143].

Parameters	Description	Size (mm)
l_1	Length of narrow parallel-sided portion	60
l_2	Distance between broad parallel-sided portions	110
l_3	Overall length	180
r	Radius	65
b_1	Width of narrow portion	10
b_2	Width of ends	20
h	Preferred thickness	4
L_0	Gauge length	50
L	Initial distance between grips	115

The specimens were tested using the 10-tonne universal testing machine (Instron) at a loading rate of 1 mm·min^{-1}. There was no strain gauge attached to the test specimens as the strain was expected to be more than 10% which is higher than the maximum strain of the strain gauge. Therefore, the cross-head displacement and applied force were measured directly from the machine via data acquisition system. Then, the tensile stress was computed using equation 3.1 while the tensile strain was calculated using equation 3.8.

$$\epsilon = \frac{\Delta L}{L}, \tag{3.8}$$

where ϵ is tensile strain in loading direction.
ΔL is change in length due to applied load [mm].
L is initial distance between grips [mm].

In mechanical testing, which the cross-head displacement is used to calculate applied strain as in the current research, it is customary to calibrate the measured displacement by taking into account the compliance of the machine ($C_{Machine}$) [144]. Normal procedure to evaluate the machine compliance is to perform a tensile test of a stiff material. Then, load-displacement curves obtained from the machine and the strain gauge are plotted against each other. The setup for tensile testing is based on an assumption that the loading system behaves as two springs in series. One spring represents the machine and another spring represents the specimen [145]. Therefore, the total stiffness recorded by the cross-head displacement (k_T) is related to the stiffnesses of the machine ($k_{Machine}$) and the specimen ($k_{Material}$) through equation 3.9.

$$\frac{1}{k_T} = \frac{1}{k_{Machine}} + \frac{1}{k_{Material}}. \tag{3.9}$$

It should be noted that the total stiffness (k_T) can be obtained from the slope of the load against displacement plot from the machine's cross-head reading while the stiffness of the material ($k_{Material}$) is obtained from the slope of load against displacement plot from strain gauge reading.

From equation 3.9, the total compliance measured by the cross-head displacement (C_T), which is a reciprocal of the total stiffness, is simply a sum of machine compliance ($C_{Machine}$) and compliance of the analysed material ($C_{Material}$). This relationship is shown in equation 3.10.

$$C_T = C_{Machine} + C_{Material}. \tag{3.10}$$

In the current study, the compliance of the testing machine was evaluated from the tensile test of flat carbon/PU composite in the warp direction. An example of load-displacement curves obtained from the machine cross-head and the strain gauge is presented in figure 3.23.

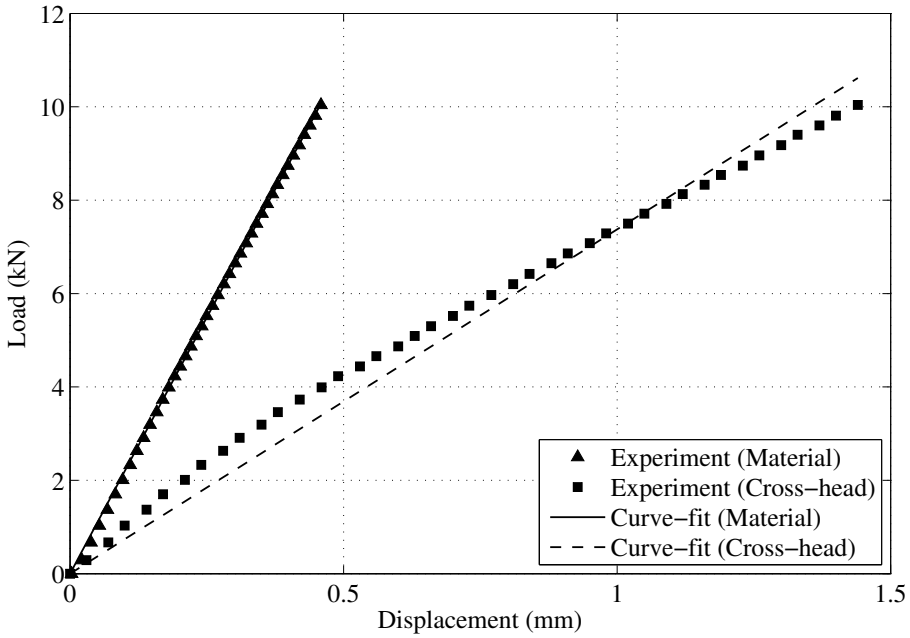


Figure 3.23: An example of load-displacement plot used to calculate the machine compliance.

The average values of the cross-head and strain gauge compliances are C_T = 0.151 μm/N and $C_{Material}$ = 0.05 μm/N, respectively. According to equation 3.10, the measured compliances yield a machine compliance of $C_{Machine}$ = 0.102 μm/N.

Once the value of machine compliance has been evaluated, the real elongation of the material (ΔL_{real}) can be determined from the measured cross-head displacement (ΔL_T) and applied load (P) using equation 3.11.

$$\Delta L_{real} = \Delta L_T - PC_{Machine}. \tag{3.11}$$

A typical stress-strain relationship of Biresin® G27 LR is shown in figure 3.24. The stress-strain curve of the neat resin exhibits ductile behaviour with linear elastic region between 0% and 1.5% strain and nonlinear plastic region from 1.5% to approximately 7% strain where the specimen ruptured. As in evaluation of tensile modulus of composite laminates in weft direction, the modulus of pure resin was calculated from the initial slope of the stress-strain

curve. Another parameter of interest that could be obtained from experimental test of the neat resin is the maximum strain at break. Average values of tensile Young's modulus and ultimate tensile strain as well as the ultimate tensile strength are presented and compared with the values from manufacturer in table 3.12.

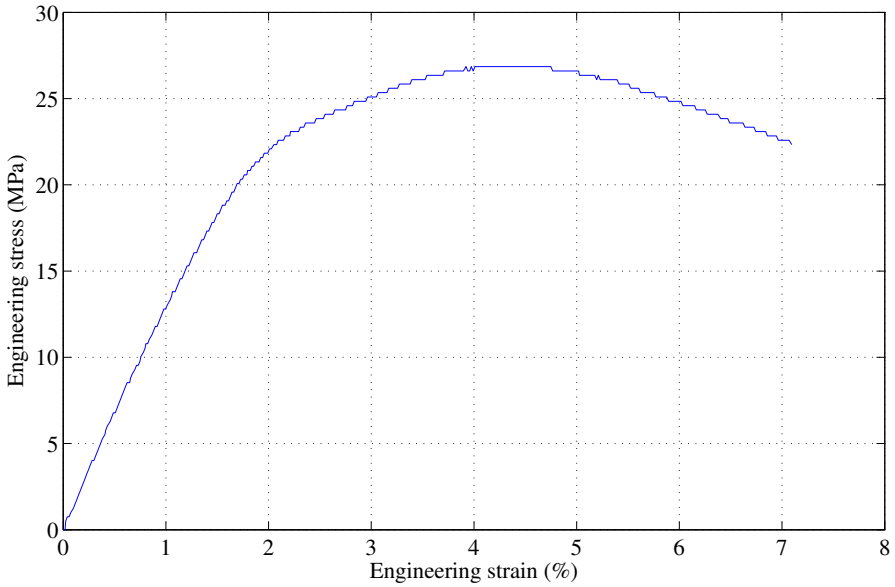


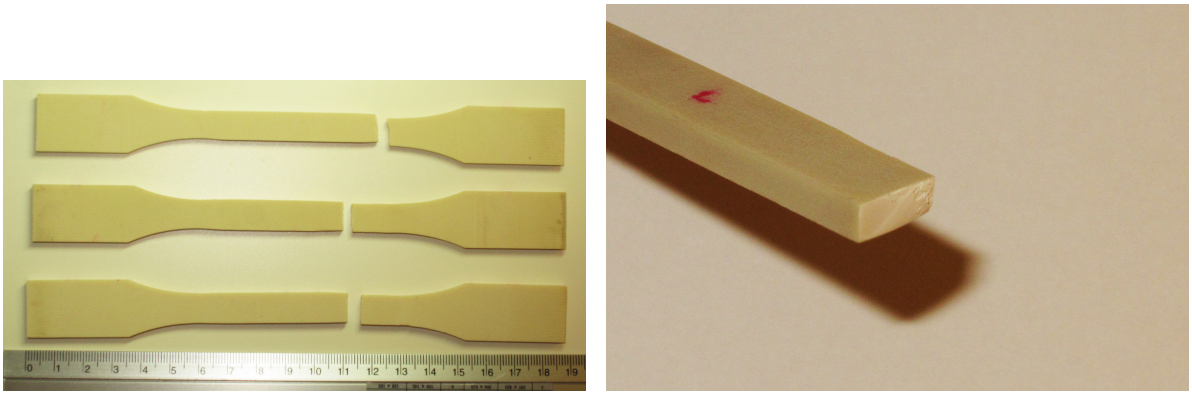
Figure 3.24: Example of stress-strain curve of tensile test of Biresin® G27 LR.

Table 3.12: Comparison of mechanical properties obtained from experiment and technical data sheet.

Property	**Experiment**	**Data sheet [136]**	**Discrepancy (%)**
Young's modulus (MPa)	1,290.66 (12.74)[a]	730	76.80
Ultimate tensile strain (%)	7.23 (1.03)[a]	30	-75.90
Ultimate tensile strength (MPa)	27.62 (0.50)[a]	25	10.48

[a] Value in parentheses indicates standard deviation.

The mechanical properties obtained from the experiment and presented in table 3.12 show consistent results as indicated by low values of standard deviation. However, the experimental results are not in a good agreement with the technical data sheet, especially the ultimate tensile strain and tensile Young's modulus, despite using the same ISO standard for testing.



(a) Example of failed specimens **(b)** Fracture surface

Figure 3.25: Images of failed specimens and fracture surface

Figure 3.25 shows images of failed specimens from the neat resin test. It can be observed that the fracture surface is flat, which indicates low strain at break. This agrees well with the stress-strain plot shown in figure 3.24.

As mentioned in previous section that low maximum strain of carbon/PU composite could be a result from mechanical properties of the neat resin, it was proved through experimental test that the ultimate tensile strain of the pure resin is approximately one-fifth of the value suggested by manufacturer. Moreover, the strain at which the resin started to deform plastically was relatively low (approximately 1.5%) and this contributed to early matrix yielding at low strain, which caused changes in stiffness of the composite. Another feature observed during the tensile test of carbon/PU composite that could be attributed to low elongation at break of the neat resin was the low rupture strain of the composite.

3.3 Chapter Summary

Carbon reinforced polyurethane laminates were introduced as an alternative to carbon/epoxy laminates for morphing wing applications. The mechanical properties were evaluated through experimental tests, namely tensile, compression and in-plane shear. The test specimens were prepared using RIFT which is one variant of the vacuum-assisted RTM process. This manufacturing technique was selected as opposed to hand lay-up process as it gives a better quality.

In tensile tests, changes in stiffness at 0.1% strain were observed from

stress-strain curves in the warp and weft directions. This was caused by the straightening out of the crimped fibres and matrix cracking initiation. The compression tests were performed to evaluate the compressive strengths in both warp and weft directions. The optical micrographs of compressive specimens showed that the fracture plane was characterised by a kink band shear. The in-plane shear stress-strain curves also exhibited nonlinearity due to fibre-matrix debonding, which caused internal friction during fibre sliding under applied load. It can be noticed from the experimental results of flat specimens that the values of standard deviation were high. This was caused by slight inconsistency during manufacturing process as the resin infusion rate was controlled manually using a G-clamp. Therefore, the resin flow rate of each run was not exactly the same as others. As a result, the quality of the laminates from each run was different. It is recommended that this problem can be resolved by connecting a disposable valve at the inlet to control the resin flow rate.

One unexpected issue observed from the tensile test results was low ultimate tensile strain and yield strain. Therefore, a tensile test of neat resin was performed in order to compare the value of maximum strain at break against the technical data sheet from the manufacturer. The results from neat resin test suggested that the average maximum strain is 7%, approximately one-fifth of the 30% specified by the manufacturer. This mismatch of the maximum strain could be considered as one factor that leads to low value of ultimate tensile strain of the carbon/PU laminates.

Chapter 4

Carbon Fibre Reinforced Polyurethane Corrugated Composite

The main concept proposed in this research is to utilise corrugated structure as a skin for morphing wing applications. This type of structure offers flexibility in the direction perpendicular to the corrugations (transverse direction). In the direction parallel to the corrugation (longitudinal direction), the corrugated structure remains stiff and, therefore, is able to withstand aerodynamic loads.

The corrugated structure in this study was fabricated from carbon fibre reinforced polyurethane composite as presented in chapter 3. The cross-sectional profile of the corrugation can be manufactured in various forms. Each profile affects the structural response and must be investigated. It is not only the cross-sectional profile that affects behaviour of the corrugated structure, dimensions such as amplitude (A) and unit cell length (λ) of a corrugation, also have influences on the structural response under applied load and need to be studied. In the current research, three different profiles as shown in figure 4.1 were considered, which are sinusoidal, trapezoidal and U-shape. Different amplitudes and unit cell lengths were analysed using a commercial finite element package, ABAQUS (version 6.10). The FE model incorporated surface-based cohesive behaviour with damage initiation and evolution criteria to simulate delamination between two adjacent plies in composite materials. In order to validate the FE model before using it in a parametric study, the results from the sinusoidal model was compared with the results from the tensile test of

the corrugated composite. Once the FE model was validated, a parametric study of corrugated composite was performed. Many FE models of different corrugated profiles and sizes were generated to investigate structural response numerically and compared the results with more limited analytical models. The detail of such analysis is presented in subsequent sections.

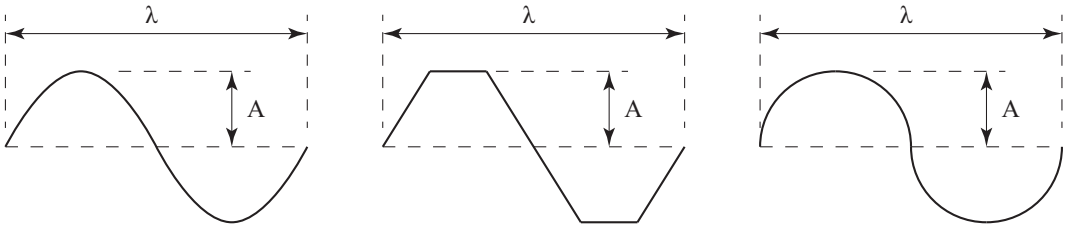


Figure 4.1: Different cross-sectional profiles of the corrugation.

4.1 Tensile Test of Corrugated Composite

Before constructing a complex model for numerical analysis, especially the model that consists of cohesive elements or surfaces to simulate damage arisen from delamination, a tensile test of corrugated composite was performed to obtain a reference result in order to validate the FE model.

4.1.1 Infusion of corrugated composite panel

Preliminary infusions

As RIFT has been selected as the main fabrication process of carbon fibre reinforced polyurethane composite, only one tool face is needed for the infusion. A corrugated one-part mould was manufactured from an aluminium block by a CNC milling machine. 'Sine wave' corrugation was chosen for ease of dry fabric layup and vacuum bagging due to lack of vertical walls and sharp corners. It was also chosen for reproducibility of the geometry. The corrugation contour was modelled by importing the coordinates generated in an Excel spread sheet as opposed to using the spline feature in Pro/Engineer (Wildfire 5.0). This was to ensure that the shape was a true sine function. The schematic drawing, photo and dimensions of the corrugated mould are shown in figures 4.2 and 4.3 and table 4.1, respectively.

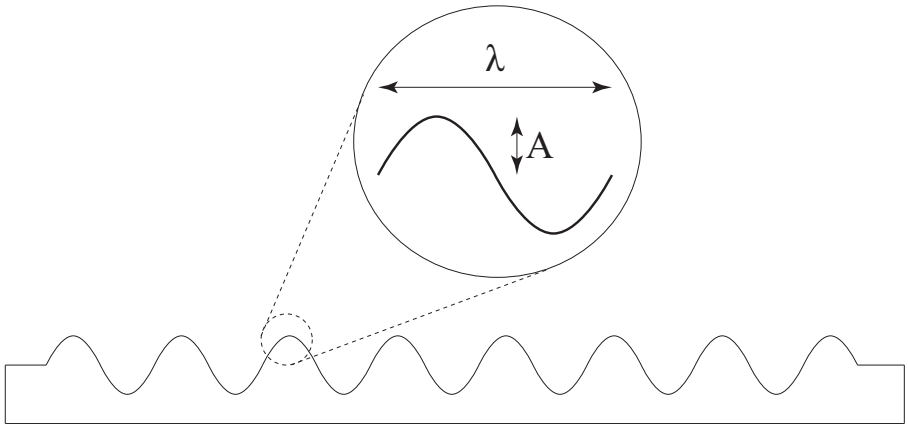


Figure 4.2: Schematic drawing of the corrugated mould.

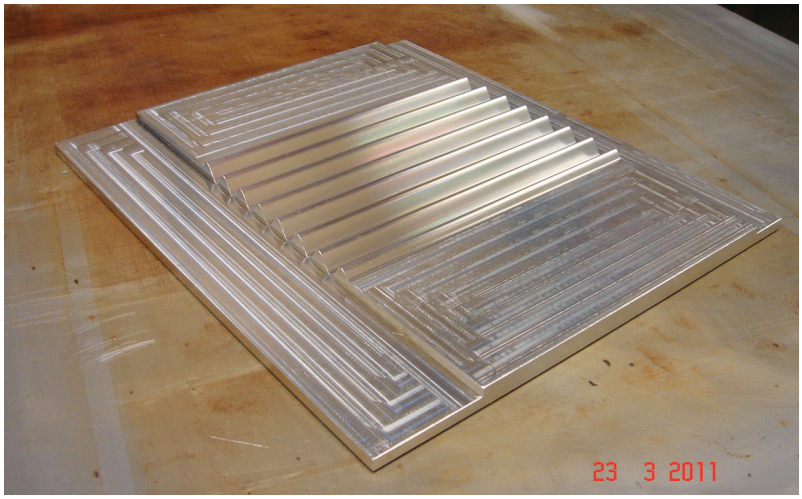


Figure 4.3: Photo of the aluminium corrugated mould.

The corrugated composite panels were fabricated using RIFT similar to the procedures used to manufactured flat specimens as shown in figure 4.4. The objective of this stage is to develop a suitable technique for making good quality corrugated carbon/polyurethane composite panels. Many techniques for manufacturing flat composite panels have been developed and discussed in chapter 3. Previously for flat panels, it was relatively easy to do lay-up process as all the layers were placed flat on top of each other. There was no need to

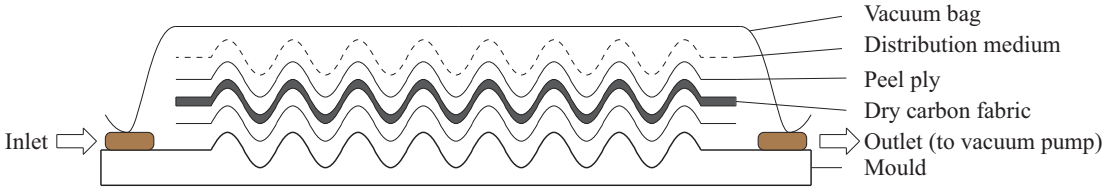


Figure 4.4: Lay-up sequence for RIFT of corrugated panels.

Table 4.1: Dimensions of the corrugated mould.

Dimensions	Values
Amplitude of corrugation (A)	5 mm
Wavelength of corrugation (λ)	20 mm
Total width of the mould	250 mm

drape the fabric into a complex shape. It was also easy to vacuum bag and seal flat laminates. However, with the corrugations, these processes became much more difficult.

Because of the corrugations, the mould cannot be wrapped with release film as before. To prevent the panels and excess resin from adhering to the aluminium mould, a Frekote® 700-NC (from Henkel) mould release agent was applied on the top surface of the mould. Unlike the flat panel where dry fabrics could be infused directly under vacuum, for corrugated panel fabrication, the fabric was needed to be pre-formed prior to resin infusion. This is because without pre-forming, it is difficult to control how fabric will drape into shape under vacuum. Moreover, the vacuum bag will exert pressure at the peaks of the corrugations and prevent any further movement of the laminates. This causes dry fabric to 'bridge' the trough rather than draping along the contour of corrugations. It was important that there was no bridging of fabric during infusion process, as it would lead to accumulation of resin pockets at the trough of corrugations. A temporary adhesive spray (Airtac 2 by Airtech) was used to keep each layer in place during lay-up process. This spray is formulated especially for carbon fibre, so it does not have any effect on the composites.

The lay-up sequence of the corrugated panel was very similar to the flat panels, except that there was only one layer of distribution media, which was placed on the top of the fabrics. In the preliminary run, it was found that the distribution media could not be bonded to the mould using adhesive spray. It was very difficult to place it onto the corrugations. Therefore, a peel ply was placed directly on the mould as a first layer. The method was as follows. First the temporary adhesive was sprayed on the peel ply and it was placed on the flat area on one side of the mould, ensuring that the alignment was correct. Starting with one end, fingers were used to press the ply onto the mould and into the corrugations. It was important that the ply was laid flat with no air pockets or wrinkles. It was found in early runs that any wrinkles on

the peel ply would be reflected on the panel's surface. Once the peel ply was completely laid, the carbon fabric could be placed on top in the same manner, again with the adhesive spray to hold it in place. After that, one more layer of fabric and peel ply were placed one after another. The final layer was the distribution media as mentioned above. The temporary adhesive spray could not be used, so pieces of sticky tape were used to hold it in place. The next step was placing and sealing the vacuum bag. The sealant tape was placed around the lay-up as shown in figure 4.5. It can be seen that it was placed along the corrugations. This is to guide the vacuum bag into the corrugations, and minimised 'bridging' of the bag at the troughs. Thus, the pressure could be applied uniformly on the laminates even at the bottom of the troughs. Inlet and outlet tubes were placed in the same manner as in the fabrication of the flat panel. The vacuum bag was then placed and sealed onto the sealant tape. The inlet tube was clamped using a G-clamp and the outlet was connected to a vacuum pump to check for air leakages. It was found that there were a lot of leakages around the corrugations, as the sealant tape tends to bridge at the troughs. It was difficult to re-seal because the sealant tape did not adhere well to the mould surface as it was covered by the mould release agent. Once the bagging area was airtight, the resin could be infused. Resin preparation and infusion process were exactly the same as in the manufacturing of flat panel. However, with the corrugations, infusion time was longer than in the flat panel even though the panel was only two-ply thick. This is because it was difficult for the resin to flow up the inclined part of the corrugation. Therefore, there was a lot of resin accumulated at the troughs of the corrugation. Once, the resin reached the outlet, the inlet tube was clamped tightly to stop further resin entering the bagging area. The outlet tube was left connected to the vacuum pump to further remove air bubbles. At this point air leakage into the bagging area had to be monitored closely. The air tended to leak from the sealing around the corrugations. However, it was a very small leak and could be easily stopped once noticed by applying pressing on the tacky tape. The composite were left to cure in the mould for 90 minutes as suggested by Sika. The corrugated panel was much harder to demould than a flat one. This had to be done with great care to make sure that there was no damage occurred on the panel, since it was very thin and fragile. Despite only one layer of distribution media was used, there were no dry spots on the lower side of the panel. This was probably because the panel was only two-ply thick. The surface finish could be affected by the quality of each layer of the layup, any

wrinkles or gaps in any of the layer would be reflected onto the panels. The bottom surface seemed to have a smoother and flatter surface than the top surface due to one solid tool face was used. The upper surface was constrained by a flexible vacuum bag, hence, the shape could not be fully controlled. Figure 4.6 shows upper and lower surfaces of the panel from the preliminary run. There were some weave distortions along the bottom of the corrugations, which led to formation of resin pockets. On the bottom surface, there were a lot of resin rich areas. All of the resin pockets were on the bottom of the corrugation.

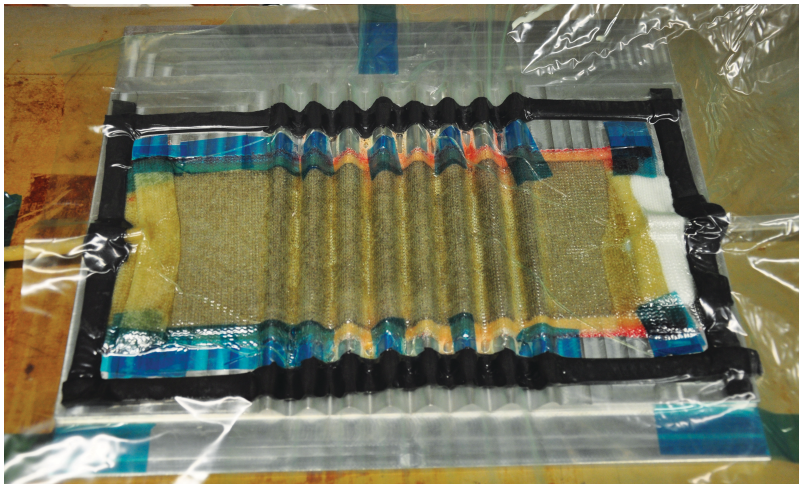
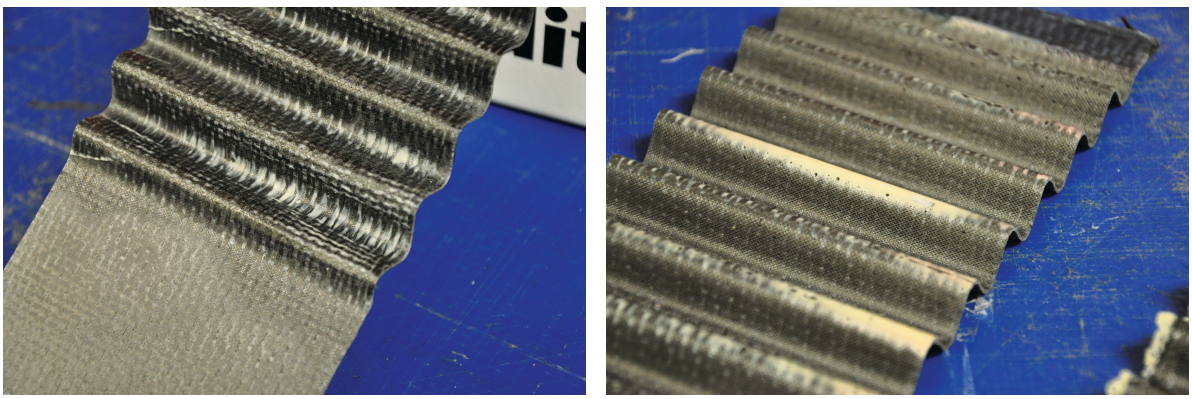


Figure 4.5: Infusion process of a preliminary run.



(a) Top surface **(b)** Bottom surface

Figure 4.6: Top and bottom surfaces of a panel from a preliminary run.

The main problem found in the preliminary run was during the lay-up process. It was difficult to place the carbon fibre fabric into the corrugations by hand, as the weave tended to deform and the fabric did not attach to the bottom surface of the trough. Another problem with using hands was that when

the fabric was forced into the next corrugation, the lay-up in the previous corrugation tended to slip and lifted off the mould. Even though the temporary adhesive spray was used, it was still relatively easy for the fabric to move and displace. A gap between the fabric and peel ply would result in having pockets of excess resin on the lower surface of the panel. This is undesirable because it causes nonuniform thickness having thicker bit around the troughs than other areas. Therefore, if the fabric could be laid carefully with no gap in each layer, the quality of the composite would be improved.

During the infusion process, it was discovered that the vacuum bag could not contact the bottom of the corrugation. There were gaps between the laminates and the vacuum bag. This was because the bag could not deform and was unable to stretch so that the trough areas could not be compressed. This allowed the resin to accumulate on the bottom of the laminates and slow down the infusion rate. This also meant that the pressure on the laminates was not uniform and could lead to variation in the thickness. Despite having sealed the bag along the corrugation, bridging still occurred.

Demoulding was more difficult for corrugated panel than for the flat ones. Thus, a great amount of force was required to remove it from the mould. This implies that it was more likely that the fragile panel would be damaged. Ideally, the mould release agent should prevent resin bonding to the mould's surface and the panel could be easily removed. However, because spray adhesive was used to keep the laminates in place during lay-up process, the use of the mould release agent was not fully effective. Another problem with temporary adhesive spray was that it adhered to the surface of the mould. Hence, each time the infusion was performed, a thin layer of resin residue was deposited onto the surface. If left untreated the layer will grow thicker and could affect the surface of the panel. Therefore, adhesive residue had to be scraped off at the end of each infusion.

Improvement of infusion process

The quality of the lay-up could be improved by using polyurethane inserts (as a substitute to male part) to push and guide the fabric into place. Inserts were made by casting the Biresin® G27 LR directly in the mould. The results were that the inserts had the opposite shape to the corrugations and so exactly matched the mould. Figure 4.7 shows two inserts being used to pre-form the

fabric. The improved lay-up process that utilises the PU inserts is as follows. The temporary adhesive was sprayed on the bottom side of the fabric. Then, the fabric was placed onto the flat area of the mould. After that, the sealant tape was used to prevent fabric from sliping during the pre-forming process. Slide and press the inserts along the fabric to ensure that the fabric was evenly spread onto the mould surface. Then, used one insert to push the fabric into the corrugation and ensure that it bonded to the bottom of the trough. Used another insert to push further fabric into the next corrugation while keeping the pressure on the previous insert. This was to prevent the fabric in the first corrugation from lifting off the trough during the pre-forming of the second corrugation. The process was repeated along the whole length of the fabric in the same manner. By 'walking' the inserts, the fabric should not be slide or displace. It was found that by using the inserts, the lay-up process was much quicker and easier. There was less damage to the weave pattern when the inserts were used in comparison to using hands. This was because the whole width of the tape was pushed at the same time and also due to low friction between the inserts and the fabric. Figure 4.8 shows pre-formed fabric and peel ply on the mould surface ready for infusion. It can be seen that the laminates were well laid with no gaps or air pockets.

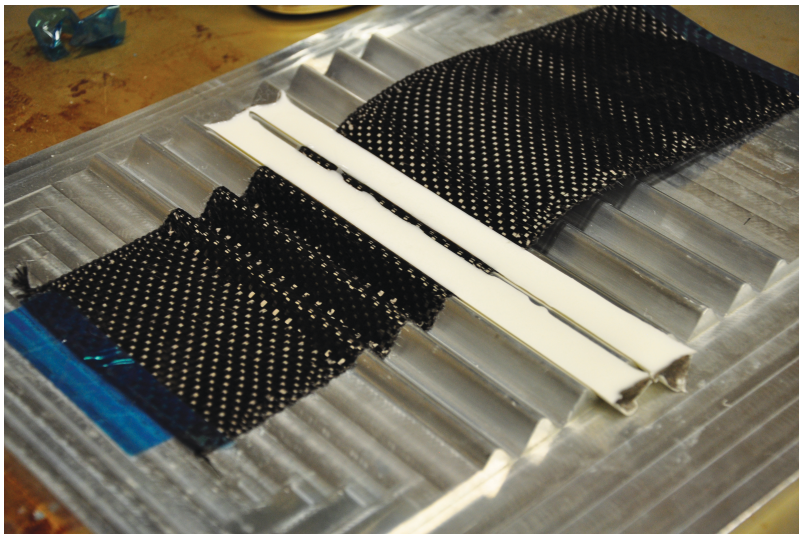


Figure 4.7: Inserts used to pre-form carbon fabric.

There were some problems with sealing the vacuum bag along the corrugations. The seal was prone to air leakage and it was difficult to keep the vacuum area airtight. The solution to this problem was to seal the bag around the flat flange of the mould as it was initially designed for. However, if the bag

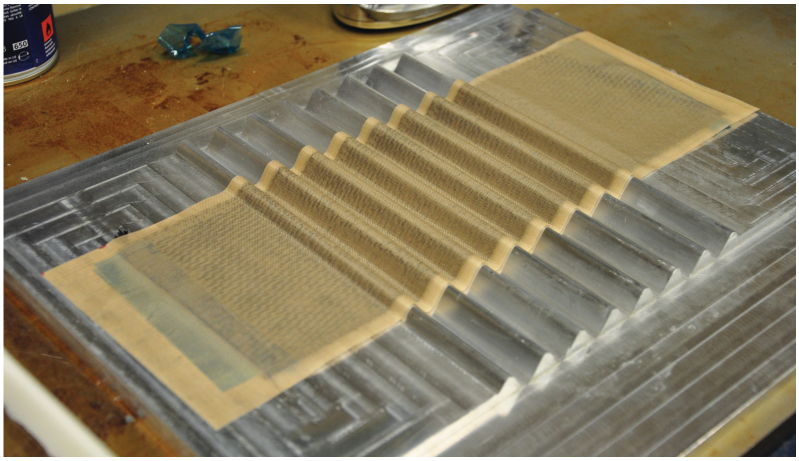


Figure 4.8: Pre-form fabric and peel ply on mould.

was sealed on the flat surface, it would not be able to deform into the bottom of the corrugations under vacuum. By sealing along the flanges, the available area was lower than sealing along the corrugations. In order to make sure that uniform pressure was applied to the whole laminates, something must be used to transfer the pressure force from the bag to the laminates, especially in the trough areas. The polyurethane inserts could be used for this application. After the fabric, peel ply and distribution media were laid, the inserts were placed on top of all of the corrugation. Because the distribution media was not so deformable, a caul plate was used to keep the inserts in place. Once all of the inserts were positioned, the sticky tape was used to attach the inserts and the laminates to the mould so that the caul plate could be removed before placement of the vacuum bag. The inlet hose was clamped and the outlet hose was connected to the vacuum pump to check for air tightness. It was found that for this configuration, there was no air leak around the seal and very high pressure could be sustained.

The resin was infused once the vacuum bag was sealed. Infusion rate was noticeably slower and the clamp had to be open much wider than the previous run in order for the resin to start flowing. It seems that the inserts made it more difficult for the resin to be infused through the fabric and a lot of resin was forced to flow along the edge of the mould. The panel fabricated from this set up had a higher quality than in the preliminary runs. There were fewer resin pockets on the lower side of the panel, however, not all were removed. The surface finish was better, there were no wrinkles and dimples, caused by the inserts in the lay-up process.

An alternative to the use of inserts for applying pressure to the laminates was by making 'pleats' on the sealant tape, as shown in figure 4.9. These pleats allowed the area of the vacuum bag to be larger than that of the corrugations and, thus, provided sufficient vacuum bag area such that the bag could deform into the bottom of the trough. This provided uniform pressure onto the laminates without the use of any insert. The pleats were only made around the corrugated area, as there was no need for excess bagging area for the flat section. This configuration also allowed the sealant tape to be placed on the flat surface of the mould, which resulted in good air tight. However, it was more complicated to seal the bag onto the sealant tape due to the pleats.

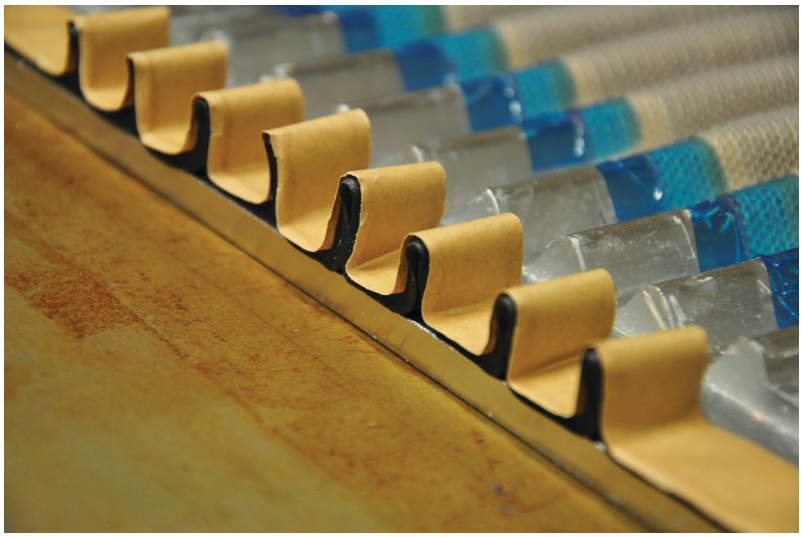


Figure 4.9: Photo of 'pleats' used in later infusions.

As air was being pumped out, the vacuum bag slowly deformed into the corrugation. However, the deformation was random and the bag did not spread out evenly into all corrugations. Thus, some of the corrugations were bridged, while the others had many folds of bags on top. In order to spread out the bag evenly to the entire surface, the vacuum pump was turned off to increase the pressure slightly to allow the vacuum bag to be shifted to appropriate place. The inserts were again used to push the bag into the corrugations. Once the bag was correctly positioned, infusion process could be done. With this set up, the resin infusion was much easier than before. The infusion rate was similar to that of the flat panel (approximately 250 ml/min). The corrugated composite panel manufactured from this method was better than using inserts alone as there was almost no resin pocket on the surface. Moreover, the thickness of

the corrugated panel was more uniform.

Comparing the two manufacturing techniques of corrugated composite panel, it can be concluded that vacuum bagging with pleats is more appropriate than solely using the inserts. This is because it gives higher quality specimens and also much simpler to setup. The problem with using the inserts is that it requires a longer time to setup and the inserts have to be discarded after the infusion as the excess resin builts up on the inserts and causing them to deform. Due to the geometry of the corrugation (sinusoidal), the gap between the insert and the mould is not constant along the corrugation, the gap at the peaks and troughs are bigger than the gap at the inclined part of the corrugations. This explains why resin flow was restricted when inserts were used. Therefore, the method that provides the most uniform pressure on the laminates is the vacuum bagging with pleats. It can be seen from figure 4.10 that, with the modified method, the surface of the panel has improved. there is no damage of the weave pattern and there is hardly any resin pocket on the lower surface.

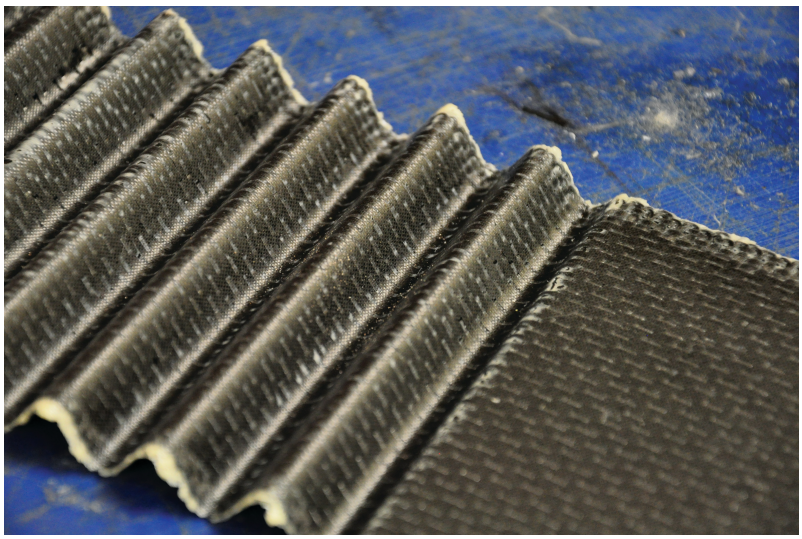


Figure 4.10: Surface finish of a corrugated composite panel from a later run.

4.1.2 Specimen preparation

Three more corrugated panels were fabricated by vacuum bagging with pleats as explained in the previous section. This was enough to produce nine tensile specimens. The dimensions of the specimens are shown in table 4.2. Three specimens could be cut from one panel, therefore, nine specimens would

be produced in total. Specimen preparation process was very similar to that of the flat tensile specimens in warp direction. The first step was to cut four GFRP end-tabs for each composite panel. Then sand blasted one side of the end-tabs to roughen the surface in order to improve bonding capability. Since the corrugated panels were very fragile, sand blast of the composite surface was not an option. Instead, a piece of sand paper was used to roughen the surface slightly. A two-part epoxy adhesive (Araldite 2011) was used to bond the end-tabs and composite panel together. The panels were left to cure overnight under vacuum to increase clamping force. In order to protect the specimens from damage caused by the vacuum table, the composite panel was placed on the top of the mould as shown in figure 4.11. The mould helped support the composite panel under pressure and prevented any deformation during the curing stage.

Table 4.2: Dimensions of the corrugated composite tensile specimen.

Dimensions	Values
Total nominal length (mm)	250
Nominal width (mm)	25
Nominal thickness (mm)	0.70
Nominal gauge length (mm)	150
Number of corrugations	7.5
Number of plies	2

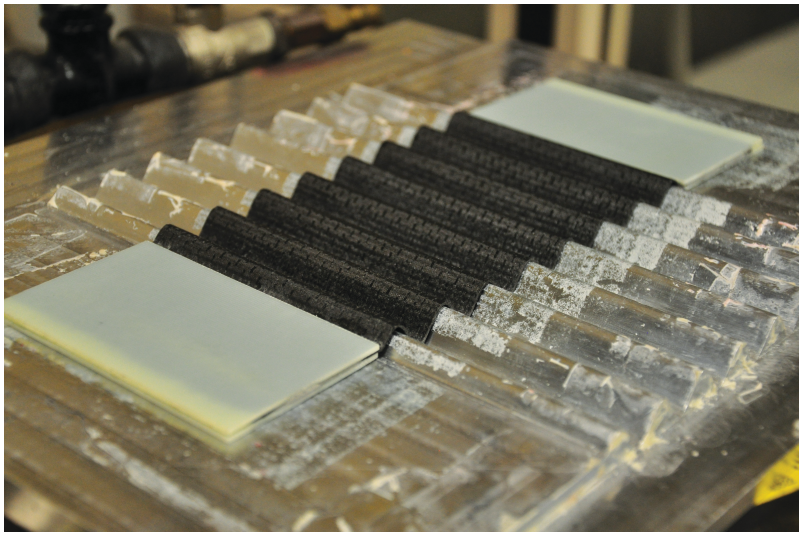


Figure 4.11: Panel placed on the mould before vacuum curing process of epoxy adhesive.

The specimens were cut to required width using a dry diamond tipped saw. Ideally, a wet diamond tipped saw should be used as it can reduce the temperature induced during cutting process which resulting in smoother cut surfaces. However, it could not be used because the corrugations made the panel too thick to fit in the cutting space. Moreover, a panel to be cut with the wet diamond tipped saw needs to be clamped and this could not be done on the corrugated composite in this study. The specimens from the first panel were labelled as followed: 1.1, 1.2 and 1.3, and the specimens machined from panel 2 and 3 were also labelled accordingly. This way any results from testing could be traced back to the panel from which the specimens were cut.

4.1.3 Tensile test of corrugated specimens

The corrugated specimens were tested experimentally in tension to determine the load-displacement relationship of the carbon/PU corrugated composite. There is no international standard for testing corrugated composites. Nonetheless, testing method was similar to tensile test of flat composite specimens. Therefore, ISO 527-4 standard [140] was used. The test was carried out on the Instron universal testing machine with 1kN load cell at a speed of 2 mm·min^{-1}. Only one specimen (specimen 1.1) was tested to failure to see how the corrugated panel would deform and fail. The rest of the specimens were tested to elastic limit only. This was because the load applied to the corrugated composite skin should not be beyond the elastic limit in order to prevent permanent damage of the corrugated skin. The tensile strain of the corrugated specimen was expected to be greater than 10% which is the maximum strain of the extensometer. Therefore, the cross-head displacement of the testing machine was used. Two outputs from the test (applied load and cross-head displacement) were recorded by a data acquisition system. The cross-head displacement readings were then corrected for machine compliance using equation 3.11 presented in section 3.2.6. The structural response of the corrugated composite structure up to failure point is shown graphically in figure 4.12.

It can be seen from the load-displacement curve how the corrugated composite structure deforms under tension. Initially, the corrugated composite deformed elastically as shown by label 1 in figure 4.12 and the load-displacement relationship was linear. However, at point 2, the elastic limit was reached and matrix cracking was initiated at this point. A 'snap' sound could also be

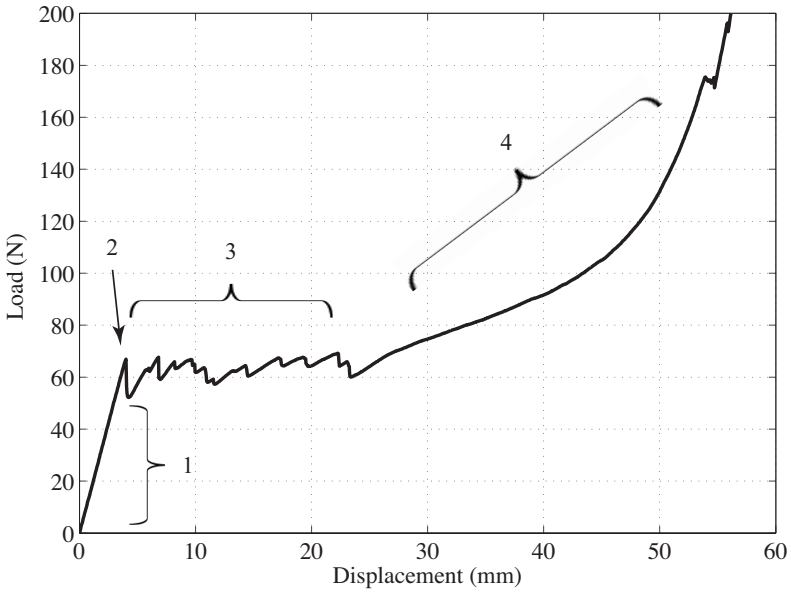
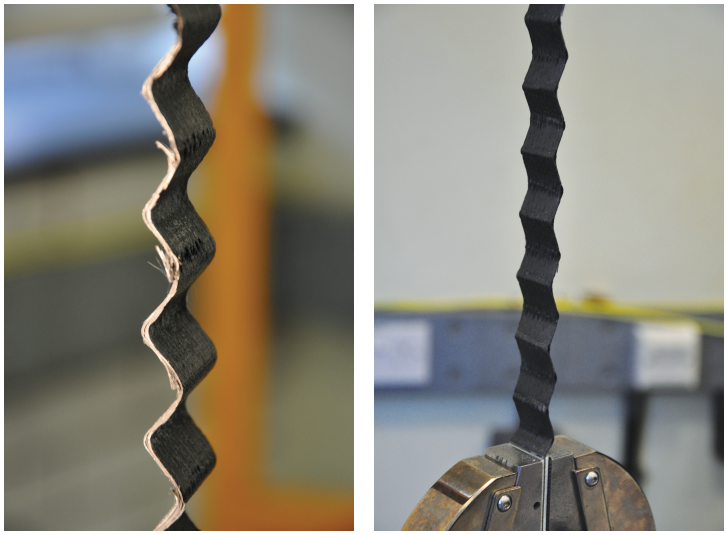


Figure 4.12: Tensile load-displacement relationship of corrugated carbon/PU laminates.

heard at this point. Matrix cracking initiation led to a sudden drop in applied load. The stage labelled 3 is the corrugation opening stage. At this stage, the curved parts of the corrugations (peaks and troughs) were failing and caused the corrugations to stretch. However, the corrugations were not stretched all at once, this occurred in stages. As one corrugation was stretched, the load rapidly dropped and this prevented the stretching of other corrugations. But as the structural displacement increased, the load was transferred to the adjacent corrugation and, therefore, the applied load started to increase again. This process was repeated until all of the corrugations were fully stretched. Figure 4.13a shows a specimen during corrugation stretching stage while figure 4.13b shows the specimen later on in the test. At this point all of the corrugation joints had been damaged and it was almost being stretched to its maximum limit. Damages on the surface were visible during stage 3. All of the damages were at the peaks and troughs of the corrugations. In stage 4, the specimen was overstretched that it was almost flat. As a result, a higher force was required to stretch the specimen further. This led to an increase in the structural elastic modulus as shown on the load-displacement curve as an increase in curve slope. The specimen ruptured at the load level of approximately 200 N.

According to figure 4.14, it could be deducted that there was a large vari-



(a) Initial stretching **(b)** Near flat stretching

Figure 4.13: A corrugated composite specimen during tensile test.

ation between load-displacement plot of each specimen in the elastic region. However, specimens cut from the same panel tend to behave in the same manner with an exception to specimens cut from panel number 3 (specimens 3.1, 3.2 and 3.3), which large variation could be observed. The plot shows that panel 1 has the steepest gradient followed by panel two and three, respectively. The discrepancies of the results suggest that there is a difference in structural properties, despite having been manufactured using the same method. One factor that affects the difference in structural properties could be the resin flow rate of each run. Similar to flat specimens, the infusion rate was controlled manually using a G-clamp. Therefore, there is a tendency that the resin infusion rate in each run was different. Although a technique was developed to manufacture high quality corrugated composites, the operation still highly depended upon operator's skills. In other words, even though the same operator manufactures all corrugated composite panels, each lay-up is still different from the others as different issues (e.g. resin infusion rate issue) may occur during each lay-up. One more factor that can affect the load-displacement relationships is pre-damage. Because the specimens were very thin and fragile, it could have been damaged during demoulding or preparation process. It was possible that the specimen 3.3 was damaged before testing, as the plot was so much different from other specimens from the same panel. Once damaged, the specimen would not be able to achieve the same maximum load as in a non-damaged one.

An optical micrograph of a cross-section from a failed corrugated speci-

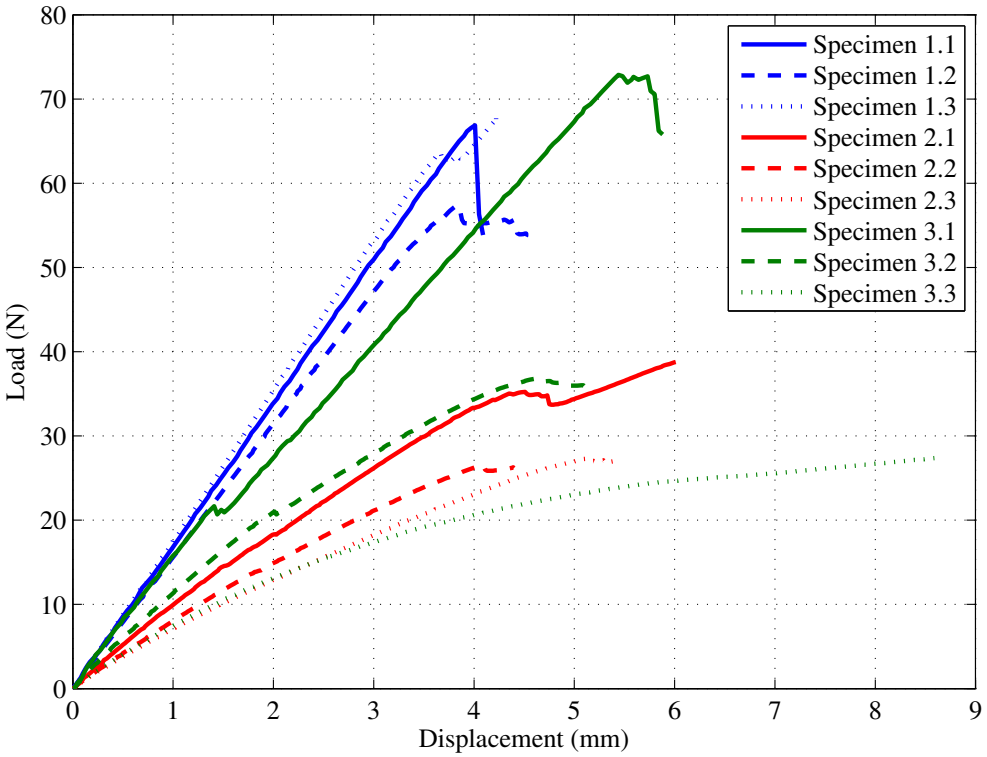


Figure 4.14: Tensile load-displacement relationship of corrugated composite specimens.

men revealed delamination between top and bottom plies (figure 4.15). This occurred during the 'opening up' stage (label 3) when the corrugations were being stretched and flattened out. Delaminations at peaks and troughs were caused by bending, which generated through-thickness tension between the compression and tension faces. However, it was more likely that the compressive failure on the compression side initiated a crack growth. There were some microbuckling regions observed on the compression face as shown in figure 4.16. This confirmed that the areas were under compression during loading of the corrugated panel. There was no damage on the tension face of the corrugation, however. This was probably because the ultimate tensile strength is approximately two times greater than the compressive strength, hence, the specimens failed in compression and delamination.

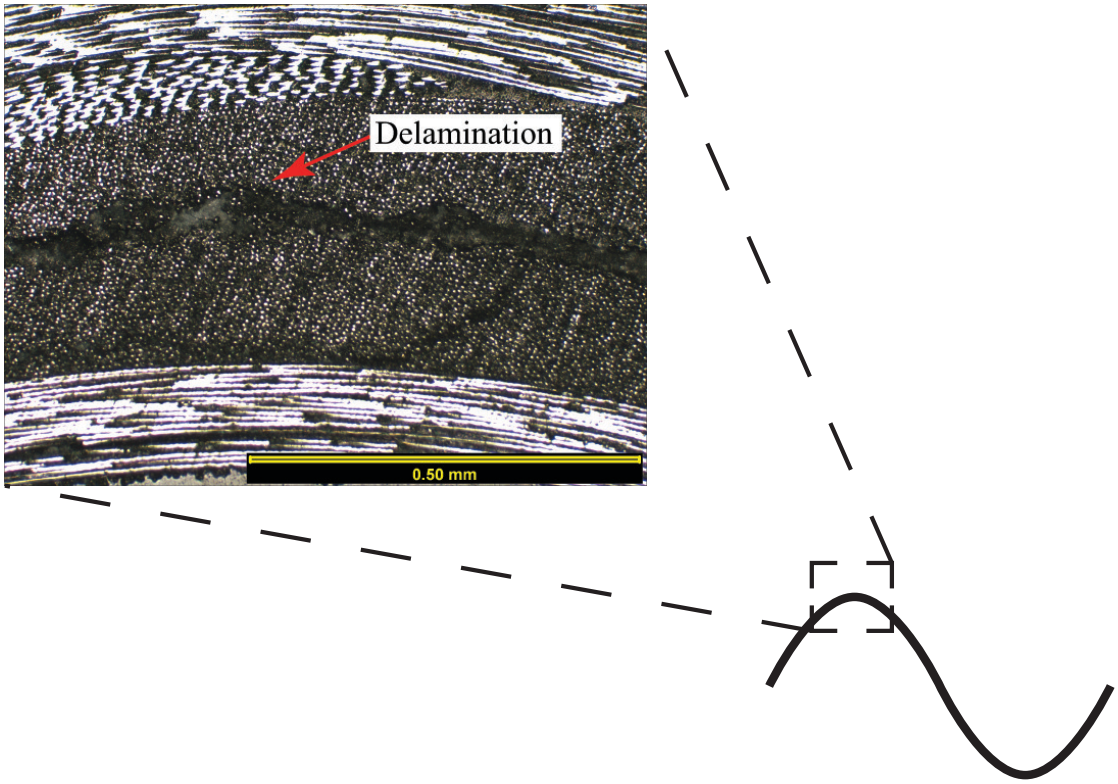


Figure 4.15: Optical micrograph of a corrugated tensile specimen showing delamination at the curved region.

4.2 Finite Element Model of Corrugated Composite

In order to perform a parametric study of different cross-sectional profiles and dimensions of corrugations economically, other methods should be employed instead of an experiment. Two methods were considered in this research: analytical analysis and numerical analysis. These methods not only avoid the manufacturing cost of the corrugated panels, but require less time than manufacturing and testing of the specimens. However, analytical models proposed by many researchers [16, 19, 146–149], which can be implemented easily, are relatively limited. They are able to capture only stage 1 of the load-displacement relationship. Moreover, the damage such as delaminaition cannot be easily defined in analytical models. Therefore, these models can only be used to predict initial response of the corrugated structure. In this research, the analytical models have not been further developed, but the models proposed by Thill *et al.* [19] were used, in conjunction with experimental result, to validate the numerical model. Alternatively, a more complex numerical analysis was performed to investigate structural behaviour of the corrugated

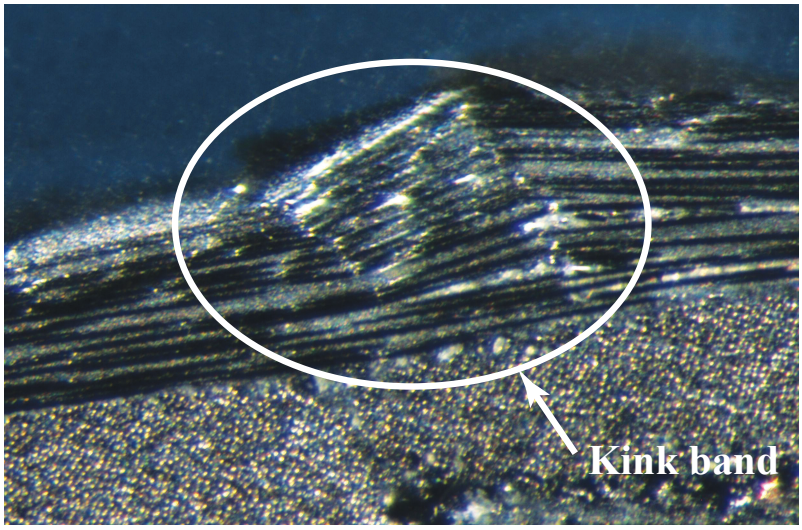


Figure 4.16: Optical micrograph of a corrugated tensile specimen showing microbuckling region on the compression face.

composite under tensile load including damages of the interface between two plies. A finite element model was generated and analysed using a commercial finite element package (ABAQUS version 6.10). In order to simulate delamination between two layers, a surfaced-based cohesive behaviour was placed between two layers of carbon fibre fabric. The definition and implementation of the cohesive surface are further explained in the subsequent sections. The numerical models not only provide initial response of the corrugated composite, but also determine the elastic limit of the structure. The finite element model developed in this section will be used later to perform a parametric study of carbon fibre/polyurethane corrugated composites.

4.2.1 Generation of finite element model of carbon fibre reinforced polyurethane corrugated composite

The finite element model of carbon/polyurethane corrugated composite generated in this section was used to simulate the structural behaviour of tensile specimens tested in section 4.1. This was done to validate the finite element model to be used in a parametric study of the corrugated composite. The model was created in ABAQUS/CAE which is the software environment used to create a model and to specify mechanical properties, boundary conditions and applied loads as well as contact and damage definitions of the model. In order to simplify the model and to reduce computational cost, only a quarter of a repeated cell (one corrugation's wavelength) was modelled. As

the corrugated specimen consisted of two layers of carbon fibre fabric, the FE model was generated in the same manner having two layers of composite separated by a layer of cohesive surface. Each layer of carbon fibre fabric was modelled as a 3-D, deformable continuum shell. The dimensions of the model is presented in table 4.3.

Table 4.3: Dimensions of the finite element corrugated composite model.

Dimensions	Values
Cross-sectional profile	Sinusoidal
Amplitude (mm)	5
Half-wavelength (mm)	10
Width (mm)	12.5
Thickness of each carbon fibre fabric layer (mm)	0.35
Number of carbon fibre fabric layer	2

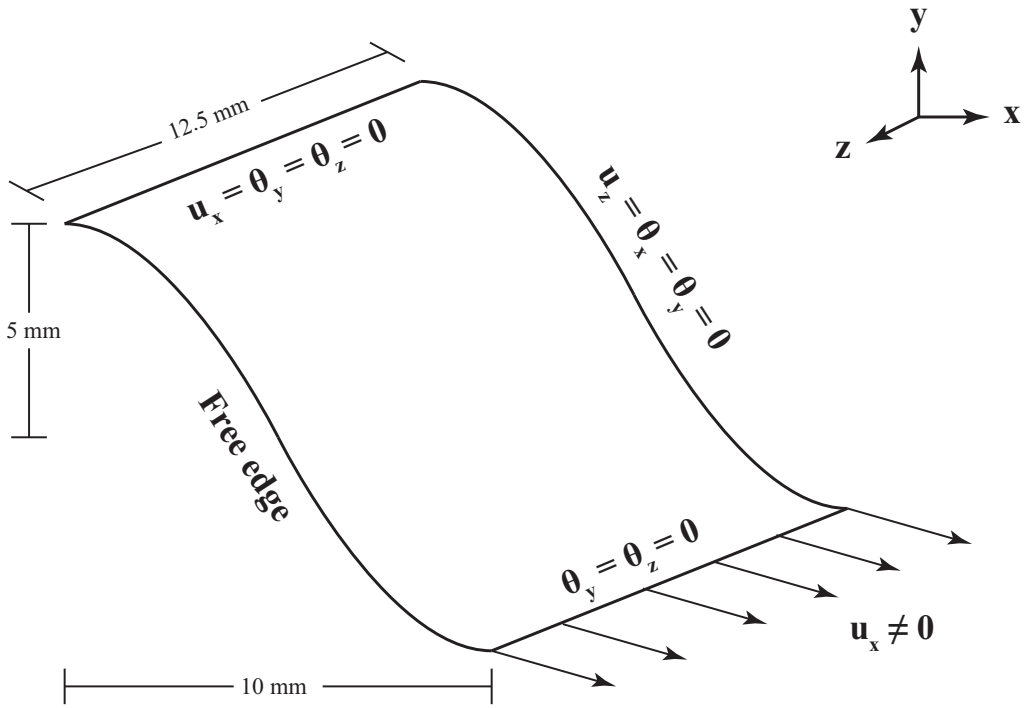


Figure 4.17: Schematic drawing of the FE corrugated model with constraints (a quarter of a repeated cell).

The material properties used to define in the FE model were obtained from the experiment of flat specimens discussed in chapter 3. The type of the elastic property defined in the model was 'lamina'. In addition to mechanical properties, a failure initiation criterion using maximum stresses was also defined.

Table 4.4 shows values of mechanical properties as well as maximum allowable stresses of the FE model.

Table 4.4: Mechanical properties of the lamina.

Variables	**Values**	**Variables**	**Values**
E_{11} (GPa)	62.47	UTS_{11} (MPa)	602.97
E_{22} (GPa)	63.10	UTS_{22} (MPa)	552.10
ν_{12}	0.06	UCS_{11} (MPa)	299.95
G_{12} (GPa)	2.04	UCS_{22} (MPa)	262.40
G_{13} (GPa)	2.04	$\tau_{12,u}$ (MPa)	38.10
G_{23} (GPa)	2.04	ρ_c (kg/m^3)	1,942

The in-plane shear modulus in x-z and y-z planes was assumed to be similar to the in-plane shear modulus in x-y plane because the in-plane shear test was only performed in one plane. Therefore, the through-thickness shear moduli of carbon/polyurethane composite could not be obtained directly from the experiment as well as from any published paper. Also, the density of the carbon/polyurethane composite was computed by weighing a panel and dividing its mass by its volume.

Once the material properties had been defined for a lamina, boundary conditions were then specified as shown in figure 4.17. As mentioned earlier that the model represents only a quarter of one wavelength, therefore, two planes of symmetry were used. The left hand edge was subjected to a symmetry plane in x-direction while the back edge was constrained by a symmetry plane in z-direction. The front edge remained free and was allowed to translate and rotate in every direction. The right hand edge of the model was constrained such that the rotations about y and z axes were prohibited. The right hand edge was restricted in this way because it was connected to another cell or wavelength in the real specimen.

In the tensile testing of the corrugated composite specimen, the specimen was pulled by the testing machine via displacement-controlled grips. Therefore, in the FE simulation, a displacement in x-direction was applied to the model at the right hand edge (refer to figure 4.17) via a connection constraint to a reference point located next to the right hand edge. This reference point was also used to obtain a reaction force which is equivalent to the applied load in the experiment. As the model would undergo large deflection, geometrical

nonlinearity must be taken into account. This could be defined in ABAQUS by simply enabling the code integrated in the software. After the material properties, boundary conditions and displacement had been applied to the model, the next step involved meshing and submitting the job to the solver. The element used in this analysis was 8-node reduced integration quadrilateral in-plane general purpose continuum shell (SC8R). This element was formulated specifically for continuum shell model. The geometry of the continuum shell element looks similar to a three-dimensional continuum elements, however, the constitutive behaviour and kinematic is similar to shell elements. At each node of the continuum shell element, only translation degrees of freedom are permitted. Figure 4.18 shows the illustration of continuum shell element. The size of the mesh was investigated to study the effects of mesh sensitivity and the results will be discussed later in this chapter. Once the meshing was completed, the model was solved using the explicit solver. In this study, the finite element analysis performed to simulate the tensile test of the corrugated composite is considered to be quasi-static. Therefore, outputs, such as external work done and internal energies, are important and need to be monitored closely. It is important to ensure that the external work done to the model is equal to the internal energy of the model, and the kinetic energy of the model remains close to zero. These outputs are indications that the displacement is gradually applied to the model and quasi-static response is obtained instead of dynamic response.

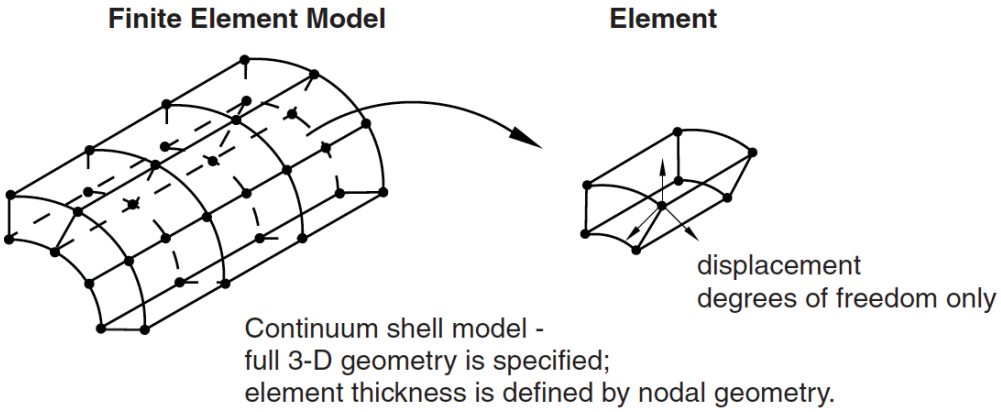


Figure 4.18: Continuum element [150].

Surface-based cohesive behaviour

An optical micrograph of the corrugated composite specimen under tensile loading (figure 4.15) reveals a separation of two carbon fibre fabric layers known as delamination. This feature is very important in laminated structures as it can grow undetected and the inspection is very difficult. In the case of the corrugated composite, the strength of the structure could be determined by the initiation of the damage between two adjacent layers of carbon fibre fabric. Therefore, in the modelling of FE corrugated model, this feature must be included and thoroughly analysed. In order to capture the delamination accurately, surface-based cohesive behaviour (also known as 'cohesive surface') provided in ABAQUS can be employed [151]. This is a very thin layer considered to have zero thickness and to be placed between two continuum shell layers. The constitutive response of the cohesive layer is very similar to the constitutive response of cohesive elements where traction-separation law is used to define initiation and propagation of damage to the point of eventual failure of the bonded interface. The cohesive surface was devised as it offers easier implementation to the FE model, especially model of composite materials which delamination is of interest. One advantage of the cohesive elements and surface is that the crack does not need to be present at the beginning of the analysis. For three-dimensional problem as in the case of this research, three components of separation are assumed to be active at a material point. These are one component perpendicular and two components parallel to the bonded interface corresponding to three different failure modes: mode I (opening), mode II (sliding shear) and mode III (tearing shear).

In ABAQUS, the surface-based cohesive behaviour has to be defined in the interaction module as opposed to cohesive elements which are defined in the material module. The governing formulae and laws of the cohesive surface are very similar to those of cohesive elements. The initial step involves a linear relationship between traction and separation of nodes between the two surfaces. For surface-based cohesive behaviour, the traction is written in terms of traction stress ($\mathbf{t}$) consisting of three components, one normal traction (t_n) and two shear tractions (t_s, t_t). The traction stress vector is related to the separation vector (δ) through an elastic constitutive matrix ($\mathbf{K}$), which is a diagonal matrix. This can be shown in equation 4.1.

$$\mathbf{t} = \begin{Bmatrix} t_n \\ t_s \\ t_t \end{Bmatrix} = \begin{bmatrix} K_{nn} & K_{ns} & K_{nt} \\ K_{ns} & K_{ss} & K_{st} \\ K_{nt} & K_{st} & K_{tt} \end{bmatrix} \begin{Bmatrix} \delta_n \\ \delta_s \\ \delta_t \end{Bmatrix} = \mathbf{K}\delta. \tag{4.1}$$

The surface-based cohesive behaviour coded in ABAQUS allows the users to simulate the degradation and complete failure of the bonded interface between two cohesive surfaces. In order to simulate degradation and failure, two key elements are required. These include a damage initiation criterion and a damage evolution law. Figure 4.19 shows a typical traction-separation response with a failure mechanism. It can be seen that the initial part of the curve is linear up to a point where a maximum traction stress is attained. This point can be defined using a damage initiation criterion. Beyond this point, the cohesive surface degrades as specified by a damage evolution law. During the damage evolution phase, it is unnecessary that the relationship between traction stress and strain is linear. The area under the traction-separation response is the critical strain energy release rate (G_c) of the corresponding failure mode.

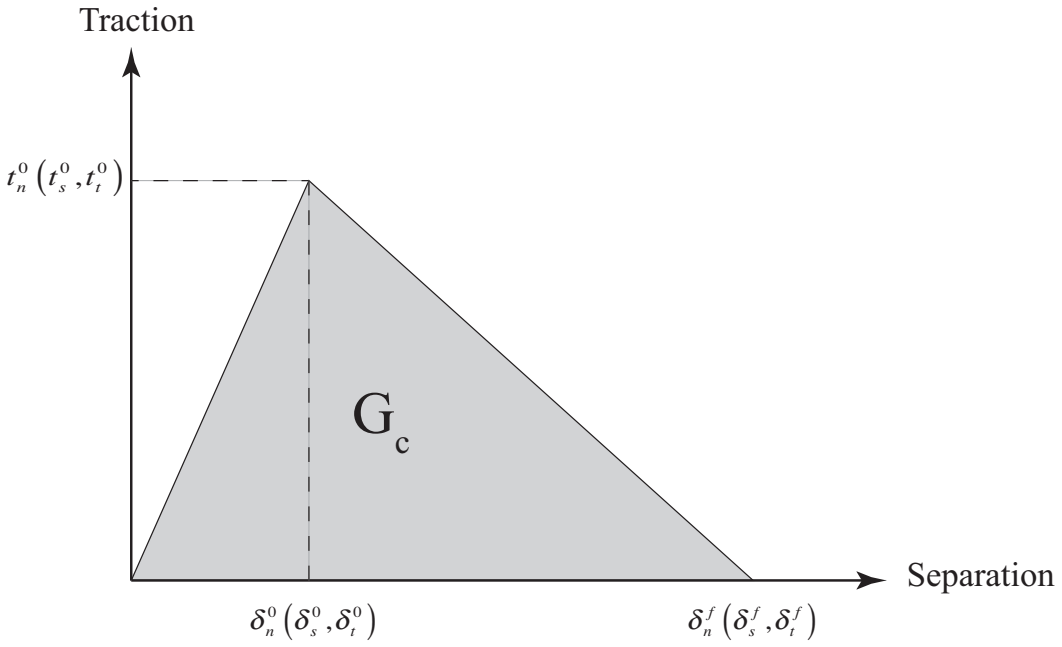


Figure 4.19: Typical traction-separation response, adapted from [151].

In the modelling of the carbon/polyurethane corrugated composite, quadratic

stress criterion was used to define the maximum traction stress. In this damage initiation criterion, the damage is assumed to initiate when a quadratic interaction function involving the contact stress ratios reaches a value of one. The mathematical representation of this criterion is expressed in equation 4.2

$$\left\{\frac{\langle t_n \rangle}{t_n^0}\right\}^2 + \left\{\frac{t_s}{t_s^0}\right\}^2 + \left\{\frac{t_t}{t_t^0}\right\}^2 = 1. \tag{4.2}$$

The variables t_n^0, t_s^0 and t_t^0 represent the maximum values of traction stress when the separation is purely in the normal direction to the bonded interface or purely in the first or the second shear direction, respectively. Similarly, δ_n^0, δ_s^0 and δ_t^0 are the maximum values of contact separation when the separation is purely along the contact normal or purely in the first or the second shear direction, respectively. The symbol $\langle\ \rangle$ represents the Macaulay brackets which are used to signify that a purely compressive displacement or a purely compressive stress state does not initiate damage.

Once the damage has initiated, the stiffness of the cohesive surface is degraded and the degradation rate is governed by the damage evolution law. The overall damage at a contact point is defined using a scalar damage variable, D_{coh}. The damage variable has a value between 0 and 1 where the value 0 means that no damage has occurred while the value 1 represents complete damage of the cohesive surface. The relationship of contact stress components and the damage variable is expressed in equation 4.3.

$$\begin{aligned} t_n &= \begin{cases} (1 - D_{coh})\bar{t}_n, & \bar{t}_n \geq 0 \\ \bar{t}_n, & \text{otherwise (no damage to compressive stiffness);} \end{cases} \\ t_s &= (1 - D_{coh})\bar{t}_s, \\ t_t &= (1 - D_{coh})\bar{t}_t, \end{aligned} \tag{4.3}$$

where the variables $\bar{t}_n, \bar{t}_s$ and $\bar{t}_t$ are contact stress components predicted by the elastic traction-separation behaviour for the current separation without damage.

In the analysis of composite structures, the delamination does not grow under either pure mode I, mode II or mode III loading but rather a combination of all three loading modes. The onset of delamination defined in equation 4.2 takes into account the interaction of stress components which suggests that the initiation of delamination under mixed mode loading may occur at the traction stress level below the maximum allowable of each mode [152]. The total displacement of mixed-mode (δ_m) can also be defined as

$$\delta_m = \sqrt{\langle \delta_n \rangle^2 + \delta_s^2 + \delta_t^2}. \tag{4.4}$$

In ABAQUS, the mixed-mode delamination propagation can be defined using two approaches: one base on energies and another one based on tractions. In the generation of corrugated FE model, the energy-based approach was used. There are two ingredients used to characterise mixed-mode delamination growth. The first ingredient is the energy dissipated due to failure, G_c, which is also known as fracture energy. The fracture energy can be defined as the area under traction-separation curve (see figure 4.19). Another ingredient is the damage variable (D_{coh}) which is used to specified the nature of evolution. ABAQUS offers many softening laws, however, in this study the power law form was used. The power law criterion states that "failure under mixed-mode conditions is governed by a power law interaction of the energies required to cause failure in the individual (normal and two shear) modes." [151]. The mathematical representation of the power law form can be expressed as

$$\left\{\frac{G_n}{G_{n,c}}\right\}^{\alpha} + \left\{\frac{G_s}{G_{s,c}}\right\}^{\alpha} + \left\{\frac{G_t}{G_{t,c}}\right\}^{\alpha} = 1, \tag{4.5}$$

with the mixed-mode fracture energy $G_c = G_n + G_s + G_t$ when equation 4.5 is satisfied. The variables G_n, G_s and G_t refer to the work done by traction in normal and two shear directions, respectively. Moreover, the quantities $G_{n,c}, G_{s,c}$ and $G_{t,c}$ represent the critical fracture energies required to cause failure in normal and two shear directions, respectively. In the equation 4.5,

the value of α was chosen to be 2.

4.2.2 Validation of the finite element corrugated model

Selection of surface-based cohesive behaviour parameters

The surface-based cohesive behaviour discussed earlier requires nine parameters. These are interface stiffness (K), maximum tension stress (t^0) and critical fracture energy (G_c) in normal and two shear directions. In the case of this study which carbon/polyurethane composite was used, the surface-based cohesive behaviour parameters are unknown and have never been published elsewhere. Moreover, the experiments to evaluate the critical fracture energies were not performed. Therefore, these parameters need to be established numerically. The first step was to obtain all surface-based cohesive behaviour parameters of the carbon/epoxy composites (shown in table 4.5) and these parameters were obtained from Ankersen [153]. These parameters were then investigated in turn to study the effects of each parameter on the load-displacement curve of carbon/polyurethane corrugated composite and compare with the experimental result. To simplify the analysis, only three parameters which are K_{nn}, t_n^0 and $G_{n,c}$ were varied while the parameters in the shear directions were modified such that the ratio between normal and shear direction of each variable remains constant.

Table 4.5: Surface-based cohesive behaviour parameters for carbon/epoxy composite [153].

$K_{nn} =$	20,000 N/mm^3	$t_n^0 =$	60 MPa	$G_{n,c} =$	0.3 N/mm
$K_{ss} =$	15,000 N/mm^3	$t_s^0 =$	80 MPa	$G_{s,c} =$	1.8 N/mm
$K_{tt} =$	15,000 N/mm^3	$t_t^0 =$	80 MPa	$G_{t,c} =$	1.8 N/mm

Turon *et al.* [154] and Ankersen and Davies [155] suggested that the interface stiffness should be theoretically infinite in order to avoid affecting the overall laminate compliance. However, practically, this would not be possible from the numerical point of view. Therefore, the highest possible value of interface stiffness should be used. Nevertheless, too high value results in convergence issues, hence, excessively stiff interface should be avoided. In the current study, the values of interface stiffness shown in table 4.5 were found to be too high and caused numerical issues. Therefore, the interface stiffnesses were reduced gradually and the simulations were repeated until a converged

result was obtained. The final values of K_{nn}, K_{ss} and K_{tt} were 7,500 N/mm^3, 5,625 N/mm^3 and 5,625 N/mm^3, respectively.

The next values to be adjusted are the maximum tension stress of the cohesive surface. Initially, the values obtained from carbon/epoxy composite (refer to table 4.5) were used. However, the predicted elastic limit of the load-displacement curve were higher than that obtained from the experiment. By reducing the maximum contact stresses, the predicted elastic limit was also reduced as shown in figure 4.20. In this analysis, the values of maximum traction stress were modified manually until the predicted elastic limit of load-displacement curve matched the experimental results. The values of t_n^0, t_s^0 and t_t^0 were finally set to 12.5 MPa, 16.67 MPa and 16.67 MPa, respectively.

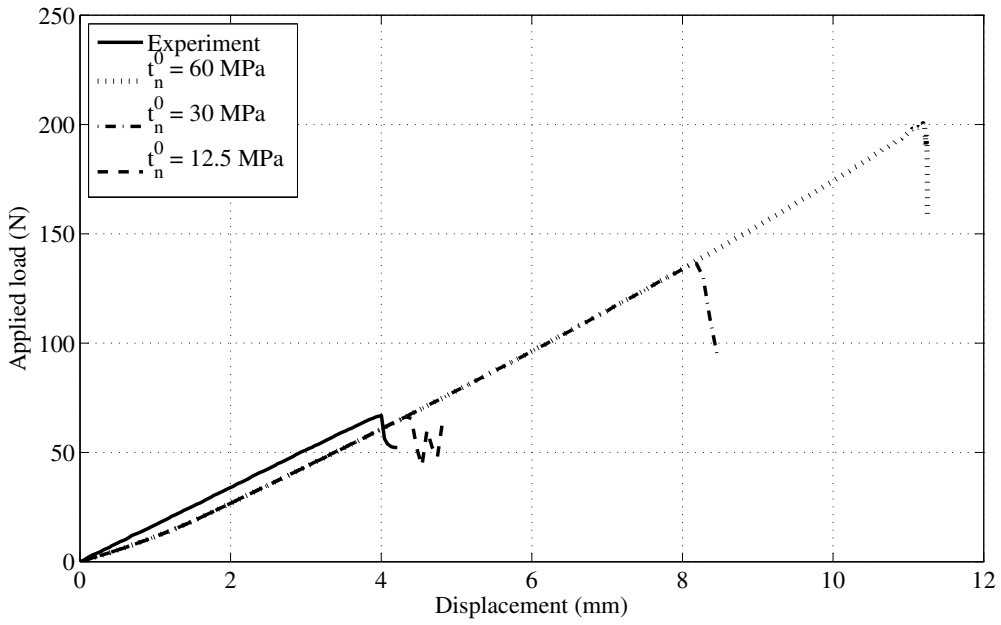


Figure 4.20: Load-displacement curves of different values of t_n^0 as compared to experimental results.

The last value to be considered is the critical energy release rate, which is the energy dissipated due to failure and can be defined as the area under traction-separation curve. Normally, the value of critical energy should be obtained from experiment. However, in this study, the experiment to evaluate critical energy was not performed due to time constraint as the surface-based cohesive behaviour was used at a later stage of the project. Therefore, the value of fracture energy in normal and two shear directions must be numer-

ically investigated. While keeping the interface stiffness and the maximum traction stress constant and varying the values of critical energy release rate in normal direction, it was found that the critical fracture energy did not contribute to changes in predicted elastic limit of the load-displacement curve.

One feature observed during the investigation of the maximum traction stress was that when the value of traction stress was lowered while keeping the fracture energy constant, the load-displacement curve became nonlinear just before the elastic limit instead of an abrupt change. This was due to the fact that the critical separations, δ^f (refer to figure 4.19), increase due to the lower traction stresses and constant fracture energies. Therefore, complete failure of the cohesive surface was delayed and resulted in a nonlinear curve near the elastic limit. In order to promote a sharp drop in load at the elastic limit, each component of the fracture energy could be decreased. Therefore, the critical separation could also be reduced to initiate complete failure of cohesive surface as shown in figure 4.21. As a result, each component of the critical energy release rate was reduced to $G_{n,c}$ = 0.075 N/mm, $G_{s,c}$ = 0.45 N/mm and $G_{t,c}$ = 0.45 N/mm.

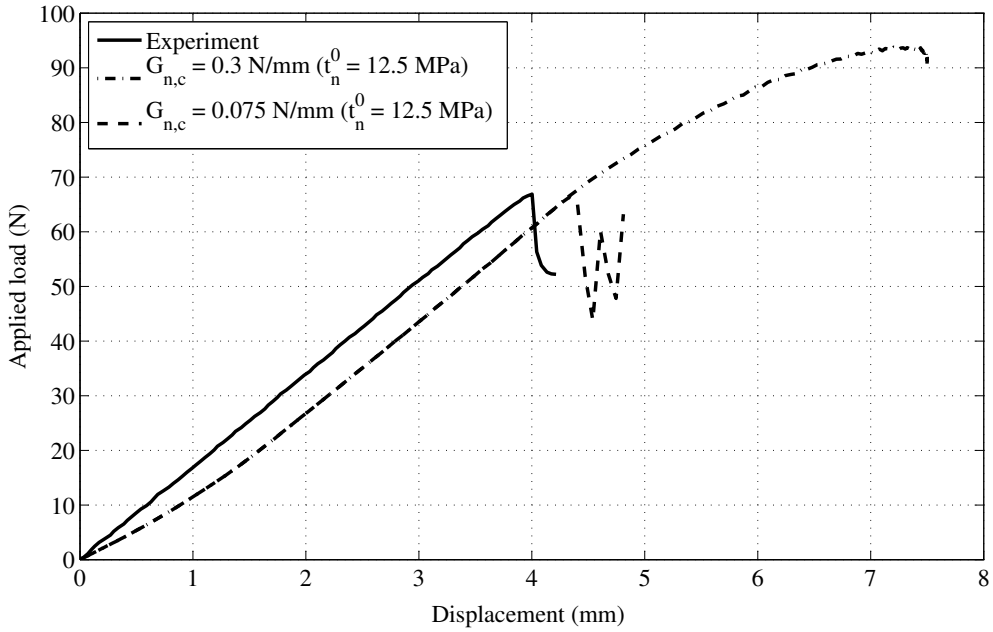


Figure 4.21: Load-displacement curves of different values of $G_{n,c}$ as compared to experimental results.

A summary of all parameters used to define surface-based cohesive be-

haviour of carbon/polyurethane is shown in table 4.6.

Table 4.6: Surface-based cohesive behaviour parameters for carbon/polyurethane composite.

$K_{nn} =$	7,500 N/mm^3	$t_n^0 =$	12.5 MPa	$G_{n,c} =$	0.075 N/mm
$K_{ss} =$	5,625 N/mm^3	$t_s^0 =$	16.67 MPa	$G_{s,c} =$	0.45 N/mm
$K_{tt} =$	5,625 N/mm^3	$t_t^0 =$	16.67 MPa	$G_{t,c} =$	0.45 N/mm

Mesh sensitivity analysis

In general, the simulation of delamination using cohesive elements requires extremely refined meshes in order to capture correct progressive stresses ahead of the crack tip. A similar requirement also applies to the implementation of contact interaction between two plies using surface-based cohesive behaviour as in the current study of carbon/polyurethane corrugated composite in tension. Therefore, it is important to investigate the effects of mesh size on the accuracy of the numerical model.

To investigate the influence of mesh size, four different element sizes ranging between 0.2 mm and 0.5 mm were used to analyse the carbon/polyurethane corrugated composite in tension. The material properties of the composite and the properties of the surface-based cohesive behaviour used in the analyses are in accordance with table 4.4 and table 4.6, respectively. The corresponding load-displacement curves together with the results of the experiment are shown in figure 4.22.

It can be clearly observed from figure 4.22 that the coarse mesh underpredicts the elastic limit significantly. This error arisen from using a coarse mesh was because softening region ahead of the crack tip could not be captured correctly [154]. Therefore, in this particular analysis, mesh size larger than 0.4 mm must be avoided as it shows inaccurate representation of delamination process.

Figure 4.23 shows the sinusoidal corrugated finite element model with delamination initiated from the curved region. This feature is similar to that observed from the optical micrograph taken from a failed specimen (figure 4.15). Therefore, the finite element model can be used to further investigate

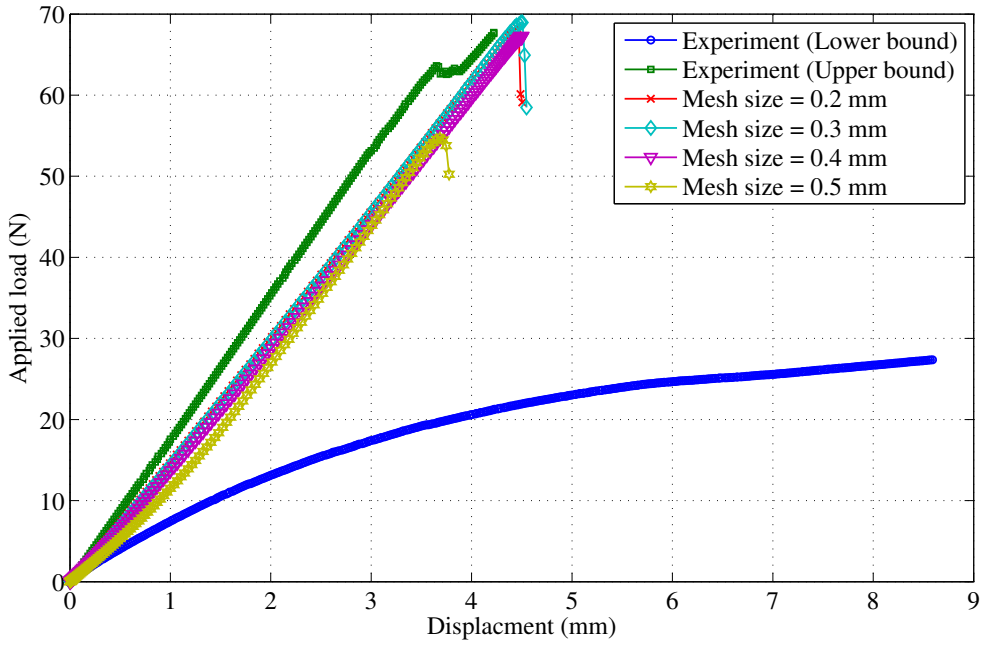


Figure 4.22: Load-displacement curves of different mesh sizes with experimental results.

the behaviours of corrugated structure of different profiles and geometries.

4.3 Parametric Study of Corrugated Composite Structure

Once the finite element model of the carbon fibre/polyurethane corrugated composite was created and verified against experimental result, it could be used to further study the effects of different cross-sectional profiles and dimensions of corrugation on structural response under tensile load. In this section, the FE model developed in the previous section was used. Three different cross-sectional profiles with different dimensions were modelled and loaded in tension. The computational results were also compared with analytical models previously developed by other researchers in the field.

4.3.1 Analytical models of corrugated composites

The simplest analytical model of corrugated structure was to treat the corrugated structure as a thin, equivalent orthotropic plate with uniform stiff-

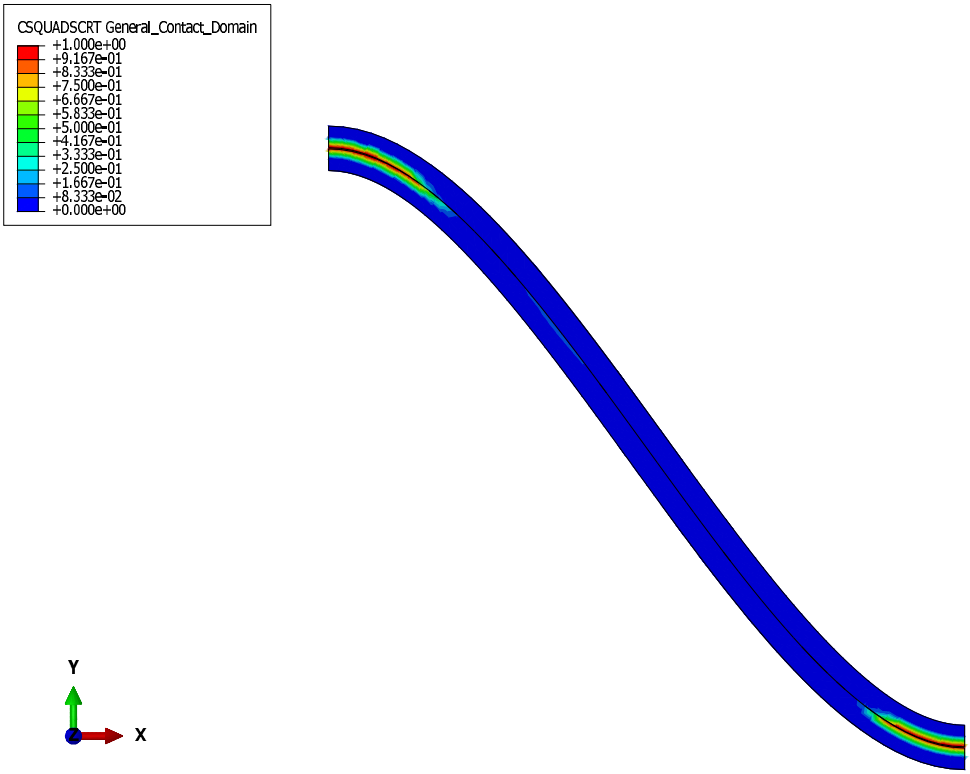


Figure 4.23: Finite element model showing delamination initiated from curved regions.

ness. Briassoulis [146] derived a set of analytical expressions for extensional and flexural rigidities of an orthotropic shell. Static and dynamic response of trapezoidal corrugated panels were investigated by Samanta and Mukhopadhyay [156], considering both extensional and bending rigidities in order to perform geometrical nonlinear analysis. A simple analytical model for corrugated composites was also proposed by Yokozeki *et al.* and was validated against experimental results. The model could be used to predict the initial stiffness of corrugated composite panels. More complicated and accurate analytical expressions of equivalent orthotropic shell for corrugations defined as circular arcs were derived by Kress and Winkler [148]. Xia and Friswell [149] also presented a homogenisation model for corrugated plate in which the stiffness of the equivalent model could be derived from the geometry of a unit cell (one wavelength of corrugation) and stiffness properties of the original corrugated panel. Although many investigators have proposed a number of analytical models to predict equivalent stiffness properties of corrugation, the modified analytical expressions given by Thill *et al.* [19] were selected in this research. The modified models were derived from strain energy principles and

Castigliano's second theorem. The notations of the modified analytical models were adapted slightly to match the geometry of finite element models considered herein. The final expressions of the equivalent stiffness properties of each corrugated cross-sectional profile are presented in table 4.7 to 4.9.

In the current research, the analytical expressions of each corrugation profile were implemented in MATLAB. To verify the analytical models, the experimental and numerical results of carbon/polyurethane corrugated composite were compared against the analytical results. According to figure 4.24, the predicted stiffness of a sinusoidal corrugation similar to the experimental specimen from analytical solutions is in a good agreement with the experimental results. However, the only limitation of the analytical solutions is that the expression can only be used to predict the initial stiffness of the corrugated structure but fail to forecast the strength of the structure.

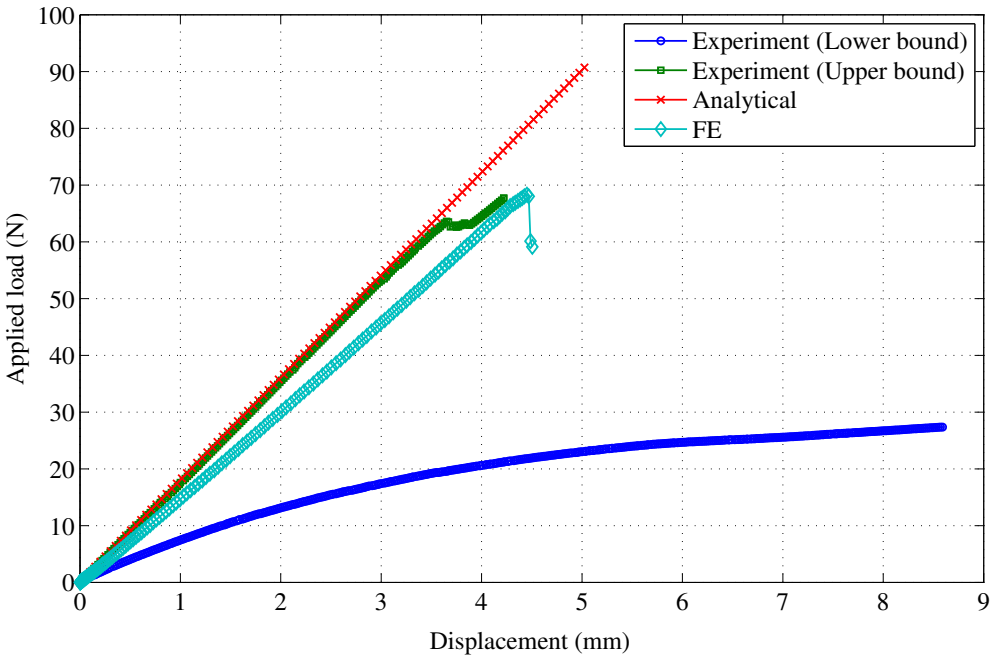
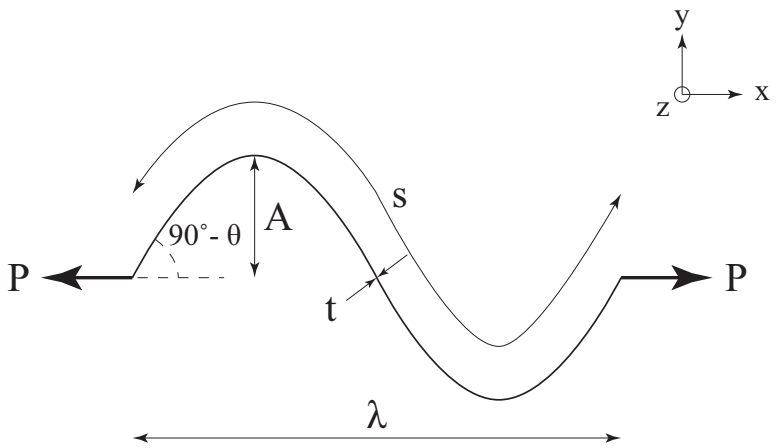


Figure 4.24: Load-displacement curves of analytical model, finite element model and experiment.

Table 4.7: Analytical expressions for sinusoidal corrugations [19].



$$(E_{xx})_{sine} = \frac{E_{11}\lambda}{2\left[sk_t + 3k_b\left(\frac{2A}{t}\right)^2\right]}, \tag{4.6}$$

$$(A_{xx})_{sine} = \frac{E_{11}\lambda}{2\left[sk_t + 3k_b\left(\frac{2A}{t}\right)^2\right]} \cdot \frac{t}{(1-\nu_{12}^2)}, \tag{4.7}$$

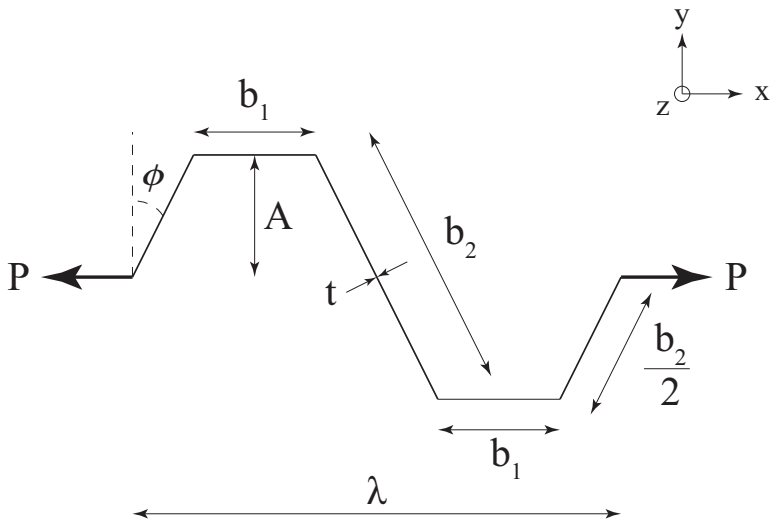
$$(u_{xx})_{sine} = \frac{2P}{E_{11}wt}\left[sk_t + 3k_b\left(\frac{2A}{t}\right)^2\right], \tag{4.8}$$

$$\theta = \arctan\left[\frac{2A\pi}{\lambda}\cos\left(\frac{2x\pi}{\lambda} + \frac{3\pi}{2}\right)\right],$$

$$k_t = \int_0^{\frac{\lambda}{2}} \cos\theta \,\mathrm{d}x, \quad k_b = \int_0^{\frac{\lambda}{2}} \frac{1}{\cos\theta}\left[\sin\left(\frac{2x\pi}{\lambda} + \frac{3\pi}{2}\right)\right]^2 \mathrm{d}x.$$

Note: Tensile and bending constants (k_t and k_b, respectively) must be evaluated numerically.

Table 4.8: Analytical expressions for trapezoidal corrugations [19].

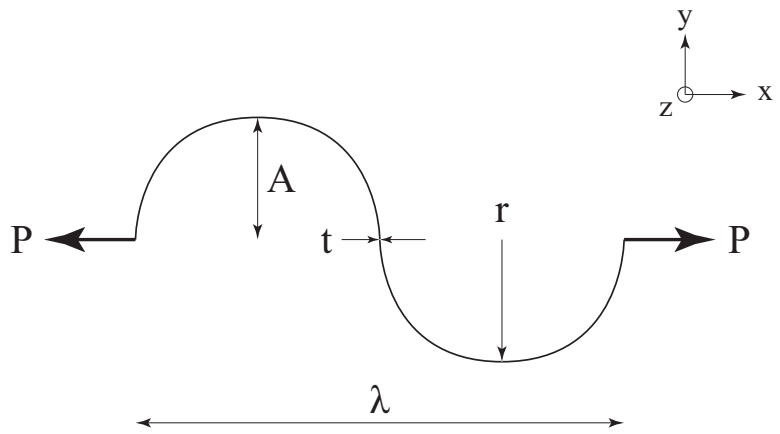


$$(E_{xx})_{trap} = \frac{2E_{11}\left(b_1 + b_2 \sin\phi\right)}{\left(\dfrac{24b_1A^2}{t^2} + 2b_1 + \dfrac{2b_2^3\cos^2\phi}{t^2} + 2b_2\sin^2\phi\right)}, \tag{4.9}$$

$$(A_{xx})_{trap} = \frac{2E_{11}}{1-\nu_{12}^2} \cdot \frac{\left(b_1 + b_2 \sin\phi\right)}{\left(\dfrac{24b_1A^2}{t^3} + \dfrac{2b_1}{t} + \dfrac{2b_2^3\cos^2\phi}{t^3} + \dfrac{2b_2\sin^2\phi}{t}\right)}, \tag{4.10}$$

$$(u_{xx})_{trap} = \frac{2P}{wE_{11}}\left(\frac{12b_1A^2}{t^3} + \frac{b_1}{t} + \frac{b_2^3\cos^2\phi}{t^3} + \frac{b_2\sin^2\phi}{t}\right). \tag{4.11}$$

Table 4.9: Analytical expressions for U-shape corrugations [19].



$$(E_{xx})_{Ushape} = \frac{E_{11}t^2 r}{12\left\{\frac{1}{3}(A-r)^3 + r\left[\frac{\pi}{4}\left(2(A-r)^2 + r^2 + \frac{t^2}{6}\right) + 2r(A-r)\right]\right\}}, \tag{4.12}$$

$$(A_{xx})_{Ushape} = \frac{E_{11}t^2 r}{12\left(1-\nu_{12}^2\right)^2\left\{\frac{1}{3}(A-r)^3 + r\left[\frac{\pi}{4}\left(2(A-r)^2 + r^2 + \frac{t^2}{6}\right) + 2r(A-r)\right]\right\}}, \tag{4.13}$$

$$(u_{xx})_{Ushape} = \frac{48P}{E_{11}wt^3} \cdot \left\{\frac{1}{3}(A-r)^3 + r\left[\frac{\pi}{4}\left(2(A-r)^2 + r^2 + \frac{t^2}{6}\right) + 2r(A-r)\right]\right\}. \tag{4.14}$$

4.3.2 Effects of cross-sectional profiles on corrugated structural response under tensile load

In order to economically investigate the effects of cross-sectional profile of corrugation on structural characteristics, finite element models of three cross-sectional profiles (sinusoidal, trapezoidal and U-shape) with and without surface-based cohesive behaviour, but similar geometry were generated following the guideline presented in section 4.2.1. The dimensions of each model are summarised in table 4.10.

Table 4.10: Dimensions of each corrugation profile used in finite element and analytical models.

Dimensions	Sinusoidal	Trapezoidal	U-shape
Amplitude (mm)	7.5	7.5	7.5
Wavelength (mm)	15	15	15
Thickness (mm)	0.70	0.70	0.70
b_1	-	5.26	-
b_2	-	15.17	-
ϕ (degrees)	-	8.5	-
Radius (mm)	-	-	3.75
Height of vertical wall for U-shape (mm)	-	-	7.5

Effects of different modelling approaches

The effects of different approaches adopted to model corrugated composite structure is discussed in this subsection. This was performed to explore the advantages and disadvantages from different possible approaches and to discuss which approach could be taken forward to model the bench-top demonstrator of the morphing wing with corrugated skin discussed in chapter 6. The approaches considered herein are as follows.

1. Continuum shell element with surface-based cohesive behaviour.
2. Continuum shell element without the surface-based cohesive behaviour.
3. Conventional shell element.
4. Composite sub-layer approach.

1. Continuum shell element with surface-based cohesive behaviour

This approach has already been discussed earlier in the chapter. Please refer to section 4.2.1 for more detail.

2. Continuum shell element without the surface-based cohesive behaviour

This approach is similar to the continuum shell model with cohesive surface except that the cohesive surface is inactive.

3. Conventional shell element

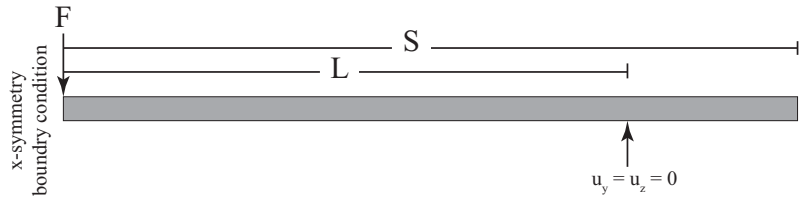
In this approach, the corrugated composite structure was modelled using conventional shell elements (reduced integration 4-noded shell element, S4R) instead of the continuum shell element.

4. Composite sub-layer approach

In this approach, the woven carbon/PU composite ply was replaced by 2 sub-layers, one in 0° direction and another one in 90° direction. However, there was a problem on how to derive mechanical properties for each layer. In order to solve this problem, the following steps were taken. The Young's modulus as well as the Poisson's ratio of the fibre were assumed to be 228 GPa and 0.33, respectively, while the Young's modulus of the polyurethane was taken from the technical data sheet to be 730 MPa and the Poisson's ratio of the polyurethane was assumed to be 0.48. Then, the rule of mixtures was used to calculate the lamina properties at various values of fibre volume fraction. These assumed ply properties were used as inputs for flexural FE models. Two flexural FE models (one in warp and another one in weft direction) were generated in ABAQUS to simulate the three-point bending tests. In order to minimise computational cost, only half of the specimen was modelled as shown in table 4.11.

As mentioned earlier that the assumed ply properties were used in the flexural FE models, the flexural modulus obtained from this method was compared with the experimental results. The mechanical properties of each sub-layer, which provide values of flexural moduli that are in good agreement with experimental results, are summarised in table 4.12 below.

Table 4.11: Dimensions of FE flexural models.



	S (mm)	L (mm)
Warp direction	100	80
Weft direction	90	80

Table 4.12: Mechanical properties of each sub-layer.

	Warp ply	Weft ply
$\mathbf{E_{11}}$ **(GPa)**	98.46	125.73
$\mathbf{E_{22}}$ **(GPa)**	1.27	1.62
ν_{12}	0.416	0.398
$\mathbf{G_{12}}$ **(GPa)**	2.04	2.04
$\mathbf{G_{13}}$ **(GPa)**	2.04	2.04
$\mathbf{G_{23}}$ **(GPa)**	2.04	2.04

Once the material properties had been defined, the models were meshed using continuum and conventional elements. The results from this approach will be discussed and compared with the results from other approaches in the next subsection.

Results and discussion

To compare the results between different approaches, a sinusoidal corrugation was modelled in ABAQUS. The amplitude, wavelength and thickness of this sinusoidal model were 7.5 mm, 15 mm and 0.66 mm, respectively. In addition, the number of woven ply was set at 2. The boundary conditions were defined in the same manner as explained in section 4.2.1 (figure 4.17). The structural stiffness in N/mm calculated from each approach is compared with analytical solution as shown graphically in figure 4.25.

It can be noticed from figure 4.25 that two approaches, namely FE without cohesive surface and FE using conventional shell, are able to predict the structural stiffness accurately as compared with the analytical results. The FE models with surface-based cohesive behaviour under-predicted the structural stiffness of the corrugated laminates. This was probably because the fracture

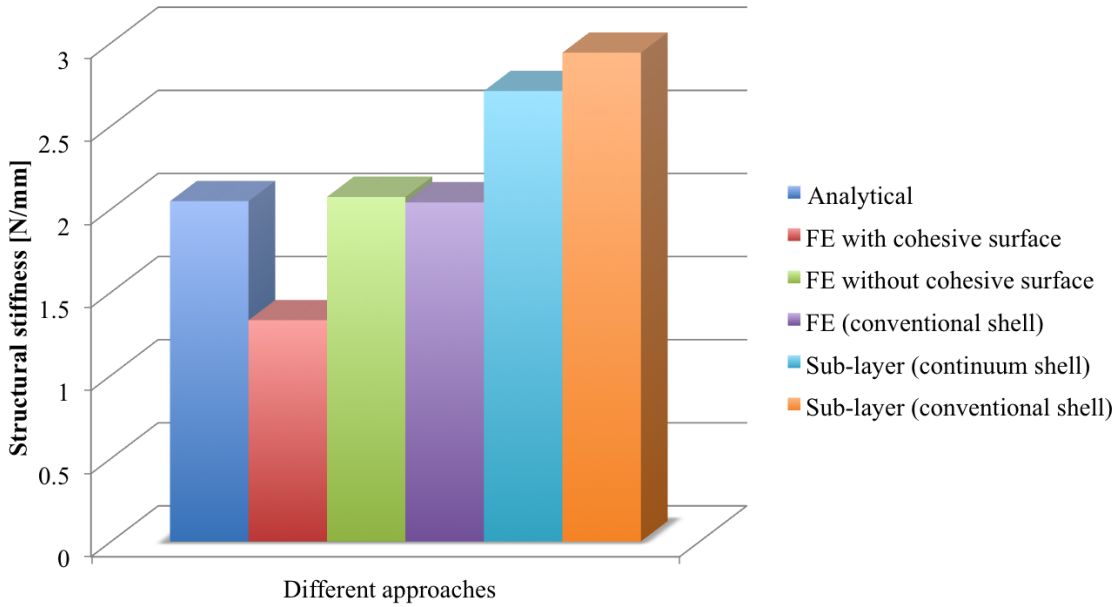


Figure 4.25: Comparison of initial stiffness (initial slope of load-displacement curve) of sinusoidal corrugated profile (A = 7.5 mm and λ = 15 mm) obtained from each approach.

toughness of the cohesive surface was not obtained from experiment, instead it was derived numerically. Therefore, if the experimental value was measured, a more accurate result could be obtained. The sub-layer approach was used for both continuum shell and conventional shell models. However, this approach was shown to over-predict the structural stiffness of the sinusoidal corrugated laminates used in this subsection. This was due to the fact the undulated fibres is not present in this model, therefore, the structural stiffness is relatively higher. This approach, however, should be useful if only one woven layer is used and bending is the primary action as can be seen in the bench-top demonstrator FE modelling discussed in chapter 6. The reason for this is that the sub-layer approach was derived from the flexural tests. The advantages and limitations of each approach are summarised in table 4.13.

Results of parametric study

Figure 4.26 shows the initial structural stiffness (initial slope of the load-displacement curve) of each model obtained from finite element and analytical analyses. It can be noticed that the corrugated models without the cohesive surface and the conventional shell models predict the structural characteristics of the corrugated laminates very closely to the analytical models. However45, the results from finite element models with cohesive surface show lower values

Table 4.13: Summary of advantages and limitations of each approach.

Modelling approach	Advantages	Limitations
FE with cohesive surface	1. Can be used to predict failure due to delamination.	1. Experimental values of fracture toughness are required for accurate result.
	2. Flexural behaviour of thin beam and plate can be predicted with accurate through-thickness stresses provided that accurate cohesive surface behaviour is available.	2. Small elements should be used in order to capture stesses ahead of the crack tip accurately.
FE without cohesive surface	1. Can be used to predict the structural stiffness with sufficient accuracy.	1. Cannot be used to predict failure due to delamination
	2. Can be used to accurately predict flexural behaviour of thin plate and beam.	
FE (conventional shell)	1. Easy to set up and provide sufficient accuracy.	1. Faliure due to delamination cannot be predicted.
	2. Pure bending of thin plate and beam can be simulated with accurate result.	
Sub-layer	1. Useful if use to simulate a single layer laminate under bending.	1. Over-predict the structural stiffness because fibre undulation is neglected.
		2. The mechanical properties of each sub-layer is derived numerically and should be used with caution to simulate model subjected to in-plane loading.

of the structural stiffness as compared with analytical models. This suggests that the properties specified for surface based cohesive behaviour need to be further investigated. A better results may be obtained if experimental values of fracture toughness were used.

The sinusoidal profile is the stiffest profile followed by the U-shape and trapezoidal, respectively. Follow the analogy of bending of the straight and curved beams, the variation in the structural stiffness of different profiles was caused by the difference in bending moment of the corrugated structure. The bending stress of the straight members of trapezoidal corrugation is the lowest. Therefore, the trapezoidal corrugation can be easily stretched, which results in the lowest structural stiffness. The corrugated profile that has the highest bending moment, and hence the highest bending stress, is the sinusoidal corrugation. As a result, it is the hardest to deform under tensile loading.

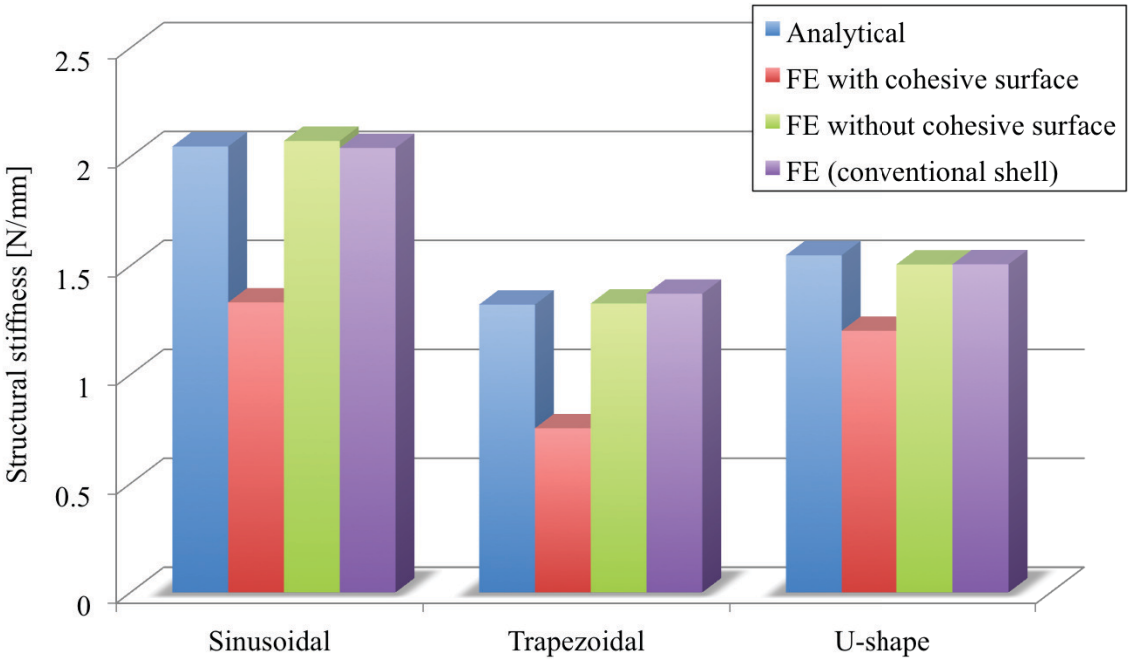


Figure 4.26: Comparison of initial stiffness (initial slope of load-displacement curve) of each corrugation profile.

Regarding the delamination of the corrugated structure, it can be noticed from figures 4.27 to 4.29 that the separation between two layers initiates from the curved sections (troughs and peaks) and propagate to the straight parts. This failure mechanism is similar in every profile.

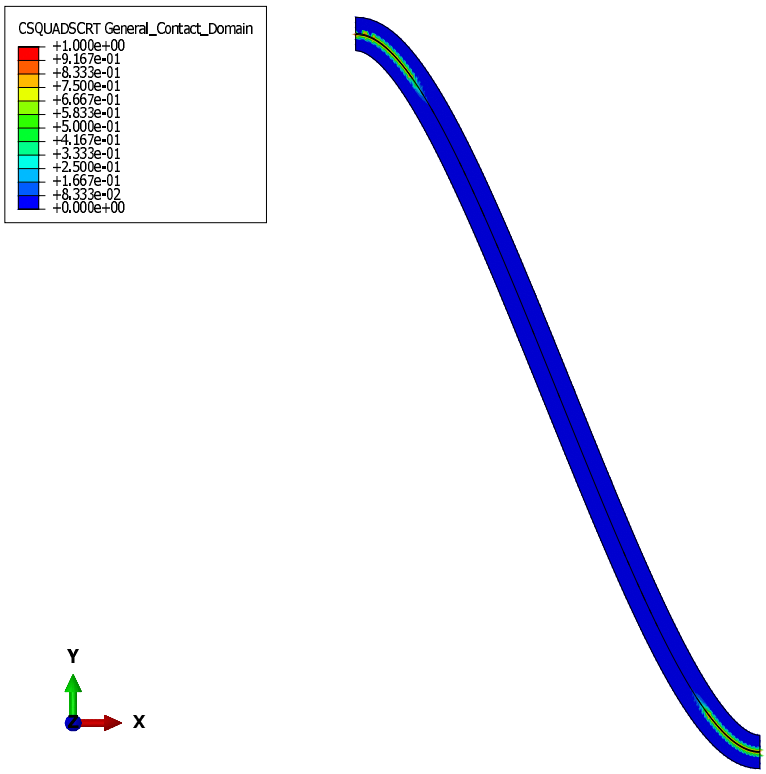


Figure 4.27: Finite element model of sinusoidal profile showing delamination.

4.3.3 Effects of dimensions of corrugation on corrugated structural response under tensile load

In order to investigate the effects of dimensions of corrugation, various finite element models with different amplitudes and unit cell length were created using similar mechanical properties and cohesive surface properties. Moreover, finite element models without cohesive surface and analytical models were also used to compare the results against the finite element method. The extensional stiffness (slope of the load-displacement curve) of each model was obtained and compared with other models of the same profile. Figures 4.30, 4.31 and 4.32 show extensional stiffness of each profile with different geometries. Similar trend can be observed from each profile. As the length of the unit cell (one wavelength) increases while keeping the amplitude constant, the structural

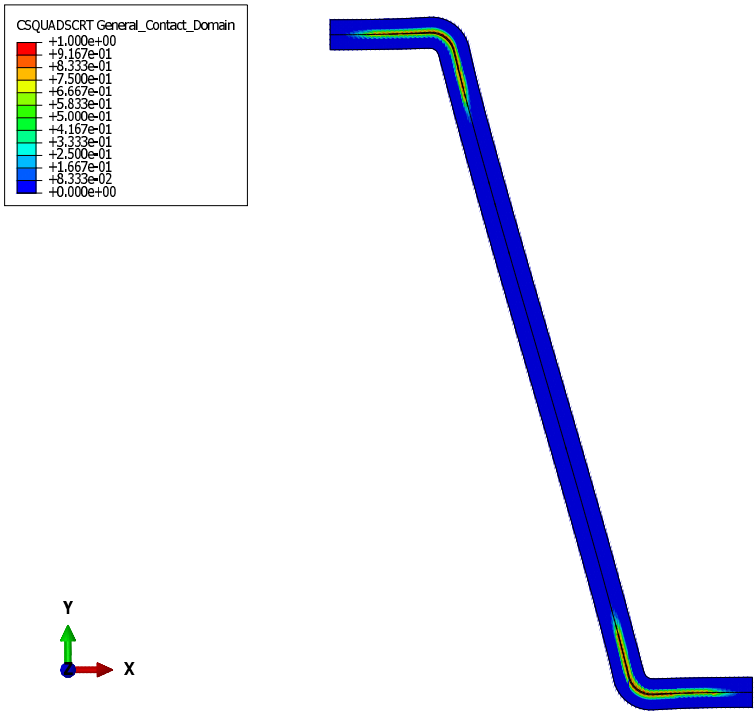


Figure 4.28: Finite element model of trapezoidal profile showing delamination.

stiffness gradually reduces. However, while keeping the unit cell length constant, the corrugation with smaller amplitude is stiffer than the one with higher amplitude. As the amplitude decreases, the corrugated structure behaves more like a flat plate. Therefore, the structural stiffness is inversely proportional to an increase in amplitude. From this analysis, it can be concluded that in order to obtain the most compliant corrugated structure, the corrugation with high amplitude and long unit cell length should be selected.

There is one thing that can be noticed from the results of parametric study of corrugation with different amplitude and unit cell length is that the results from finite element models are in a good agreement with analytical models except for case of the corrugation with an amplitude of 7.5 mm. The finite element models predict lower stiffness than the analytical models, especially in the case of trapezoidal corrugation. This is because the finite element models contain the surface-based cohesive behaviour between two composite plies, which fails at a lower stress level. As a result, this 'softer' layer allows easier movement of the corrugated panel when the displacement boundary condition is applied to the model.

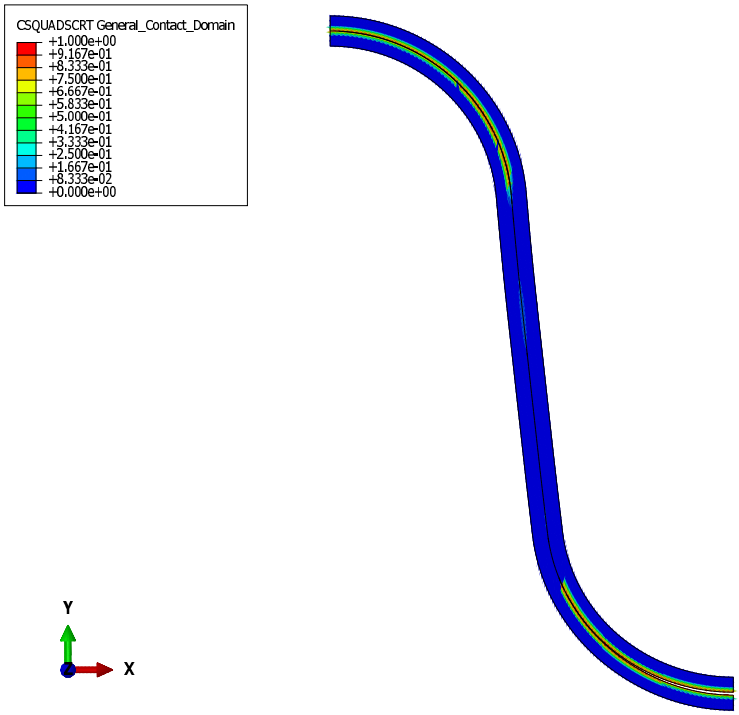


Figure 4.29: Finite element model of U-shape profile showing delamination.

4.4 Chapter Summary

This chapter presents an investigation on the structural response of carbon fibre reinforced polyurethane corrugated structure under an in-plane applied load. Carbon/polyurethane corrugated composite specimens were manufactured using the RIFT technique developed earlier to study the structural response experimentally. The experimental results were also used later to validate the finite element model. A commercial finite element analysis software, ABAQUS (version 6.10), was used as a tool to study structural behaviour of corrugated panels with different cross-sectional profiles and dimensions. Three different cross-sectional profiles, which are sinusoidal, trapezoidal and U-shape, were of interest. In order to study the effects of corrugated geometry, the amplitude and length of a unit cell (one wavelength) were varied in turn while another parameter remained fixed. In the FE model, the interaction of two layers of carbon fibre fabric was characterised by defining the properties of surfaced-based cohesive behaviour. This feature was incorporated into the model in order to capture delamination growth observed from tensile test of carbon fibre/polyurethane corrugated composite. The parameters used to characterise the surface-based cohesive behaviour were evaluated and validated against experimental results. The results from the parametric study suggested that the

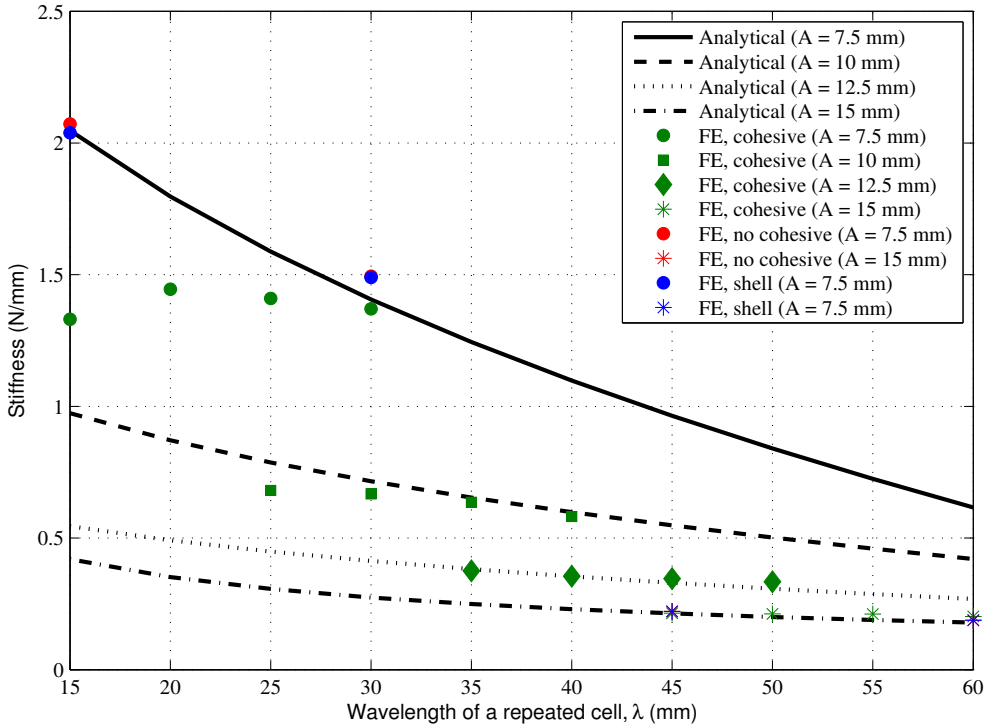


Figure 4.30: Results from parametric study of sinusoidal corrugation.

profile that has the lowest stiffness is trapezoidal followed by U-shape and sinusoidal, respectively. Therefore, the trapezoidal profile is taken forward to design the corrugated skin of the bench-top demonstrator discussed in chapter 6.

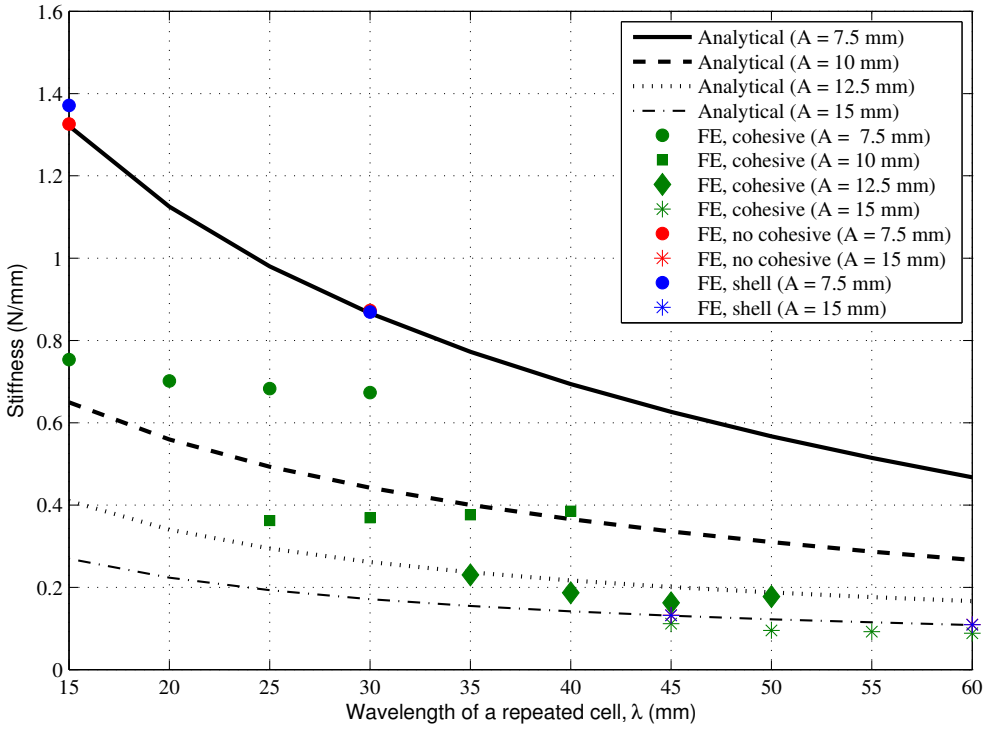


Figure 4.31: Results from parametric study of trapezoidal corrugation.

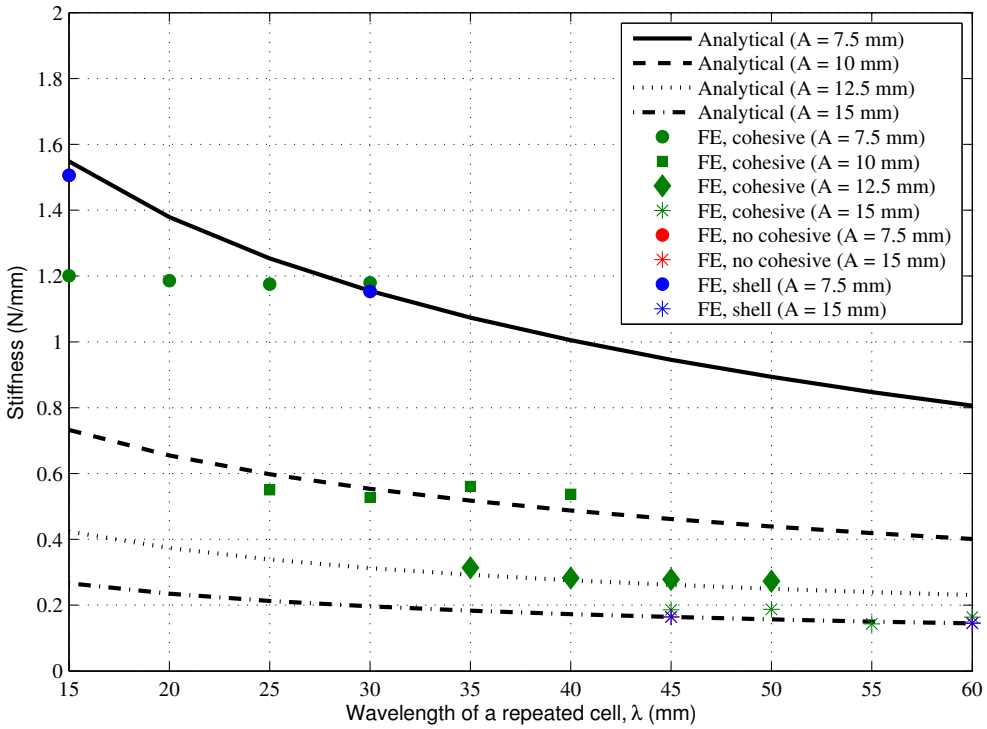


Figure 4.32: Results from parametric study of U-shape corrugation.

Chapter 5

Aerodynamic Analysis of a Morphing Wing With Corrugated Skin

In chapter 4, the structural aspect of the carbon/polyurethane corrugated composite skin was investigated. In this chapter, another important factor that affects the performance of a morphing wing with corrugated skin will be discussed. This is the aerodynamic performance at different Reynolds numbers and angles of attack. In this study, both numerical analyses and wind tunnel test were performed in order to investigate 2D aerodynamic characteristics of an aerofoil with corrugated skin on the pressure side and compared with an aerofoil that consists of a smooth skin.

5.1 Previous Studies on Aerodynamic of Corrugated Wing

It can be seen that many engineering applications are inspired by constructions from nature. This type of biologically inspired design is known as 'biomimetics'. The morphing wing is no exception. A morphing wing application, especially the corrugated skin concept, is an example of a structural design which has obtained inspiration from the cross-sectional profile of a dragonfly's wing. The non-smooth profile of a dragonfly's wing consists of well-defined corrugated configurations. These configurations, however, have never been used in conventional wings as they were regarded as aerodynamically inefficient due to discontinuities in the skin. However, recently many

aerodynamicists have revealed interesting flow features of low Reynolds number flow field around dragonfly's wing profiles. The outcome from previous research studies [9–11, 157] suggested that at low Reynolds number between 10^3 and 10^4, the corrugated profiles of a dragonfly's wing perform better, in terms of lift-to-drag characteristics, than a smooth profile. The results of these research studies were later brought forward to apply to aeronautical applications such as a morphing wing. Thill *et al.* [7] numerically and experimentally investigated a NACA 0012 aerofoil with different corrugated shapes and forms in the aft of the wing section at Reynolds numbers of 250,000, 500,000 and 1,000,000. The observed results suggested that the adverse effects resulted from corrugated skin could be minimised by selecting appropriate corrugation profiles and geometry and the speed at which the aircraft operates. Another useful outcome from the investigation by Thill *et al.* [7] was that low amplitude and wavelength of corrugation are preferred and the corrugations should be recessed in order to improve aerodynamic properties while the shape of the corrugated profile has insignificant effects. This leads to the objectives of this chapter which are to investigate and compare the aerodynamic characteristics of an aerofoil with a corrugated skin on the pressure side to those of a conventional smooth aerofoil.

5.2 Wind Tunnel Test

5.2.1 Design of wind tunnel models

In this comparative study, the aerodynamic performance of a wing with corrugated lower surface was investigated and compared with a conventional wing with a plain flap. In order to accurately compare the performance of different wings, the same aerofoil section, which was a NACA 4412 cambered aerofoil, was used. The shape of the NACA 4412 aerofoil is presented in figure 5.1. The chord length of the aerofoil (c) was 300 mm while the span (b) was chosen to be 500 mm resulting in a wing with aspect ratio (AR) of 1.67.

The wind tunnel model was manufactured by rapid prototyping using the ABS plastic, which costs £0.35/cm^3. Therefore, in order to save raw material and manufacturing costs, the conventional wing with a plain flap and a fixed wing with corrugated skin were designed as modular sections such that the plain flap of the conventional wing can be replaced by a corrugated panel. Not only consideration in cost saving, but the limitation of the rapid proto-

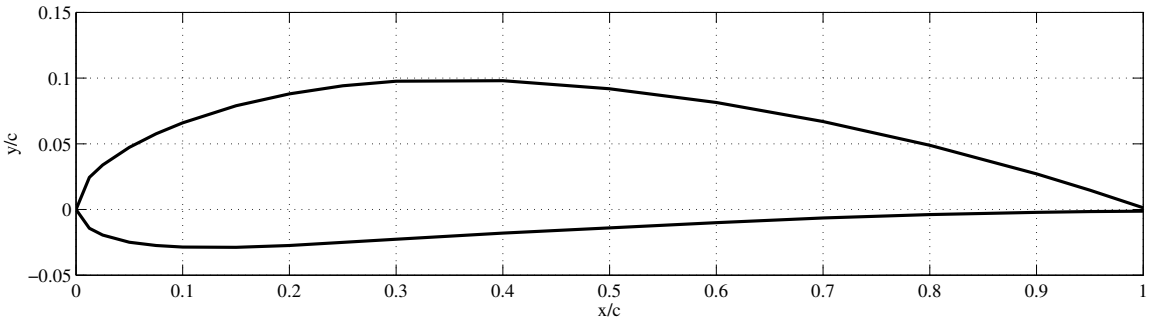
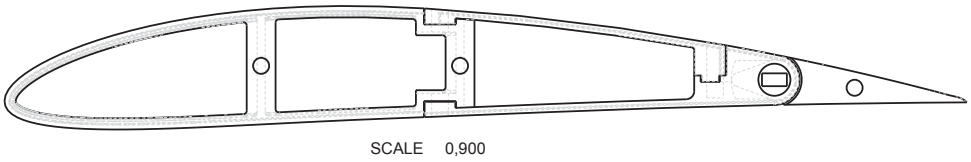


Figure 5.1: NACA 4412 aerofoil.

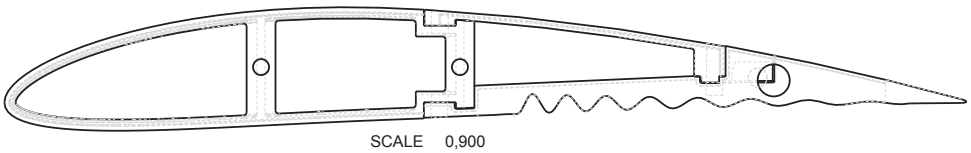
typing machine also contributed to the design of modular sections. To further reduce the costs of ABS plastic and manufacture, the wing was manufactured as a hollow extrusions with two vertical spars located at 25%chord and 47.5%chord. The thickness of the ABS skin was set to 3 mm to ensure structural integrity under aerodynamic loads. Once the parts were manufactured from the rapid prototyping machine, the surfaces were sanded and painted to produce a smooth surface finish in order to promote laminar boundary layer flow as this has a major effect on low Reynolds number performance [158].

The corrugated panel was designed to replace the lower skin and the plain flap of the conventional wing at the aft section behind the rear spar. For ease of manufacture, sinusoidal profile was used and the dimensions of the corrugation were varied from the rear spar to the trailing edge. Near the spar, the amplitude of the corrugation was high while the wavelength was small. This was because the extensional stiffness of such configuration is minimum allowing the panel to move in local x-direction with minimal power. The geometry of the sinusoidal corrugations was tailored such that, towards the trailing edge, the amplitude of the corrugations was reduced but the wavelength was increased making the corrugations near the trailing edge to be close to a flat surface. The design of corrugations in this way was also believed to reduce the drag penalty arisen from the presence of corrugations as compared to having constant wavelength and amplitude towards the trailing edge. The drawings of conventional and corrugated aerofoils are shown in figures 5.2a and 5.2b.

The wind tunnel tests were conducted in the 5 ft $\times$ 4 ft "Donald Campbell" closed loop wind tunnel at the Department of Aeronautics, Imperial College London. There is a 3-component force balance above the tunnel which can be used to measure lift, drag and pitching moment. The force balance was



(a) Smooth aerofoil



(b) Corrugated aerofoil

Figure 5.2: Schematic drawings of smooth conventional aerofoil and corrugated skin aerofoil

connected to the model via two vertical struts outside the test section and one vertical strut inside the test section. The lift and drag were measured via the struts outside the tunnel while the pitching moment was measured through a strut in the test section. The tunnel is capable of generating flow speeds of up to 40 m/s that are measured via a micromanometer connected to a pitot-static system. In order to simulate a 2D flow, two end-plates were employed to minimise the effects of tip vortices. The end-plates were designed to have similar shape to the aerofoil but bigger with the nominal distance between the edges of the aerofoil and the edges of the end-plates of 250 mm. The thickness of the end-plates was 10 mm. The material used to manufacture the end-plates was the PMMA thermoplastic as it is transparent. The outer edges away from the wing of the end-plates were rounded so as to minimise drag and limit turbulent flow near the wing. At the back of the end-plates near the trailing edge of the wing, a steel rod was placed between two end-plates and connected to the pitching moment arm.

As mentioned earlier that the force balance was attached to the wing via two vertical struts outside the test section, therefore, the wing and the end-plates must be attached to a support structure which then connected to the force balance. The design of the support structure was based on the following criteria.

- Low frontal area to reduce drag.

- High stiffness to reduce the effects of buffeting and to avoid fluttering.
- No buckling.
- Low weight.
- Low production cost.

There was another requirement that the servo motors used to drive the plain flap was designed to be housed outside the hollow section of the wing. Therefore, two rectangular aluminium plates were used as base plates to accommodate a servo motor on each side of the wing. The base plates were connected to the end plates via 4 steel rods on one side, while on the other side another steel rod was used to connect the whole structure to the force balance (figure 5.3).

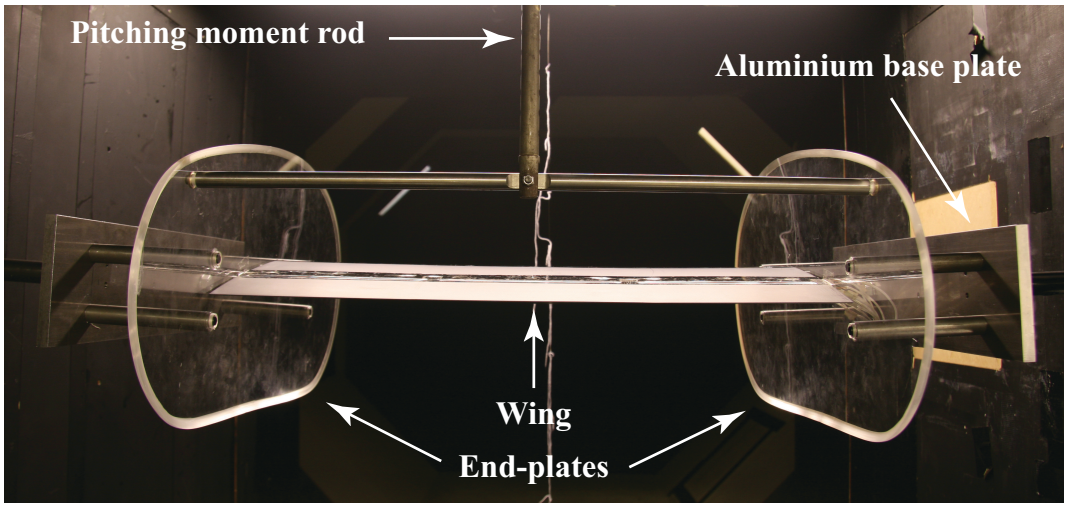


Figure 5.3: Wing setup in the wind tunnel.

5.2.2 Testing procedure

Tare test

Prior to the actual test, a 'tare test' was performed to take into account the drag generated by the support structure and end-plates in order to accurately evaluate the drag generated solely by the aerofoil. The tare test involved setting up the apparatus without the aerofoil and running the test at the preset flow speeds. In the absence of the wing, each side of the support structure was connected to the other side using a circular steel rod. The tests were performed at 4 preset flow speeds at different angles of attack ranging from -8° to 22°

at an increment of 2°. The apparatus was found to generate a considerable amount of drag but contribution to lift and pitching moment was negligible. Total drag generated by the apparatus without the wing can be estimated using equation 5.1.

$$\text{Total apparatus drag} = \text{Tare test drag} - \text{Circular rod drag}. \tag{5.1}$$

The drag generated from the circular steel rod used to connect two sides of the support structure was subtracted as it did not exist in the actual tests of the aerofoils. The circular rod drag could be approximated from the plot of drag coefficient (C_D) against Reynolds number as shown in figure 5.4.

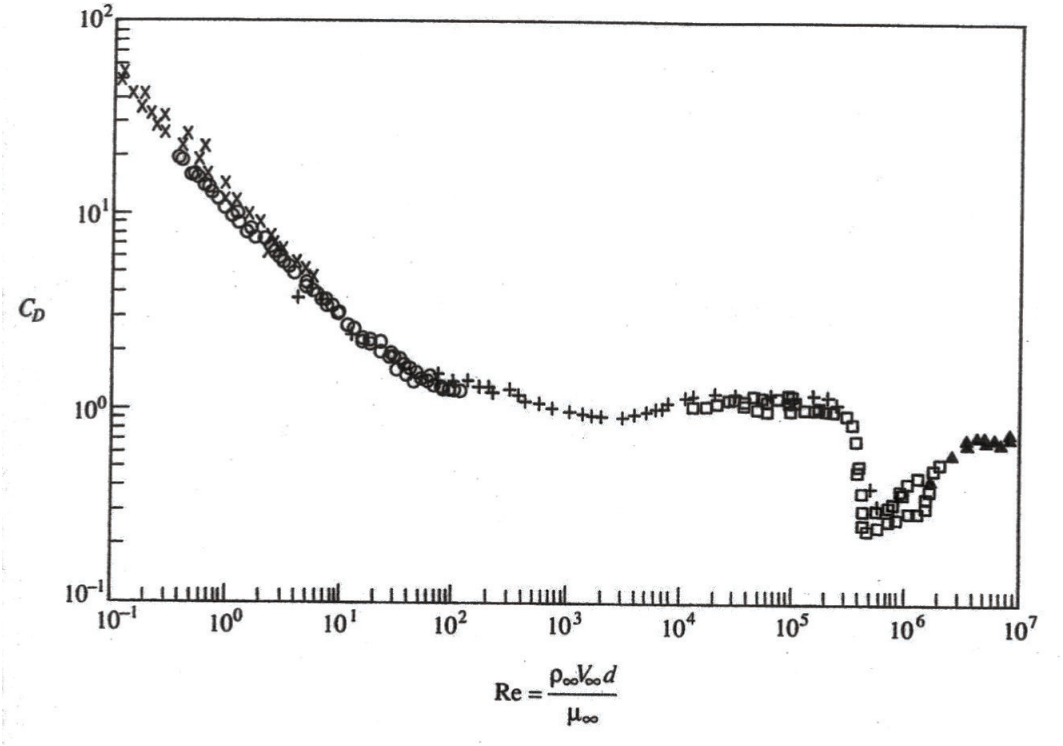


Figure 5.4: Variable of drag coefficient with Reynolds number of a cylinder [159], page 293.

Preliminary run

Once the wind tunnel model described in section 5.2.1 was setup in the wind tunnel, the next step was to take a measurement of lift, drag and pitching moment of the aerofoil. The force balance had to be operated manually by

balancing the scale shown on the control panel and the readings of lift, drag and pitching moment were recorded in a spread sheet. The angle of attack could be changed from a control panel connected to a motor above the vertical strut inside the test section. However, it was found during a preliminary run that the angle of attack reading from the control panel was inaccurate. Therefore, a digital spirit level was calibrated and connected to the support structure to measure the actual angle of attack. The wind tunnel test was performed at 4 different wind speeds which were 15 m/s, 20 m/s, 25 m/s and 30 m/s. The corresponding Reynolds numbers could be calculated from equation 5.2 and found to be 280,000, 397,000, 497,000 and 596,000, respectively.

$$Re = \frac{\rho_\infty U_\infty c}{\mu}, \tag{5.2}$$

where Re is the Reynolds number
ρ_∞ is the density of air [kg/m^3]
U_∞ is the free stream velocity [m/s]
c is the chord length of the aerofoil [m]
μ is the air dynamic viscosity [kg/(m·s)]

Wind tunnel test of the aerofoils

The conventional aerofoil with a plain flap was tested first. The flap angle was kept at 0° throughout the test to match the unmorphed trailing edge of the corrugated aerofoil. Therefore, the aerodynamic characteristics of the two configurations could be compared. The gap between the aerofoil and the flap was sealed with a piece of adhesive tape to smoothen the flow over the aerofoil. Once the conventional aerofoil was tested at all specified angles of attack, the lower surface aft of the rear spar was replaced by a corrugated panel and the same procedure was repeated. Both conventional and corrugated aerofoils were tested at each wind speed only once. It should be noted that the lift and drag recorded from the control panel were in pounds (lbs) while the pitching moment was in pound-feet (lbs-ft). The drag obtained from the experiment of two configurations was the overall drag including the drag generated from the support structure and end-plates. Therefore, the drag obtained from the tare test had to be subtracted from the drag obtained from the actual experiment.

The next step was to convert the lift and drag forces and pitching moment into dimensionless forms. As the flow over the aerofoil was assumed to be approximately two-dimensional, the expressions used to calculate lift coefficient from the lift force, drag coefficient from the drag force, and pitching moment coefficient from the pitching moment are presented in equations 5.3, 5.4 and 5.5, respectively [159].

$$C_l = \frac{l}{\frac{1}{2}\rho_\infty U_\infty c}. \tag{5.3}$$

$$C_d = \frac{d}{\frac{1}{2}\rho_\infty U_\infty c}. \tag{5.4}$$

$$C_{m,25\%c} = \frac{m_{25\%c}}{\frac{1}{2}\rho_\infty U_\infty c^2}. \tag{5.5}$$

It is noted that the pitching moment coefficient was calculated from the moment about the quarter chord point.

In the experiment, the flow field around the aerofoil and the support structure was not identical to the ideal flow field due to confining walls. Therefore, the differences between the ideal flow field and the experiment need to be corrected. The number and type of corrections depend on the type of the flow whether the flow is 2D or 3D. As the wind tunnel test in this research was considered as 2D with the use of end-plates, four important correction factors are highlighted as follows [160].

1. **Buoyancy:** Variation in the static pressure caused by boundary layer growth along the tunnel walls. This effectively accelerates the flow which is capable to move models with big frontal area backwards. Therefore, buoyancy artificially increases the drag.

2. **Wake blockage:** The blockage due to wake generated at the back of the model. The mean velocity of the flow at the back of the model is affected by the viscous layer from the model and it is lower than the freestream velocity. Therefore, to maintain continuity, the mean velocity outside the wake is higher than the freestream to balance the momentum deficit of the wake.

3. **Solid blockage:** The model in the tunnel reduces the area which the

air can flow. This results in an increased free-stream velocity around the model.

4. **Streamline curvature:** The curvature of the flow field around the model is straightened by the tunnel walls. Therefore, it appears as the model has additional camber. This effect requires correction of the lift and moment about the quarter chord point at a given angle of attack.

The mathematical representations of the relationship between uncorrected and corrected coefficients and angle of attack are shown in equations 5.6 to 5.9 for which a detailed derivation of these equations is given by Pope [160].

$$\alpha_{corrected} = \alpha + \frac{57.3\sigma_c}{2\pi}\left(C_l + 4C_{m,25\%c}\right), \tag{5.6}$$

$$C_{l,corrected} = C_l\left(1 - \sigma_c - 2\epsilon_c\right), \tag{5.7}$$

$$C_{d0,corrected} = C_{d0}\left(1 - 3\epsilon_{sb} - 2\epsilon_{wb}\right), \tag{5.8}$$

$$C_{m,25\%c,corrected} = C_{m,25\%c}\left(1 - 2\epsilon_c\right) + \left(\frac{\sigma_c C_l}{4}\right). \tag{5.9}$$

The variables σ_c and ϵ_c can be expressed as,

$$\sigma_c = \frac{\pi^2}{48}\left(\frac{c}{h}\right)^2, \tag{5.10}$$

$$\epsilon_c = \epsilon_{wb} + \epsilon_{sb}, \tag{5.11}$$

where h is the height of the test section and ϵ_{wb} and ϵ_{sb} can be defined as follows,

$$\epsilon_{wb} = \frac{c}{4h} \cdot C_d, \tag{5.12}$$

$$\epsilon_{sb} = \sigma_c \cdot \Lambda, \tag{5.13}$$

in which the parameter Λ can be extracted from the plot of Λ against aerofoil thickness ratio (t/c) as shown in figure 5.5.

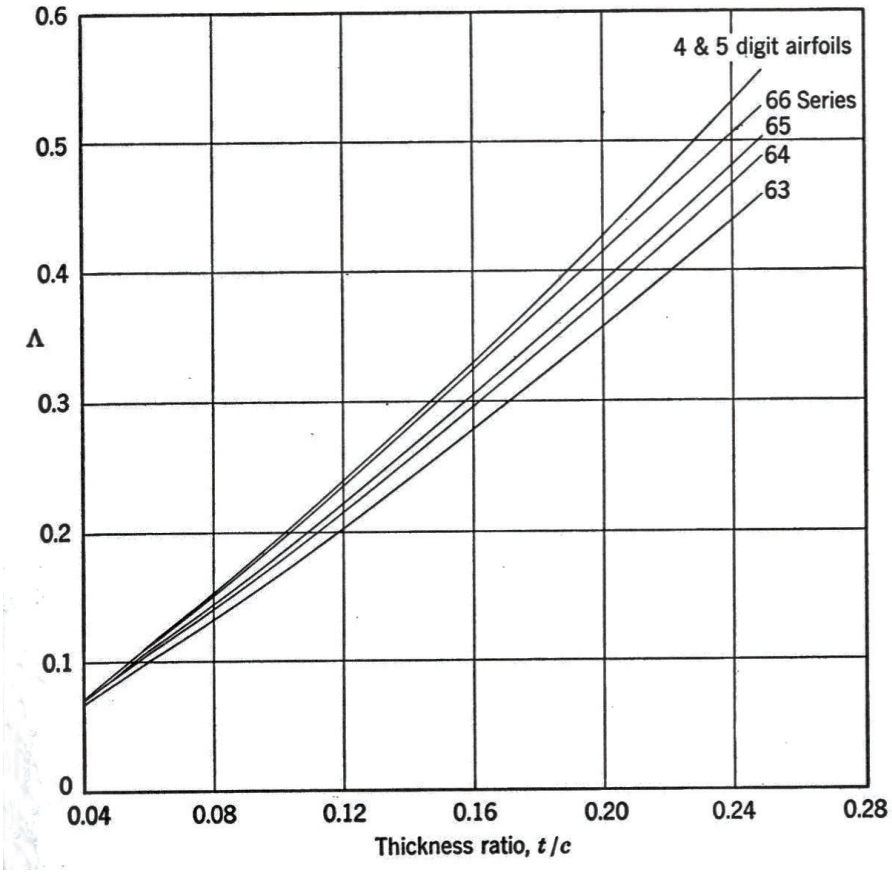


Figure 5.5: Plot of Λ against t/c [160], page 277.

5.3 Results and Discussion

In order to make a comparison of the aerodynamic characteristics between conventional aerofoil and aerofoil with corrugated skin, the conventional aerofoil was first tested in the wind tunnel and the results were compared with analytical solutions produced by two aerofoil analysis programs: XFOIL (developed by Professor Drela at MIT) [161] and AeroFoil version 3.0 (developed at the University of Virginia) [162]. Both computational codes were written based on panel method with integral boundary layer equations to calculate lift, drag and pitching moment at different angles of attack. The major difference between the two codes is that XFOIL was written in Fortran while AeroFoil 3.0 was written in Visual Basic. Therefore, the graphic user interface of AeroFoil 3.0 was designed with an intention to be the most user-friendly of its type [162]. Both XFOIL and AeroFoil 3.0 were extensively validated against experimental results, therefore, the programs could be used with confidence in this research.

It was observed during the experiment that there was a number of imperfections of the aerofoil model, support structure and force balance that could affect the test results. These possible sources of error are outlined and discussed in section 5.3.1 below.

5.3.1 Possible sources of error

Angle of attack

The angle of attack of the wing model and support structure was controlled by moving the pitching moment arm attached to the back of the end-plates up and down. However, the reading of the angle of attack on the control panel was inaccurate. Therefore, the digital spirit level was securely attached to the support structure and calibrated before every test to give true angle of attack with respect to the flow.

Rigidity of the model

According to figure 5.3, it can be seen that the wing and end-plates were connected to aluminium plates via 8 attachment points (4 on each side). Moreover, the aluminium plates were connected to the balance using a strut on each side. This structure contains excessive linkages that flex under pressure load during the test. Therefore, at higher Reynolds number and angle of attack, the whole model vibrated and the true angle of attack was difficult to obtain. Moreover, the vibration also affected the pitching moment readings which, subsequently, yielded inconclusive data on pitching moment.

3-D effects

Wingtip vortices create a downwash that influences flow upstream of a wing by reducing the effective angle of attack. The strength of the vortices is proportional to lift generated by the wing and therefore it would vary between the models that were tested. In this study, the effects of wingtip vortices were reduced by the use of end-plates. However, in order to minimise the wingtip vortices and to simulate 2-D flow, the wing should be extended to the tunnel walls and the support structure should be removed. This was not done because the cost of the ABS plastic was relatively expensive and the rapid prototyping machine was limited to create a model of the size of 200 $\times$ 200 $\times$ 300 mm. Therefore, to reduce raw material and manufacturing costs and to avoid excessive number of seams on the model, the end-plates were adopted.

Other sources of error

Temperature in the wind tunnel was measured using a thermometer positioned inside the working section. Measurements taken throughout the experiment suggested that temperature rises by around 2°C over the duration of a day of testing. Assuming a linear variation in density with temperature, the rate of change of density was calculated as -0.0044 (kg/m^3)/°C. This translates to a percentage change in density per degree Celsius of 0.365%. Lift, drag and pitching moment are proportional to density and, hence, the effect of temperature on these parameters is negligible.

Flow speed fluctuates slightly due to limitations of the wind tunnel. For example, when set to 15 m/s, the actual speed varied between 14.9 m/s and 15.1 m/s. Lift and drag are proportional to U_∞^2, which lies between 222.01 and 228.01 for the aforementioned wind speeds. The maximum deviation in U_∞^2 of 6 translates to a percentage error of 2.67% which would have very little effect on the results.

5.3.2 Comparison between smooth conventional aerofoil and analytical results

It was expected that data obtained experimentally from wind tunnel testing would not perfectly match computational predictions made using XFOIL and AeroFoil 3.0. This was due to the fact that the experiments involved some uncertainties arising from 3-D effects due to the presence of end-plates and support structure. Also, the discrepancies of the test results were partly from the flexibility of the support structure. However it was necessary to confirm that differences between theoretical and experimental data were presented and that they could be explained. Large fluctuations in measurements made it impossible to obtain conclusive results with respect to pitching moment. Therefore, only lift and drag coefficients are presented and compared with analytical solutions and among different aerofoil geometries.

Figures 5.6 and 5.7 show lift and drag coefficients of the smooth conventional aerofoil with a plain flap at Reynolds number of 280,000. The results obtained from the wind tunnel tests are plotted alongside theoretical predictions from XFOIL and AeroFoil 3.0. A complete set of lift and drag curves at different angles of attack of the smooth conventional aerofoil at other preset

Reynolds numbers are shown in Appendix B.

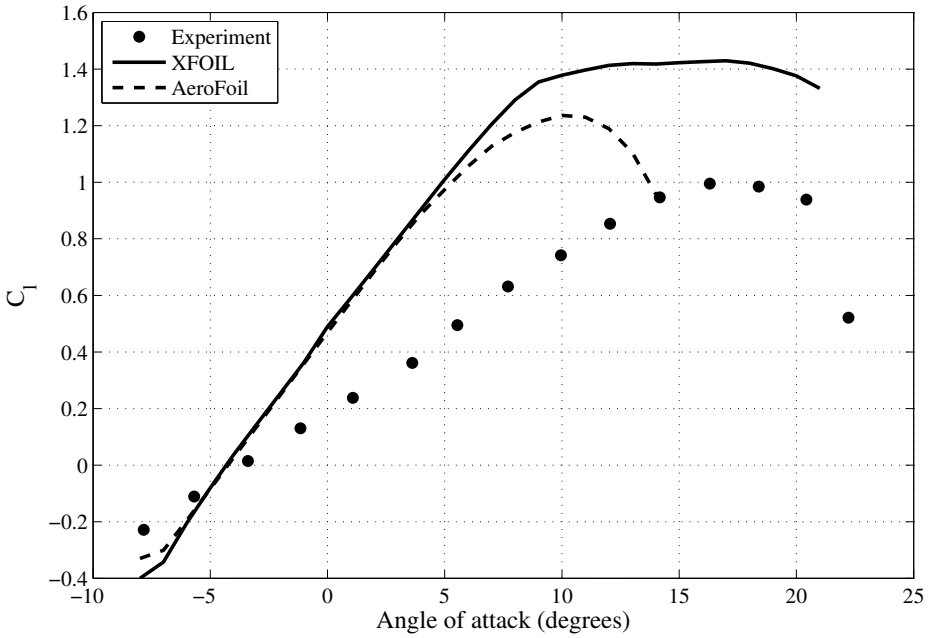


Figure 5.6: Lift coefficient of conventional wing at different angles of attack (Re = 280,000).

It can be seen from the lift curves that the lift curve slopes from aerofoil analysis programs (XFOIL and AeroFoil 3.0) are almost identical. However, the stall angles are different. The stall angles obtained from AeroFoil 3.0 are slightly lower than that generated from XFOIL. This is probably due to different implementation methods of the theory in which XFOIL was written in FORTRAN, while AeroFoil 3.0 was written in Visual Basic. When comparing the theoretical predictions with experimental results, it can be clearly observed that the lift curve slopes from the experiment are shallower than the slopes of theoretical results. This also affects the stall angle of the wind tunnel model. The angle at which the lift starts to decrease from the experiment at Reynolds number of 280,000 (figure 5.6) is approximately 16°. If the experimental lift curve was adjusted such that the slope matches the theory, the stall angle would have been close to that predicted from the theory. The discrepancies in lift curve slope and stall angle are caused by the fact that the wing with endplates and support structure contain linkages which are able to move during the testing. Although the digital spirit level was used, it was attached to the support structure outside the test section. Therefore, the true angle of attack of the wing may be slightly different to the reading obtained from the digital

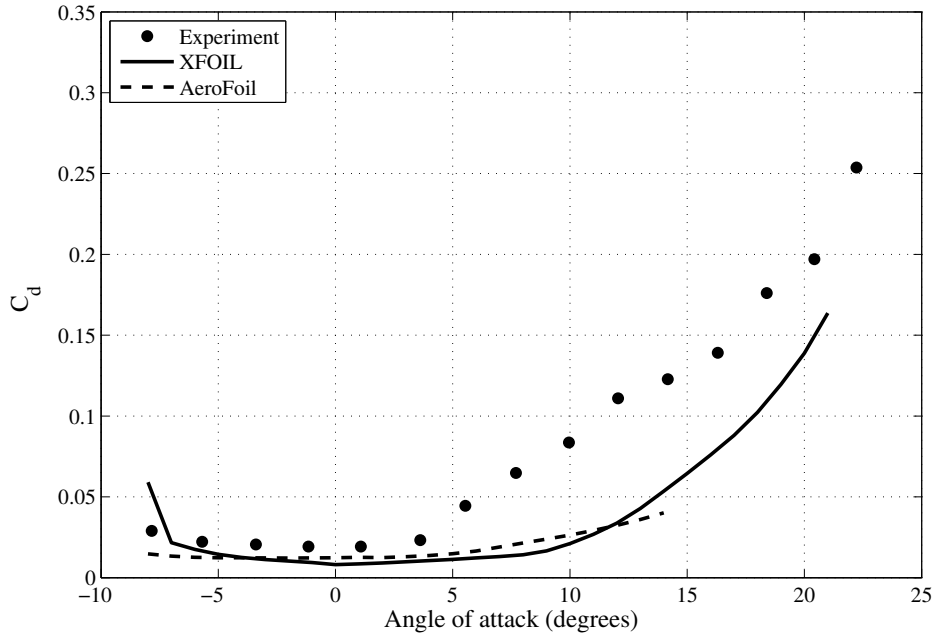


Figure 5.7: Drag coefficient of conventional wing at different angles of attack (Re = 280,000).

spirit level due to fluttering. Other factors that could affect the lift are the presence of the small end-plates and short wing span. The end-plates were relatively small compared to the side walls and this could introduce the flow in spanwise direction. These 3-D effects, when combined with short wing span, may significantly reduce the lift.

All the drag curves show that experimental drag is higher than theoretical, especially at higher angles of attack, which strengthens the argument that flexibility of the model and 3-D effects are the major cause of deviation from the theory. The difference in drag between experimental and theoretical results at higher angles of attack suggests that the effects of structural flexibility is greater than the 3-D effects. At high Reynolds numbers (497,000 and 596,000) and small angle of attack, the minimum drag coefficient falls below zero which is impossible for an object to have negative drag. This suggests that there was an error or improper calibration of the force balance. Unfortunately, this error was not further investigated experimentally as it was discovered during data processing after the experiment.

5.3.3 Comparison between smooth conventional and corrugated aerofoils

Once the wind tunnel test of the conventional aerofoil was completed, the lower surface and plain flap were replaced by a corrugated panel and the aerofoil was set up in the wind tunnel using the same support structure. The test procedure was repeated and the lift, drag and pitching moment were recorded manually. Similar to the testing of the smooth conventional aerofoil, the pitching moment readings were fluctuated and very difficult to adjust the scale on the control panel. Therefore, no conclusive results with respect to pitching moment are presented in this section.

The corrugated aerofoil was tested in the wind tunnel at 4 different preset speeds similar to the tests of conventional aerofoil at angles of attack ranging from -8° to 22°. Figure 5.8 shows a comparison between experimental results and analytical results obtained from AeroFoil 3.0 for both conventional and corrugated aerofoils. It can be seen that there is a discrepancy between experimental results and analytical solution with the sources of error discussed in section 5.3.1. Therefore, for the comparison purposes, only the experimental results from the smooth conventional and corrugated aerofoils are presented.

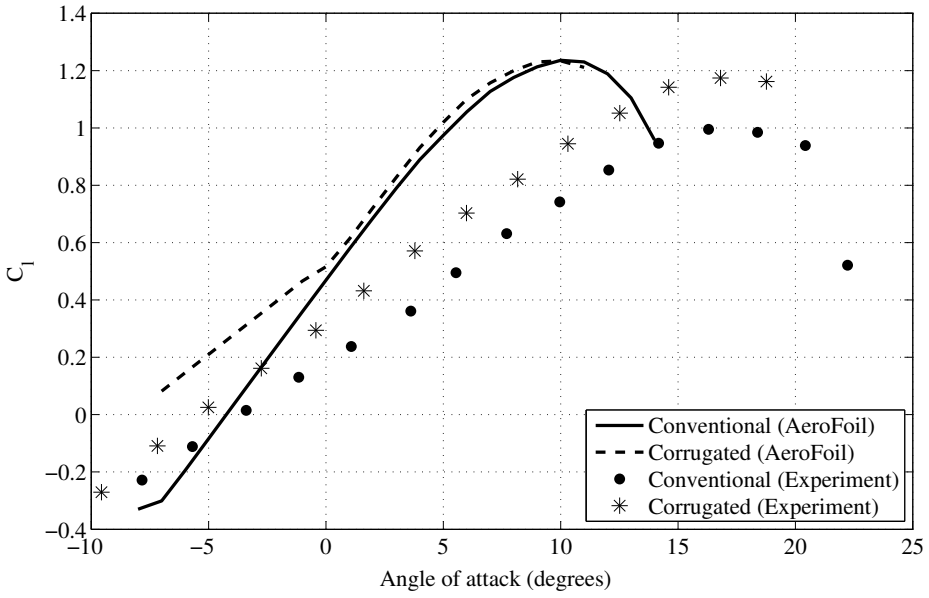


Figure 5.8: Analytical and experimental lift curves of conventional and corrugated aerofoils (Re = 280,000).

Aerodynamic properties such as lift and drag curves and lift-to-drag characteristics of the two configurations (conventional and corrugated) at Reynolds number of 280,000 are compared and presented in figures 5.9 to 5.11. A complete set of comparative results is displayed in Appendix B.

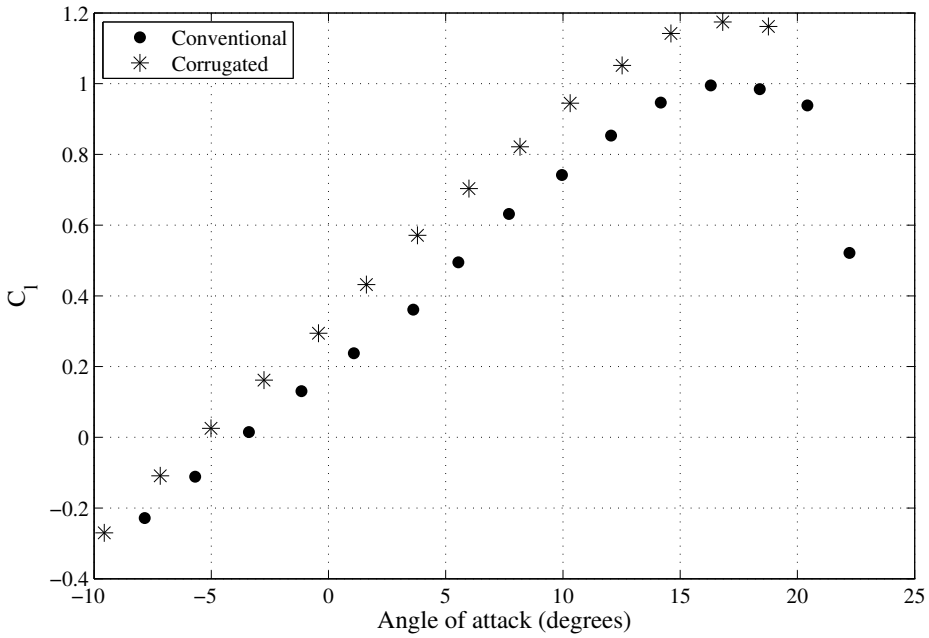


Figure 5.9: Lift coefficient of corrugated wing at different angles of attack (Re = 280,000).

The results from the comparative study of smooth conventional and corrugated aerofoils show that the lift produced by the corrugated aerofoil is higher than that from the conventional aerofoil at every preset wind speed while the stall angles and lift curve slopes remain relatively similar. However, it is evident that the corrugated skin generates more drag than the smooth skin, especially at high Reynolds numbers and angles of attack. When considering the drag polar plots of the two configurations, it can be observed that at Reynolds number of 280,000 the corrugated aerofoil performs very well compared to the smooth aerofoil. In the region where the drag is low, the lift-to-drag characteristics of the two aerofoils are almost identical. However, as the drag increases, the lift generated by the corrugated aerofoil is slightly higher than the smooth conventional aerofoil at the same level of drag. As the Reynolds number increases, the aerodynamic performance of the corrugated skin aerofoil at low angle of attack deteriorates, as compared to the aerofoil with smooth skin, while at high angle of attack the aerodynamic performance

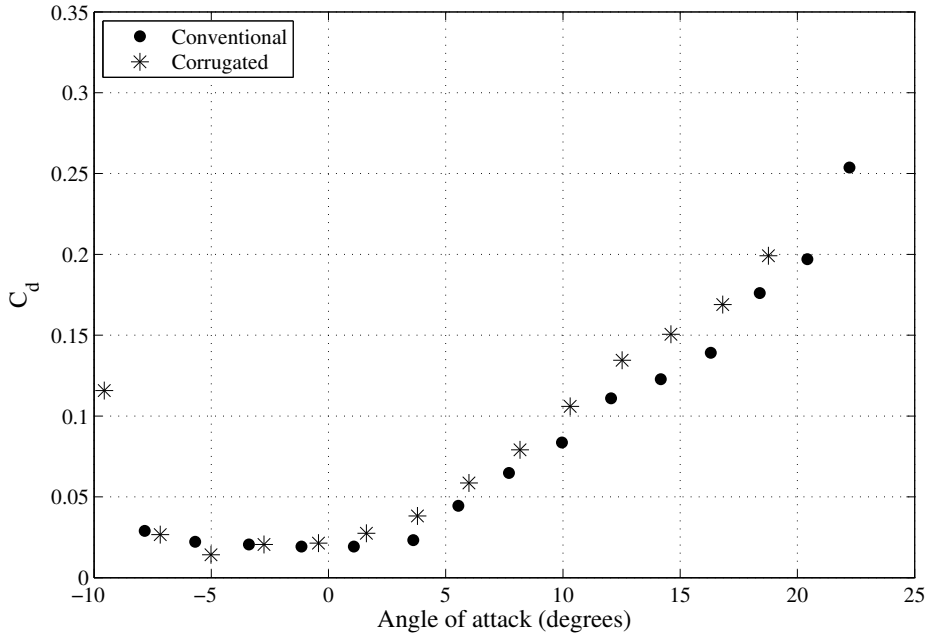


Figure 5.10: Drag coefficient of corrugated wing at different angles of attack (Re = 280,000).

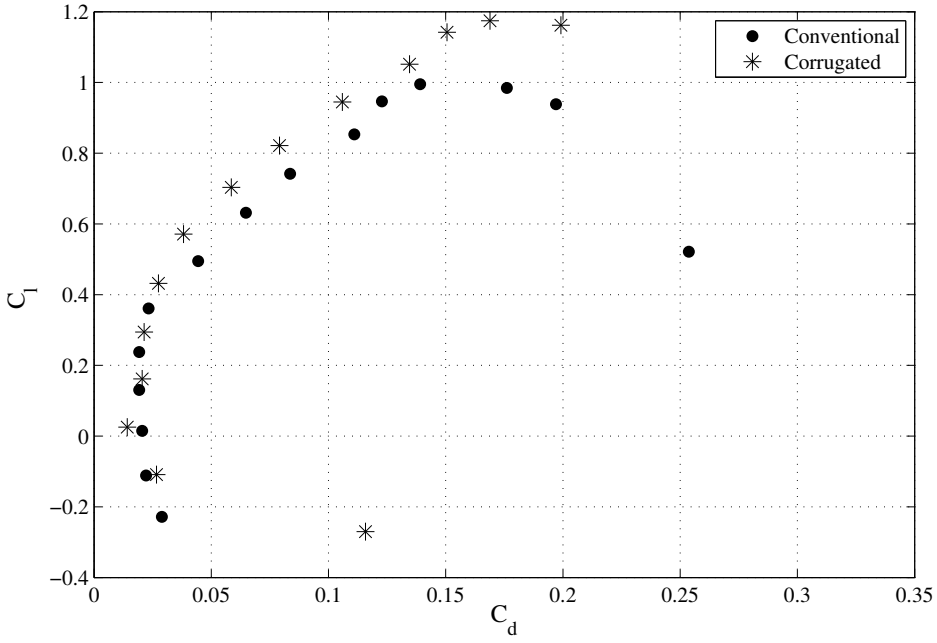


Figure 5.11: Drag polar of corrugated wing at different angles of attack (Re = 280,000).

of the two configurations is relatively similar. The main findings of this comparative investigation partly match the results from the research study by

Mazzola [157] on corrugated profiles of dragonfly's wing sections except that the lowest Reynolds number in the current research is higher than the highest Reynolds number in the studies of dragonfly's wing sections. Therefore, the discussion of flow features around the corrugated dragonfly's wing sections could be adopted to explain the comparative results of the current study. At low Reynolds number (Re = 280,000 in this case), the corrugations generate unsteady vortices in the valley sections which promote the transition of boundary layer from laminar to turbulent rapidly. These rotating vortices in the valley sections energise the flow outside the troughs such that the boundary layer gains sufficient energy to overcome the adverse pressure gradient, hence, the flow separations are suppressed. This mechanism provides more lift at all angles of attack and less drag at angles of attack close to 0°. As the angle of attack increases, the separation point moves upstream and, therefore, loss of lift together with a significant increase in drag were observed.

The findings of this comparative study suggest that the aerofoil with lower corrugated skin at the aft section, in which the corrugated skin is tailored to have smoother surface towards the trailing edge, is aerodynamically efficient for Reynolds number below 280,000. At this Reynolds number, the corrugated skin generates more lift but relatively low drag at every angle of attack due to the effects of the rotating vortices in the valley sections of the corrugations. Although not investigated in this study, the detrimental effects caused by corrugations should be less at lower Reynolds number. This leads to a conclusion that the aerofoil with tailored corrugated skin concept is feasible for a small UAV that operates at a Reynolds number of approximately 10^5.

5.3.4 Further recommendations

During the process, a number of areas for further study were found that could be carried out as extensions to this study. In addition, shortcomings of the approach to this study highlighted improvements that could be made in similar investigations that may be carried out in the future. These could be categorised as numerical analysis and experimental work.

Numerical analysis

It was not possible to examine the aerodynamic characteristics of the wing with corrugated skin analytically due to shortcomings of XFOIL. Although a

corrugated aerofoil model could be successfully imported to XFOIL, converged results were difficult to obtain. This was probably due to the limitation of the panel code to cope with the separation of the flow and rotating vortices generated in the valley sections of the corrugations. Therefore, to resolve the problem, a CFD model of corrugated aerofoil could be constructed and tested numerically to validate the experimental results.

In order to investigate the effects of different corrugation profiles and geometries on aerodynamic performance of an aerofoil efficiently, a CFD model of a smooth conventional aerofoil could be developed and validated against an analytical model and published experimental data. Then this model could be modified such that the corrugated skin feature is incorporated. This allows the investigator to gather useful information on the effects of corrugation's shape and size before performing a costly wind tunnel test. Moreover, the CFD model can provide a virtual interpretation of the flow field in the corrugations which can be used to further explain the aerodynamic properties of the corrugated aerofoil.

It should be highlighted that, in this chapter, no aerodynamic comparative study of different corrugated profiles was performed. This was because a CFD corrugated aerofoil model was required in order to perform an accurate analysis. Without the results from the comparative study of different corrugated profiles and lack of a CFD corrugated model, it was also difficult to perform an optimisation process to evaluate the most aerodynamically efficient corrugated profile and geometry. Moreover, the optimisation process in this case also requires a complex optimisation routine to locally design the best corrugated profile and its dimensions.

Experimental work

Time and cost constraints led to wind tunnel models being built as rigid extrusions that were used to obtain valuable data. However a more thorough examination of the concepts could have been conducted by employing deformable models that would enable testing across the entire range of trailing edge deflections. Larger models with pressure tappings connected to a multitube manometer would have generated images of pressure distributions that could have led to a more detailed understanding of the phenomena observed during testing.

In this research, the tailored corrugated skin aerofoil was compared against only a smooth conventional aerofoil. Therefore, the differences in aerodynamic performance between the tailored corrugated skin and a corrugated aerofoil with constant wavelength and amplitude were not quantified. Therefore, more corrugated panels with constant wavelength and amplitude along chordwise direction should be manufactured and tested experimentally and compared with the aerodynamic performance of the tailored corrugated skin concept. In addition, Particle Image Velocimetry (PIV) can be employed to capture the actual flow field near the corrugated skin.

Splitter plates could be used for wind tunnel experiments in order to minimise 3-D effects and create closer representations of 2-D aerofoil performance. However these would require careful design to ensure fully developed boundary layer flow, and the effects of interaction with the wing boundary layer would have to be accounted for.

In the present study, the force balance was controlled manually by adjusting the scales on the control panel. This method depends heavily on the operator. It was observed during the experiment that at high Reynolds number and angle of attack, the scales on the control panel were difficult to balance. This was due to the oscillations of the wing and the support structure. This issue could be overcome by reducing the linkages of the structure or span the wing across the side walls of the test section. Moreover, the automated control system and data acquisition system could be employed to take the time-averaged readings automatically. The automated system could potentially reduce the time taken to record the readings from the force balance and the whole process could be iterated to ensure repeatability.

5.4 Chapter Summary

This chapter presents a comparative study of two aerofoils: a smooth conventional aerofoil and an aerofoil with a corrugated skin on the pressure side aft of the rear spar. Both aerofoils were tested in a closed loop wind tunnel at four different Reynolds numbers in order to determine the aerodynamic characteristics of each aerofoil. The smooth conventional aerofoil was tested first and the results were validated against an analytical model. The theoretical results were

obtained from two aerofoil analysis programs: XFOIL and AeroFoil 3.0. There were large discrepancies in the lift curve slopes and drag plots between experimental and theoretical results. The differences were due to many factors. The fact that the aerofoil model and end-plates were connected to the force balance through a support structure, which allows the whole setup to flex under aerodynamic loads, contributes to a fluctuation in angle of incidence during the test. Another factor attributed to an error in test results would be 3-D effects arising from support structure and end-plates. When combined with the short span of the wing model, the 3-D effects may significantly alter the test results. Realisation of the disagreement between experimental and theoretical results led to a comparative study of the smooth conventional aerofoil and corrugated aerofoil without a reference to theoretical framework. The lower surface and a plain flap of the smooth aerofoil were replaced by a corrugated panel in which the corrugation geometry changes along the chordwise direction. This concept was believed to have benefits structurally and aerodynamically. The corrugated aerofoil was set up in the wind tunnel using similar support structure as in the case of smooth aerofoil and the same testing procedure was executed for comparative purposes. The lift, drag and polar plots at each Reynolds number were plotted and the results suggested that at Reynolds number of 280,000, the corrugated aerofoil performed very similarly to the smooth aerofoil at low angle of attack in terms of lift-to-drag characteristics. At higher angle of attack, interestingly, the corrugated skin outperformed the smooth skin. However, as the Reynolds number increases, the aerodynamic performance at low angle of attack of the corrugated aerofoil was slightly worse than the smooth aerofoil while at higher angle of attack, the corrugated aerofoil performed similarly to the smooth conventional aerofoil. This was because the unsteady vortices induced in the valley sections of the corrugations energise the flow outside the troughs such that the boundary layer gains enough energy to overcome adverse pressure gradient and the flow separation is delayed. At high angle of attack, the separation point moves towards the leading edge and, as a result, the lift drops while the drag increases dramatically. The conclusion drawn from the comparative study suggests that the aerofoil with tailored corrugated skin on the pressure side is feasible to be used for a morphing wing of a small UAV that operates at Reynolds number of approximately 10^5.

Chapter 6

Conceptual Design of a Corrugated Composite Aerofoil Bench-top Model

In previous chapters, mechanical characteristics of carbon/polyurethane corrugated composite and aerodynamic performance of the aerofoil with lower corrugated skin have been investigated. In this chapter, a conceptual design of a bench-top model of a wing section with corrugated skin is presented. The bench-top model was designed based on the results obtained from mechanical and wind-tunnel testings to proof the concept. The main feature of the model includes a linear actuation mechanism, which is used to control camber change. In addition to the design of the aerofoil with corrugated skin, the limitations and recommendations for further development of the bench-top model and the corrugated composite skin concept are also discussed.

6.1 Design and Analysis of the Bench-top Model

The bench-top model was designed with a consideration to fulfil the following requirements.

1. A relatively inexpensive and simple actuation mechanism can be fitted inside the model.

2. The camber of the aerofoil can be changed by deflecting the trailing edge up and down at high speed in order to gain control authority.

3. Low manufacturing costs.

The requirements outlined above led to a selection of a symmetrical aerofoil section, NACA 0014, as shown in figure 6.1. The symmetrical aerofoil would provide similar up/down trailing edge deflection about the camber line. It was also decided that the chord length of the model remains similar to the wind tunnel model presented in chapter 5, which is 300 mm, and a single spar located at 25% chord is sufficient to maintain the shape of the aerofoil under aerodynamic and actuation loads. A study by Ranasinghe [163] suggested that an aerofoil with a fixed leading edge and a movable aft section performs aerodynamically better than the aerofoil with movable leading and trailing edges. This also reduces structural complexity of having an actuation mechanism in the forward portion of the wing. Therefore, in the current research, the leading edge of the aerofoil could not be moved and the only movable part is the aft section of the aerofoil behind the spar. This resulted in the design of the bench-top model having only the aft portion mounted on the aluminium wall, which represents the spar, while the D-nose was omitted to save manufacturing costs and greatly simplify the model. Therefore, the total length of the trailing edge portion becomes 225 mm. Another factor needed to be taken into account was the width of the carbon fibre tape as mentioned in chapter 3. The width of the carbon fibre tape is 100 mm, however, the edges need to be trimmed off after the resin infusion process. Therefore, the useable width of the carbon tape is approximately 80 mm, which led to a total width of the bench-top model of 80 mm.

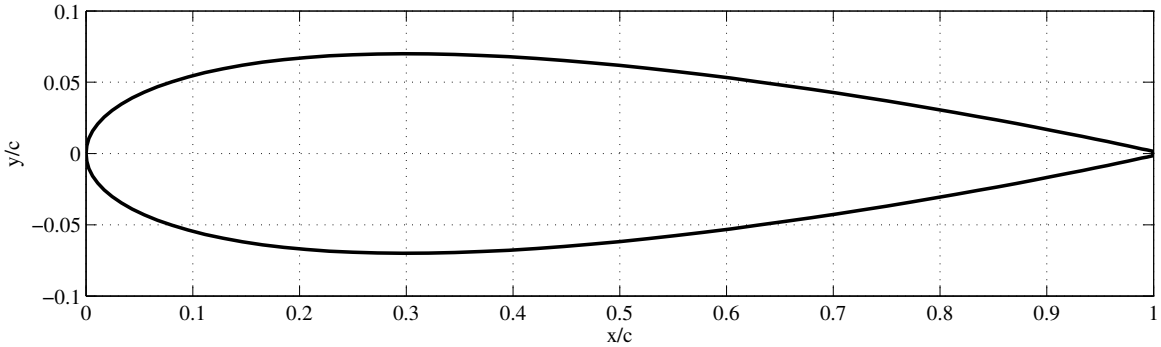


Figure 6.1: NACA 0014 aerofoil.

The bench-top model consists of a smooth upper skin and a corrugated lower skin. The carbon/polyurethane composite was initially proposed to be used for both upper and corrugated lower skin. However, in order to simplify manufacturing process and to save tooling and manufacturing costs, the upper

smooth skin was printed from a 3-D printer by Objet (Objet Connex 350™). This is the state-of-the-art printer that can print more than one materials in a single model and it also has a capability to combine more than one materials to obtain another material such as ABS-like plastic. In the current research, the material used to print the upper skin of the aerofoil model was the VeroBlack FullCure 870. The properties of this material are presented in table 6.1. The lower corrugated surface was manufactured from carbon/polyurethane composite proposed in chapter 3. The detail of the manufacturing process of each component of the bench-top model will be discussed in section 6.2.

Table 6.1: Properties of VeroBlack FullCure 870 [164].

	ASTM	**Value**
Tensile strength (MPa)	D-638-03	50 – 65
Elongation at break (%)	D-638-05	10 – 25
Modulus of elasticity (MPa)	D-638-04	2,000 – 3,000
Flexural strength (MPa)	D-790-03	75 – 110
Flexural modulus (MPa)	D-790-04	2,200 – 3,200
T_g (°C)	DMA, $E_{>>}$	52 – 54
Polymerised density (g/cm^3)	ASTM D792	1.17 – 1.18

One of the requirements outlined above is the need for a simple and cheap actuation mechanism. In the preliminary design, various types of smart actuators such as, SMAs and SMPs, piezoelectric materials, etc., were considered in order to select the most suitable one for the morphing wing application. To obtain control authority, the shape of the aerofoil should be changed rapidly. Therefore, a fast response from the actuator is required. Another factor that should be taken into consideration when selecting the actuator is the force generated by the actuator. A suitable actuator should generate sufficient force to change the shape of the aerofoil. According to the review of various types of smart materials and actuators presented in chapter 2, the actuator that is the most suitable for the adaptive wing is the piezoelectric actuator. It offers fast response and high force, and moderate stroke can be achieved by stacking the piezoelectric actuators together. In the design of the bench-top model, the extensional modulus of the corrugated skin is lower than the extensional modulus of the smooth upper skin. Based on this property, a linear actuation mechanism consisting of two actuation arms connecting the actuator to the trailing edge is proposed. This type of actuation mechanism is considered to be simple and easy to manufacture as the actuation arms can also be printed

from the 3-D printer. The linear movement of the actuator is changed into a rotational movement of the trailing edge. A number of piezoelectric linear actuators were considered. However, it was difficult to find a piezoelectric actuator that generates high force and high stroke. There was one linear actuator from Physik Instrumente [165], which provides high force and sufficient movement. The model name is N-216 NEXLINE and its photo is shown in figure 6.2. This actuator has a travel range of 20 mm and provides push/pull forces of up to 600 N. However, the limitation of this particular actuator is its price. One unit without a controller costs approximately £336, therefore, it is not suitable for the bench-top demonstrator.



Figure 6.2: N-216 NEXLINE from Physik Instrumente [165].

A new actuator was required to replace the expensive piezoelectric linear actuator. Final selection was made towards a conventional linear actuator, which is cheaper than the piezoelectric actuator. The linear actuator used to drive the actuation mechanism of the bench-top model is Firgelli L-16 with a maximum stroke of 50 mm. This actuator can be connected to and controlled by a computer via a USB port using the Firgelli Linear Actuator Controller LAC [166]. Another distinctive feature of this actuator is that it can be driven using a number of power supply types including batteries as shown in figure 6.3.

The results from the parametric study of corrugated composite structure presented in chapter 4 suggested that the trapezoidal profile has the lowest extensional stiffness among other profiles considered herein. In addition, the extensional stiffness also varies with the geometry (amplitude and unit cell

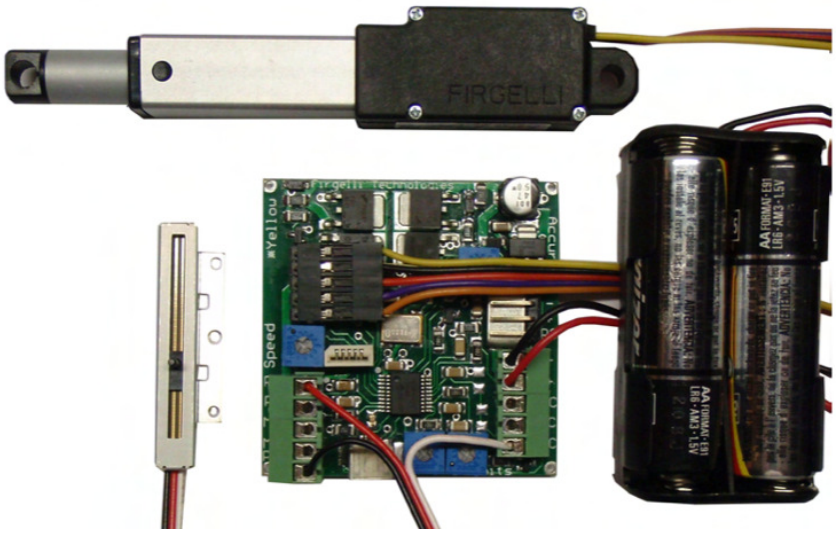


Figure 6.3: Firgelli linear actuator with controller LAC, potentiometer and batteries [166].

length) of the corrugation. As the amplitude increases, the structural stiffness decreases. Unlike the amplitude, the structural stiffness of a corrugated structure increases as the unit cell length increases. In terms of aerodynamic performance, it was discussed in chapter 5 that at Reynolds number of 280,000, the tailored corrugated skin on the pressure side outperformed the conventional smooth aerofoil. While at higher Reynolds numbers, the corrugated skin performed slightly worse than the smooth skin at low angle of attack. However, as the angle of attack increases, the lift-to-drag characteristics of the corrugated aerofoil improved to the same level as the smooth aerofoil. It should also be highlighted that the aerodynamic optimisation has not been performed to determine which corrugated profile gives the best overall performance, therefore, the design of the corrugated skin of the bench-top model presented in this chapter is largely based on the structural analysis discussed in chapter 4. The results obtained from structural and aerodynamic analyses of the corrugated structure led to a design of tailored corrugated skin of the bench-top model, having changing corrugation geometry along the chordwise direction. In order to accommodate a large movement of the skin, the trapezoidal profile was selected. However, the geometry of the corrugation varies from the spar to the trailing edge. Near the spar, less stiff corrugations are required in order to allow large movement when the actuation load is applied, therefore, high amplitude corrugations were used. Towards the trailing edge, the extensional stiffness of the corrugations can be increased gradually by reducing the amplitude of the corrugations. This also helps improve aerodynamic characteristics of the

aerofoil as the skin becomes smoother closer to the trailing edge. It should be noted that the amplitude of the corrugations is limited by the actuation arm located half way between upper and lower surfaces as discussed earlier. In order to obtain the minimum stiffness possible for a given amplitude, the unit cell length of the corrugations should also be adjusted. However, from the parametric analysis of the trapezoidal corrugation presented in chapter 4, it can be noticed that for high amplitude configuration, the structural stiffness is less sensitive to a change in the unit cell length. Therefore, the unit cell length of each corrugation was selected to be in a good proportion to the amplitude. In other words, the corrugation with large amplitude and short unit cell length should be avoided. A summary of the dimensions of each corrugation on the lower surface of the aerofoil model is presented in table 6.2 and the picture of the complete model (aft section) is shown in figure 6.4.

Table 6.2: Dimensions of the corrugated lower skin of the bench-top model.

Corrugation number	Amplitude (mm)	Unit cell length (mm)	Corner radii (mm)
1 (near spar)	7.5	7.5	2
2	7.5	7.5	2
3	7.5	7.5	2
4	5	10	2
5	5	10	2
6 (near trailing edge)	3.25	7.5	2

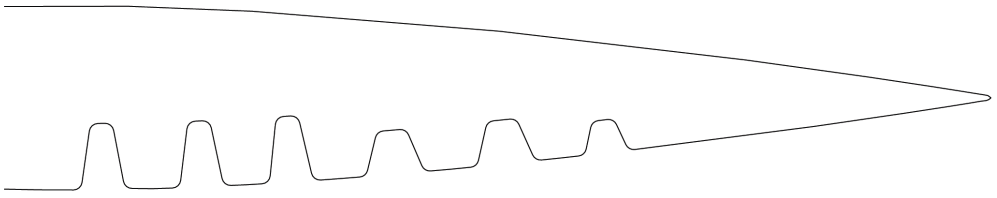


Figure 6.4: Schematic drawing of the aerofoil section with corrugated lower skin.

6.1.1 Finite element analysis of the bench-top model

To analyse the integrity of the model and to predict the force required to drive the actuation mechanism, a finite element model of the corrugated

aerofoil was generated and analysed using a finite element analysis software, ABAQUS (version 6.10). Figure 6.5 shows the finite element model of the bench-top demonstrator. It can be seen that the model is simplified such that the upper and lower surfaces were modelled as a deformable 3-D conventional shell and the actuation arms were modelled as a beam with rectangular cross-section according to the actual dimensions of the arms. The joints where the two actuation arms are connected and another joint where an actuation arm is connected to the trailing edge were modelled using the pin constraint. In order to reduce computational cost, only a half of the model was created and a symmetric boundary condition in z-direction was imposed. The ends of the upper and lower surfaces, where they are connected to the spar, were fixed, thus no translational and rotational movements are allowed. The end of the actuation arm near the spar was subjected to a restriction in translation in y- and z-directions, while the translation in x-direction was allowed as in the actual model.

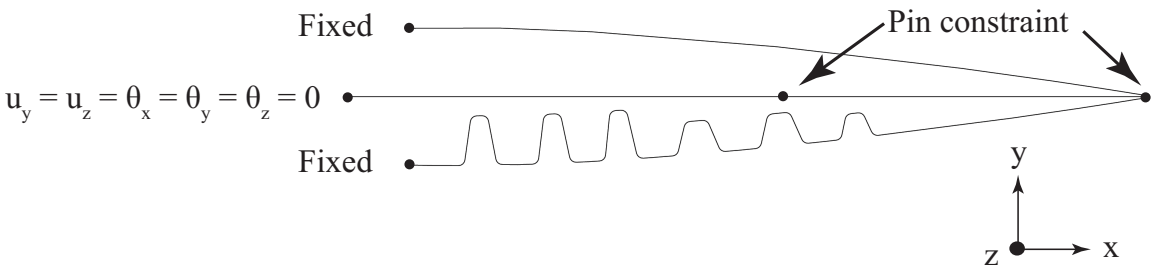


Figure 6.5: Finite element model of the bench-top demonstrator with boundary conditions.

The upper skin and the actuation beam were manufactured using the Objet 3-D printer. The material used to fabricate these components was the Vero Black FullCure 870. The material properties provided by Objet is, however, in a range between upper and lower bounds. Therefore, an average value was used in the FE model. It was assumed that the VeroBlack FullCure 870 was an isotropic material with the modulus of elasticity of 2,500 MPa and Poisson's ratio of 0.393. The thickness of the upper skin was calculated to be 3mm, which has equivalent mechanical properties as 2 plies of carbon/polyurethane composite. The corrugated lower skin was considered to be fabricated from one ply of carbon/polyurethane composite. Therefore, the mechanical properties of the composite obtained experimentally (refer to table 4.4, chapter 4) were used.

The next step in setting up the FE model is to apply the actuation load. Instead of applying a force to the actuation arm, a displacement boundary condition was applied and the reaction force was determined from the FE solution. This way, the force measured in the experiment can be compared with the FE model. To simulate a push/pull movement of the actual actuator, a displacement was applied in positive and negative x directions.

Another feature included in the FE analysis was the contact simulation between actuation arms and the skin. Three contact pairs were setup and these were the actuation arms and the skin, the actuation arms and the curved structures, and the actuation arms and the trapezoidal structures.

Once the model was created and the boundary conditions were imposed, each component of the model was meshed separately. A summary of the mesh of each instance is shown in table 6.3 and the image of the FE aerofoil model is shown in figure 6.6.

Table 6.3: A summary of the mesh of each instance of the FE aerofoil model.

Component	**Seed length (mm)**	**Element type**
Upper and lower skins	1	4-node general-purpose shell (S4)
Actuation arms	2	2-node linear beam (B31)

Figures 6.7 and 6.8 show the results of the FE model with the trailing edge deflected downwards and upwards, respectively. It should be noted that the corrugated skin bulges upwards pressing against the actuation arm when the trailing edge deflects downwards. This may cause damages to the corrugated composite skin. Therefore, soft curved structures, as shown in figure 6.9, were attached to the top skin to prevent the corrugated lower skin from pressing against the actuation arm. These curved structures were made from a rubber material (TangoBlack FullCure 970) which could be printed from the Objet 3-D printer. The TangoBlack FullCure 970 was also assumed to be an isotropic material with the modulus of elasticity of 0.3 MPa and Poisson's ratio of 0.49.

After the model was modified, the simulation was repeated and the maximum stress of each component of the bench-top demonstrator was checked to ensure no failure is caused for the full range of required trailing edge deflection.

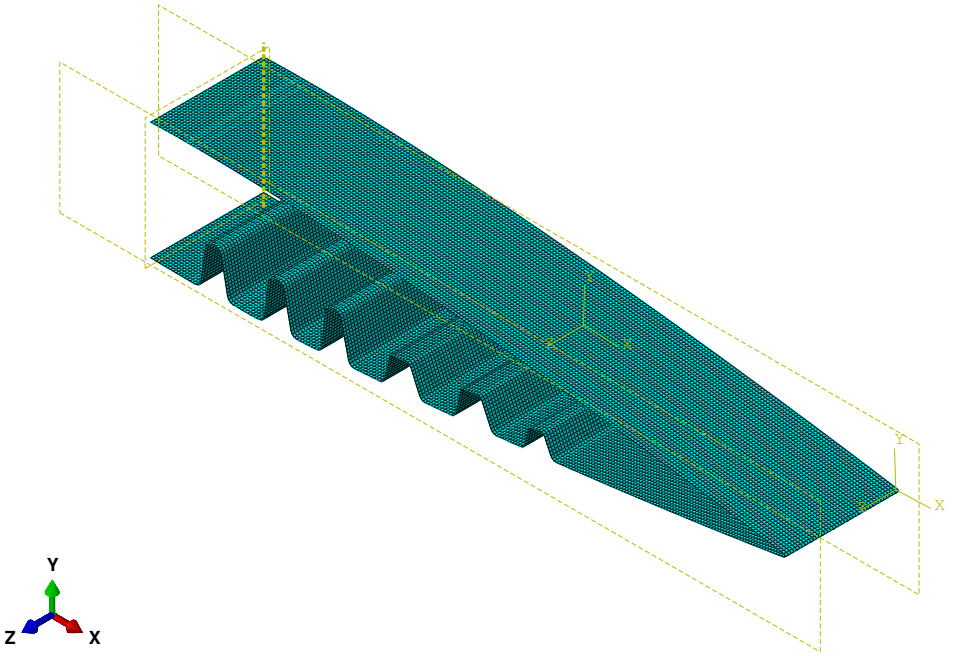


Figure 6.6: Finite element model of the bench-top demonstrator with mesh.

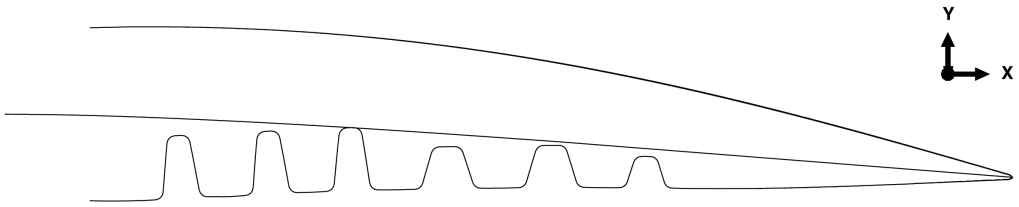


Figure 6.7: Trailing edge downwards deflection.

Corrugated skin modelling using sub-layer approach

The sub-layer approach was proposed in chapter 4 that the woven ply is considered as consisting of 2 unidirectional plies (one in 0° direction and another one in 90° direction). This approach was derived from the results of flexural tests and was thought to be useful for a single ply composite under bending. Therefore, this approach was used in the modelling of the corrugated skin of the bench-top demonstrator. The results of this approach will be compared and discussed later in section 6.3.1 of this chapter.

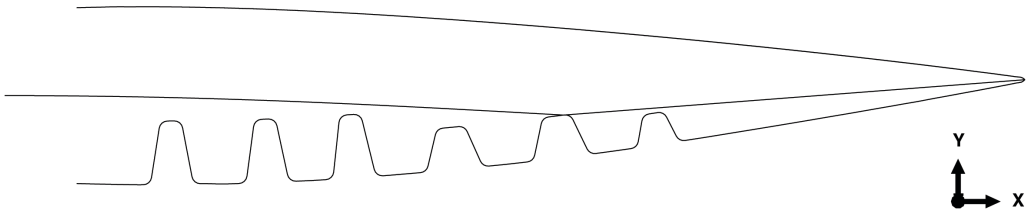


Figure 6.8: Trailing edge upwards deflection.

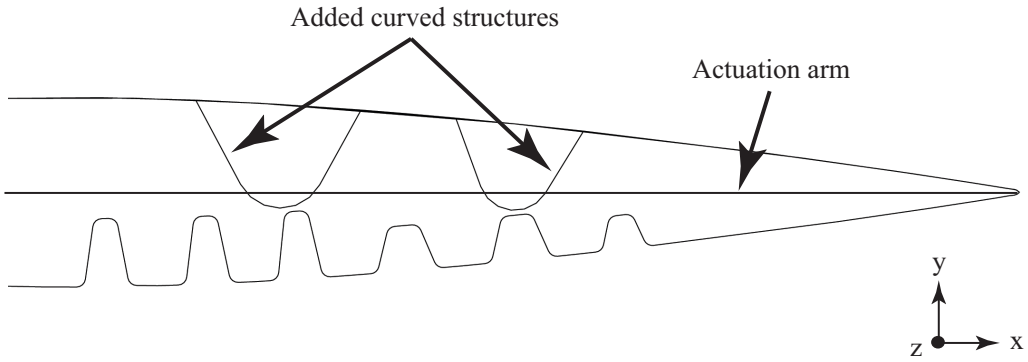


Figure 6.9: Finite element model with curved structures added to the top skin.

6.2 Manufacturing

The printed part of the bench-top demonstrator was created in Pro/Engineer (Wildfire 5.0) and submitted to the 3-D printer. One modification made to the aerofoil after the first model was printed was to add two trapezoidal structures to the top skin at the mid-span as shown in figure 6.10. This was to prevent the front actuation arm from bending upwards, while it could be prevented from bending downwards by the corrugations on the bottom skin. The trapezoidal structures were printed using the VeroBlack FullCure 870 material.

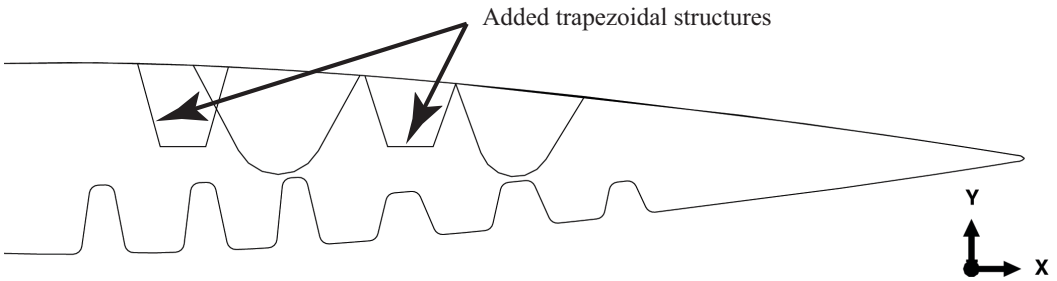


Figure 6.10: Finite element model with trapezoidal structures added to the top skin.

The corrugated laminates were manufactured using the RIFT technique

developed in chapter 4. It should be emphasised that only a single layer of carbon fibre fabric was used. The mould, as shown in figure 6.11, was machined from a polyurethane tooling block (SikaBlock®). The surface of the mould had to be treated before lamination could begin. This was done by applying the Biresin® high-temperature epoxy sealer to the surface of the mould. The sealer was applied by brush and rubbed with a cotton cloth to get a thin layer of sealer. Then the mould had to be put into an oven for 1 hour at 60°. This process was repeated for three times. The last step was to use a piece of sandpaper (grade 1200) to wet-grind the mould in order to obtain a smooth surface. Once the surface of the mould was properly prepared, PTFE spray was applied a couple of times onto the surface of the mould to ensure easy release.

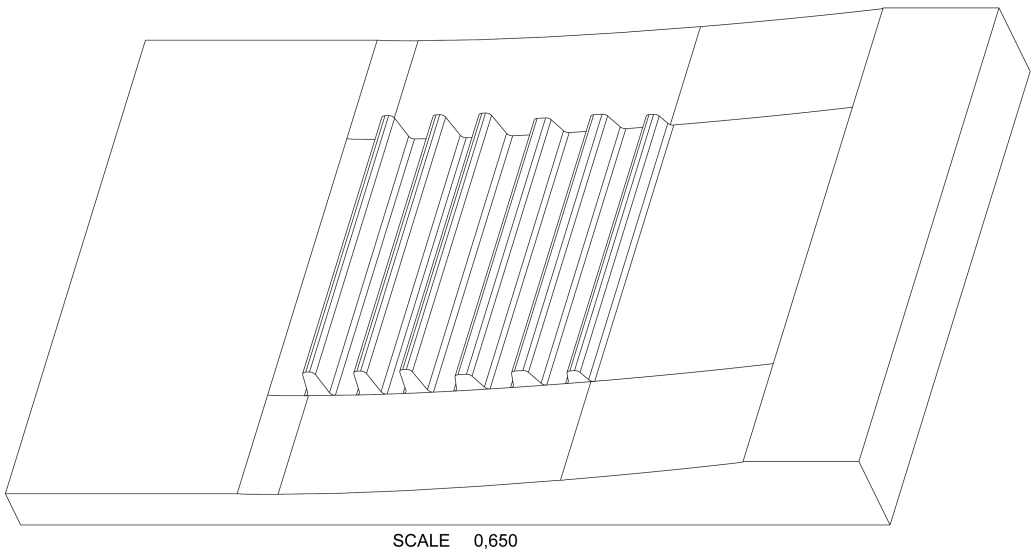


Figure 6.11: Mould used for the corrugated composite lower skin.

The RIFT process was done in a similar manner to the procedure presented in chapter 4. However, due to small radius at the corners of the trapezoidal profile, it was difficult to obtain a corrugated panel with the same quality as the sinusoidal panels presented in chapter 4. Some resin rich areas, especially at the corners were observed. If a larger radius was used, this problem could have been avoided.

The edges of the corrugated panel were trimmed by 10 mm on each side. Then it was bonded to the printed parts and the complete aerofoil was assem-

bled with the aluminium wall and base as presented in figure 6.12.

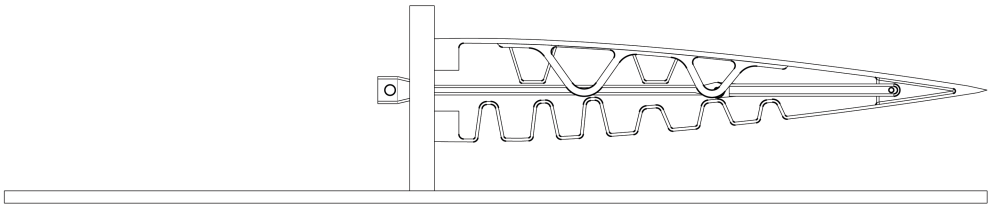


Figure 6.12: Assembly of the bench-top demonstrator.

6.3 Experimental Testing

The main purpose of the experimental testing was to evaluate the actuation force required to change the camber of the bench-top model as well as the amount of trailing edge deflection as compared to the numerical results obtained from finite element analysis.

The apparatus for the experiment consists of the wing section assembly, as shown in figure 6.12, connected to the force gauge via a rigid link to ensure accurate force measurement. The force gauge was also clamped rigidly to the test bench. The linear actuator was, then, connected to the controller, which was connected to a computer via a USB port. The speed and movement of the linear actuator could be controlled from a computer using the software provided by the manufacturer (Firgelli). The complete experimental set-up is shown in figure 6.13.

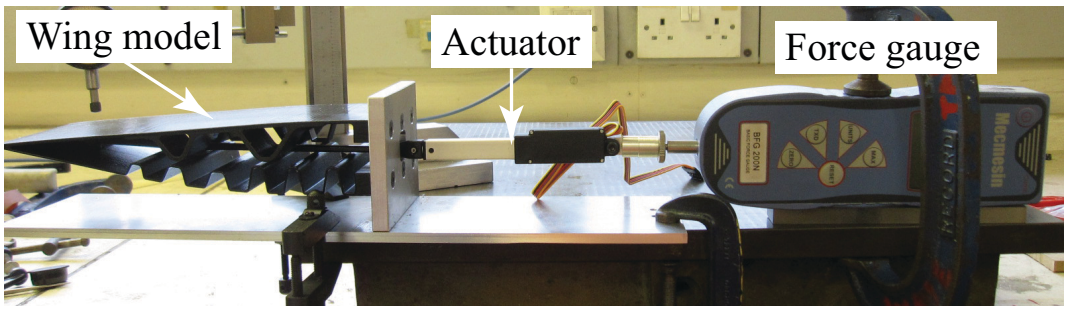


Figure 6.13: Complete setup of experimental testing of corrugated aerofoil.

In this experimental testing, three outputs were required, which are actuation force, linear movement of the actuator's arm and trailing edge deflection. The actuation force could be measured directly from the digital force gauge, and the linear movement of the actuator's arm was measured manually using a digital vernier calliper. The trailing edge deflection was measured using an optical technique. A DSLR camera was used to take a photo of the trailing edge deflection after each actuation process. Then, the images taken from the experiment were processed to obtain a deflection angle from a reference point using a free image processing software called ImageJ [167].

6.3.1 Results and discussion

The results obtained from the image processing software show that the maximum downward and upward deflections were 4 degrees and 6 degrees as shown in figures 6.14 and 6.15, respectively.

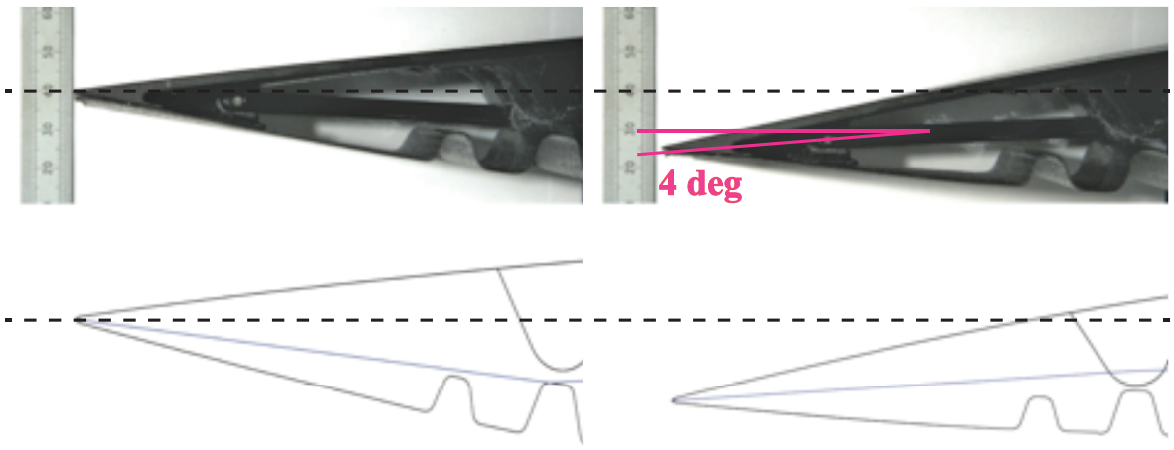


Figure 6.14: Tralling edge deflection (downward) of actual model and FE model.

Figures 6.14 and 6.15 show images of trailing edge deflection of the benchtop demonstrator from experiment and compared with images from the finite element analysis. It can be clearly observed that the trailing edge deformation between the experiment and the finite element model is similar. The downward deflection was caused by a pull force from the actuator, while a push force caused the trailing edge to deflect upward.

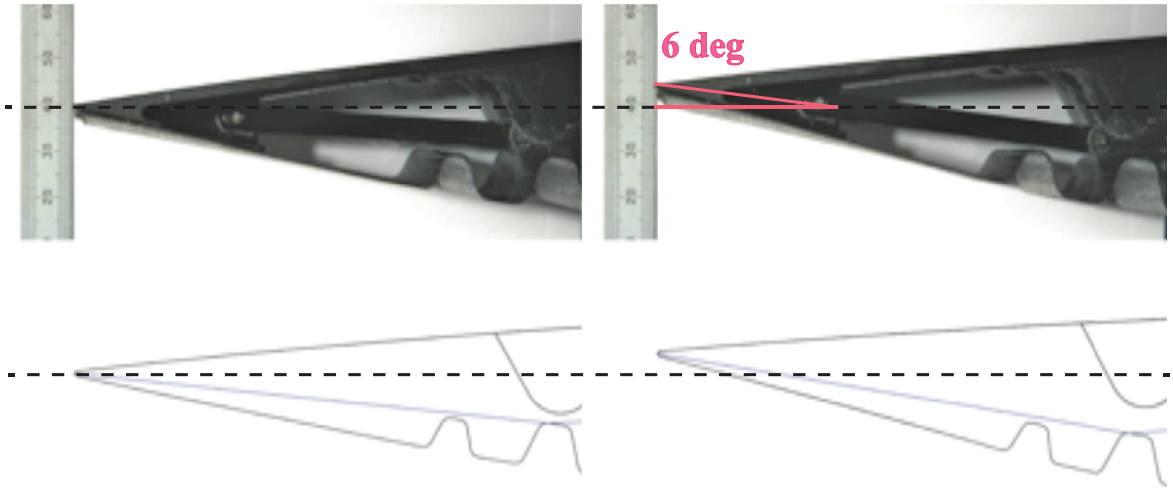


Figure 6.15: Tralling edge deflection (upward) of actual model and FE model.

The bench-top model was experimentally tested three times in order to show repeatability. Figure 6.16 shows a plot of required actuation force against movement of the actuation arms of the bench-top demonstrator. The results from the experiment are compared with the results from finite element analysis.

According to figure 6.16, the positive values on x- and y-axis indicate extension of the actuation arm and push force while the negative values show contraction of the shaft and pull force. The results from the experiment can be divided into 3 regions: 2 linear regions with positive slope and a flat region. The flat region in the experimental curves, however, does not appear in the finite element result because this part of the curves represents the flexibility in the joints of the bench-top model. Therefore, if the slack in the physical model is eliminated, the experimental results should be in a good agreement with the numerical analysis. Considering the FE curve, it can be noticed that the slope of the curve changes. This was because the actuation arm was in contact with the skin. Another feature that can be noticed from figure 6.16 is that the experimental curves from different run lie closely with each other. This confirms repeatability and structural integrity.

It can also be noticed from figure 6.16 that when the sub-layer approach was used, the relationship of the required actuation force and the movement of the actuator's shaft calculated from the finite element analysis agrees relatively well with the experimental results. This suggests that the sub-layer approach

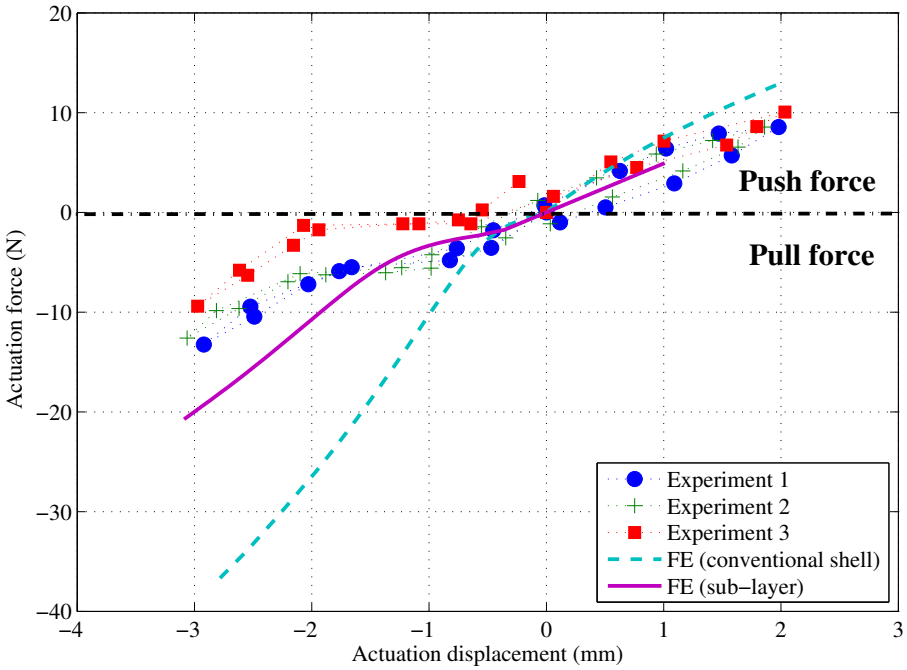


Figure 6.16: Plot of required actuation force against actuation arm movement.

derived from flexural tests is suitable for single layer composite under bending such as the corrugated skin of the bench-top demonstrator in this research.

The mechanical efficiency of the bench-top demonstrator is another parameter that is of interest. This could be evaluated through a simple experiment by hanging a known weight at the trailing edge of the aerofoil model and repeat the experiment as shown in figure 6.17. The mechanical efficiency of the bench-top demonstrator can be expressed as a ratio of work done to lift up the hanging weight to the work done by the actuator. This relationship is shown in the equation 6.1.

$$\text{Mechanical efficiency} = \frac{\text{Work done to lift the weight}}{\text{Work done by the actuator}}. \tag{6.1}$$

The work done is defined as the product of force applied to a point and the displacement of that point moved by the force in the direction of the force. In this case, the work done to lift the weight can be defined as the product of the weight and the displacement that the weight is lifted. Similarly, the work done from the actuator is the product of the force generated by the actuator and the displacement that the shaft moves. This can be summarised as follows.

$$(\text{Work done})_{\text{weight}} = \int_{\delta_0}^{\delta_1} W_g \cdot d\delta_{weight} \tag{6.2}$$

$$(\text{Work done})_{\text{actuator}} = \int_{\delta_0}^{\delta_1} F_{actuator} \cdot d\delta_{shaft} \tag{6.3}$$

where W_g is the weight of the hanging weight ($W_g = mg$) [unit: N]
$d\delta_{weight}$ is the displacement of the weight during actuation process [unit: mm]
$F_{actuator}$ is the actuation force generated by the actuator [unit: N]
$d\delta_{shaft}$ is the measured shaft displacement [unit: mm]

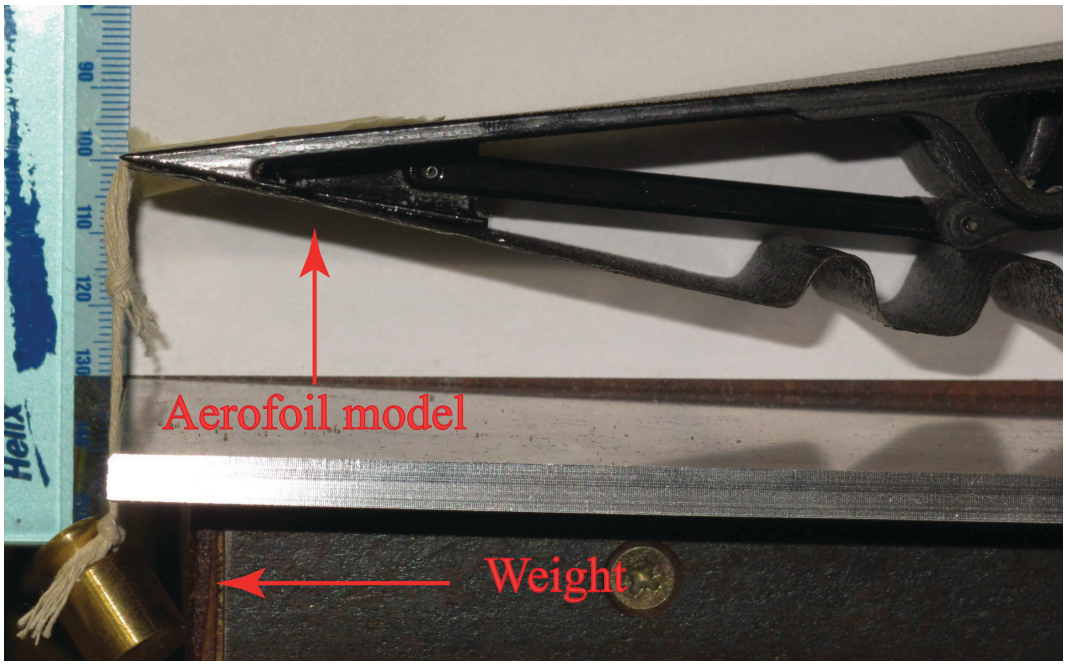


Figure 6.17: Aerofoil model with the weight attached to the trailing edge.

In this experiment, three different known weights (20g, 50g and 100g) were attached to the trailing edge in turn and the trailing edge was deflected upwards to lift the weight. Then, the measurement of the actuator's shaft movement was taken along with the reading of the actuation force. The trailing edge deflection was captured by the DSLR camera and later processed using the image processing software to determine the amount of trailing edge movement.

Table 6.4 presents the experimental results used to evaluate the mechanical efficiency of the bench-top demonstrator. The results indicate that the value of the mechanical efficiency from each run is slightly different with the average

value of 0.28. There is a number of factors that affects the results of each test.

The first factor is the accuracy of the apparatus used to measure the force and the displacement of the actuator's shaft. The precision of the force gauge is ±0.05 N. However, during the measurement the force reading fluctuates between 0.1 and 0.15 N. The accuracy of the actuator's shaft movement measured from a digital vernier calliper is ±0.03 mm. The movement of the trailing edge was determined manually using the image processing software, therefore, the accuracy of the trailing edge movement would be ±1 mm.

The second factor is the printed materials. It should be noted that the experiment was performed over a period of 3 days and it was noticed prior to the experiment that the printed materials creep, especially under direct sunlight. The printed materials are cured by the UV generated in the printer, therefore, the UV from the sunlight can also cause the material to distort even when the model is left at room temperature. At the end of the experiment the shape of the aerofoil changed slightly due to loading and creep. Therefore, the results from later tests become more inaccurate.

Table 6.4: Mechanical efficiency evaluation of the bench-top demonstrator.

Weight	**(Work done)$_{\text{weight}}$**	**(Work done)$_{\text{actuator}}$**	**Mechanical efficiency**
20g	4.90 N·mm	20.25 N·mm	0.24
50g	4.41 N·mm	20.68 N·mm	0.21
100g	10.79 N·mm	27.57 N·mm	0.39
			Average = 0.28

6.3.2 Material problems observed during the experimental testing

During the experimental testing of the aerofoil section with lower corrugated skin, it was observed that the printed materials creeps so that the shape of the aerofoil distorts. Therefore, it should be addressed that these printed materials should be used with care, especially when they are used to construct a thin or shell structure. It is recommended that these materials are replaced by stiffer materials such as ABS plastic.

6.4 Chapter Summary

In this chapter, a bench-top model consisting of a printed upper smooth skin and actuation arms, and corrugated composite lower skin was manufactured. The upper smooth skin and the actuation arm were printed from the state-of-the-art 3-D printer from Objet. The corrugated lower skin was fabricated from the carbon/polyurethane composite laminates using RIFT as discussed in chapter 4. The bench-top demonstrator represents the aft section of the aerofoil and the D-nose section was omitted. This was because the aerofoil with a fixed leading edge and a movable aft section performs aerodynamically better than the aerofoil with movable leading and trailing edge. The camber of the bench-top model was changed by driving a linear actuator. This linear actuator can be controlled using a free software provided by the manufacturer via a USB port and can be powered using batteries.

The bench-top demonstrator was experimentally tested to prove the corrugated skin concept and to illustrate structural integrity. The experimental results show that the maximum trailing edge deflection upward and downward was 6 degrees and 4 degrees, respectively. The degree of deflection was mainly limited by the internal structures such as the trapezoidal structures on each side of the top skin and the sinusoidal structure in the middle of the top skin, which restrain the movement of the wing during actuation process.

Chapter 7

Concluding Remarks

This chapter presents a summary of the main findings of this research programme and also discusses recommendations for possible further research.

7.1 Conclusions

The overall performance of an air vehicle could be enhanced if the current high-lift devices are replaced by a seamless wing which can change its shape during flight. This morphing wing idea was inspired by the wings of birds and insects, and has recently been the subject of extensive research studies around the world. Although many morphing wing concepts were proposed and discussed in the literature review presented in chapter 2, the corrugated skin concept was selected as the main focus of this research programme. As the morphing wing requires a compromise between stiffness and flexibility, the corrugated skin concept is, therefore, considered as a promising solution because the corrugated structure provides stiffness in one direction and flexibility in another.

It was decided to manufacture the corrugated skin from carbon fibre reinforced plastic and to provide sufficient compliance a polyurethane resin (Biresin® G27 LR from Sika®) was selected. A brief history and basic chemical and mechanical properties of this resin were discussed in chapter 2. The combination of carbon fibre and polyurethane resin is not a conventional composite material. Therefore, its mechanical properties are not widely available and so an evaluation of basic mechanical properties of the carbon fibre reinforced polyurethane composite flat laminates was performed and presented in chapter 3. Three types of mechanical testing, which are tensile, compression

and shear, were performed. The specimens were fabricated using the RIFT process. This is one variant of the RTM but only the bottom mould is required, while the top mould is replaced by a flexible vacuum bag. The tensile test results as well as the optical micrographs of a failed specimen suggests that the composite laminates failed because the crimped fibres were straightened and this initiated matrix cracking. In the compression test, the optical micrographs show a kink band formation caused by local shear stresses between reinforcement and the matrix. This also causes instability that leads to fibre microbuckling. The stress-strain curves obtained from the in-plane shear test exhibit nonlinearity. This is due to fibre-matrix debonding, which causes internal friction during fibre sliding under applied load.

Once the mechanical properties of carbon/polyurethane composite laminates were obtained, an analysis of the corrugated composite structure could be performed. In chapter 4, a finite element analysis of three different corrugated profiles (sinusoidal, trapezoidal and U-shape) using ABAQUS (version 6.10) was performed. In the finite element model, the properties of the surface-based cohesive behaviour were defined in order to capture delamination growth. An experimental test on sinusoidal carbon/polyurethane composite laminates was performed in order to validate the finite element model. It was found that the numerical and experimental structural stress-strain relationships agree well. Moreover, the predicted delamination growth is observed on the optical micrograph taken from a failed corrugated specimen. The finite element model and the surfaced-based cohesive behaviour were then used to parametrically investigate the effects of different corrugated profiles and corrugated geometries on the structural response of the corrugated structure under applied tensile load. The results from the parametric study suggested that the profile that has the lowest extensional stiffness is the trapezoidal profile followed by U-shape and sinusoidal, respectively. In terms of geometry, the structural stiffness of the corrugation is inversely proportional to both unit cell length and amplitude of the corrugation.

In the design process of the morphing wing with corrugated skin, one aspect that must not be overlooked is the aerodynamic performance of such wing as compared to a conventional wing. In chapter 5, a comparative study of two aerofoils (conventional aerofoil and aerofoil with lower corrugated skin) was performed. Both aerofoils were tested at four different Reynolds numbers and

different angle of attacks in order to determine the aerodynamic characteristics of each aerofoil. After the wind tunnel test was complete, lift, drag and polar plots of each aerofoil were created and compared against each other. The experimental results suggest that at Reynolds number of 280,000, the corrugated aerofoil performs similarly to the smooth aerofoil at low angle of attack in terms of lift-to-drag characteristics. At higher angle of attack, interestingly, the corrugated skin outperforms the smooth skin. However, as the Reynolds number increases, the aerodynamic performance at low angle of attack of the corrugated aerofoil is slightly worse than the smooth aerofoil while at higher angle of attack, the corrugated aerofoil performs similarly to the smooth conventional aerofoil. This is because the unsteady vortices induced in the valley sections of the corrugations energise the flow outside the troughs such that the boundary layer gains enough energy to overcome the adverse pressure gradient and flow separation is delayed. At high angle of attack, the separation point moves towards the leading edge and, as a result, the lift drops while the drag increases dramatically. The conclusion drawn from the comparative study suggests that the aerofoil with tailored corrugated skin on the pressure side is feasible for a morphing wing of a small UAV that operates at Reynolds number of approximately 10^5.

After the structural and aerodynamic analyses were complete, a bench-top demonstrator was manufactured to investigate the morphing performance of the concept. The bench-top demonstrator was initially considered to consist of a single spar and a moveable aft section, while the D-nose section was static. In order to simplify the model and to save manufacturing costs, only the aft portion of the model was manufactured. The model consists of three parts: an upper skin printed from the Objet 3-D printer, a lower corrugated skin manufactured from carbon/polyurethane composite laminates and two actuation arms also printed from the Objet 3-D printer. The actuator used to change the camber of the wing was initially considered to be a piezoelectric linear actuator. However, the cost of one unit was very high, therefore, a conventional linear actuator was purchased instead. The wing was tested experimentally to evaluate the integrity, the range of deflected shapes and the repeatability of the wing. The experimental results show that the trailing edge deflection upward and downward could reach 6 degrees and 4 degrees, respectively.

7.2 Recommendations for Future Research

In chapter 3, it was noticed during the manufacturing process of flat composite specimens that the resin flow rate during infusion is crucial. The resin infusion rate should be controlled in order to obtain consistent quality of the final product. Therefore, it is recommended that a disposable valve could be used instead of a G-clamp at the inlet to control the resin flow rate. In addition, the most suitable flow rate can also be further investigated.

The experimental and numerical testing of the corrugated composites presented in chapter 4 were performed only in tension. Additional information on the flexural response would be beneficial. Therefore, a bending test on corrugated composite specimen is recommended.

In chapter 4, the critical fracture energies of the surfaced-based cohesive behaviour used in the finite element analysis of the corrugated structures were determined numerically. However, these parameters could be obtained experimentally and, therefore, an experimental test to obtain these parameters should be performed to accurately predict the delamination growth.

The experimental results from the wind tunnel testing discussed in chapter 5 show discrepancies as compared to the analytical solution. This was due to the design of the supporting structure and the end-plates. The supporting structure contains many linkages which fluctuates during the test, especially at high angle of attack and high speed. Therefore, a redesign of the supporting structure that contains fewer, more rigid linkages is recommended. The end-plates used in the wind tunnel testing were small such that the 3-D flow affects the results. It is recommended that the splitter plates that span across the height of the test section should be used. An alternative solution would be to span the wing across the width of the wind tunnel to reduce the effects of spanwise air flow.

Although the bench-top demonstration model shows that the carbon/ polyurethane corrugated morphing wing concept works in the sense that the trailing edge of the aerofoil could be deflected up and down, the degree of deflection could be improved. In the current model, the trailing edge movement is limited by the internal structure. Therefore, if the internal structure is redesigned, the deflection of the trailing edge could be improved.

References

[1] ISO. *BS EN ISO 14125: Fibre-reinforced plastic composites - Determination of flexural properties*, 1998.

[2] G. D. Padfield and B. Lawrence. The birth of flight control - an engineering analysis of the wright brothers' 1902 glider. *The Aeronautical Journal*, 107(1078):697–718, December 2003.

[3] M.J. Abzug and E.E. Larrabee. *Airplane stability and control: a history of the technologies that made aviation possible.* Cambridge Aerospace Series. Cambridge University Press, 2005.

[4] Akhilesh K. Jha and Jayanth N. Kudva. Morphing aircraft concepts, classifications, and challenges. In *Proceedings of SPIE–the international society for optical engineering*, volume 5388, pages 213–224, 2004.

[5] L. Iannucci, M. Evans, E. Patoor, and D. Osmont. Morphing Wing Design. In *MCM-ITP Conference*, Lille, France, June 2009.

[6] A. Wickenheiser, E. Garcia, and M. Waszak. Evaluation of bio-inspired morphing concepts with regard to aircraft dynamics and performance. *Proc. SPIE*, 5390:202–211, 2004.

[7] C. Thill, J. D. Downsborough, S. J. Lai, and I. P. Bond. Aerodynamic study of corrugated skins for morphing wing applications. *The Aeronautical Journal*, 114(1154):237–244, 2010.

[8] P B S Lissaman. Low-Reynolds-Number Airfoils. *Annual Review of Fluid Mechanics*, 15(1):223–239, 1983.

[9] Masatoshi Tamai, Zhijian Wang, Ganesh Rajagopalan, Hui Hu, and Guowei He. Aerodynamic performance of a corrugated dragonfly airfoil compared with smooth airfoils at low reynolds numbers. *SciencesNew York*, 483(January):1–12, 2007.

[10] A.B. Kesel. Aerodynamic characteristics of dragonfly wing sections compared with technical aerofoils. *Journal of experimental biology*, 203(20):3125–3135, 2000.

[11] Won Kap Kim, Jin Hwan Ko, Hoon Cheol Park, and Doyoung Byun. Effects of corrugation of the dragonfly wing on gliding performance. *Journal of theoretical biology*, 260(4):523–530, 2009.

[12] S. Barbarino, O. Bilgen, R. M. Ajaj, M. I. Friswell, and D. J. Inman. A Review of Morphing Aircraft. *Journal of Intelligent Material Systems and Structures*, 22(9):823–877, 2011.

[13] Y.J.K. Ryoong. A morphing wing concept based on symmetrical composite laminates and piezoceramic MFC actuators. MSc report, Department of Aeronautics, Imperial College London, 2006.

[14] T. Bein, H. Hanselka, and E. Breitbach. An adaptive spoiler to control the transonic shock. *Smart Materials and Structures*, 9(2):141–148, 2000.

[15] C. Thill, J. Etches, I. Bond, K. Potter, and P. Weaver. Morphing skins. *Aeronautical journal*, 112(1129):117–139, 2008.

[16] Tomohiro Yokozeki, Shinichi Takeda, Toshio Ogasawara, and Takashi Ishikawa. Mechanical properties of corrugated composites for candidate materials of flexible wing structures. *Composites Part A: Applied Science and Manufacturing*, 37(10):1578–1586, 2006.

[17] C. Thill, J. A. Etches, I. P. Bond, K. D. Potter, and P. M. Weaver. Corrugated composite structures for aircraft morphing skin applications. In *18th International Conference of Adaptive Structures and Technologies*, Ottawa, Ontario, Canada, October 2007.

[18] Christophe Thill, Julie A Etches, Ian P Bond, Kevin D Potter, Paul M Weaver, and Michael R Wisnom. Investigation of trapezoidal corrugated aramid/epoxy laminates under large tensile displacements transverse to the corrugation direction. *Composites Part A Applied Science and Manufacturing*, 41(1):168–176, 2010.

[19] C. Thill, J. A. Etches, I. P. Bond, K. D. Potter, and P. M. Weaver. Experimental and parametric analysis of corrugated composite structures for morphing skin applications. In *19th International Conference*

on Adaptive Structures and Technologies, Ascona, Switzerland, October 2008.

[20] C. Thill, J. A. Etches, I. P. Bond, K. D. Potter, and P. M. Weaver. Composite corrugated structures for composite corrugated structures for morphing wing applications. *Smart Mater. Struct.*, 19(12), 2010.

[21] L. Iannucci and A. Fontanazza. Design of morphing wing structures. In *3rd SEAS DTC Technical Conference*, Edinburgh, 2008.

[22] A. Yousefi Koma and D. G. Zimcik. Applications of smart structures to aircraft for performance enhancement. *Canadian aeronautics and space journal*, 49(4):163–172, 2003.

[23] D.J. Leo. *Engineering analysis of smart materials systems*. John Wiley & Sons, 2007.

[24] J.L. Pons. *Emerging Actuator Technologies: A Micromechatronic Approach*. John Wiley & Sons, 2005.

[25] Anna-Maria R. McGowan, Dan D. Vicroy, Ronald C. Busan, and Andrew S. Hahn. Perspectives on highly adaptive or morphing aircraft. In *NATO RT AVT-168 Symposium*, Lisbon, Portugal, 2009.

[26] Jason Bowman, Brian Sanders, Bryan Cannon, Jayanth Kudva, Shiv Joshi, and Terrence Weisshaar. Development of next generation morphing aircraft structures. *Aerospace*, (April):1–10, 2007.

[27] A. M. Wickenheiser and E. Garcia. Aerodynamic modeling of morphing wings using an extended lifting-line analysis. *Journal of aircraft*, 44(1):10–16, 2007.

[28] D. Moorhouse, B. Sanders, M. von Spakovsky, and J. Butt. Benefits and design challenges of adaptive structures for morphing aircraft. *Aeronautical journal*, 110(1105):157–162, 2006.

[29] Kenneth Smith, Jeffrey Butt, and Michael R Von Spakovsky. A study of the benefits of using morphing wing technology in fighter aircraft systems. In *Proceedings of the 39th AIAA Thermophysics Conference*, pages 1–12, June 2007.

[30] R. W. Wlezien, G. C. Horner, A. R. McGowan, S. L. Padula, M. A. Scott, R. J. Silcox, and J. O. Simpson. The aircraft morphing program. In *Proceedings of SPIE*, volume 30, pages 176–187. SPIE, 1998.

[31] B. D. Roth and W. A. Crossley. Application of optimization techniques in the conceptual design of morphing aircraft. In *AIAA's 3rd Annual Aviation Technology, Integration, and Operations (ATIO) Tech*, Denver, Colorado, USA, 2003.

[32] Brian Roth, Chris Peters, and William A Crossley. Aircraft sizing with morphing as an independent variable: Motivation, strategies and investigations. In *48th AIAA/ASME/ASCE/AHS/ASC Structures, Structural Dynamics and Materials Conference*, Honolulu, Hawaii, USA, 2007.

[33] J.J. Spillman. The use of variable camber to reduce drag, weight and costs of transport aircraft. *The Aeronautical Journal*, 96(951):1–9, 1992.

[34] Shiv Joshi, Sekaripuram Ramakrishnan, Zeb Tidwell, and William Crossley. Comparison of morphing wing strategies based upon aircraft performance impacts. *A Collection of technical papers - AIAA/ASME/ASCE/AHS Structures, Structural Dynamics, and Materials Conference*, 3:2348–2354, 2004.

[35] A. R. Rodriguez. Morphing aircraft technology survey. In *45th AIAA Aerospace Sciences Meeting and Exhibition*, Reno, Nevada, USA, 2007.

[36] G. Reich and B. Sanders. Introduction to morphing aircraft research. *Journal of Aircraft*, 44(4):1059, 2007.

[37] E Pendleton. Back to the future – How active aeroelastic wings are a return to aviation's beginnings and a small step to future bird-like wings. In *RTO AVT Symposium on Active Control Technology for Enhanced Performance Operational Capabilities of Military Aircraft Land Vehicles and Sea Vehicles*, number RTO MP-051, pages K3–1–K3–7. NATO Research and Technology Organization, 2000.

[38] P. A. Toensmeier. Radical departure. *Aviation Week and Space Technology*, 162(21):72–73, May 2005.

[39] H.F. Parker. The Parker variable camber wing. Report No. 77, NACA, 1920.

[40] Anna-Maria R McGowan, David E Cox, Barry S Lazos, Martin R Waszak, David L Raney, Emilie J Siochi, and S Paul Pao. Biologically-Inspired Technologies in NASA's Morphing Project. *Structures and Materials*, 5051:1–13, 2003.

[41] Anna-Maria R. McGowan, Anthony E. Washburn, Lucas G. Horta, Robert G. Bryant, David E. Cox, Emilie J. Siochi, Sharon L. Padula, and Nancy M. Holloway. Recent results from NASA's morphing project. In *Proceedings of SPIE*, volume 4698, pages 97–111. SPIE, 2002.

[42] NASA. `http://www.nasa.gov/centers/dryden/multimedia/imagegallery/Morph/index.html`, 2010 Last accessed April 2012.

[43] Peter Weiss. Wings of change. *Science News*, 164(23):pp. 359+362+365, 2003.

[44] R. W. DeCamp and R. Hardy. Mission Adaptive Wing Advanced Research Concepts. In *Proceedings of the AIAA Atmospheric Flight Mechanics Conference*, 1984.

[45] R. R. Larson. AFTI/F-111 MAW Flight control system and redundancy management desription. Technical memorandum NASA TM-88267, NASA, February 1987.

[46] John W Smith, Wilton P Lock, and Gordon A Payne. Variable-camber systems integration and operational performance of the AFTI/F-111 Mission Adaptive Wing. Technical memorandum NASA TM-4370, NASA, April 1992.

[47] S. B. Smith and D. W. Nelson. Determination of the aerodynamic characteristics of the mission adaptive wing. *Journal of Aircraft*, 27:950–958, 1990.

[48] USAF. AFTI/F-111 Mission Adaptive Wing briefing to industry. Technical report AFWAL-TR-88-3082, U.S. Air Force Wright Aeronautical Laboratories, October 1988.

[49] David Voracek, Ed Pendleton, Eric Reichenbach, Kenneth Griffin, and Leslie Welch. The Active Aeroelastic Wing phase I flight research through January 2003. Technical memorandum NASA/TM-2003-210741, NASA, April 2003.

[50] Edmund W Pendleton, Denis Bessette, Peter B Field, Gerald D Miller, and Kenneth E Griffin. Active Aeroelastic Wing flight research program: Technical program and model analytical development. *Journal of Aircraft*, 37(4):554–561, 2000.

[51] E Pendleton, K Griffin, M W Kehoe, and B Perry. A flight research program for active aeroelastic wing technology. In *IFASD International Forum on Aeroelasticity and Structural Dynamics*, June 2007.

[52] R. Clarke, M. J. Allen, R. P. Dibley, J. Gera, and J. Hodgkinson. Flight test of the F/A-18 Active Aeroelastic Wing airplane. In *Proceedings of AIAA Atmospheric Flight Mechanics Conference and Exhibit*, San Francisco, California, USA, August 2005.

[53] J. N. Kudva. Overview of the DARPA smart wing project. *Journal of intelligent material systems and structures*, 15(4):261–267, 2004.

[54] A P Jardine, J D Bartley-Cho, and J S Flanagan. Improved design and performance of the SMA torque tube for the DARPA Smart Wing Program. In *Proceedings of SPIE*, volume 3674, pages 260–269, 1999.

[55] Jayanth N. Kudva, Brian P. Sanders, Jennifer L. Pinkerton-Florance, and Ephrahim Garcia. DARPA/AFRL/NASA Smart Wing program: final overview. In *Smart Structures and Materials 2002: Industrial and Commercial Applications of Smart Structures Technologies*, volume 4698 of *Proc. SPIE*, pages 37–43, 2002.

[56] Jonathan D Bartley-Cho, Donny P Wang, Christopher A Martin, Jayanth N Kudva, and Mark N West. Development of high-rate, adaptive trailing edge control surface for the Smart Wing phase 2 wind tunnel model. *Journal of Intelligent Materials Systems and Structures*, 15(4):279–291, 2004.

[57] Brian Sanders, Dave Cowan, and Lewes Scherer. Aerodynamic performance of the smart wing control effectors. *Journal of Intelligent Materials Systems and Structures*, 15(4):293–303, 2004.

[58] J P Florance, A W Burner, G A Fleming, C A Hunter, S S Graves, and C A Martin. Contributions of The NASA Langley Research Center to the DARPA/AFRL/NASA/Northrop Grumman Smart Wing Program. In *AIAA Dynamics Specialists Conference*, Norfolk, Virginia, USA, 2003.

[59] R. G. Musgrove. Eccentric actuator. United States Patent 4,286,761, September 1981.

[60] R. G. Musgrove. Apparatus for producing pivotal movement. United States Patent 3,944,170, March 1976.

[61] Derek R Bye and Paul D McClure. Design of a morphing vehicle. In *48th AIAA/ASME/ASCE/AHS/ASC Structures, Structural Dynamics and Materials Conference*, Honolulu, Hawaii, USA, 2007.

[62] M H Love, P S Zink, R L Stroud, D R Bye, S Rizk, and D White. Demonstration of morphing technology through ground and wind tunnel tests. In *48th AIAA/ASME/ASCE/AHS/ASC Structures, Structural Dynamics and Materials Conference*, Honolulu, Hawaii, USA, April 2007.

[63] T G Ivanco, R C Scott, M H Love, S Zink, and T A Weisshaar. Validation of the Lockheed Martin morphing concept with wind tunnel testing. In *48th AIAA/ASME/ASCE/AHS/ASC Structures, Structural Dynamics and Materials Conference*, Honolulu, Hawaii, USA, 2007.

[64] J Flanagan, R Strutzenberg, R Myers, and J Rodrian. Development and flight testing of a morphing aircraft, the NextGen MFX-1. In *48th AIAA/ASME/ASCE/AHS/ASC Structures, Structural Dynamics and Materials Conference*, Honolulu, Hawaii, USA, 2007.

[65] G R Andersen, D L Cowan, and D J Piatak. Aeroelastic modeling, analysis and testing of a morphing wing structure. In *48th AIAA/ASME/ASCE/AHS/ASC Structures, Structural Dynamics and Materials Conference*, Honolulu, Hawaii, USA, 2007.

[66] NextGen Aeronautics. `http://www.nextgenaero.com/`, 2007, Last accessed April 2012.

[67] FlexSys Inc. `http://www.flxsys.com/`, 2012, Last accessed April 2012.

[68] Sridhar Kota. Design and application of compliant mechanisms for morphing aircraft structures. In *Proceedings of SPIE*, volume 5054, pages 24–33. SPIE, 2003.

[69] Joel A Hetrick, Russell F Osborn, Sridhar Kota, Peter M Flick, and Donald B Paul. Flight Testing of Mission Adaptive Compliant Wing. In *48th AIAA/ASME/ASCE/AHS/ASC Structures, Structural Dynamics and Materials Conference*, Honolulu, Hawaii, USA, 2007.

[70] S. Vasista, L. Tong, and K. C. Wong. Realization of morphing wings: A multidisciplinary challenge. *Journal of Aircraft*, 49(1):11–28, 2012.

[71] M P Bendsøe and O Sigmund. *Topology optimization: theory, methods, and applications*. Springer Verlag, 2nd edition, 2003.

[72] Liu Shili, Ge Wenjie, and Li Shujun. Optimal design of compliant trailing edge for shape changing. *Chinese Journal of Aeronautics*, 21(2):187–192, 2008.

[73] M Santer and S Pellegrino. Topological optimization of compliant adaptive wing structure. *AIAA Journal*, 47(3):523–534, 2009.

[74] Lucio F Campanile. Belt-rib concept for variable-camber airfoils: recent developments. In *Proceedings of SPIE*, volume 3985, pages 110–120, 2000.

[75] Lucio F Campanile and D Sachau. Belt-rib concept: A structronic approach to variable camber. *Journal of Intelligent Material Systems and Structures*, 11(3):215–224, 2000.

[76] L Campanile and S Anders. Aerodynamic and aeroelastic amplification in adaptive belt-rib airfoils. *Aerospace Science and Technology*, 9(1):55–63, 2005.

[77] Hans Peter Monner, E. Breitbach, T. Bein, and H. Hanselka. Design aspects of the adaptive wing – the elastic trailing edge and the local spoiler bump. *The Aeronautical Journal*, 104(1032):89–95, 2000.

[78] Hans Peter Monner. Realization of an optimized wing camber by using formvariable flap structures. *Aerospace Science and Technology*, 5(7):445–455, 2001.

[79] Leonard D Wiggins, Matthew D Stubbs, Christopher O Johnston, Harry H Robertshaw, Charles F Reinholtz, and Daniel J Inman. A design and analysis of a morphing Hyper-Elliptic Cambered Span (HECS) wing. In *45th AIAA/ASME/ASCE/AHS/ASC Structures, Structural Dynamics and Materials Conference*, Palm Springs, California, USA, 2004.

[80] Matthew D Stubbs. Kinematic design and analysis of a morphing wing. Master's thesis, Virginia Polytechnic Institute and State University, Blacksburg, Virginia, USA, December 2003.

[81] B S Lazos and K D Visser. Aerodynamic comparison of Hyper-Elliptic Cambered Span (hecs) wings with conventional configurations. In *Proceedings of the 24th AIAA Applied Aerodynamics Conference*, volume 42, pages 1614–1620, 2006.

[82] Deepak Ramrakhyani, Smita Bharti, Mary Frecker, and George Lesieutre. Aircraft structural morphing using tendon-actuated compliant cellular trusses. *Journal of Aircraft*, 42(6):1614–1620, 2005.

[83] Shawn E Gano and John E Renaud. Optimized unmanned aerial vehicle with wing morphing for extended range and endurance. In *9th AIAA/ISSMO Symposium and Exhibit on Multidisciplinary Analysis and Optimization*, September 2002.

[84] R. S. Lakes. Deformation mechanisms in negative Poisson's ratio materials: structural aspects. *Journal of Materials Science*, 26(9):2287–2292, 1991.

[85] D. Prall and R. S. Lakes. Properties of a chiral honeycomb with a Poisson's ratio of -1. *International Journal of Mechanical Sciences*, 39(3):305–314, 1996.

[86] Alessandro Spadoni, Massimo Ruzzene, and F. Scarpa. Dynamic response of chiral truss-core assemblies. *Journal of Intelligent Materials Systems and Structures*, 17(11):941–952, 2006.

[87] D. Bornengo, F. Scarpa, and C. Remillat. Evaluation of hexagonal chiral structure for morphing airfoil concept. In *Proceedings of the Institution of Mechanical Engineers, Part G: Journal of Aerospace Engineering*, volume 219, pages 185–192, 2005.

[88] Jamie Martin, Jean-Jacques Heyder-Bruckner, Chrystel Remillat, Fabrizio Scarpa, Kevin Potter, and Massimo Ruzzene. The hexachiral prismatic wingbox concept. *Physica Status Solidi (b)*, 245(3):570–577, 2008.

[89] Alessandro Spadoni and Massimo Ruzzene. Static aeroelastic response of chiral-core airfoils. *Journal of Intelligent Material Systems and Structures*, 18:1067–1075, 2007.

[90] Alessandro Spadoni and Massimo Ruzzene. Numerical and experimental analysis of the static compliance of chiral truss-core airfoils. *Journal of Mechanics of Materials and Structures*, 2(5):965–981, 2007.

[91] Paolo Bettini, Alessandro Airoldi, Giuseppe Sala, Luca Di Landro, Massimo Ruzzene, and Alessandro Spadoni. Composite chiral structures for morphing airfoils: Numerical analyses and development of a manufacturing process. *Composites Part B Engineering*, 41(2):133–147, 2010.

[92] R. G. Loewy. Recent developments in smart structures with aeronautical applications. *Smart Materials and Structures*, 6(5):R11–R42, 1997.

[93] M. C. Ray and N. Mallik. Finite element analysis of smart structures containing piezoelectric fiber-reinforced composite actuator. *AIAA Journal*, 42(7):1398–1405, 2004.

[94] D Varelis and D A Saravanos. Mechanics and finite element for nonlinear response of active laminated piezoelectric plates. *AIAA Journal*, 42(6):1227–1235, 2004.

[95] Marc Behl and Andreas Lendlein. Shape-memory polymers. *Materials Today*, 10(4):20–28, 2007.

[96] Cornerstone Research Group. `http://www.crgrp.com/`, 2011, Last accessed May 2012.

[97] C. S. Loh, H. Yokoi, and T. Arai. New shape memory alloy actuator: Design and application in the prosthetic hand. In *Proceedings of 2005 IEEE Engineering in Medicine and Biology 27th Annual Conference*, Shanghai, China, September 2005.

[98] C. Mavroidis. Development of advanced actuators using shape memory alloys and electrorheological fluids. *Research in Nondestructive Evaluation*, 14:1–32, 2002.

[99] T. James, A. Menner, A. Bismarck, and L. Iannucci. Morphing skins: Development of new hybrid materials. In *Proceedings of Fourth Annual Conference*. SEAS DTC, July 2009.

[100] Woo Ram. Kang, Eun Ho. Kim, Min Soo. Jeong, In. Lee, and Seok Min Ahn. Morphing wing mechanism using an SMA wire actuator. *International Journal of Aeronautical and Space Sciences*, 13(1):58–63, 2012.

[101] Gangbing Song and Ning Ma. Robust control of a shape memory alloy wire actuated flap. *Smart Materials and Structures*, 16(6):N51–N57, 2007.

[102] Yoseph Bar-Cohen. *Electroactive Polymers (EAP) Actuators as Artificial Mucles Reality, Potential and Challenges*, volume PM136. SPIE PRESS, 2004.

[103] Q. M. Zhang, C. Huang, F. Xia, and J. Su. *Electric EAP*, chapter 4, pages 95–148. Electroactive Polymer (EAP) Actuators as Artificial Muscles. SPIE PRESS, 2nd edition, 2004.

[104] R Samatham, K J Kim, D Dogruer, H R Choi, M Konyo, and J D Madden. *Active Polymers : An Overview*, chapter 1, pages 1–36. Electroactive Polymers for Robotic Applications. Springer London, 2007.

[105] Michael I Friswell and Daniel J Inman. Morphing Concepts for UAVs. In *21st Bristol UAV Systems Conference*, Bristol, UK, 2006.

[106] F Mattioni, P Weaver, K Potter, and M Friswell. Analysis of thermally induced multistable composites. *International Journal of Solids and Structures*, 45(2):657–675, 2008.

[107] Peter Giddings, Christopher Bowen, Aki Salo, H Alicia Kim, and Alan Ive. Bistable composite laminates: effects of laminate composition on cured-shape and response to thermal load. *Composite Structures*, 92(9):2220–2225, 2010.

[108] P Giddings, C R Bowen, R Butler, and H A Kim. Characterisation of actuation properties of piezoelectric bi-stable carbon-fibre laminates. *Composites Part A Applied Science and Manufacturing*, 39(4):697–703, 2008.

[109] C. R. Bowen, R. Butler, R. Jervis, H. A. Kim, and A. I. T. Salo. Morphing and shape control using unsymmetrical composites. *Journal of Intelligent Material Systems and Structures*, 18(1):89–98, 2007.

[110] P Portela, P Camanho, P Weaver, and I Bond. Analysis of morphing, multi stable structures actuated by piezoelectric patches. *Computers & Structures*, 86(3–5):347–356, 2008.

[111] F Mattioni, A Gatto, P M Weaver, M I Friswell, and K D Potter. The application of residual stress tailoring of snap-through composites for variable sweep wings. In *47th AIAA/ASME/ASCE/AHS/ASC Structures, Structural Dynamics and Materials Conference*, Newport, Rhode Island, USA, 2006.

[112] Hiroshi Kobayashi, Chikara Yamaguchi, and Akira Nishizawa. Aerodynamic characteristics of variable camber composite wing. In *Fifth International Symposium on Advanced Fluid Information (AFI-2005) - IFS-JAXA Joint Symposium*, Sendai, Japan, 2005.

[113] Michael Thomas Kikuta. Mechanical properties of candidate materials for morphing wings. Master's thesis, Virginia Polytechnic Institute and State University, December 2003.

[114] W. Meckel, W. Goyert, and W. Wieder. *Thermoplastic Elastomers*. Hanser Publishers, 1996.

[115] O. Bayer, H. Rinke, W. Siefken, L. Ortner, and H. Schild. German Patent DE 728 981 to I.G. Farben, 1937.

[116] R. E. Christ and W. E. Hanford. Treatment of polyesters such as those for sheets treatment of polyesters such as those for sheets or coatings. U.S. Patent 2,333,639 to DuPont, 1940.

[117] D. H. Coffey, J. G. Cook, and W. H. Lake. Synthetic polymeric materials. British Patent GB 574 134, to ICI Ltd, 1945.

[118] J.G. Drobny. *Handbook of Thermoplastic Elastomers*. PDL handbook series. William Andrew Pub., 2007.

[119] Günter Oertel. *Polyurethane handbook : chemistry, raw materials, processing, application, properties*. Carl Hanser, GmbH & Co., 2nd edition, 1993.

[120] I. Clemitson. *Castable Polyurethane Elastomers*. CRC Press, 2008.

[121] Thor L. Smith. Strength of elastomers—a perspective. *Polymer Engineering & Science*, 17(3):129–143, March 1977.

[122] Geoffrey Arthur Haggis, Michael Edward Benet Jones, and Michael Horace Knight. Carbon fibre-reinforced polyurethane composites. U.S. Patent 3,669,920 to ICI, 1972.

[123] Takao Fukami and Yoshizumi Kataoka. Composition superior in quick-curing for fiber-reinforced polyurethane resin. U.S. Patent 5,234,975 to Nippon Polyurethane Industry, 1993.

[124] Jenő Borda, Sándor Kéki, Istvánné Ráthy, Ildikó Bodnár, and Miklós Zsuga. Novel polyurethane elastomer continuous carbon fiber composites: Preparation and characterization. *Journal of Applied Polymer Science*, 103(1):287–292, 2007.

[125] G. Shonaike and T. Matsuo. Fabrication and mechanical properties of glass fibre reinforced thermoplastic elastomer composite. *Composite Structures*, 32:445–451, 1995.

[126] Larry D. Peel. *Fabrication and Mechanics of Fiber-Reinforced Elastomers*. PhD thesis, Brigham Young University, December 1998.

[127] Larry D. Peel and David W Jensen. The response of fiber-reinforced elastomers under simple tension. *Journal of Composite Materials*, 35(2):96–137, 2001.

[128] E A Bubert, B K S Woods, C S Kothera, and N M Wereley. Design and fabrication of a passive 1-D morphing aircraft skin. In *49th AIAA/ASME/ASCE/AHS/ASC Structures, Structural Dynamics and Materials Conference*, Schaumburg, Illinois, USA, 2008.

[129] Larry D Peel, James Mejia, Ben Narvaez, Kyle Thompson, and Madhuri Lingala. Development of a simple morphing wing using elastomeric composites as skins and actuators. *Journal of Mechanical Design*, 131(9):091003–1–091003–8, September 2009.

[130] J Summerscales and T J Searle. Low-pressure (vacuum infusion) techniques for moulding large composite structures. *Proceedings of the I MECH E Part L Journal of MaterialsDesign and Applications*, 219(1):45–58, 2005.

[131] Christopher Williams, John Summerscales, and Stephen Grove. Resin infusion a review under flexible tooling (RIFT). *Composites*, Part A(7):517–524, 1996.

[132] D. Abraham, S. Matthews, and McIlhagger R. A comparison of physical properties of glass fibre epoxy composites produced by wet lay-up with autoclave consolidation and resin transfer moulding. *Composites Part A: Applied Science and Manufacturing*, 29(7):795–801, 1998.

[133] Kirk Tackitt and Shawn Walsh. Experimental study of thickness gradient formation in the vartm process. *Materials and Manufacturing Processes*, 20(4), 2005.

[134] Hexcel. *Hexflow RTM 6 Product Data*. Available from `http://hexflow.com/Resources/DataSheets/RTM-Data-Sheets/RTM6_global.pdf`, Last accessed June 2012.

[135] West Coast Polychem Pvt. Ltd. `http://www.westcoastpolychem.com/products_adiprene.html`, 2009, Last accessed June 2012.

[136] Sika Deutschland GmbH. *Biresin® Biresin G27 LR Product Data*. Available from `http://www.johnburn.co.uk/docs/datasheets/Biresin%20G27%20LR%20PU%20Vac-casting%20[1].pdf`, 2008, Last accessed June 2012.

[137] Gurit Ltd. 0/90° Fabrics. Available from `http://www.gurit.com`, 2012, Last accessed June 2012.

[138] Eurocarbon. Certificate of Conformance (Art. Nr. 180, Carbon Tape). 2002, Retrieved via private communication in October 2011.

[139] ISO. *BS EN ISO 527-1: Plastics. Determination of tensile properties. General principles*, 1996.

[140] ISO. *BS EN ISO 527-4: Plastics. Determination of tensile properties. Test conditions for isotropic and orthotropic fibre-reinforced plastic composites*, 1997.

[141] ISO. *BS EN ISO 14129: Fibre-reinforced plastic composites. Determination of the in-plane shear stress/shear strain response, including the in-plane shear modulus and strength by the ±45° tension test method*, 1998.

[142] J. M. Hodgkinson. *Mechanical testing of advanced fibre composites*. CRC Press, 2000.

[143] ISO. *BS EN ISO 527-2: Plastics. Determination of tensile properties. Test conditions for moulding and extrusion plastics*, 1994.

[144] S R Kalidindi and A Abusafieh. Accurate characterization of machine compliance for simple compression testing. *Experimental Mechanics*, 37(2):210–215, 1997.

[145] E. Huerta, J. E. Corona, and A. I. Oliva. Universal testing machine for mechanical properties of thin materials. *Revista Mexicana de Física*, 56(4):317–322, August 2010.

[146] D Briassoulis. Equivalent orthotropic properties of corrugated sheets. *Computers & Structures*, 23(2):129–138, 1986.

[147] Richard A Shimansky and Milind M Lele. Transverse Stiffness of a Sinusoidally Corrugated Plate. *Mechanics of Structures and Machines*, 23(3):439–451, 1995.

[148] G. Kress and M. Winkler. Corrugated laminate homogenization model. *Composite structures*, 92(3):795–810, 2010.

[149] Y. Xia, M.I. Friswell, and E.I. Saavedra Flores. Equivalent models of corrugated panels. *International Journal of Solids and Structures*, 49(13):1453 – 1462, 2012.

[150] SIMULIA. *ABAQUS 6.10 Analysis User's Manual Volume 4*. Dassualt Systémes, USA.

[151] SIMULIA. *ABAQUS 6.10 Analysis User's Manual Volume 5*. Dassualt Systémes, USA.

[152] P.P. Camanho, C.G. Dávila, and M.F. de Moura. Numerical simulation of mixed-mode progressive delamination in composite materials. *Journal of Composite Materials*, 37(16):1415–1438, 2003.

[153] Jesper Ankersen. Private communication, November 2011.

[154] A. Turon, C. Dávila, P. Camanho, and J. Costa. An engineering solution for mesh size effects in the simulation of delamination using cohesive zone models. *Engineering Fracture Mechanics*, 74(10):1665–1682, 2007.

[155] J. Ankersen and G. A. O. Davies. Interface elements - advantages and limitations in CFRP delamination modelling. In *International conference on composite*, volume 17, 2009.

[156] Asokendu Samanta and Madhujit Mukhopadhyay. Finite element static and dynamic analyses of folded plates. *Engineering Structures*, 21(3):277–287, 1999.

[157] Andrea Mazzola. *Low Reynolds number aerodynamics : computational study of the aerodynamic characteristics of a dragonfly aerofoil*. VDM Verlag, 2009.

[158] M.S. Selig and B.D. McGranahan. Wind tunnel aerodynamic tests of six airfoils for use on small wind turbines. Technical Report NREL/SR-500-34515, National Renewable Energy Laboratory (NREL), 2004.

[159] John David Anderson. *Fundamentals of aerodynamics*. McGraw-Hill, 5th edition, 2011.

[160] Alan Pope. *Wind-tunnel testing*. Wiley; Chapman & Hall, 2nd edition, 1954.

[161] Mark Drela. `http://web.mit.edu/drela/Public/web/xfoil/`, 2008 Last accessed November 2012.

[162] AeroFoil Engineering. `http://www.aerofoilengineering.com`, November 2010, Last accessed August 2012.

[163] Lahiru Ranasinghe. Morphing wing studies. MSc report, Imperial College London, 2011.

[164] Objet Ltd., `http://www.objet.com`. *Materials Data Sheets*, Last accessed August, 2012.

[165] Physik Instrumente. `http://www.physikinstrumente.com/en/products/prdetail.php?sortnr=1000765`, Last accessed December 2012.

[166] Firgelli Technology Inc., Canada. *Firgelli USB Control and Configuration*.

[167] National Institutes of Health. `http://rsbweb.nih.gov/ij/disclaimer.html`, 2004 Last accessed November 2012.

Appendix A

Experimental Test Results of Flat Specimens

This appendix presents raw experimental test results of flat carbon/polyurethane composite laminates in tension, compression and in-plane shear. In addition, evaluation of testing machine compliance and tensile test results of neat resin are also presented.

A.1 Tensile Test

The tensile test of flat carbon/polyurethane composite laminates was performed in accordance to ISO 527 part 1 [139] and part 4 [140] standards in two directions: warp and weft. In each direction, a biaxial strain gauge was used to measure the strain at 0° and 90° directions. Straight-sided specimens with end-tabs were manufactured and the dimensions of the specimens are provided in table A.1.

Figures A.1 and A.2 show stress-strain relationship of carbon/polyurethane composite laminates in the warp direction at 0° and 90°, respectively.

Figures A.3 and A.4 show the stress-strain curves of the carbon/polyurethane composite laminates in the weft direction at 0° and 90°, respectively.

Table A.1: Dimensions of flat tensile specimens

Type of test **Standards**	**Tensile** **ISO 527 [139, 140]**	
Direction	**Warp**	**Weft** [a]
Length (mm)	250	90
Width (mm)	25	25
Thickness (mm)	2	2
Gauge length (mm)	150	30

[a] Dimensions are different from those specified in the standards/test method due to limited width of the carbon fibre tape.

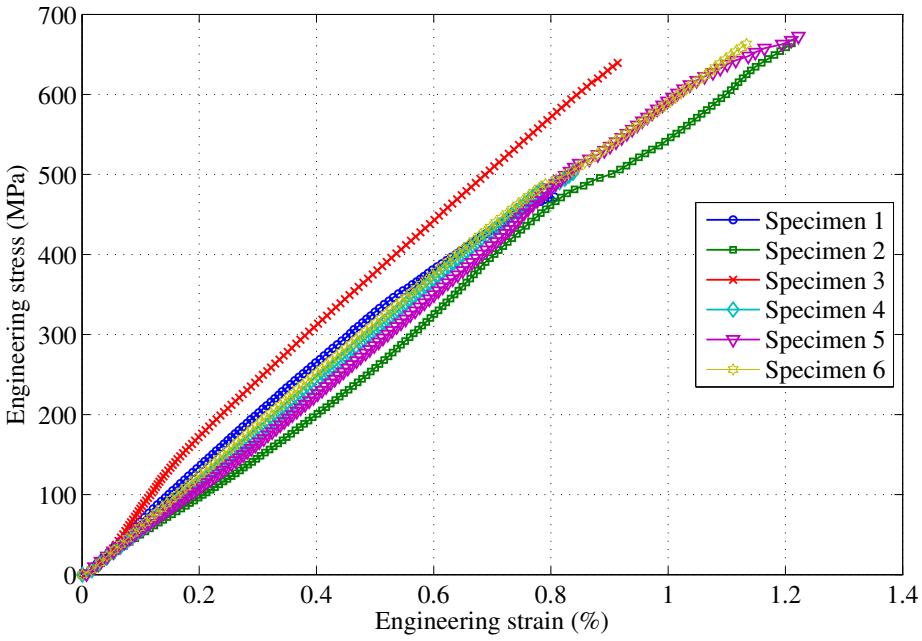


Figure A.1: Stress-strain curves of tensile test in warp direction (longitudinal).

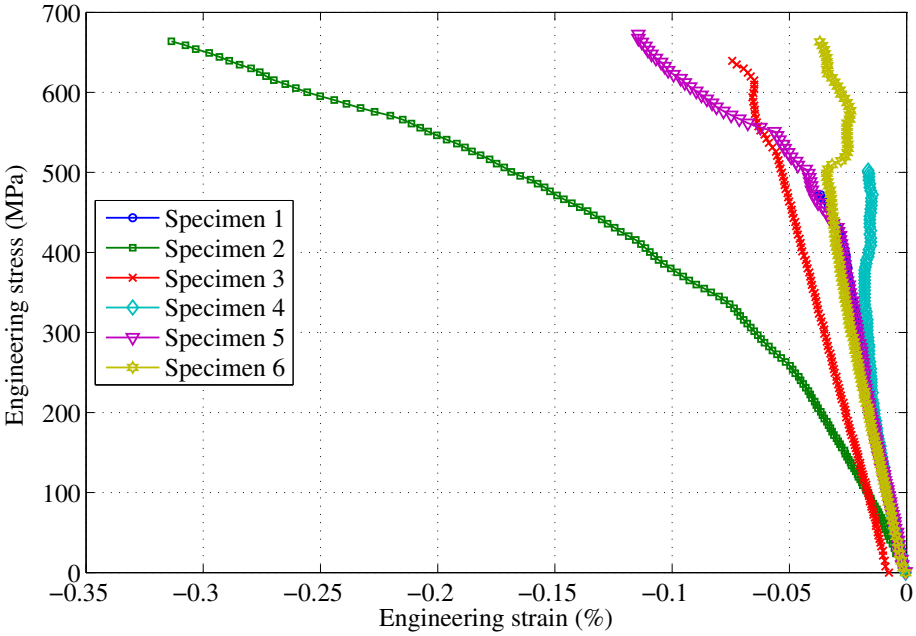


Figure A.2: Stress-strain curves of tensile test in warp direction (transverse).

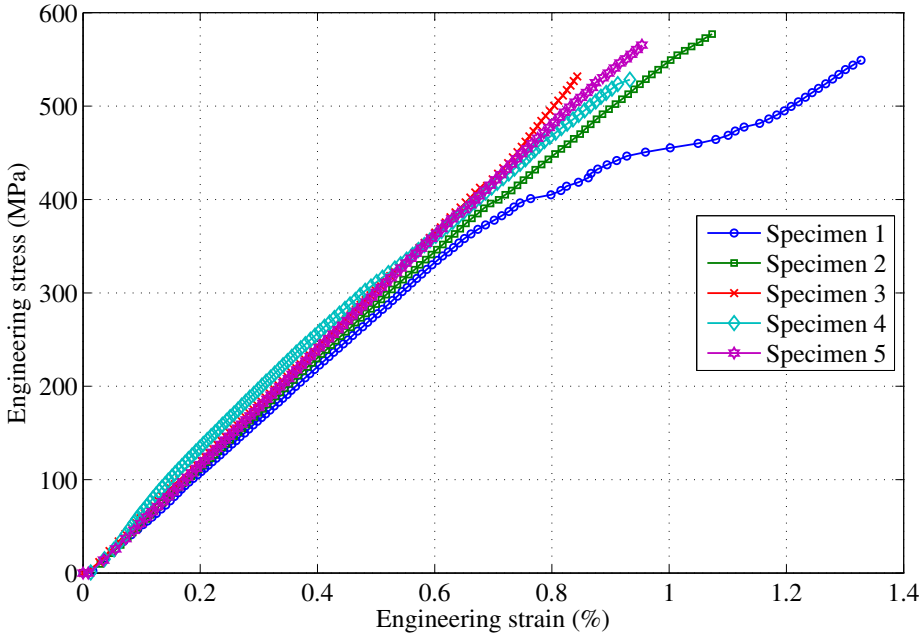


Figure A.3: Stress-strain curves of tensile test in weft direction (longitudinal).

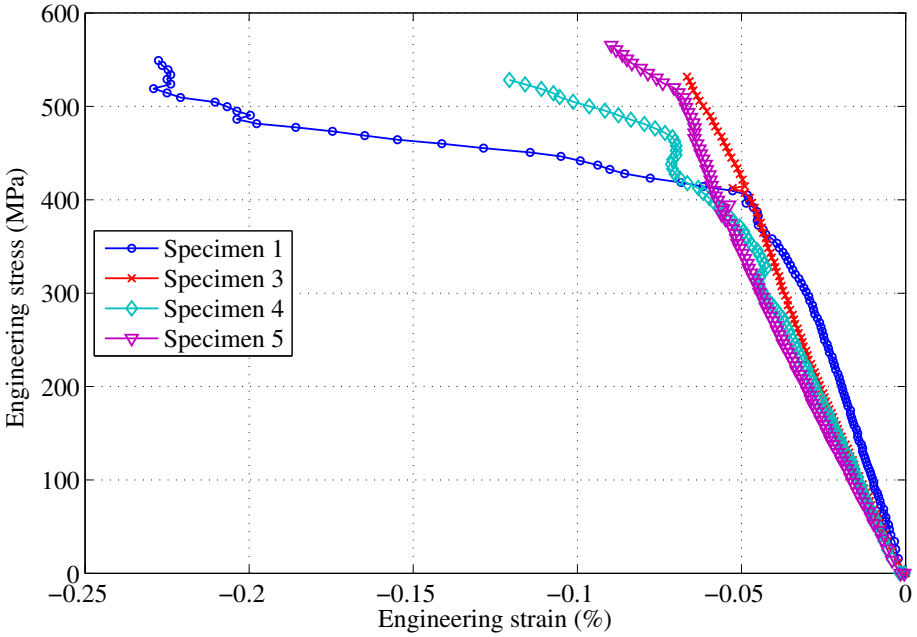


Figure A.4: Stress-strain curves of tensile test in weft direction (transverse).

From the stress-strain plots presented above, the Young's modulus of the carbon/polyurethane composite laminates are derived from the average slope of the stress-strain curves above nonlinear regime (approximately 0.2% strain). Moreover, the maximum strengths in warp and weft directions as well as the Poisson's ratio can also be evaluated and are presented in table A.2.

Table A.2: Raw data from tensile test.

Specimen number	E_{11} **(GPa)**	E_{22} **(GPa)**	UTS_{11} **(MPa)**	UTS_{22} **(MPa)**	ν_{12}
1	63.15	58.97	472.01	553.41	0.0446
2	54.94	61.86	663.72	577.15	0.0898
3	67.77	61.04	639.30	536.24	0.0927
4	64.62	71.41	502.18	528.29	0.0387
5	60.95	62.22	677.48	565.40	0.0429
6	63.40	-	663.10	-	0.0504
Average	62.47	63.10	602.97	552.10	0.0599
S.D.	3.94	4.31	83.15	18.03	0.022

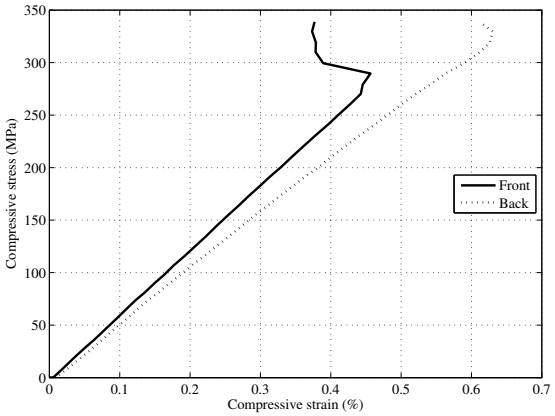
A.2 Compression Test

Similar to the tensile tests, compression tests were performed in the warp and weft directions. The specimens used in the compression tests were straight-sided with end-tabs at each end. The dimensions of the compressive specimens are shown in table A.3. Two uniaxial strain gauges were attached to the front side and the back side of the specimens in order to ensure that no column buckling occurred. The raw test results are shown in figures A.5, A.6 and A.7.

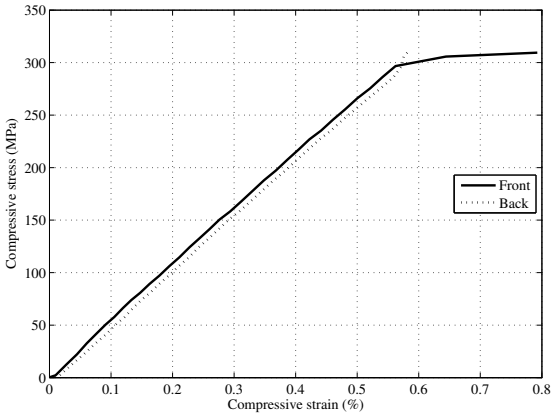
Table A.3: Dimensions of flat compressive specimens

Type of test Standards	**Compression ICSTM**	
Direction	**Warp**	**Weft** [a]
Length (mm)	100	85
Width (mm)	9.90	9.90
Thickness (mm)	4	4
Gauge length (mm)	10	10

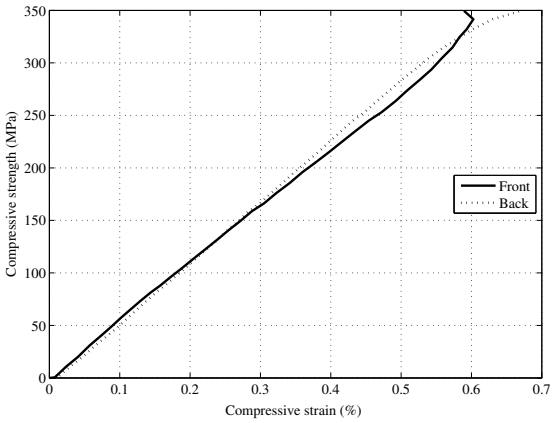
[a] Dimensions are different from those specified in the standards/test method due to limited width of the carbon fibre tape.



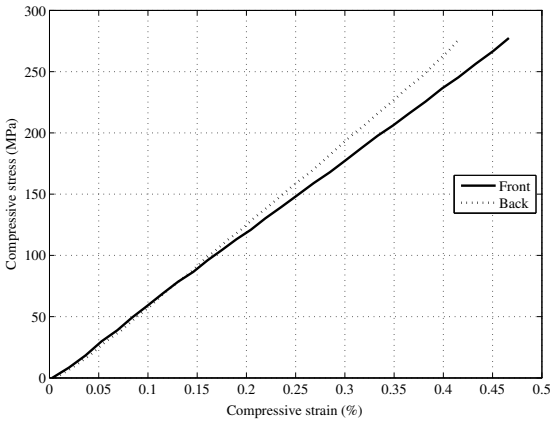
(a) Specimen 1



(b) Specimen 2

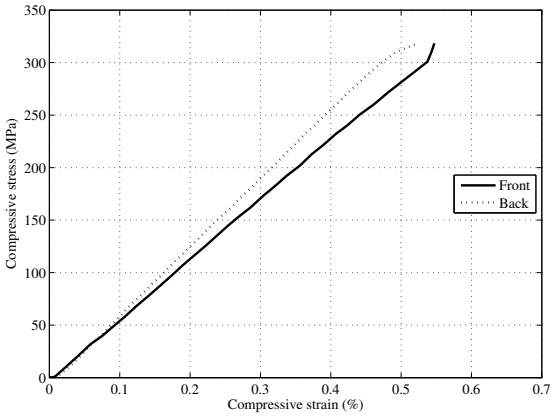


(c) Specimen 3

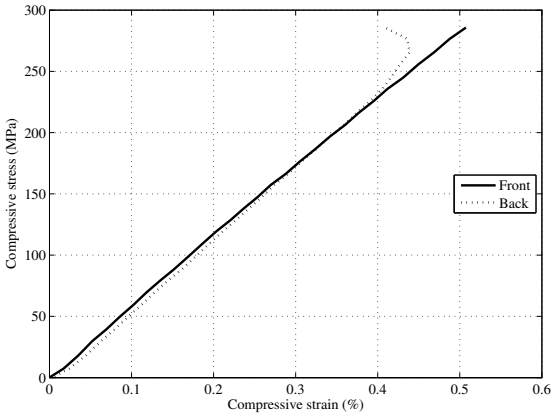


(d) Specimen 4

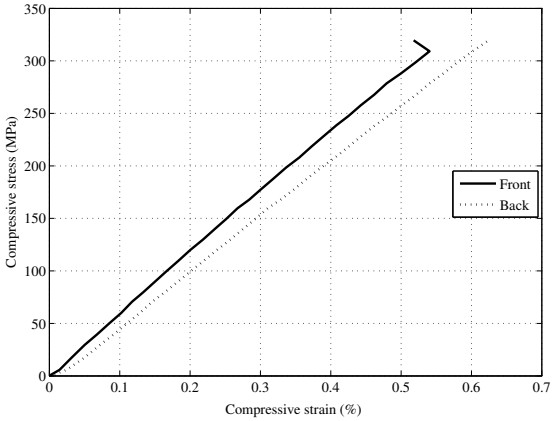
Figure A.5: Stress-strain curves of compressive specimens in warp direction.



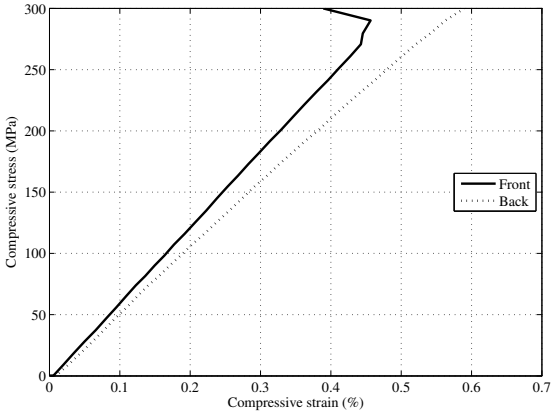
(a) Specimen 5



(b) Specimen 6

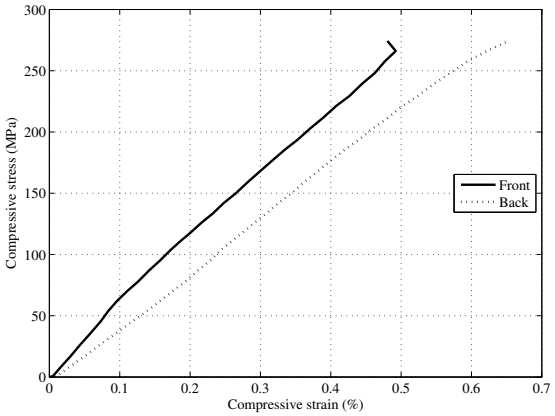


(c) Specimen 7

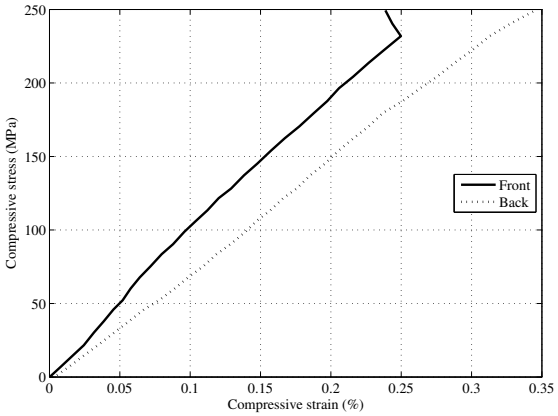


(d) Specimen 8

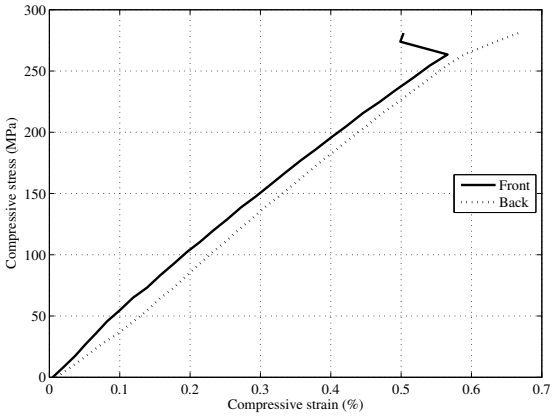
Figure A.6: Stress-strain curves of compressive specimens in warp direction (continued).



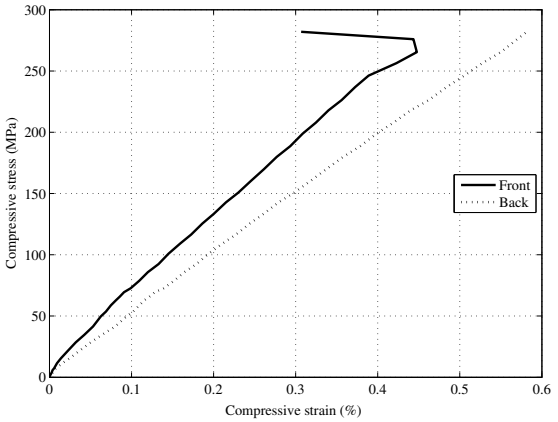
(a) Specimen 1



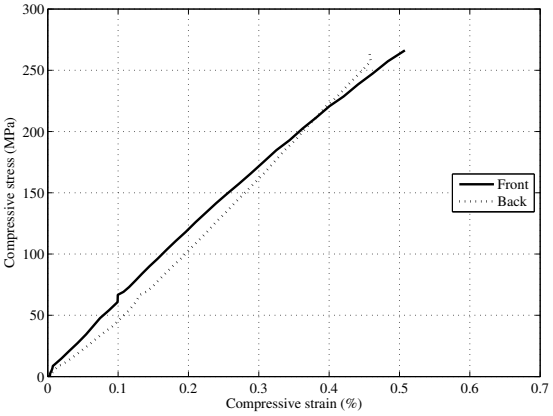
(b) Specimen 2



(c) Specimen 3



(d) Specimen 4



(e) Specimen 5

Figure A.7: Stress-strain curves of compressive specimens in weft direction.

In the compression test of the carbon/polyurethane composite laminates, the compressive moduli and strengths in warp and weft directions were evaluated from the stress-strain curves presented in figures A.5, A.6 and A.7. The compressive modulus and strength of each specimen and the average values are presented in table A.4.

Table A.4: Raw data from compression test.

Specimen number	$E_{c,11}$ **(GPa)**	UCS_{11} **(MPa)**	$E_{c,22}$ **(GPa)**	UCS_{22} **(MPa)**
1	57.46	289.62	49.71	266.04
2	53.20	296.71	84.75	240.38
3	55.02	341.57	48.98	263.46
4	62.72	277.42	54.11	275.91
5	61.44	318.42	55.49	266.22
6	58.72	276.59	-	-
7	55.86	309.12	-	-
8	57.57	290.15	-	-
Average	57.75	299.95	58.61	262.40
S.D.	2.98	20.69	13.31	11.80

A.3 In-plane Shear Test

The in-plane shear test was perform to experimentally measure the shear modulus and strength of the carbon/polyurethane composite laminates. The shear stress-strain curve of each specimen is shown in figure A.8. The shear modulus and the shear strength of each specimen and the average values are shown in table A.5.

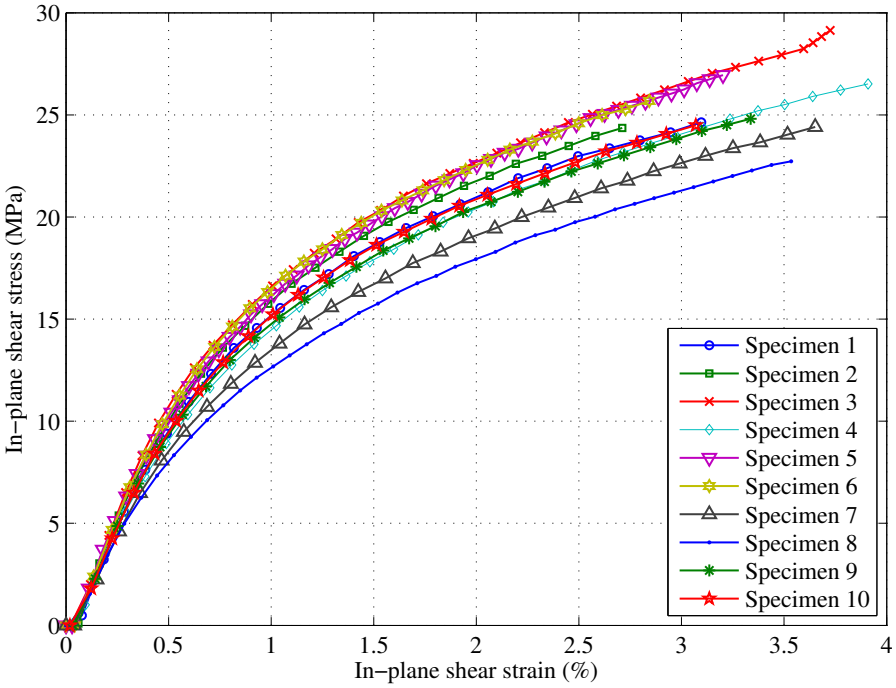


Figure A.8: Stress-strain curves of in-plane shear test.

Table A.5: Raw data from in-plane shear test.

Specimen number	G_{12} **(GPa)**	**Shear strength (MPa)**
1	2.11	38.62
2	2.19	38.45
3	2.22	40.55
4	1.98	37.34
5	2.16	38.57
6	2.22	39.72
7	1.82	36.14
8	1.68	35.59
9	1.99	37.51
10	2.01	38.54
Average	2.04	38.10
S.D.	0.17	1.43

A.4 Flexural test

The flexural test was performed to evaluate the moduli and strengths of carbon/polyurethane composite specimens in warp and weft directions. The raw data of from flexural test of each specimen is shown in tables A.6 and A.7 below.

Table A.6: Raw data from flexural test in warp direction.

Specimen number	E_f **(GPa)**	**Flexural strength (MPa)**
1	61.56	459.53
2	61.11	449.56
3	60.03	475.26
4	57.61	452.04
Average	60.08	459.10
S.D.	1.77	11.58

Table A.7: Raw data from flexural test in weft direction.

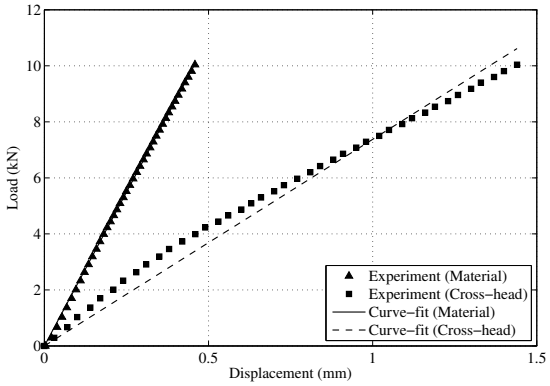
Specimen number	E_f **(GPa)**	**Flexural strength (MPa)**
1	47.16	360.64
2	45.87	367.76
3	47.37	369.07
Average	46.80	365.82
S.D.	0.81	4.54

A.5 Evaluation of machine compliance

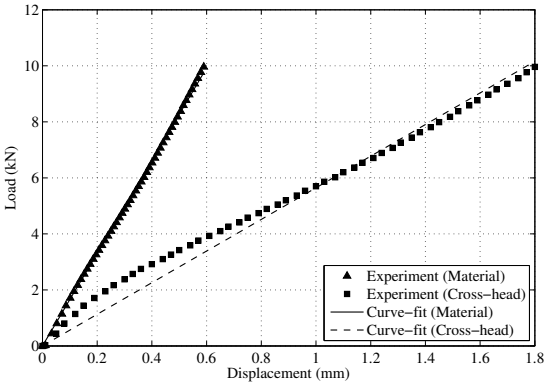
As discussed in chapter 3 that the compliance of the machine needs to be evaluated to correctly adjust the cross-head displacement measured from the testing machine in the case that strain gauges are not used. The procedure to evaluate the machine compliance involves the tensile test of a stiff material. Then the total compliance (C) of the testing fixture, which is the reciprocal of the stiffness (k), is a summation of the compliance of the material and the compliance of the machine [144, 145]. Therefore, the machine compliance can be calculated from equation A.1.

$$C_{Machine} = C_T - C_{Material}. \tag{A.1}$$

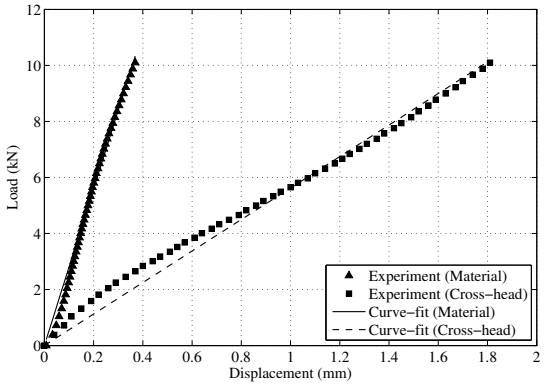
In this research, the results from the tensile testing of flat carbon/polyurethane composite laminates were used to calculate the compliance value of the testing machine. Figures A.9 and A.10 show load-displacement curves measured from the machine and the strain gauge of each specimen together with a curve-fit lines. The stiffnesses of each specimen can be directly obtained from the slope of the load-displacement curves.



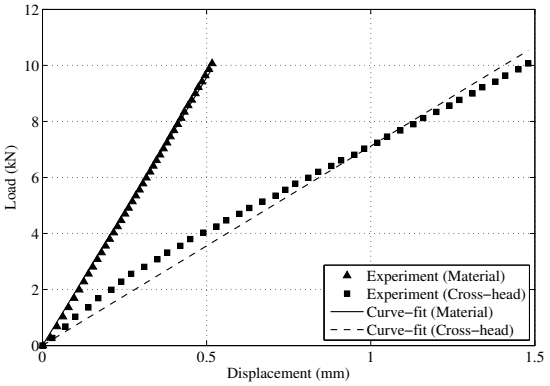
(a) Specimen 1



(b) Specimen 2

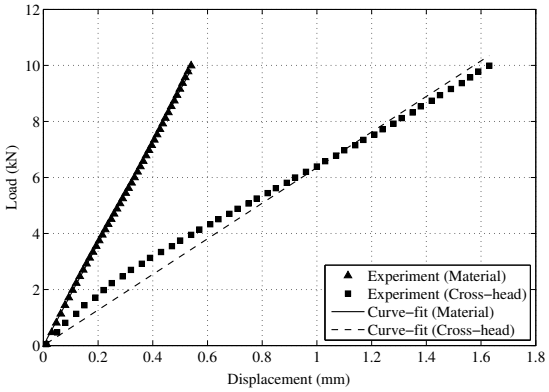


(c) Specimen 3

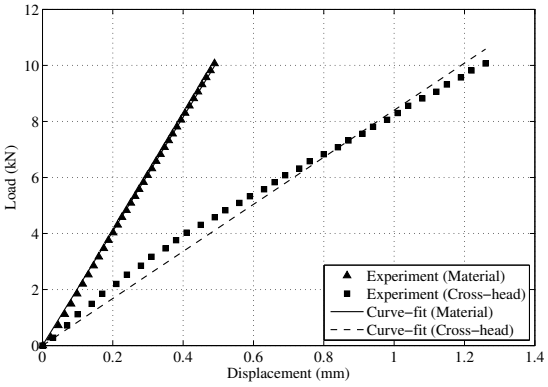


(d) Specimen 4

Figure A.9: Load-displacement curves measured from machine cross-head and strain gauge used to calculate the machine compliance.



(a) Specimen 5



(b) Specimen 6

Figure A.10: Load-displacement curves measured from machine cross-head and strain gauge used to calculate the machine compliance (continued).

Using equation A.1, the machine compliance can be calculated. The average value of the machine compliance is shown in table A.8.

Table A.8: Data used to calculate machine compliance.

Specimen number	$k_{Material}$ **(kN/mm)**	k_T **(kN/mm)**	$C_{Material}$ **(mm/kN)**	C_T **(mm/kN)**	$C_{Machine}$ **(mm/kN)**
1	21.949	7.374	0.046	0.136	0.090
2	16.538	5.645	0.060	0.177	0.117
3	28.008	5.623	0.036	0.178	0.142
4	19.128	7.118	0.052	0.141	0.088
5	18.233	6.351	0.055	0.157	0.103
6	20.394	8.401	0.049	0.119	0.070
Average	20.708	6.752	0.050	0.151	**0.102**
S.D.	3.673	0.992	0.008	0.022	0.023

A.6 Neat Resin Tensile Test

It was noticed after processing the tensile test results of the flat carbon/polyurethane composite laminates that the value of ultimate tensile strain was approximately 1%. Therefore, a neat resin tensile test was performed in order to check whether the maximum tensile strain of the resin matches the value stated in the technical data sheet provided by the manufacturer.

Figure A.11 shows stress-strain curves of the neat resin test of 5 specimens.

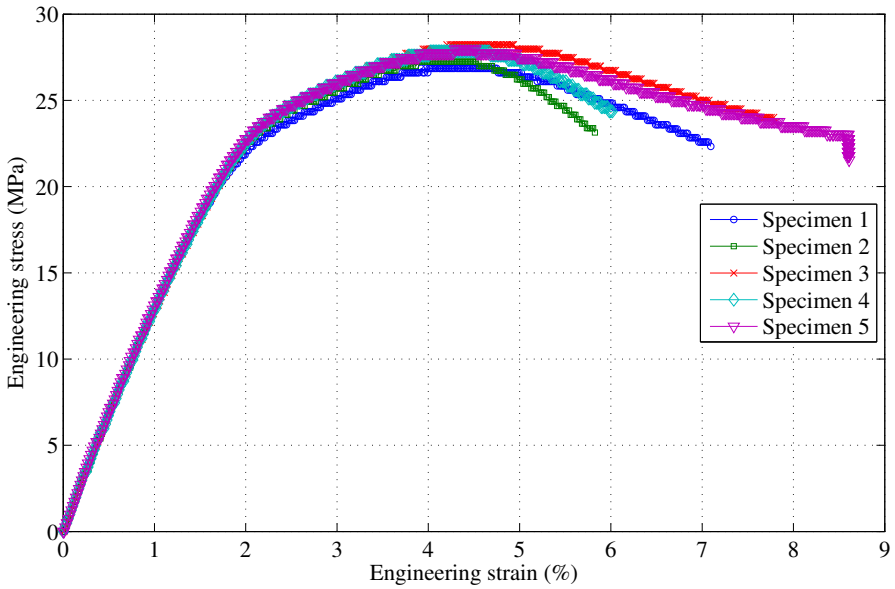


Figure A.11: Stress-strain curves of neat resin tensile test.

The Young's modulus and the maximum stress and strain of the polyurethane resin used in this research can be derived from the stress-strain curves shown in figure A.11. The Young's modulus is evaluated from the initial slope (0.2%strain) of the curves. These values are summarised and shown in table A.9.

Table A.9: Raw data from neat resin tensile test.

Specimen number	E **(MPa)**	**Maximum** σ **(MPa)**	**Maximum** ϵ **(%)**
1	1,301.09	26.85	7.25
2	1,290.62	27.24	6.00
3	1,279.69	28.22	7.98
4	1,273.87	27.84	6.21
5	1,308.01	27.96	8.70
Average	1,290.65	27.62	7.23
S.D.	12.74	0.50	1.03

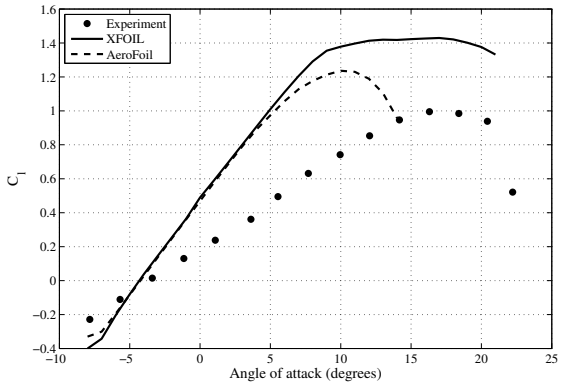
Appendix B

Wind Tunnel Test Results

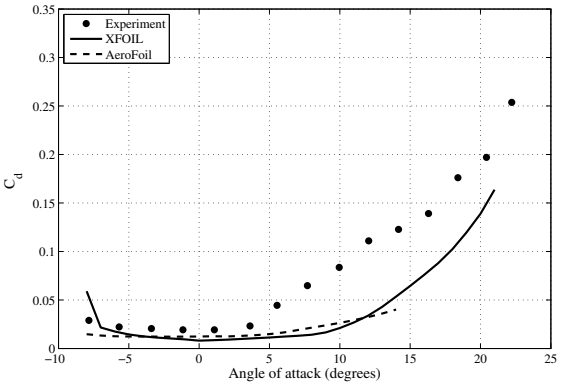
This appendix shows raw data of the wind tunnel testing of an aerofoil with corrugated lower surface and compared with a conventional aerofoil section with a plain flap.

B.1 Aerodynamic Characteristics of Conventional Wing (NACA 4412)

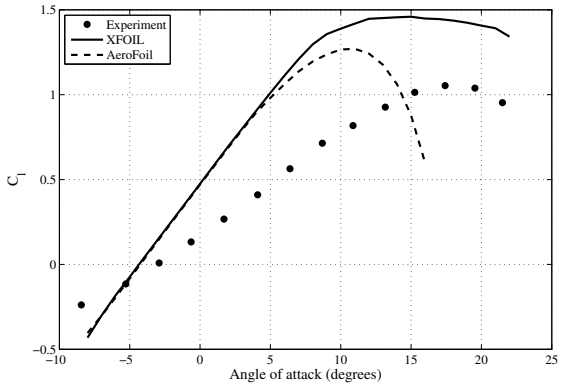
In this section, the conventional aerofoil with a plain flap was experimentally tested at different Reynolds numbers and the results were compared with analytical results obtained from XFOIL and AeroFoil 3.0. It can be clearly observed that the lift curve slope of the experiment does not match the lift curve slope of the analytical solution. The possible sources of error were discussed in chapter 4. Figures B.1 and B.2 show the lift and drag results at different Reynolds numbers ranging from 280,000 to 596,000.



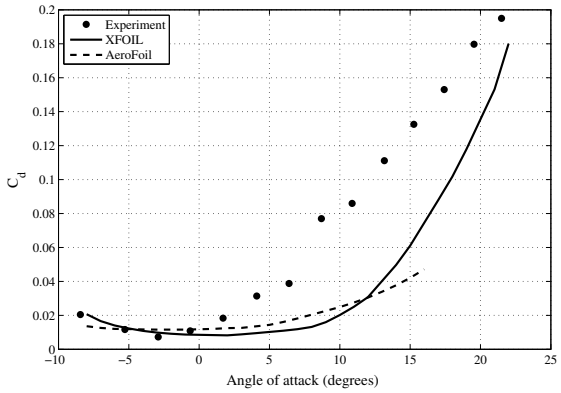
(a) Lift at Re = 280,000



(b) Drag at Re = 280,000

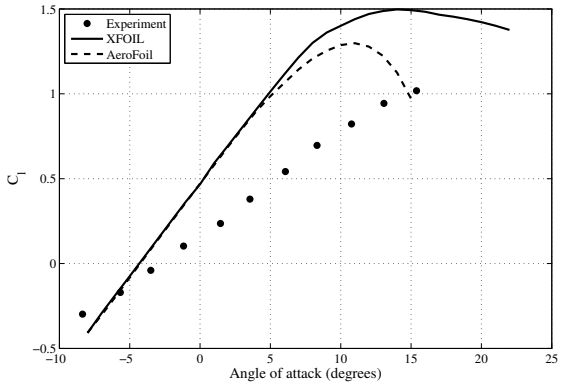


(c) Lift at Re = 397,000

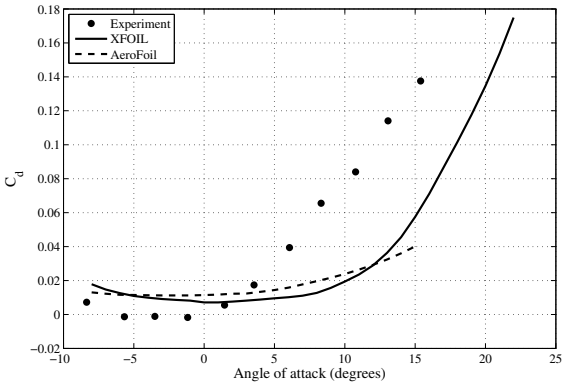


(d) Drag at Re = 397,000

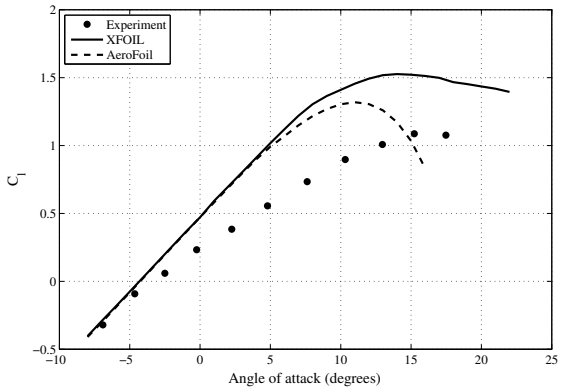
Figure B.1: Lift and drag curves of conventional wing at different Reynolds numbers.



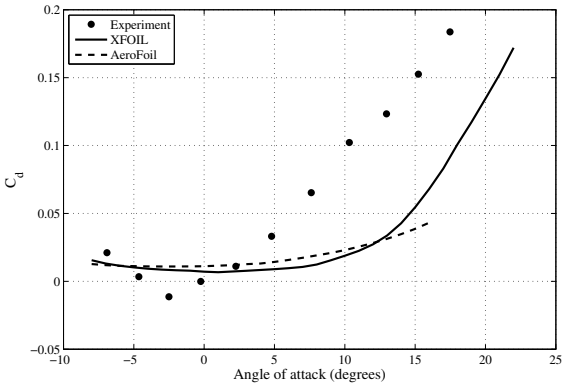
(a) Lift at Re = 497,000



(b) Drag at Re = 497,000



(c) Lift at Re = 596,000

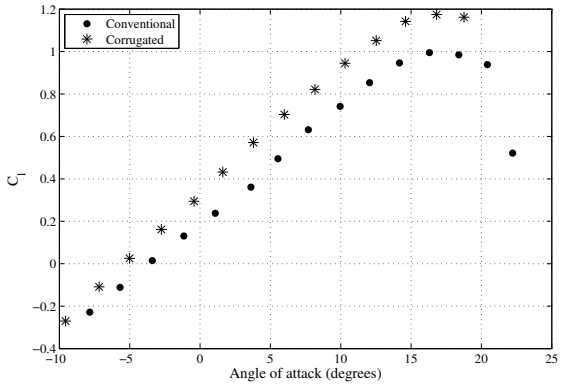


(d) Drag at Re = 596,000

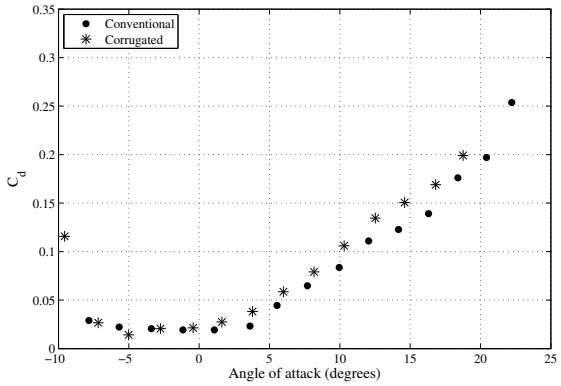
Figure B.2: Lift and drag curves of conventional wing at different Reynolds numbers (continued).

B.2 Comparison Between Conventional and Corrugated Wings

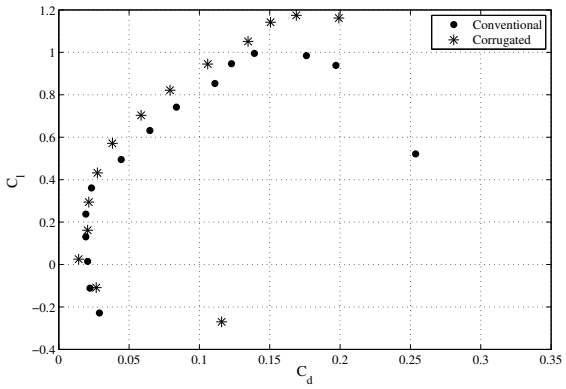
Figures B.3 to B.6 show the lift, drag and polar plots from the wind tunnel testing of corrugated aerofoil as compared against the conventional aerofoil with a plain flap. This was performed to evaluate the performance of each aerofoil at different Reynolds numbers.



(a) Lift curves

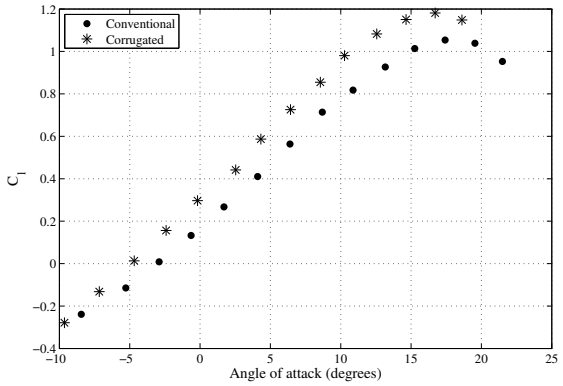


(b) Drag curves

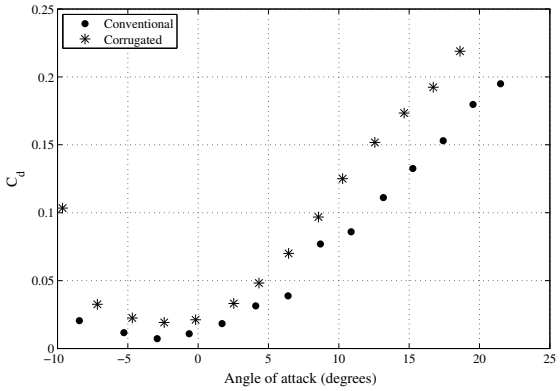


(c) Drag polar

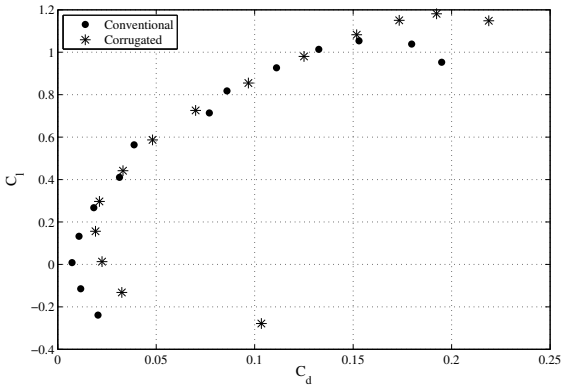
Figure B.3: Comparison of aerodynamic properties at Re = 280,000.



(a) Lift curves

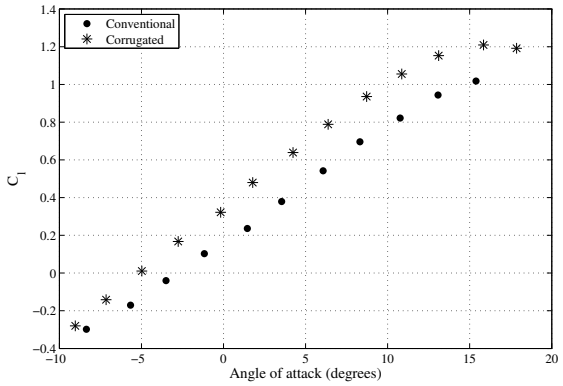


(b) Drag curves

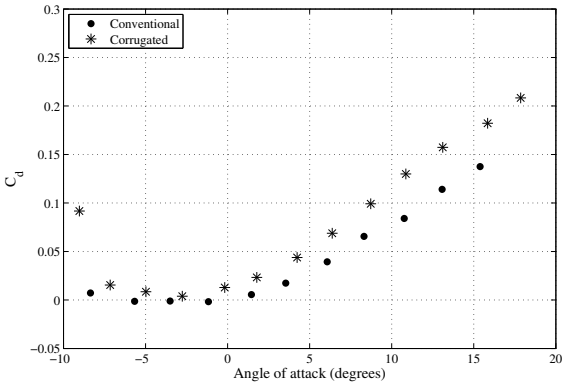


(c) Drag polar

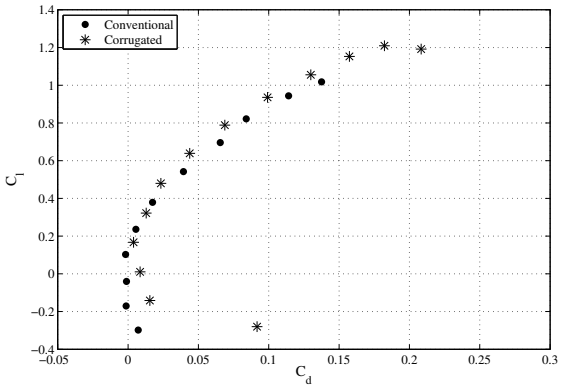
Figure B.4: Comparison of aerodynamic properties at Re = 397,000.



(a) Lift curves

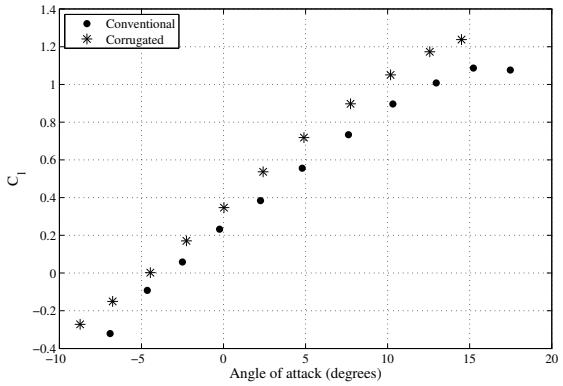


(b) Drag curves

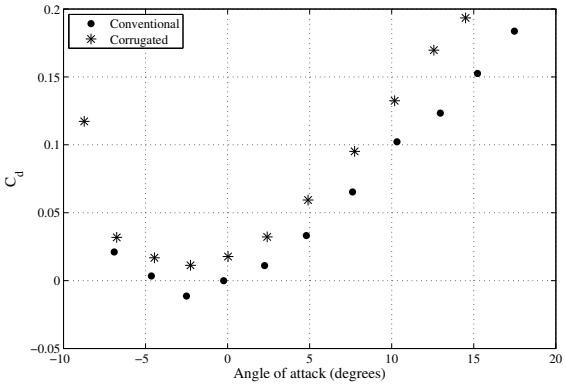


(c) Drag polar

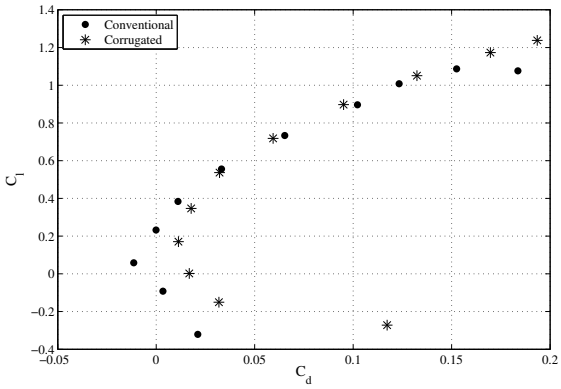
Figure B.5: Comparison of aerodynamic properties at Re = 497,000.



(a) Lift curves



(b) Drag curves



(c) Drag polar

Figure B.6: Comparison of aerodynamic properties at Re = 596,000.